Three-dimensional structure and scaling of a canonical turbulent boundary layer

by

Rahul Deshpande
ORCID ID : 0000-0003-2777-2919

Submitted in partial fulfilment of the requirements
of the degree of Doctor of Philosophy

April 2021

Department of Mechanical Engineering

THE UNIVERSITY OF MELBOURNE

Declaration of Authorship

This is to certify that:

- the thesis comprises only my original work towards the PhD except where indicated in the Preface,
- due acknowledgement has been made in the text to all other material used,
- the thesis is fewer than 100 000 words in length, exclusive of tables, maps, bibliographies and appendices.

Signed: Rahul Deshpande

Date: 19th January 2021

Abstract

Wall-bounded turbulent flows are pervasive in nature and are also encountered in many engineering applications; common examples include the flow over an airplane wing, or the atmospheric boundary layer over the Earth's surface, etc. A dominant feature present within these flows is the appearance of recurring eddies or so-called coherent structures that are highly three-dimensional (3-D) in geometry and are statistically significant over a wide range of scales. This has led to the proposal of various coherent structure-based models in the literature, with the attached eddy model (AEM) of wall-turbulence being the most popular amongst them. Their predictive capabilities, however, are still lacking due to the dearth of 3-D information on the coherent motions which they model. The present thesis reports a new and unique set of multi-point hotwire measurements conducted in a frictional Reynolds number, $Re_\tau \sim \mathcal{O}(10^4)$ canonical turbulent boundary layer (TBL) to reconstruct the 3-D statistical picture of these energy-containing motions. The measurements are complemented by performing a similar reconstruction using published direct numerical simulation datasets at $Re_\tau \sim \mathcal{O}(10^3)$, thereby facilitating an examination of the scaling of these structures, in flows spanning over a decade of Re_τ. Results of these investigations provide direct empirical support towards the AEM, with the prospect of further enhancing its efficiency by defining the representative eddy geometry based on data-driven estimates.

The first part of the thesis focuses on investigating characteristics of the inertially dominated wall-coherent structures (i.e. the ones extending down to the wall), which are responsible for the increased skin-friction in high-Re_τ TBLs. Their geometric characteristics are investigated in the wall-parallel plane by estimating, for the first time, the 2-D cross-spectrum of the streamwise velocity using the synchronous velocity fluctuations measured at a log-region (z_o) and near-wall (z_r) location. Constant energy contours of this spectrum, which are representative of the energy distribution across the range of streamwise (λ_x) and spanwise (λ_y) wavelengths, are found to follow the $\lambda_x/z_o \approx 7(\lambda_y/z_o)$ relationship in the large-scale range, indicative of geometric self-similarity. This suggests that a self-similar structure conforming to Townsend's attached eddy hypothesis (Townsend, 1976) is ingrained in the flow, and can be conceptually modelled using the AEM framework given by Perry and Chong (1982). The very-large-scale wall-coherent structures (i.e. the superstructures), on the other hand, do not conform to Townsend's attached eddies and are found to have a similar spanwise width as the largest motions in the self-similar hierarchy. This result, which is found via a scale-specific coherence analysis of the velocity fluctuations, also reveals the periodic organization of the superstructures along the spanwise direction. Finally, an analysis of the scale-specific phase of the coherence reveals

the streamwise inclination angle of the large wall-coherent motions, which is found to be nominally 45°. This fulfills the minimum geometric information required to statistically model these energetic wall-coherent motions based on the AEM.

The second part of the thesis focuses on investigating the range of energy-containing structures coexisting in the log-region, which contribute significantly to the bulk turbulence production in high-Re_τ wall-bounded flows. Townsend (1961) hypothesized that these structures can be segregated into active and inactive motions, where the active motions are solely responsible for producing the Reynolds shear stress, the key momentum transport term in these flows. While the wall-normal component of velocity is associated exclusively with the active motions, the wall-parallel components of velocity are associated with both active and inactive motions. To test this hypothesis, the present study proposes a methodology to segregate the active and inactive components of the 2-D energy spectrum (Φ_{ii}, where i denotes the velocity-component) at z_o, thereby permitting to test the self-similarity characteristics of the former which are central to theoretical models for wall-turbulence. The methodology utilizes the multi-point dataset, in conjunction with a spectral linear stochastic estimation-based procedure, to linearly decompose the total energy at z_o (Φ_{ii}) into contributions predominantly from the active (Φ^a_{ii}) and inactive (Φ^{ia}_{ii}) motions. This is confirmed by Φ^a_{ii} exhibiting wall-scaling for both λ_x and λ_y. The Reynolds shear stress cospectra, estimated solely from the active contributions, is also found to closely match the one obtained conventionally from the dataset, thereby providing direct empirical support for the concept of active and inactive motions. Both Φ^a_{ii} and Φ^{ia}_{ii} contours are found to depict geometric self-similarity in the log-region, suggesting that this entire region can be conceptually modelled using the AEM framework. Inactive contributions from the attached eddies also bring out the pure k^{-1}-scaling for the associated 1-D spectra (where k is the streamwise/spanwise wavenumber), lending further empirical support to the AEM.

Preface

This thesis is submitted under the 'thesis-with-publications' category outlined in the Graduate Research Training Policy of The University of Melbourne, Australia. Each of the published papers/conference proceedings have been included as an individual chapter of the thesis. Chapters 4, 6, 7 and 9 have been published in peer-reviewed journals while chapters 5 and 8 have been published as peer-reviewed conference proceedings.

I was the main contributor to all the work, and was responsible for all phases of the research reported in this thesis. I developed the conceptual framework, designed and conducted all the experiments, analyzed the data and wrote the manuscripts. My thesis supervisors, Prof. Ivan Marusic and Prof. Jason Monty, supervised the entire project and contributed to the manuscript preparation. My colleague, Dr. Dileep Chandran contributed to the publication used in chapter 4. Apart from the aforementioned co-authors, the quality of the manuscripts was also enhanced by the inputs from the anonymous referees during their respective peer-review process. The details of the published chapters, and my relative contribution to each one of them is outlined below:

- *Chapter 4:* Published by the Journal of Fluid Mechanics on 2^{nd} March, 2020. Personal contribution: 55%. Reference: **Deshpande, R.**, Chandran, D., Monty, J.P. & Marusic, I. (2020). Two-dimensional cross-spectrum of the streamwise velocity in turbulent boundary layers. *Journal of Fluid Mechanics* 890, R2. DOI: https://doi.org/10.1017/jfm.2020.139.

- *Chapter 5:* Published in the Proceedings of the 22^{nd} Australasian Fluid Mechanics Conference. Personal contribution: 60%. Reference: **Deshpande, R.**, Monty, J.P. & Marusic, I. (2020). Large-scale spanwise periodicity in a canonical turbulent boundary layer. In *Proceedings of 22nd Australasian Fluid Mechanics Conference, Brisbane, Australia.* DOI: https://doi.org/10.14264/933c23f.

- *Chapter 6:* Published by the Journal of Fluid Mechanics on 2^{nd} September, 2019. Personal contribution: 60%. Reference: **Deshpande, R.**, Monty, J.P. & Marusic, I. (2019). Streamwise inclination angle of large wall-attached structures in turbulent boundary layers. *Journal of Fluid Mechanics* 877, R4. DOI: https://doi.org/10.1017/jfm.2019.663.

- *Chapter 7:* Published by the Journal of Fluid Mechanics on 5^{th} March, 2021 Personal contribution: 60%. Reference: **Deshpande, R.**, Monty, J.P. & Marusic, I. (2021). Active and inactive components of the streamwise velocity in wall-bounded turbulence. *Journal of Fluid Mechanics* 914, A5. DOI: https://doi.org/10.1017/jfm.2020.884.

- *Chapter 8:* Published in the Proceedings of the 22^{nd} Australasian Fluid Mechanics Conference. Personal contribution: 60%. Reference: **Deshpande, R.**, Monty, J.P. & Marusic, I. (2020). Active and inactive motions in wall turbulence. In *Proceedings of 22nd Australasian Fluid Mechanics Conference, Brisbane, Australia.* DOI: https://doi.org/10.14264/ad70392.

- *Chapter 9:* Published by the Experiments in Fluids journal on 2^{nd} March, 2020. Personal contribution: 60%. Reference: **Deshpande, R.**, Monty, J.P. & Marusic, I. (2020). A scheme to correct the influence of calibration misalignment for cross-wire probes in turbulent shear flows. *Experiments in Fluids* 61(85). DOI: https://doi.org/10.1007/s00348-020-2918-8.

While the main content in each of these chapters is the same as the corresponding papers, certain terminology and symbols (from the original papers) have been changed in order to ensure the coherency of the thesis. Parts of the thesis have also been presented/selected for presentation at the following conferences:

- **Deshpande, R.**, Monty, J.P. & Marusic, I. Spatial organization of wall-coherent and incoherent structures in turbulent boundary layers. *25^{th} International Congress on Theoretical and Applied Mechanics*, to be held in Milano, Italy in August 2021.

- **Deshpande, R.**, Monty, J.P. & Marusic, I. Dissecting turbulent boundary layers: uncovering the organized flow in the log-region. *GKB100: Fluid mechanics in the spirit of G. K. Batchelor*, to be held in DAMTP, University of Cambridge, UK in March 2021.

- **Deshpande, R.**, Chandran, D., Monty, J.P. & Marusic, I. Towards data-driven modelling of coherent motions in wall turbulence. *Division of Fluid Dynamics 2020 Meeting of The American Physical Society*, organized via a virtual platform from Chicago, USA in November 2020.
- **Deshpande, R.**, Monty, J.P. & Marusic, I. Correcting hotwire misalignment errors for wall-bounded turbulence measurements. *11^{th} International Symposium on Turbulence and Shear Flow Phenomena*, organized in Southampton, UK in July 2019 (Deshpande et al., 2019b).

I was fortunate to be awarded with several scholarships and travel grants to support myself financially during my PhD. My participation in the aforementioned conferences would have been impossible without the financial support I received from these travel grants, as well as from the research grant (from ARC) which sponsored my research. Here, I would like to acknowledge the various institutions for financially supporting me during my PhD:

- *Melbourne Research Scholarship* from The University of Melbourne.
- *Rowden White Scholarship*, established with a donation from Sir Alfred Edward Rowden White, from The University of Melbourne.
- *Conference Travel/Professional Development bursary* from the Melbourne School of Engineering, The University of Melbourne.
- *Conference Travel Scholarship* funded by the Melbourne School of Engineering, The University of Melbourne.
- *Burgers Program for Fluid Dynamics* at the University of Maryland for facilitating my participation in the Turbulence Summer School, 2018.
- *ICTAM travel grant* to attend the ICTAM 2020+1 in Milano, Italy.
- *Discovery project grant* from the Australian Research Council (ARC), DP180100447.

Acknowledgements

The training I received during my PhD journey gave me an insight into the academic way of life, and an opportunity to look at the world through the lens of an academic. And to be able to experience this under the guidance of very senior and renowned researchers, namely my supervisors Prof. Ivan Marusic and Prof. Jason P. Monty, is something for which I consider myself as extremely blessed. I would like to thank them for the time and effort they invested into nurturing me as a researcher. The countless meetings I had with them, from discussing fluid mechanics to cricket, would always be cherished.

I am grateful to my graduate committee members, Prof. Nicholas Hutchins and Dr. Simon Illingworth, for not only ensuring that my thesis progresses as per schedule, but also providing several technical suggestions towards my experiments and data analysis. Besides the senior academic staff, I would also like to thank the following Research Fellows and senior colleagues in the Fluids group: Drs. Dileep Chandran, Rio Baidya, Charitha de Silva, Woutijn Baars and Anagha Madhusudanan, for helpful discussions related to the work and experiments presented in this thesis. I consider myself extremely fortunate to have got a chance to interact and learn about their work in person, which has profoundly inspired the work in this thesis.

I am grateful to the turbulence research groups at Madrid and Texas, headed by Profs. Jimenez and Moser respectively, for making their direct numerical simulation (DNS) datasets publicly available. The new experiments presented in this thesis could be conducted in a smooth and well-planned manner only due to the availability of these datasets. I must acknowledge contributions from the technical support staff in the Fluids group, Messrs Geoff Duke, Derek Jacquest and William Ross, for their help in building my experimental setup. Thanks are also due to the administrative staff of the Mechanical Engineering department, Ms. Kim Robinson, Jan May and Caroline Barrie, who assisted me with proof reading of my articles, managing tutoring responsibilities, etc.

I owe a special thanks to the fellow PhD students in the Fluids group, who were like an extended family to me in Melbourne. Amongst them, I would like to particularly thank Mr. Tushar Sikroria and Dr. Vijay Gudla, who were also very supportive flatmates. I would always be grateful for your company during our weekend cafe visits, and for the various engaging chats during these last 3.5 years. I would also like to thank my fellow PhD friends from the 'Saturday dinner' group: Shaktivesh, Tanmay, Deepak, Achyut, Aravind and Shubham for the very memorable weekend meet-ups and travels we did together.

I would like to acknowledge Prof. Sanjay Mittal's research group at IIT Kanpur, where I got my first research experience as a Masters student, which eventually encouraged me to take up a PhD. I believe that my experiences at both my alma maters – IIT (BHU) Varanasi and IIT Kanpur, have helped me get through my PhD, for which I am very grateful. Last but not the least, I would like to thank my family – my wife Shivani, parents and my sister, for their unconditional love and support throughout my PhD. This wouldn't have been possible without the essential teachings I got from them, as a family. I am also grateful to the support offered by Mr. Milind Kabir and family, who never let me feel I was away from home, throughout my stay in Melbourne.

Contents

Declaration of Authorship ii

Abstract iii

Preface v

Acknowledgements viii

List of Figures xiv

List of Tables xxv

Nomenclature xxvii

1 Introduction 1
- 1.1 Motivation . . . 2
- 1.2 Aims and thesis outline . . . 5

2 Review of the relevant literature 9
- 2.1 The boundary layer concept . . . 9
- 2.2 Classical scaling arguments . . . 11
  - 2.2.1 Mean velocity profile . . . 11
  - 2.2.2 Townsend's local equilibrium hypothesis . . . 14
  - 2.2.3 Spectral scaling arguments . . . 15
- 2.3 Coherent structures in wall-turbulence . . . 20
  - 2.3.1 Inner-outer interactions . . . 25
  - 2.3.2 Taylor's hypothesis . . . 28
- 2.4 Attached eddy model of wall-turbulence . . . 28
  - 2.4.1 Attached eddy model of Perry and Chong (1982) . . . 30
- 2.5 Evidence of the geometric self-similarity in a wall-bounded flow . . . 33
  - 2.5.1 k_x^{-1}-scaling law . . . 33
  - 2.5.2 Two-dimensional energy spectrum . . . 35

2.5.3 Energy decomposition using linear stochastic estimation 38
2.5.3.1 Data-driven decomposition: spectral linear stochastic estimation 40
2.5.3.2 Data driven filter: linear coherence spectrum 41

3 Experimental details **44**
3.1 Wind tunnel facilities 44
3.1.1 HRNBLWT 44
3.1.1.1 Sensor traversing systems used for measurements 46
3.1.1.2 Sensor positioning 48
3.1.1.3 Pressure measurement 50
3.1.2 Channel flow facility 51
3.1.2.1 Traversing and sensor alignments 52
3.1.2.2 Pressure measurement 53
3.2 Multi-point single-wire measurements 53
3.2.1 Hotwire sensors and anemometry details 53
3.2.2 Probe calibration 55
3.2.3 The measurement campaign 55
3.3 Single-point X-probe measurements 61
3.3.1 X-wire probe 61
3.3.1.1 Effective angle method 63
3.3.2 The measurement campaign 64
3.3.3 Hotwire anemometry details 67
3.3.4 2-D calibration 68

4 Two-dimensional cross-spectrum of the streamwise velocity in turbulent boundary layers **71**
4.1 Preface to the chapter 71
4.2 Abstract 72
4.3 Introduction and motivation 72
4.4 Experimental and numerical data 75
4.5 Results and discussions 78
4.5.1 Physical interpretation of $\Phi_{uu}^{cross,w}$ and how it differs from Φ_{uu} . . . 78
4.5.2 Low versus high Re_τ 2-D spectra 80
4.5.3 Is a wall-filter sufficient to extract purely self-similar structures? . . 84
4.6 Concluding remarks 86

5 Large-scale spanwise periodicity in a canonical turbulent boundary layer **87**
5.1 Preface to the chapter 87
5.2 Abstract 88
5.3 Introduction 88
5.4 Experimental and numerical data 90
5.5 Results 91
5.5.1 Large-scale spanwise periodicity 93
5.5.2 Self-similarity of the wall-coherent motions 94

5.6 Conclusions . . . 96
5.7 Acknowledgements . . . 96

6 Streamwise inclination angle of large wall-coherent structures in turbulent boundary layers 97
6.1 Preface to the chapter . . . 97
6.2 Abstract . . . 98
6.3 Introduction . . . 98
6.4 Methodology adopted to isolate large wall-coherent structures . . . 101
6.5 Experimental and numerical data . . . 102
6.6 Results and discussions . . . 105
6.6.1 Variation in scale-specific wall-coherence with spanwise offset . . . 105
6.6.2 Variation of mean structure inclination angle with spanwise offset . . . 106
6.6.3 Scale-specific inclination angle of wall-coherent structures . . . 108
6.6.4 Implications on LES and AEH-based simulations . . . 110
6.7 Concluding remarks . . . 111

7 Active and inactive components of the streamwise velocity in wall-bounded turbulence 113
7.1 Preface to the chapter . . . 113
7.2 Abstract . . . 114
7.3 Introduction and motivation . . . 114
7.3.1 Active and inactive motions . . . 116
7.3.2 Present contributions . . . 118
7.4 ZPG TBL datasets . . . 119
7.4.1 Multi-point measurements at $Re_\tau \approx 14\,000$ . . . 120
7.4.2 DNS dataset . . . 123
7.5 Energy decomposition into active and inactive contributions . . . 124
7.6 Active component of the streamwise velocity spectrum . . . 127
7.7 Inactive component of the streamwise velocity spectrum . . . 130
7.7.1 Inactive contributions from the self-similar attached eddies . . . 132
7.8 Concluding remarks . . . 135

8 Active and inactive motions in wall turbulence 141
8.1 Preface to the chapter . . . 141
8.2 Abstract . . . 142
8.3 Introduction . . . 142
8.4 Experimental and numerical data . . . 147
8.4.1 High-Re_τ experimental dataset . . . 149
8.4.2 Low-Re_τ DNS datasets . . . 150
8.5 Methodology to decompose inactive and active contributions to the total energy . . . 150
8.6 Active motions . . . 153
8.6.1 Reynolds shear stress co-spectra . . . 154
8.7 Conclusions . . . 156

8.8 Acknowledgements 157

9 A scheme to correct the influence of calibration misalignment for cross-wire probes in turbulent shear flows 158
9.1 Preface to the chapter 158
9.2 Abstract 159
9.3 Introduction 159
9.4 Experimental set-up 163
9.4.1 Physical experiments 163
9.4.1.1 Flow facilities 163
9.4.1.2 Hotwire sensor and anemometry details 164
9.4.1.3 Probe calibration and data processing technique 165
9.4.2 Synthetic experiments 167
9.5 2-D calibration misalignment 168
9.5.1 2-D calibration misalignment: identification and subsequent processing 169
9.5.2 2-D calibration misalignment: effect on velocity statistics and spectra 170
9.6 Correction scheme 173
9.6.1 Re_τ-invariance of the turbulent kinetic energy in the small scales . . 173
9.6.2 Defining the correction scheme 175
9.7 Comparing uncorrected and corrected statistics 178
9.8 Summary of the steps for implementing the correction scheme 180
9.9 Summary and conclusions 180
9.10 Appendix A: accounting for the drift in hotwire voltage 182
9.11 Appendix B: methodology to correct the time series of v or w 183
9.12 Appendix C: investigating the effect of X-probe spatial resolution 184
9.13 Appendix D: database of energy spectra obtained from synthetic experiments 186

10 Conclusions 187
10.1 Summary and conclusions 187
10.1.1 Attached eddy modelling of the wall-coherent motions 188
10.1.2 Attached eddy modelling of the inertial region 190
10.2 Possible directions for future work 191

Bibliography 193

List of Figures

1.1 A flowchart depicting the structure of the present thesis. 6

2.1 (a) Tangential velocity profile in a laminar boundary layer on a flat plate made visible by tellurium. (b) A turbulent boundary layer made visible by a vertical light sheet illuminating the tiny oil droplets introduced into the flow. U_∞ refers to the mean freestream speed and dashed red lines in (b) highlight 'eddies' of various sizes in the turbulent flow. Both (a,b) have been adapted from Van Dyke (1982). 10

2.2 (a) Simplified schematic of a streamwise developing turbulent boundary layer over a flat plate with freestream velocity, U_∞. (b) Schematic showing the mean velocity profile at a particular streamwise position, X along with the different flow regions proposed for a turbulent boundary layer based on the scaling arguments. 12

2.3 Summary of the scalings exhibited by various spectral regions in the 1-D streamwise u-spectra in the logarithmic region. Adapted from Perry et al. (1986). 16

2.4 Schematic of the expected distributions of the premultiplied u-spectra with (a) inner-flow scaling and (b) outer-flow scaling. Adapted from Perry et al. (1986). 16

2.5 Summary of the scalings exhibited by various spectral regions in the 1-D streamwise w-spectra in the logarithmic region. Adapted from Perry et al. (1986). 19

2.6 Schematic of the expected distributions of the premultiplied w-spectra with (a) inner-flow scaling and (b) outer-flow scaling. Adapted from Perry et al. (1986). 19

2.7 Hairpins as a dominant coherent structure in a wall-bounded flow: (a) Theodorsen's (1952) conceptualization of a horseshoe/hairpin vortex. (b) Hairpin vortices observed via flow visualization in a boundary layer (Perry and Chong, 1982). (c) Hairpin-shaped structures observed in the instantaneous field obtained from DNS of a ZPG TBL by Wu and Moin (2009). (d,e) Organization of hairpins as a packet to form larger 'ramp-like' structures conceptualized (in (e)) by Head and Bandyopadhyay (1981) based on their flow visualization in (d). Blue arrow indicates mean flow direction. . . 22

2.8 (a) Scenario of nested packets of hairpins (in yellow) in a boundary layer conceptualized and illustrated by Adrian et al. (2000). They hypothesized the packets to be aligning along streamwise direction to create long streamwise momentum zones (in blue), with speeds lower than the mean streamwise velocity. (b) Three-dimensional plot of the conditional-averaged velocity field obtained from a DNS of a turbulent channel flow by del Álamo et al. (2006). Red and blue isosurfaces represent low and high speed regions, while the green isosurface represents the discriminant of the velocity gradient tensor, which can be considered surrogate of the vorticity. Blue arrow indicates direction of the mean flow velocity. 24

2.9 (a) Energy exchange cycle representing the 'bottom-up' transport of energy. A, B and C represent three successive ejections ($u < 0$, $w > 0$) carrying energy away from wall, which after a certain distance gives rise to a sweep ($u > 0$, $w < 0$) which moves towards the wall. (b) Schematic showing the very-large-scale-motions or superstructures extending from the log-region down to the wall, to superpose their signature as well as modulating the near-wall region. These regulate the 'top-down' transport of energy which is non-local. Figures (a) and (b) have been adapted from Offen and Kline (1975) and Marusic et al. (2010a), respectively. 26

2.10 Schematic depicting three hairpin vortices as representative attached eddies of varying heights ($\mathcal{H}_i$), along with the associated streamline pattern generated by each eddy. Adapted from Perry et al. (1986). 30

2.11 (a) Seven representative Λ-hairpin vortices arranged along the streamwise direction (with spacing Δx) to form a hairpin packet representative of an eddy of height, $\mathcal{H}$. Here, solid lines indicate vortex rods. (b) Streamwise velocity field induced by the vorticity in the representative packet-eddy shown in (a). (c) Three hierarchies of the representative packet-eddy considered to model the flow in a ZPG TBL. (a,c) have been adapted from Baidya et al. (2014) while (b) has been adapted from Baidya et al. (2017). Blue arrow indicates direction of the mean flow velocity. 32

2.12 (a) An illustration of the two-dimensional (2-D) u-energy spectrum with the grey region, bounded by the two power laws (in red), representing a region of uniform energy. (b) 2-D u-spectrum at $z^+ \approx 2.6\sqrt{Re_\tau}$ computed from an attached eddy model for a ZPG TBL at $Re_\tau \approx 26\,000$. (c,d) 2-D u-spectra reconstructed experimentally at $z^+ \approx 2.6\sqrt{Re_\tau}$ in a ZPG TBL at (c) $Re_\tau \approx 2\,400$ and (d) $Re_\tau \approx 26\,000$. Solid and dashed blue lines in (b-d) denote $\lambda_y \sim \lambda_x$ and $\lambda_y \sim (\lambda_x)^{1/2}$ relationship, respectively. (a) has been adapted from Chung et al. (2015), while (b-d) has been adapted from Chandran et al. (2017). 36

2.13 (a) Premultiplied 1-D u-spectra at $z^+ \approx 100$ for a ZPG TBL at $Re_\tau = 14\,000$ (solid grey line), triple decomposed via data-driven filters into Φ_W^i (dashed dark blue line), Φ_{WL} (solid red line) and Φ_L^c (solid light blue line). (b,c) Φ_{WL} and the premultiplied 1-D u-spectra estimated at z^+ across the log-region for the same dataset as in (a), plotted as a function of λ_x scaled with (b) z and (c) δ, respectively. Terminology has been discussed in §2.5.3. The figure has been adapted from Baars and Marusic (2020a). 38

2.14 (a) Wall-parallel flow field of instantaneous u-fluctuations and (b) the associated two-dimensional u-spectrum at $z_o^+ \approx 100$ computed from the $Re_\tau \approx 2000$ Channel dataset of Encinar et al. (2018). (c) Wall-parallel flow field of instantaneous u-fluctuations and (d) the associated two-dimensional u-spectrum estimated at $z_o^+ \approx 100$ via SLSE technique with $z_r^+ \approx 300$. Adapted from Madhusudanan et al. (2019). 41

2.15 (a) Premultiplied 1-D u-energy spectra at $z_r^+ \approx 4.4$ (dashed line) and $z_o^+ \approx 473$ (solid line) for a ZPG TBL at $Re_\tau = 14\,000$. (b) γ_L^2 corresponding to the u-spectra considered in (a). (c) Energy spectrogram of the u-velocity component (in colour) for the same ZPG TBL dataset as in (a), with the corresponding coherence spectrogram (denoted by solid lines) overlaid on top of it. Solid lines denote γ_L^2 contour levels 0.1:0.1:0.9. Adapted from Baars et al. (2017). 42

3.1 Schematic of the large Melbourne wind tunnel facility (HRNBLWT) housed inside the Walter Bassett Aerodynamics Laboratory at the University of Melbourne. Adapted from Kulandaivelu (2012). 45

3.2 A photograph showcasing the multi-traverse system (T_{1-3}), which facilitates the movement of the four hotwire probes (HW_{1-4}), installed inside the working section of the HRNBLWT. 47

3.3 Schematic of the channel flow facility in the Walter Bassett Aerodynamics Laboratory of the University of Melbourne. Adapted from Ng (2011). . . . 51

3.4 Schematic depicting the relative positioning and movement of the four hotwire probes (HW_{1-4}) during the multi-point measurements in the HRNBLWT. (a-d) Four specific arrangements have been classified based on the relative wall-normal locations of the HW_{1-2} (at z_o) and HW_{3-4} (at z_r) in the various experiments (table 3.1), with (a) Arrangement 1 corresponding to $100 \lesssim z_o^+ \approx z_r^+ \lesssim 0.15Re_\tau$, (b) Arrangement 2 corresponding to $z_o^+ \approx z_r^+ \approx 15$, (c) Arrangement 3 corresponding to $100 \lesssim z_o^+ \lesssim 0.15Re_\tau$, $z_r^+ \approx 15$ and (d) Arrangement 4 corresponding to $100 \lesssim z_o^+ \lesssim 318$, $z_r^+ \approx 0.15Re_\tau$. Blue arrows indicate direction of the mean flow velocity along x. The instantaneous u-fluctuations plotted in the isometric view have been extracted from the ZPG TBL DNS dataset of Sillero et al. (2013) and are used simply for representative purposes. In these representative flow fields, blue and red contours correspond to low and high streamwise momentum motions, respectively. . 58

3.5 (a) Cross-correlation coefficient ($\widetilde{\mathcal{R}}_{u_o u_r}$) reconstructed from the u-signals acquired at various spanwise offsets during the multi-point measurements. Here, a measurement corresponding to each of the four different arrangements classified in figure 3.4 has been considered as an example, with $z_o^+ \approx 318$ in case of Arrangements 1, 2 and 4. (b) Premultiplied 1-D spanwise u-spectra corresponding to each of the $\widetilde{\mathcal{R}}_{u_o u_r}$ profiles shown in (a). 59

3.6 Premultiplied 1-D streamwise spectra computed from u-signals acquired by HW_{1-2} (in grey) at all spanwise offsets (Δy_{1-4}) during the multi-point experiment corresponding to $z_o^+ \approx z_r^+ \approx 15$ (Arrangement 2). These spectra are compared with the near-wall spectra (denoted by solid lines of other colours) obtained previously by Hutchins et al. (2009) in the same facility at similar flow conditions. (b) 1-D γ_L^2 computed from the u-signals acquired by HW_2 (at z_o) and HW_3 (at z_r) at the start of the multi-point measurements (i.e. $\Delta y_1 \approx 0$) corresponding to Arrangements 3 (solid lines) and 4 (dashed lines). Dark to light shading denotes the increase in z_o. Dash-dotted magenta line represents the empirical fit for γ_L^2 proposed by Baars et al. (2017). 61

3.7 Schematic of a typical X-wire configuration used to measure two velocity components in the same plane as the plane parallel to both the wires. The two wires are shown separately in the schematic for clarity. U is the instantaneous velocity vector which is inclined at ϑ with respect to the mean flow (U_∞) direction, x. ζ_i denotes the angle between the instantaneous flow vector and the wire i, with $i = 1$ or 2. Adapted from Bruun (1996). 62

3.8 Schematic of a (a) uv and (b) uw X-probe depicting the various geometric parameters (l_i, Δs_i, θ) used to define the measurement volume of an X-probe, with i representing the direction of measurement. The two sensors are indicated by red and blue lines, with the light shaded planes of the same colour denoting the respective sensor planes. Adapted from Baidya (2016). 66

3.9 Schematic of the jet orientation relative to a uv X-probe (indicated by the sensor plane). β corresponds to rotation in the sensor plane, while α corresponds to rotation normal to the sensor plane. Adapted from Baidya (2016). 68

3.10 X-probe voltage pairs (E_1, E_2) acquired from a typical 2-D calibration. ◯ represents the mean voltage pair estimated from the calibration for various jet velocities (U_{jet}) and jet angles (α or β depending on the X-probe type) with respect to the freestream direction. (–) lines represents the constant jet velocity lines and (- -) represents the constant jet angle lines at which the 2-D calibration was conducted. 69

3.11 The velocity-voltage surface plot fitted from the 2-D calibration for the (a) streamwise (U) and (b) lateral velocity (V or W) component. Black dots indicate the 2-D calibration points while the white dots indicate the 1-D calibration points. 70

4.1 (a) Schematic of the experimental set-up in HRNBLWT showing relative positioning and movement of the four hot-wire probes (HW_1-HW_4) for reconstructing the 2-D correlation corresponding to (i) Φ_{uu} and (ii) $\Phi_{uu}^{cross,w}$. Mean flow direction is along x. (b) Correlation coefficients ($\widetilde{\mathcal{R}}_{u_o u_r}$) as a function of spanwise separation $\Delta y/\delta$, computed for $z_o^+ \approx 2.6\sqrt{Re_\tau}$ and $\Delta x = 0$. 77

4.2 (a) 3-D representation of $\widetilde{\mathcal{R}}_{u_o u_r}$ for dataset $\mathcal{S}_1$ with $z_o^+ \approx 2.6\sqrt{Re_\tau}$ (=120) as a reference and $15 \lesssim z_r^+ < 150$ to plot isosurfaces for $\widetilde{\mathcal{R}}_{u_o u_r} = 0.1$ (green) and -0.04 (red). Wall-parallel planes at $z_r^+ \approx 2.6\sqrt{Re_\tau}$ and 15 have positive $\widetilde{\mathcal{R}}_{u_o u_r}$ contours as solid lines at levels 0.0:0.1:1.0 and a dashed red contour for -0.04. (b) Experimentally ($\mathcal{E}_1$) reconstructed $\widetilde{\mathcal{R}}_{u_o u_r}$ at equivalent z_o^+ and z_r^+ as in (a) and the same contour levels. (c,d) Φ_{uu} and $\Phi_{uu}^{cross,w}$ for datasets (c) $\mathcal{S}_1$ and (d) $\mathcal{E}_1$ obtained on computing 2-D FFT of corresponding 2-D $\widetilde{\mathcal{R}}_{u_o u_r}$ plotted in (a) and (b). Contours in (c) and (d) represent energy levels 0.15:0.10:0.55. Dot-dashed magenta and dashed blue lines represent the square-root and linear relationship, respectively. 79

4.3 (a,b) 2-D energy spectra for $z_o^+ \approx 2.6\sqrt{Re_\tau}$ and various z_r^+ at constant energy level of 0.2 for datasets (a) $\mathcal{S}_1$ and (b) $\mathcal{E}_1$. Light yellow background indicates $\lambda_x/z_o > 14$. (c) Schematic of the AEH-based model considered, shown here having three distinct hierarchies of self-similar wall-coherent eddies with the largest eddy (in black) of the order of δ. $\mathcal{L}$ and $\mathcal{W}$ denote the length and width of an eddy hierarchy, respectively. (d) 2-D spectrum obtained from the AEH-based model for $Re_\tau \approx 15\,000$ and $z_o^+ \approx 2.6\sqrt{Re_\tau}$. Solid black contour is qualitatively equivalent ($\sim 0.5(\Phi_{uu}^{AEH})_{max}$) to the one in (b). In (a,b,d), dot-dashed magenta, dashed blue and solid yellow lines denote $\lambda_y/z_o \sim (\lambda_x/z_o)^{1/2}$, $\lambda_y/z_o \sim \lambda_x/z_o$ and $\lambda_x/\lambda_y = 7$ relationships, respectively. 81

4.4 (a,b) Contours at a constant energy level of $0.35(\Phi_{uu}^{AEH})_{max}$, $0.35(\Phi_{uu}^{cross,w})_{max}$ (dataset $\mathcal{E}_1$) and $0.35(\Phi_{uu})_{max}$ (dataset $\mathcal{E}_1$) for z_o^+ across the log-region (table 4.1) plotted as a function of wavelengths scaled with (a) δ and (b) z_o. Dark to light shade indicates increase in z_o^+. For each of the respective spectrum, maximum value at $z_o^+ \approx 2.6\sqrt{Re_\tau}$ was considered as a reference to normalize the energy spectra at all z_o^+. Dashed blue lines represent the linear power law relationship for respective spectra. 83

4.5 (a) Energetic ridges of Φ_{uu} (light shaded) and $\Phi_{uu}^{cross,w}$ (dark shaded) for $z_o^+ \approx 2.6\sqrt{Re_\tau}$ from dataset $\mathcal{E}_1$, plotted against δ-scaled wavelengths alongside power laws indicated by dot-dashed lines. (b) 1-D spanwise and streamwise (cross-)spectrum obtained on integrating corresponding Φ_{uu} ($\Phi_{uu}^{cross,w}$) for $z_o^+ \approx 2.6\sqrt{Re_\tau}$ from $\mathcal{E}_1$. Also highlighted are the peaks of the 1-D spectrum (A'_{1x}, A'_{1y}) and cross-spectrum (A^w_{1x}, A^w_{1y}). (c) $\frac{A'_{1x}}{A'_{1y}}$ and $\frac{A^w_{1x}}{A^w_{1y}}$ estimated at all z_o^+ corresponding to $\mathcal{E}_1$ (table 4.1) by following the methodology shown in (b). 85

5.1 Contours of the coherence function, Γ calculated for the experimental dataset for (c) $z_o^+ \approx 2.6\sqrt{Re_\tau}$, $z_r^+ \approx 15$ and (d) $z_o^+ \approx 0.15Re_\tau$, $z_r^+ \approx 15$, as depicted in the respective schematics of the hotwire setup (a,b). Solid blue and dashed red contours respectively indicate Γ contours with values varying logarithmically in the range (0.05,0.95) and (-0.22,-0.02), in the direction of the arrows shown in (c). The spanwise wavelength estimates (λ_y) denoted in (c,d) correspond to the dominant spanwise Fourier mode noted for the ZPG TBL in the literature (Tomkins and Adrian, 2005; de Silva et al., 2020). 92

5.2 Contours of the coherence function, Γ calculated for the (a,b) DNS and (c,d) experimental datasets for (a,c) $z_o^+ \approx z_r^+ \approx 2.6\sqrt{Re_\tau}$ and (b,d) $z_o^+ \approx 2.6\sqrt{Re_\tau}$, $z_r^+ \approx 15$. Solid blue, dashed red and solid black contours indicate $+\Gamma$, $-\Gamma$ and $\Gamma \approx 0$, respectively while the dash-dotted green line represents the linear relationship, $\lambda_x \sim \Delta y$, representative of the self-similarity. Magnitude of Γ, for both the blue and red contours, increases in the same manner as shown in figures 5.1(c,d). (e) Two-point amplitude modulation coefficient ($\mathcal{R}_{AM}$) calculated from the experimental dataset for various Δy following (5.2). 94

6.1 Schematic showing the (a) isometric, (b) y-z plane and (c) x-z plane view of a hierarchy of self-similar wall-coherent eddies (shown as simplified cuboids) representing the log region of a ZPG TBL. Four hierarchy levels are considered each represented by different colours. Symbols represent various probe locations. Eddy signatures identified by respective probes, over a streamwise distance of a, are shown in (a). L_i, W_i and H_i denote the streamwise, spanwise and wall-normal extent of a hierarchy level. θ_m^w and θ_s^w denote mean and individual structure angles, respectively. Figure concept adopted from Baidya et al. (2019a). 101

6.2 (a) Schematic of the experimental set-up in HRNBLWT showing locations of the near-wall (HW_r) and log region (HW_o) reference probe. Mean flow direction is along x. The experiment begins with HW_o placed vertically above HW_r ($\Delta y = 0$;(i)) and is followed by the spanwise traverse ($\Delta y > 0$;(ii)) of HW_o. (b) γ_L^2 computed as a function of λ_x and Δy on correlating u from HW_o and HW_r for data set $\mathcal{E}_1$. The grey scale and line contours correspond to γ_L^2 for $z_o^+ \approx 2.6\sqrt{Re_\tau}$ and $3.9\sqrt{Re_\tau}$, respectively. Both contours are at levels 0.05:0.1:0.85. The red dashed line is used to highlight the streamwise spectral cut-off $\lambda_{x,c}$ corresponding to $\Delta y/\delta = 0.1$. 104

6.3 Cross-correlation of u measured at z_r and z_o, for various $\Delta y/\delta$, for data sets listed in table 6.2. (a)-(d) and (e)-(h) are correlations obtained from raw and large-wavelength pass filtered velocity time series, respectively with filter cut-off $\lambda_{x,c}(z_o,z_r,\Delta y)$ based on $\gamma_L^2(z_o,z_r,\Delta y) = 0.05$ computed for respective data sets. Red dashed and grey dot-dashed lines indicate $\Delta x/\delta$ corresponding to $\theta_m^w = 14°$ and 45° respectively for datasets $\mathcal{E}_1$ and $\mathcal{S}_1$, and $\theta_m = 14°$ and 45° respectively for dataset $\mathcal{E}_2$. Here, $\theta_m = \text{atan}((z_o\text{-}z_r)/\Delta x_p)$. Yellow bullets in (e)-(h) highlight the peak in the cross-correlation. 107

6.4 (a) Average structure inclination angle (θ_m^w) as a function of $\Delta y/\delta$ obtained by locating the peak of $\hat{R}_{u_o u_r}$ for data sets $\mathcal{E}_1$ and $\mathcal{S}_1$. (b,c) Scale-specific phase (Ψ) of the cross-spectra ($\phi_{u_o u_r}$), computed at various Δy, expressed as a physical inclination angle (θ^w) for $z_o^+ \approx$ (b) $2.6\sqrt{Re_\tau}$ and (c) $3.9\sqrt{Re_\tau}$ for data set $\mathcal{E}_1$. 109

7.1 (a) Schematic of the experimental set-up in HRNBLWT showing relative positioning and movement of the four hot-wire probes (HW_{1-4}) for reconstructing the 2-D correlation corresponding to (i) Φ_{uu} and (ii) Φ_{uu}^{cross}. Mean flow direction is along x. In the case of (ii), HW_{3-4} are positioned at either $z_r \ll z_o$ or $z_r \gg z_o$, depending on the desired experiment (table 7.1). (b) Constant energy contours for $\Phi_{uu}(z_o^+ = z_r^+ \approx 15) = 0.15$, computed from the present experimental and the converged DNS dataset of Sillero et al. (2014), plotted as a function of viscous-scaled wavelengths. Estimates from the DNS are box-filtered along y to mimic the spatial resolution of the hotwire sensors. Figure concept for (a) has been adopted from Deshpande et al. (2020a). 121

7.2 (a,c) Constant energy contours for $\Phi_{uu}(z_o^+)$, $\Phi_{uu}^{cross}(z_o^+, z_r^+ \approx 15)$ and $\Phi_{uu}(z_r^+ \approx 15)$ at energy level of 0.15 plotted for (a) $z_o^+ \approx 100$ and (c) $z_o^+ \approx 0.15Re_\tau$. (b,d) Constant energy contours for $\Phi_{uu}^{ia}(z_o^+)$ and $\Phi_{uu}^{a}(z_o^+)$, computed via (7.8) and (7.9), plotted at the same energy level and z_o^+ as in (a,c), respectively. In (a-d), contours on the left side correspond to those computed from the DNS data while those on the right are from the experimental data. Dashed green lines represent the linear relationship, $\lambda_y \sim \lambda_x$. 125

7.3 (a,b) Constant energy contours for $\Phi_{uu}^{a}(z_o^+)$ at energy level of 0.15 plotted for various z_o^+ as a function of wavelengths scaled with (a) z_o and (b) δ. Contours in red and blue correspond to Φ_{uu}^{a} estimated for the experimental and DNS datasets respectively (table 7.1), with dark to light shading indicating an increase in z_o^+ following $100 \lesssim z_o^+ \lesssim 0.15Re_\tau$ for Re_τ corresponding to respective datasets. Dashed green lines represent the linear relationship, $\lambda_x = 3\lambda_y$. (c,d) $\Phi_{uu}^{a}(z_o^+)$ integrated across λ_y and λ_x to obtain its corresponding 1-D version as a function of (c) λ_x and (d) λ_y respectively, each plotted with wavelengths scaled by z_o. Same colour coding is followed as that described for (a,b). (e,f) Pre-multiplied streamwise 1-D cospectra/spectra for the (e) Reynolds shear stress and (f) wall-normal velocity plotted as a function of λ_x scaled with z_o. This data is from the $Re_\tau \approx 10\,000$ dataset of Baidya et al. (2017) for various z_o^+. Dark to light shading corresponds to the increase in z_o^+ following $100 \lesssim z_o^+ \lesssim 0.15Re_\tau$, where $Re_\tau \approx 10\,000$. 128

7.4 Constant energy contours for (a,b) $\Phi_{uu}(z_o^+)$ and (c,d) $\Phi_{uu}^{ia}(z_o^+)$ at energy level of 0.15 plotted for various z_o^+ as a function of wavelengths scaled with (a,c) z_o and (b,d) δ, respectively. All data in (a-d) corresponds to the high-Re_τ experimental dataset reported in table 7.1, with dark to light shading indicating an increase in z_o^+ following $100 \lesssim z_o^+ \lesssim 0.15Re_\tau$. Dashed green lines represent the linear relationship, $\lambda_y \sim \lambda_x$. 130

7.5 Comparison of the normalized streamwise turbulence intensities obtained by integrating Φ_{uu} ($= \overline{u^2}^+$), Φ^a_{uu} ($\approx \overline{u^2}^+_{\text{active}}$), Φ^{ia}_{uu} ($\approx \overline{u^2}^+_{\text{inactive}}$) and $\Phi^{ia,AE}_{uu}$ ($\approx \overline{u^2}^+_{\text{inactive,AE}}$) for the high-$Re_\tau$ experimental dataset described in table 7.1. Also plotted for comparison is the well-resolved $\overline{u^2}^+$ measured by Samie et al. (2018) across a ZPG TBL maintained at an Re_τ comparable to the present experimental dataset. The dashed green line in (b) represents the logarithmic decay of $\overline{u^2}^+$ described by (7.1) with $A_1 = 0.98$ (Baars and Marusic, 2020b), while the dash-dotted golden line in (a) represents a constant $\overline{u^2}^+ = 2.7$. 132

7.6 (a) Constant energy contours for $\Phi_{uu}(z_o^+)$, $\Phi^{cross}_{uu}(z_o^+, z_r^+ \approx 0.15Re_\tau)$ and $\Phi_{uu}(z_r^+ \approx 0.15Re_\tau)$ at energy level of 0.15 plotted for $z_o^+ \approx 100$ and 318. (b) Constant energy contours for $\Phi^{ia,AE}_{uu}(z_o^+)$ and $\Phi^{ia,SS}_{uu}(z_o^+)$, computed via (7.10) and (7.11), plotted at the same energy level and z_o^+ as in (a). All contours in (a,b) are computed from the high-Re_τ experimental data. Dashed green lines represent the linear relationship, $\lambda_y \sim \lambda_x$. 133

7.7 $\Phi_{uu}(z_o^+)$ and $\Phi^{ia,AE}_{uu}(z_o^+)$ integrated across λ_y and λ_x to obtain their corresponding premultiplied 1-D version as a function of λ_x ($\Phi_{uu,x}$, $\Phi^{ia,AE}_{uu,x}$; in solid line) and λ_y ($\Phi_{uu,y}$, $\Phi^{ia,AE}_{uu,y}$; in dash-dotted line), respectively, for $z_o^+ \approx$ (a) 100, (a) 200 and (c) 318. Also highlighted are the peaks/plateaus of $\Phi^{ia,AE}_{uu,x}$ and $\Phi^{ia,AE}_{uu,y}$ (A_{1x}, A_{1y}), along with those of $\Phi_{uu,x}$ and $\Phi_{uu,y}$ (A'_{1x}, A'_{1y}). 134

7.8 Contours for the linear transfer kernel (black), for $z_r^+ \approx 15$, and the near-wall 2-D spectra (magenta) for the (a) u- and (b) w-velocity component. Here, the transfer kernels are computed at various z_o^+ from the DNS dataset of Sillero et al. (2014), described in table 7.1. Dark to light shading indicates an increase in z_o^+ following $100 \lesssim z_o^+ \lesssim 0.15Re_\tau$. The contour levels for the transfer kernels, $|H_L|^2$ and $|G_L|^2$ correspond to approximately 10% of the maximum value recorded for the kernel at the respective z_o^+, while that for $\Phi_{ww}(z_r^+ \approx 15)$ has intentionally been kept very low to highlight no overlap with the associated transfer kernel, $|G_L|^2$. 139

8.1 (a) Streamwise, spanwise and wall-normal velocity signatures from a typical attached eddy of height $\mathcal{H}$, where the blue and red regions denote the low- and high-momentum regions for the corresponding velocity fluctuations. (b) Townsend eddy intensity functions (I) for attached eddies of three different heights $\mathcal{H}_i$, with $\mathcal{H}_1 < \mathcal{H}_2 < \mathcal{H}_3$. Here, u_i, v_i and w_i denote the velocity signatures from the corresponding attached eddies which are sensed by the hotwire (HW) probe depending on its wall-normal position z, indicated by a dash line. 144

8.2 (a,c) Constant energy contours for $\Phi_{uu}(z_o^+)$, $\Phi^{cross}_{uu}(z_o^+, z_r^+ \approx 15)$ and $\Phi_{uu}(z_r^+ \approx 15)$ at energy level of 0.15 plotted for (a) $z_o^+ \approx 2.6\sqrt{Re_\tau}$ and (c) $z_o^+ \approx 0.15Re_\tau$. (b,d) Constant energy contours for $\Phi^{ia}_{uu}(z_o^+)$ and $\Phi^{a}_{uu}(z_o^+)$, computed via (8.9) and (8.10), plotted at the same energy level and z_o^+ as in (a,c), respectively. In (a-d), contours on the left and right side correspond to those computed from datasets $\mathcal{B}_1$ and $\mathcal{B}_2$, respectively. Dashed green lines represent the linear relationship, $\lambda_y \sim \lambda_x$. The figure has been adapted from Deshpande et al. (2021). 151

8.3 Constant energy contours for (a,d) $\Phi^a_{uu}(z_o^+)$, (b,e) $\Phi^a_{vv}(z_o^+)$ and (c,f) $\Phi_{ww}(z_o^+)$ ($\approx \Phi^a_{ww}(z_o^+)$) plotted for various z_o^+ as a function of wavelengths scaled with (a-c) z_o and (d-f) δ. Contours in black, blue and red correspond to $\Phi^a_{ii}(z_o^+)$ estimated for datasets $\mathcal{C}_1$, $\mathcal{B}_1$ and $\mathcal{B}_2$, respectively. Dark to light shading indicate an increase in z_o^+ following $2.6\sqrt{Re_\tau} \leq z_o^+ \leq 0.15Re_\tau$, for Re_τ corresponding to the respective datasets. Dashed green, magenta and brown lines represent the linear relationships empirically noted for Φ^a_{uu}, Φ^a_{vv} and Φ_{ww}, respectively. 154

8.4 Constant energy contours for $\Phi_{uw}(z_o^+)$ (in red) and $\Phi^a_{uw}(z_o^+)$ (in black) computed for datasets (a) $\mathcal{C}_1$ and (b) $\mathcal{B}_1$ and plotted for various z_o^+ as a function of wavelengths scaled with z_o. Dark to light shading indicates an increase in z_o^+ following $2.6\sqrt{Re_\tau} \leq z_o^+ \leq 0.15Re_\tau$, for Re_τ corresponding to the respective datasets. 156

9.1 A schematic representation of the misalignment between the wind-tunnel coordinate system (x-y-z) and the coordinate system for the 2-D jet calibrator (x'-y'-z') for an X-probe oriented to measure the u and v velocities. Sensors are represented by solid lines in red. The angles (a) ϕ' and (b) ψ' correspond to the in-plane and out-of-plane misalignment with reference to the sensor plane (which is x-y for the uv X-probe), respectively. Also highlighted is the sensor length (l^+), spacing between the two sensors (Δs^+) and angle (θ) made by each sensor with x, with subscripts denoting the direction in which they are measured. 161

9.2 Procedure to account for misalignment while processing 2-D calibration of a uv-CX probe, explained by using an 'accurate' 2-D calibration as a reference: (a) Voltage pairs obtained by varying the U_{jet} and β for an *accurate* and misaligned 2-D calibration along with the voltages obtained from the 1-D calibration in $HRNBLWT$ just before the measurement. (b) Voltages in (a) interpolated onto a linearly distributed set of U_{jet} and β based on effective angle method. (c) Comparison of 2-D calibration voltage pairs corresponding to $\beta = 0°$ (highlighted by gray background in (b)) with 1-D calibration to obtain the angular offset ϕ'. (d) The same voltage pairs as in (c), but compared individually for the two sensors to obtain the voltage offset $\Delta E_1(U_{jet})$ and $\Delta E_2(U_{jet})$. (e) Comparison between voltage pairs from the *accurate* and the misaligned calibration, with the latter shifted after application of the voltage offset estimated in (d). 166

9.3 Viscous-scaled profiles of (a) mean streamwise velocity and streamwise turbulence intensity and (b) spanwise turbulence intensity obtained on processing the high-Re_τ boundary layer data set using the *accurate* and misaligned 2-D calibrations. In case of the misaligned calibration, data processing is carried out using both AO and VO methods. In (b), the corrected turbulence intensity is plotted with a vertical shift and compared with $\overline{v^2}^+$ obtained from the *accurate* 2-D calibration. 171

9.4 Viscous-scaled 1-D premultiplied streamwise energy spectra of the (a) streamwise and (b) spanwise velocity obtained on processing the high-Re_τ boundary layer data set using the *accurate* and misaligned 2-D calibrations. In case of the misaligned calibration, data processing is carried out using the VO method only. In (b), the corrected spectra of the spanwise velocity is plotted with a vertical shift and compared with spectra obtained from the *accurate* 2-D calibration. 171

9.5 Viscous-scaled profiles of (a) streamwise and (b) spanwise turbulence intensity obtained on processing the high Re_τ boundary layer data set using 2-D calibrations with known misalignments in the range -5° < ϕ' < 5°. Dashed green lines represent $\phi' < 0$, while dot-dashed red represent $\phi' > 0$ with the shading intensity increasing with the degree of misalignment for both cases. Note that all calibrations are processed via the VO method only. 172

9.6 Viscous-scaled turbulence intensity profiles of the (a) streamwise, (b) spanwise and (c) wall-normal velocity decomposed into small-scale component based on a cut-off wavelength of $\lambda_x^+ \approx 210$ for various data sets: lines (- -) and (-) represent channel DNS data at $Re_\tau = 1\,000$ and 5 200 respectively (Lee and Moser, 2015). (□) represents ZPG TBL DNS data at $Re_\tau \approx 2\,000$ (Sillero et al., 2013). (◯) in dark shading represent ZPG TBL data from present physical experiments at $Re_\tau \approx 10\,000$ processed via *accurate* 2-D calibration, while those in light shading represent statistics from the corresponding synthetic experiments. 173

9.7 Viscous-scaled premultiplied energy spectra of the (a) streamwise, (b) spanwise and (c) wall-normal velocity components at $z^+ \approx 100$ for $Re_\tau \approx 10\,000$ ZPG TBL data set (heavy black) and $Re_\tau \approx 1\,000$ channel data set (dark red) acquired using CX probe (table 9.1) and processed using a misaligned 2-D calibration. Dot-dashed lines in light shading represent data from the synthetic experiments corresponding to the probe volume in the physical experiments. The yellow background highlights the wavelength range $0 < \lambda_x^+ < 210$. 175

9.8 Percent deviation of r from the correction ratio r^c across the measurement locations (z^+), computed for the physical experiments with a misaligned calibration. Symbols represent physical experiments with various X-probes as mentioned in table 9.1, with (–) and (- -) line types representing a uv and uw X-probe, respectively. For the case of high-Re_τ experimental data (◯), deviations only up to $z^+ \approx 300$ have been shown. Zero labels corresponding to each profile are vertically offset by 10% from one another and the light yellow background highlights deviation in the range ±2% for each profile. . 176

9.9 Corrected viscous-scaled premultiplied energy spectra of the (a) spanwise and (b) wall-normal velocity components at $z^+ \approx 100$ for $Re_\tau \approx 10\,000$ ZPG TBL data set (heavy black) and $Re_\tau \approx 1\,000$ channel data set (dark red) acquired using CX probe (table 9.1) and processed using a misaligned 2-D calibration. Dot-dashed lines in light shading represent spectra from the synthetic experiments corresponding to the probe volume in the physical experiments. The yellow and blue backgrounds highlight the wavelength range $0 < \lambda_x^+ < 210$ and $190 < \lambda_x^+ < 210$, respectively. 177

9.10 The uncorrected (dark, partially-filled) and corrected (dark, fully-filled) (a) streamwise, (b,e) spanwise, (c,f) wall-normal and (d,g) Reynolds shear stresses for the $Re_\tau \approx 1\ 000$ channel flow experiments. The uncorrected statistics are plotted in (a-d), while the corrected ones are plotted in (e-g). Symbols represent experiments with various X-probes as mentioned in table 9.1. Empty symbols in light shading represent statistics from the corresponding synthetic experiments. (- -) represents the unfiltered statistics from the channel DNS at $Re_\tau = 934$. Note the vertical shift in profiles. . . 179

9.11 Procedure to account for drift while processing 2-D calibration of an X-probe, explained by using an *accurate* 2-D calibration as a reference: (a) Voltage pairs obtained by varying the U_{jet} and β for an *accurate* and *drifted* 2-D calibration along with voltages obtained from the 1-D calibration in $HRNBLWT$ just before the measurement. (b) Voltages in (a) interpolated onto a linearly distributed set of U_{jet} and β based on EAM. (c) Comparison between voltage pairs from the *accurate* and *drifted* calibration, with the latter shifted after application of the voltage offset estimated by following the procedure shown in figure 9.2(d). 183

9.12 Viscous-scaled profiles of (a) mean streamwise velocity and streamwise turbulence intensity and (b) spanwise turbulence intensity obtained on processing the high-Re_τ boundary layer data set using the *accurate* and *drifted* 2-D calibrations. Data processing, in case of the *drifted* calibration, is carried out using the VO method. 184

9.13 (a,c) Corrected viscous-scaled wall-normal turbulence intensity profiles and (b,d) premultiplied energy spectra of the wall-normal velocity at $z^+ \approx 100$ (marked by black line in a,c) obtained from various X-probes for a channel flow. These profiles are selectively plotted in a way to demonstrate the effect of varying Δs^+ (a,b) and l^+ (c,d). Colour coding corresponding to the X-probes is given in table 9.1. Dark and light shading represents data from the $Re_\tau \approx 1\ 000$ channel flow experiments and the corresponding synthetic experiments, respectively. Note the vertical shift in profiles for the synthetic experiments. 185

List of Tables

3.1 A summary of the various multi-point measurements conducted in HRNBLWT, classified into four different arrangements based on the relative wall-normal positioning of the hotwire probes. Terminology has been described in §3.2.3 and figure 3.4. Values highlighted in bold represent the upper limit of the log-region, $z^+ \approx 0.15\delta^+$ (Marusic et al., 2013). 56

3.2 A summary of the various single-point measurements conducted using various X-probes. Terminology has been described in § 3.3.2. 65

4.1 A summary of the various datasets containing synchronized multi-point u-signals at z_r and z_o for various spanwise offsets, Δy. Terminology has been described in §4.4. Values highlighted in bold indicate the approximate z^+-location for the beginning of the log-region, $2.6\sqrt{Re_\tau}$ (Klewicki et al., 2009), underlined represent $z^+ \approx 3.9\sqrt{Re_\tau}$ and the ones with superscript (*) represent the upper limit of the log-region, $z^+ \approx 0.15\delta^+$ (Marusic et al., 2013). 76

5.1 A summary of the data sets containing synchronized multipoint u-measurements at z_r^+ and z_o^+, which are separated by various spanwise offsets, Δy. l^+ represents the spatial resolution of the sensor/grid along the spanwise direction. $z_o^+ \approx 2.6\sqrt{Re_\tau}$ and $0.15Re_\tau$ corresponds to the lower and upper bound of the log-region, respectively (Deshpande et al., 2020a). 90

6.1 A summary of the streamwise inclination angles of coherent motions in a ZPG TBL, estimated (θ_s, θ_m^w) or assumed (θ_s^w) in various studies. Friction Reynolds number, Re_τ is defined based on friction velocity (u_τ) and TBL thickness (δ). While, Re_θ is based on free-stream velocity (U_∞) and momentum thickness. Terminology for angles has been described in §6.3. #This study was for a fully developed turbulent channel flow and their Reynolds number is defined based on channel centreline velocity and half-width. ‡ Results are for atmospheric surface layer under neutrally buoyant conditions. 99

6.2 A summary of the various data sets containing synchronized multipoint measurements at a near-wall (z_r) and log region (z_o) reference location at various spanwise offsets, Δy. l^+ represents the spatial resolution of the sensor/grid along the spanwise direction. 103

7.1 A summary of the ZPG TBL datasets comprising synchronized multi-point u-signals at z_r^+ and z_o^+ used to compute two types of 2-D u-spectra, Φ_{uu} and Φ_{uu}^{cross}. The terminology has been described in §7.4.1 and figure 7.1. Underlined values represent the approximate upper bound of the log-region ($0.15Re_\tau$; Marusic et al. (2013)), while the values in bold represent the near-wall reference location. Superscript '+' denotes normalization in viscous units. 120

8.1 Table summarizing the various published wall-turbulence datasets, with synchronized multi-point velocity signals across several z_r^+ and z_o^+, utilized to estimate two different types of two-dimensional spectra, Φ_{ii} and Φ_{ii}^{cross}. Terminology used in the table has been defined in the text, where i represents the velocity fluctuations u, v or w. Highlighted values (in bold) are used to indicate the reference location close to the wall, while $2.6\sqrt{Re_\tau}$ and $0.15Re_\tau$ are the lower and upper bounds of the log-region (Marusic et al., 2013). Normalization in viscous units is denoted by the superscript '+'. 148

9.1 A summary of the various physical experiments conducted. Terminology has been described in § 9.4.1.2. Synthetic experiments were conducted corresponding to the viscous-scaled measuring volume (a function of l^+ and Δs^+) for each case mentioned. Statistics from these synthetic experiments are plotted with the same symbol and a lighter color shade as for the corresponding physical experiments. A checkmark (✓) in the last column refers to experimental cases where all available 2-D calibrations were misaligned, i.e. no 'accurate' 2-D calibration could be conducted. 162

Nomenclature

Roman symbols

$\mathcal{F}$	Fourier transformation
$\mathcal{L}$, $\mathcal{W}$, $\mathcal{H}$	length, width and height of the statistical eddy
L	streamwise shift
A	additive universal constant in the logarithmic law of the wall
A_1	universal constant in the logarithmic law for the streamwise turbulence intensity obtained from the attached eddy hypothesis, or the plateau in the 1-D energy spectra of u
A_2	universal constant in the logarithmic law for the spanwise turbulence intensity obtained from the attached eddy hypothesis, or the plateau in the 1-D energy spectra of v
B	additive characteristic constant in the velocity defect log law
B_i	characteristic additive constant for the streamwise, spanwise and wall-normal turbulence intensities obtained from the attached eddy hypothesis; $i = 1, 2, 3$
C_p	coefficient of pressure
d	diameter of a hotwire sensor
f_c	frequency cut-off due to frequency response of the sensor
f_{max}	maximum energetic frequencies in turbulent boundary layers
f_s	hotwire data sampling frequency
h	channel half-height

j	unit imaginary number
K_0	universal Kolmogorov constant
l	etched length of a hotwire sensor
L_η	Kolmogorov length scale
p	kinematic pressure
R_0	hotwire sensor resistance at ambient temperature
R_{AM}	amplitude modulation coefficient
R_w	hotwire sensor resistance at elevated temperature
$R_{u_o u_r}$	two-point cross-correlation function of u acquired at wall-normal locations z_o and z_r
Re	Reynolds number
Re_τ	Reynolds number based on friction velocity or Kármán number, $Re_\tau = U_\tau \delta / \nu$
T	hotwire data sampling duration during measurements
T_c	hotwire data sampling duration during calibration
U	mean streamwise velocity
u, v, w	streamwise, spanwise and wall-normal velocity fluctuations
U_η	Kolmogorov velocity scale
U_τ	mean friction velocity
x, y, z	streamwise, spanwise and wall-normal directions
E_1, E_2	mean hotwire voltages
H_L, G_L	linear transfer functions
k_x, k_y	streamwise and spanwise wavenumbers
U_∞	freestream velocity
U_b	bulk velocity

U_{cl}	centreline velocity
U_{eff}	effective cooling velocity
U_{jet}	jet exit velocity

Greek symbols

α	jet rotation angle normal to the sensor plane
β	jet rotation angle in the sensor plane
δ	boundary layer thickness
η	wall-normal distance normalized by the boundary layer thickness, $\eta = z/\delta$
κ	von Kármán constant in the logarithmic law of the wall
ν	kinematic viscosity
ρ	density of fluid
Δs	spacing between the two sensors in a x-wire sensor
Δx, Δy, Δz	streamwise, spanwise and wall-normal offset between hotwire probes
Γ	coherence function
γ_L^2	linear coherence spectrum
λ_x, λ_y	streamwise and spanwise wavelengths
ϕ'	calibration misalignment in the sensor plane
Ψ	principal rate of mean strain
ψ'	calibration misalignment normal to the sensor plane
τ_w	mean shear stress at the wall
ε	turbulent energy dissipation
Φ_{ij}	premultiplied energy spectrum of velocity components i,$j = u$, v or w, normalized in viscous units

ϕ_{ij}	energy spectrum of velocity components i,$j = u$, v or w
$\phi_{u_o u_r}$	cross-spectrum of the u acquired at wall-normal locations z_o and z_r
θ_m^w	streamwise inclination angle of a mean wall-coherent structure
θ_s^w	streamwise inclination angle of an individual wall-coherent structure

Special symbols

$\mathcal{O}$	order of

Superscript

$+$	indicates viscous scaling. Viscous-scaled wall-normal distance, streamwise velocity fluctuation and time scales are given by $z^+ = zU_\tau/\nu$, $u^+ = u/U_\tau$ and $t^+ = tU_\tau{}^2/\nu$, respectively
$*$	complex conjugate
a	active component of the energy spectrum or the velocity fluctuations
cross	spectrum reconstructed using velocity signals acquired at wall-normal locations z_o and z_r, with $z_o \neq z_r$
ia	inactive component of the energy spectrum or the velocity fluctuations

Other symbols	$[\Im(\ldots)]$imaginary part of
$\mathcal{O}(\ldots)$	order of
$\Re(\ldots)$	real part of

Abbreviations

1-D, 2-D, 3-D	one-dimensional, two-dimensional and three-dimensional
AEH	attached eddy hypothesis
AEM	attached eddy model
DC	direct current

DNS	direct numerical simulations
HRNBLWT	High Reynolds Number Boundary Layer Wind Tunnel
HW_i	hotwire in the multi-point measurement, where $i = 1, 2, 3, 4$
LSM	large-scale motion
MUCTA	Melbourne Univeristy constant temperature anemometry
OHR	overheat ratio
PIV	particle image velocimetry
sDNS	filtered DNS
SS	superstructures
T_i	traverse system in the experimental setup, where $i = 1, 2, 3$
TBL	turbulent boundary layer
VLSM	very-large-scale motion
X-wire	cross-wire
ZPG	zero pressure gradient

Dedicated to my dearest aai-baba, baiko and mani,
for their unconditional love and support.

Chapter 1

Introduction

Fluid mechanics has been a topic of key research interest for the scientific community particularly over the past century. Over this period, it has been investigated both theoretically and experimentally to explain the various natural phenomena occurring around us, and to understand how it influences the numerous engineering applications used in everyday life. These applications require a fundamental knowledge of fluid mechanics operating over a broad range of scales – from the micro-scales which are relevant to biomedical applications, to the very large scales existing in Earth's surface layer. The present thesis focuses on the particular class of fluid flows interacting with a wall or a solid surface, where the fluid is forced to conform to the no-slip condition at the wall, leading to a region with a strong shear/velocity gradient known as the boundary layer (Prandtl, 1904). This region is responsible for the resistance experienced by the fluid in its relative motion against the wall (commonly known as drag), which is encountered in several engineering applications such as the flow in a pipeline, or that over an aircraft or an automobile. The majority of these 'wall-bounded' flows, as they are commonly referred to, are turbulent in nature, and are characterized by a chaotic, random and unpredictable variation in the instantaneous boundary layer statistics such as velocity and pressure.

The complex nature of the turbulent boundary layer (TBL) is attributed to non-linear interactions across a hierarchy of length and time scales existing in a turbulent flow (Tennekes and Lumley, 1972). The range of scales existing in a wall-bounded flow is quantified by the friction Reynolds number, or Karman number, which is defined as $Re_\tau = \delta/(\nu/U_\tau)$. Here, δ refers to the TBL thickness, while ν/U_τ is the viscous length scale, with ν and U_τ the kinematic viscosity and friction velocity, respectively. Hence, physically, Re_τ can be considered as a characteristic dimensionless parameter representing the ratio of the largest

to the smallest length scale in the flow. In most engineering applications associated with the transportation industry, high-Re_τ ($> 10^5$) wall-bounded flows, which are characterized by an increased separation of scales, are encountered (Smits and Marusic, 2013). Fundamental understanding of these flows, however, is limited given that such flows can only be investigated experimentally, and only with the availability of well-designed large-scale research facilities equipped with state-of-the-art measurement sensors (Marusic et al., 2010c). The majority of currently available well-resolved datasets, on the other hand, are obtained computationally via direct numerical simulations (DNS) of the governing Navier-Stokes equations, and are restricted to low to moderate Re_τ ($\lesssim 5\,000$) owing to computing limitations. Recent reviews by Klewicki (2010), Marusic et al. (2010b), Smits et al. (2011) and Jiménez (2012, 2018) document the current state of understanding of the flow physics of wall-turbulence, which may be referred to by interested readers.

1.1 Motivation

As stated previously, the majority of wall-bounded flows encountered in applications associated with the transportation industry are at high Re_τ ($> 10^5$), and hence turbulent in nature. In comparison to laminar flows, these turbulent flows have better mixing capabilities and can transfer more momentum, resulting in greater drag force opposing the relative movement between the wall and the fluid. As a consequence, as much as 50% of the aircraft fuel, and entire pumping power in the pipeline networks (Marusic et al., 2010a) are consumed in overcoming this resistance, underscoring the need to understand the fundamental processes in wall-bounded flows. A greater understanding of wall-bounded flows would facilitate modelling of the very high-Re_τ flows, observed in Earth's surface layer, which are otherwise very expensive to recreate in laboratory settings. Such a development would contribute not only towards an improved understanding of complex multi-scale physical processes, but also help on the economical front, by reducing the operating costs for the aforementioned engineering applications. For example, the ability to predict high-Re_τ TBL characteristics can be exploited to manipulate the processes associated with the momentum transfer across the shear layer to achieve drag reduction, which would benefit the transportation sector by reducing their energy expenditures.

Although the turbulence community has put in efforts to predict or model the wall-bounded turbulence ever since its discovery (Prandtl, 1904), it was the revelation of the existence of 'organized' or 'coherent' motions in the turbulent shear flow, in the 1970s (Brown and Roshko, 1974; Brown and Thomas, 1977), which really gave a strong impetus to this work.

These structures are known to be statistically significant in terms of their contribution to the turbulence production and Reynolds stresses, consequently playing a crucial role in the overall flow dynamics (Adrian et al., 2000; Ganapathisubramani et al., 2003). The discovery of these motions facilitated the proposal of one of today's principal schools of thought in turbulence research, which considers the random, unpredictable turbulent flow to be essentially an amalgamation of a plethora of such coherent motions (Adrian, 2007). This means that the complexity of the former can be largely explained by understanding the relatively simplified behaviour of the latter. Extensive research in this topic has found these motions to be highly anisotropic and three-dimensional (3-D) in geometry (Adrian et al., 2000; Marusic and Adrian, 2010; Herpin et al., 2013). Most of this research has, however, come from the low Re_τ DNS datasets, which have a very narrow range of scales. For these flows, turbulent production is limited to the near-wall region, and hence associated with the relatively smaller, viscosity-dominated coherent structures predominating this region. However, in high-Re_τ flows, the bulk of turbulence production is contributed by large inertial scales that coexist in the log-region (Marusic et al., 2010b; Smits et al., 2011; Lee and Moser, 2019). These large motions, however, aren't statistically dominant in a low-Re_τ flow. This encourages an investigation of energetic large-scale coherent structures existing across the entire shear layer of a high-Re_τ wall-bounded flow. Previous experimental efforts towards the same cause have been mostly limited to investigations in 1-D and 2-D by using hotwire anemometry and particle image velocimetry (PIV), with the latter also limited by the flow field size (and consequently unable to capture the very large-scale motions). To this end, the present thesis reports multi-point measurements performed in the Melbourne high-Re_τ TBL facility using hotwire anemometry, to reconstruct the 3-D statistical picture of the organized flow in high-Re_τ canonical wall-bounded flows. These measurements involve installation of the hotwire sensors on a unique experimental setup which is capable of traversing the sensors over a large range of relative spanwise and wall-normal offsets, thereby facilitating reconstruction of the 3-D cross-correlations of the streamwise (u) velocity component across the shear layer. The analysis on the aforementioned high-Re_τ experimental dataset is complemented by a similar analysis on the publicly available published DNS datasets of del Álamo et al. (2004) and Sillero et al. (2014), to examine the flow characteristics across a decade of Re_τ, $\mathcal{O}(10^3)$ – $\mathcal{O}(10^4)$.

Amongst these multi-point measurements, special emphasis is laid on investigating the characteristics of the energetic motions which not only co-exist in the log-region, but also have their spatial signatures extending all the way down to the wall (also referred to as wall-coherent motions). Several studies over the past decade have shown these motions to be superimposing onto and modulating the near-wall cycle (Hutchins and Marusic,

2007; Mathis et al., 2009; Marusic et al., 2010a), and consequently also influencing the net skin-friction experienced at the wall (Deck et al., 2014; de Giovanetti et al., 2016; Abbassi et al., 2017). An improved understanding of this 'inner-outer' interaction can facilitate development of flow-control schemes (both passive or active) assisted via data-driven models. Previous efforts along these lines have seen immense success – for example, Marusic et al. (2010a) proposed a semi-empirical model which accurately predicted the instantaneous u-velocity signal in the near-wall region by using the u-signal measured in the log-region as an input. The same concept was later extended by Mathis et al. (2013) to predict the wall-shear stress fluctuations. The predictive capabilities of these studies were, however, limited only to the streamwise direction, given that data was only available from the wall-normal (2-D) plane. The present measurements can facilitate extension of the predictive capabilities along both wall-parallel directions.

Another interesting aspect with respect to the wall-coherent motions is their geometrically self-similar characteristics noted by numerous studies over the last two decades (del Álamo et al., 2006; Lozano-Durán et al., 2012; Baars et al., 2017; Yoon et al., 2020; Hwang et al., 2020). This has led to the aforementioned studies proposing the wall-coherent motions as candidate eddies for the attached eddy model of wall-turbulence (Perry and Chong, 1982; Marusic and Monty, 2019), which is based on Townsend's attached eddy hypothesis (Townsend, 1976). The model assumes the wall-bounded flow to be an assemblage of geometrically self-similar packets of hairpin vortices, of various sizes with associated population densities, randomly distributed in space (Marusic, 2001; Marusic and Monty, 2019). While studies in the past have focused a lot on the shape and size of statistically significant eddies existing in the outer region of the high-Re_τ TBL (Adrian et al., 2000; Adrian, 2007), most of which are very distant from the wall, there hasn't been much empirical investigation dedicated towards the geometric characteristics and 3-D flow organization of the wall-coherent eddies, which can be facilitated by the present measurements. Apart from the wall-coherent motions, high-Re_τ wall-bounded flow also comprises of statistically significant motions which are incoherent to the wall (Baars and Marusic, 2020a; Yoon et al., 2020; de Silva et al., 2020). Recent work by Yoon et al. (2020) and de Silva et al. (2020) on low-Re_τ datasets has noted these motions, which coexist in the log-region,to be also exhibiting self-similar characteristics akin to Townsend's attached eddies. This makes the investigation of their geometric characteristics also of interest to the wall-turbulence community, which can be pursued here for high-Re_τ flows. An improved understanding of both wall-coherent and incoherent motions would facilitate the reduced-order and/or conceptual modelling of the entire inertial (log) region of wall-bounded flows!

1.2 Aims and thesis outline

The current state of understanding of the high Re_τ TBL, discussed in §1.1, motivates the investigation of the following research problems:

Aim 1: Test the notion of geometric self-similarity, along both the streamwise and spanwise directions, for energetic wall-coherent motions of u coexisting in the log-region.

Aim 2: Investigate the spanwise geometry and organization of wall-coherent u-motions in the log-region.

Aim 3: Estimate the streamwise inclination angle of the large wall-coherent motions of the streamwise velocity, by physically isolating them from the influence of the relatively smaller motions coexisting in the log-region.

Aim 4: Develop a methodology to segregate the energy contributions associated with the active and inactive components (Townsend, 1976) of all three velocity components in wall-bounded turbulent flows.

Aim 5: Develop an experimental procedure to accurately estimate the velocity statistics processed from an X-wire probe, and validate them via synthetic experiments conducted on a DNS dataset which take into account the spatial resolution of the probe.

The structure of this thesis, which has also been depicted via a flowchart in figure 1.1, is as follows: chapter 2 gives a brief review of the literature relevant to the objectives of this thesis. Particular emphasis in this chapter has been given to the attached eddy model (AEM) based on Townsend's attached eddy hypothesis (Townsend, 1976), as well as on the data analysis techniques used in recent literature to statistically extract these attached eddies from the various other eddy-types coexisting in the flow. Chapter 3 describes the methodology of the two different types of measurements: (a) multi-point measurements using single wires, and (b) single-point measurements using X-wire probes, conducted as part of this thesis. Also included is a brief description of the experimental facilities and the instrumentation used for the experiments.

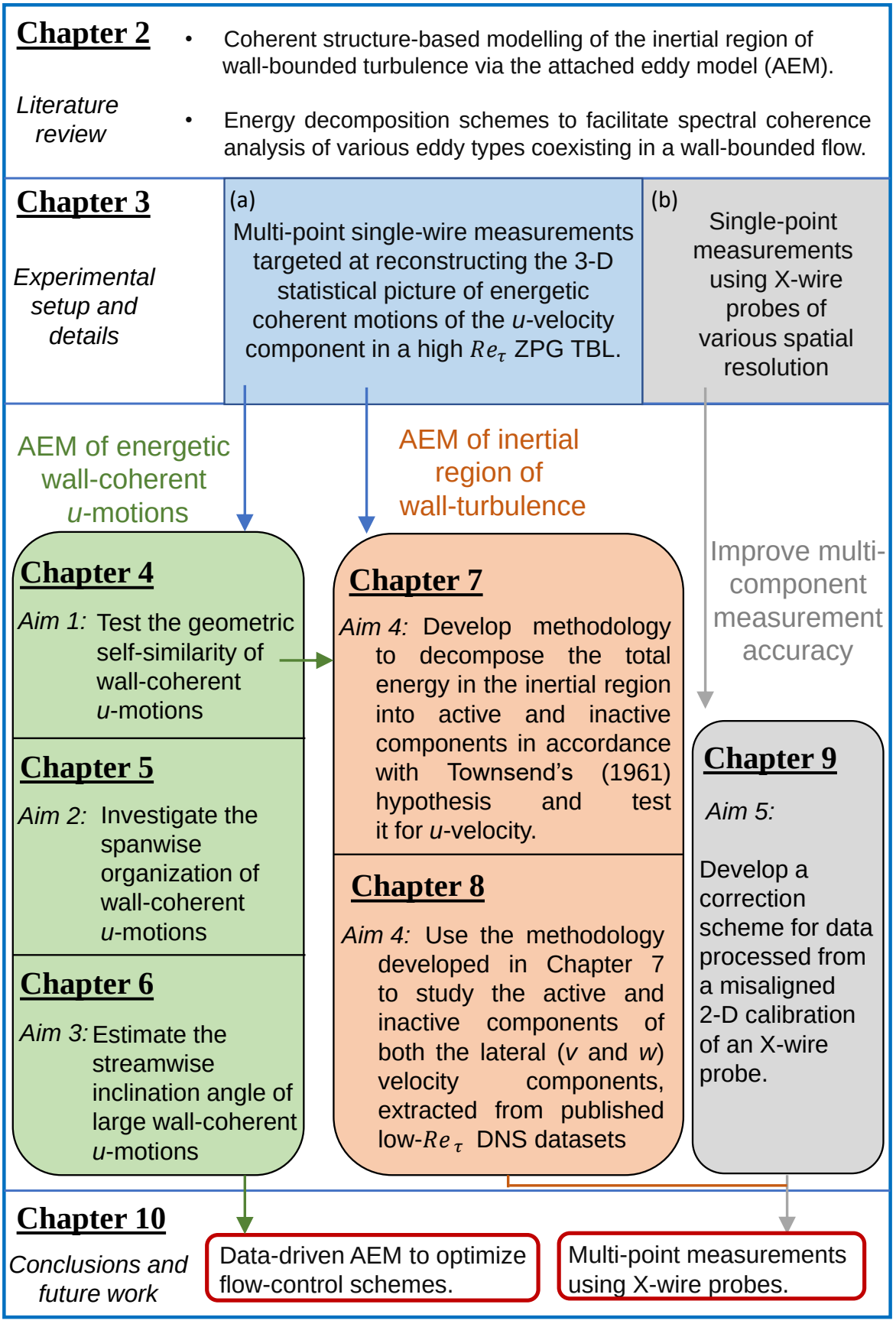

FIGURE 1.1: A flowchart depicting the structure of the present thesis.

Chapter 4 is an article published in the *Journal of Fluid Mechanics*, titled "Two-dimensional cross-spectrum of the streamwise velocity in turbulent boundary layers" (Deshpande et al., 2020a). This study addresses *Aim 1* by reconstructing, for the first time, the 2-D cross-spectrum of the streamwise velocity component from the multi-point TBL datasets across a decade of $Re_\tau \sim \mathcal{O}(10^3)$ – $\mathcal{O}(10^4)$. This spectrum is representative of the scale-specific energy contributions from the wall-coherent motions coexisting in the inertial (log) region, and is tested here for self-similarity arguments in accordance to the attached eddy model of Perry and Chong (1982) and Perry et al. (1986). This forms the basis for modelling these energetic motions via statistically representative vortex structures varying self-similarly in geometry, as per the attached eddy hypothesis, to predict statistics for an even higher-Re_τ TBL.

Chapter 5 is based on an article published in the *Proceedings of 22nd Australasian Fluid Mechanics Conference*, titled "Large-scale spanwise periodicity in a canonical turbulent boundary layer" (Deshpande et al., 2020b). This study addresses *Aim 2* by performing a scale-specific coherence analysis on the multi-point datasets across a decade of Re_τ. An understanding of the flow organization of the energetic coherent motions can facilitate development of a semi-empirical attached eddy model, wherein the sizes and relative positioning of the representative vortex structures are defined based on the estimates obtained directly from the data.

Chapter 6 is an article published in the *Journal of Fluid Mechanics*, titled "Streamwise inclination angle of large wall-attached structures in turbulent boundary layers" (Deshpande et al., 2019a). This study addresses *Aim 3* by conducting a spectral coherence analysis on the multi-point TBL datasets. The estimated streamwise inclination angle can be considered while defining the geometry of the representative vortex structures in the attached eddy-based modelling of the high-Re_τ TBL.

Chapter 7 is an article published in the *Journal of Fluid Mechanics*, titled "Active and inactive components of the streamwise velocity in wall-bounded turbulence" (Deshpande et al., 2021). This study addresses *Aim 4*, and tests the efficacy of the proposed decomposition methodology for the u-velocity component by implementing it on the multi-point experimental as well as DNS datasets. The methodology utilizes the 2-D cross-spectrum analyzed previously in chapter 4 as an input to decompose the total streamwise turbulent energy in the inertial region into two sub-components. In chapter 8, the same methodology is implemented on the lateral velocity components extracted from previously published low-Re_τ DNS datasets. This work is published in the *Proceedings of 22nd Australasian Fluid Mechanics Conference*, titled "Active and inactive motions in wall turbulence" (Deshpande

et al., 2020c). Chapters 7 and 8 together establish the validity of Townsend's hypothesis on the active and inactive motions (Townsend, 1961, 1976) by testing it on all three velocity components, paving the way towards attached eddy-based modelling of the inertial region of wall turbulence.

Chapter 9 is an article published in the *Experiments in Fluids* journal, titled "A scheme to correct the influence of calibration misalignment for cross-wire probes in turbulent shear flows" (Deshpande et al., 2020d). This study addresses *Aim 5* by proposal of a scheme to correct the erroneous statistics processed from a misaligned 2-D calibration of an X-wire probe. The scheme would facilitate multi-component multi-point measurements in the high-Re_τ TBL, to be conducted in the near future, to firmly establish the validity of Townsend's hypothesis (*Aim 4*) for the lateral velocity components. The thesis finally concludes in chapter 10 by summarizing the key findings from chapters 4 – 9, along with a brief discussion on the possible future studies which may evolve out of the observations reported in this thesis.

Chapter 2

Review of the relevant literature

This chapter briefly reviews literature relevant to the research problems considered in this thesis (§1.2), and is divided into the following sections:

- Concept of the boundary layer
- Classical scaling arguments
- Coherent structures in wall-turbulence
- Attached eddy model of wall-turbulence
- Evidence of the geometric self-similarity in a wall-bounded flow
- X-wire probes

The review presented here, however, isn't exhaustive and is written with the intention to provide sufficient foundation for the reader to follow the results and discussions in the chapters ahead. Literature relevant to the specific chapters or sections of the thesis have been referenced at appropriate places throughout.

2.1 The boundary layer concept

The concept of a boundary layer was first introduced by Prandtl (1904). This boundary layer exists whenever there is a relative motion of a fluid over the surface of any body. The layer begins at the wall, where the fluid velocity relative to the body is zero owing to

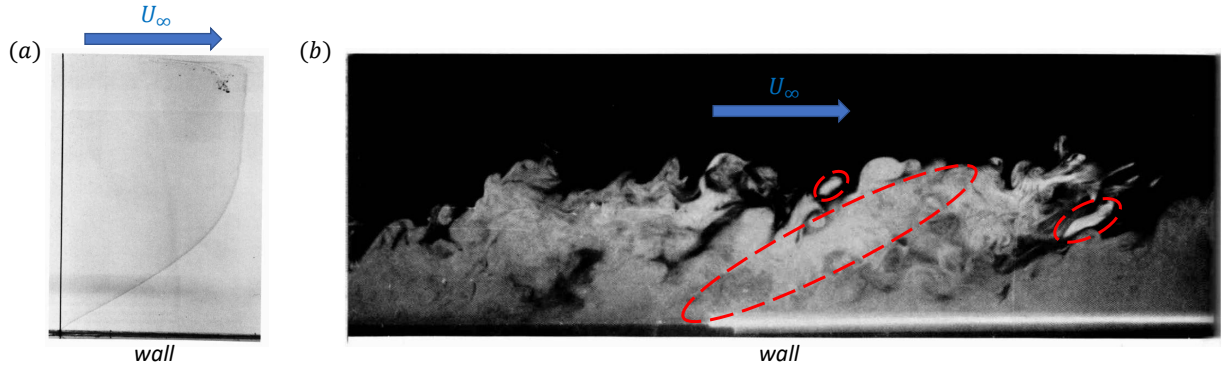

FIGURE 2.1: (a) Tangential velocity profile in a laminar boundary layer on a flat plate made visible by tellurium. (b) A turbulent boundary layer made visible by a vertical light sheet illuminating the tiny oil droplets introduced into the flow. U_∞ refers to the mean freestream speed and dashed red lines in (b) highlight 'eddies' of various sizes in the turbulent flow. Both (a,b) have been adapted from Van Dyke (1982).

the no-slip condition, and exists up to the height where the flow velocity asymptotically matches with that of the freestream. The presence of the no-slip condition creates a steep velocity gradient in the direction normal to the wall, due to the rapid transition of the mean flow velocity over a very thin region. Existence of this shear layer effectively segregates the flow over the body into two regions based on the influence of the fluid viscosity: the viscosity plays a crucial role in the region near the surface of the body, i.e. in the boundary layer, while its influence is less significant in the freestream. The skin friction component of the drag force, experienced by the body, is due to the existence of the boundary layer. Momentum is transferred across this layer, from the freestream onto the surface of the body, which tends to retard the relative motion between the body and the fluid. It should be noted here that such a shear layer can be formed for a flow over any wall, either inside or outside a duct. The former are classified as internal flows, while the latter are external flows. Canonical cases in internal flows include the pressure driven flow in a rectangular (channel) or a circular (pipe) duct. These flows, when fully developed, do not have a 'freestream' due to the shear layer encompassing the entire cross-section of the geometry. A zero-pressure gradient boundary layer, on the other hand, is considered the canonical case for the external flows. These three flows together make up the canonical wall-bounded flows.

The nature of wall-bounded flows is dependent on the Reynolds number (Re), which is a characteristic of the fluid velocity, viscosity and the flow geometry. When the Reynolds number is very low, the flow inside the shear layer is ordered and laminar, which is showcased by the flow visualization over a flat plate in figure 2.1(a). However, as the Reynolds

number increases, the wall-bounded flow becomes highly chaotic, random and multi-scale in nature, owing to which it is termed as a turbulent flow (Tennekes and Lumley, 1972). Figure 2.1(b) shows the flow visualization of a turbulent boundary layer (TBL), with three 'eddies' of different sizes highlighted to suggest the existence of a range of scales in the flow. Turbulent wall-bounded flows are known to comprise of a plethora of such eddies (Brown and Thomas, 1977; Robinson, 1991; Jiménez, 2018), which are in turn responsible for the momentum transport in the wall-normal direction, as well as across the various scales existing in the flow (Tennekes and Lumley, 1972; Lee and Moser, 2019). A detailed discussion on these eddies will continue ahead in §2.3. What follows first is a discussion on the variation of certain key flow statistics, which have been found to be influenced by different flow parameters, depending on the distance from the wall.

2.2 Classical scaling arguments

2.2.1 Mean velocity profile

As per dimensional analysis of a turbulent wall-bounded flow, the mean velocity profile depends on the mean local wall shear stress (τ_w), the characteristic large-scale of the wall-bounded geometry (δ), the distance from the wall (z) and the kinematic viscosity of the fluid (ν). δ, thus, corresponds to the half-height of the channel for a turbulent channel flow, radius of the pipe in the case of turbulent pipe flows and thickness of the turbulent boundary layer for external flows. The arguments presented in this section, hence, are valid for all canonical flows in general. However, since the present thesis focuses predominantly on the TBL, the discussion ahead will be mostly associated with this flow. Figure 2.2(a) depicts a simplified schematic of a zero-pressure gradient (ZPG) TBL developing over a flat plate in the streamwise direction, x. Throughout this thesis, x, y and z indicate the streamwise, spanwise and wall-normal coordinates, respectively, with u, v and w denoting the velocity components in the respective direction. Symbols in upper-case denote mean flow quantities while those in lower-case represent fluctuating flow quantities, with the latter estimated via the Reynolds decomposition (i.e. subtracting the mean flow from the instantaneous flow). Coming back to the mean velocity profile, while the variables listed above do influence the overall shape of the profile (figure 2.2(b)), historical arguments suggest not all of these are statistically significant in the various 'regions' of the boundary layer demarcated in figure 2.2(b). In the region very close to the wall, referred as the inner region, Prandtl (1925) proposed that the variables which influence the mean streamwise

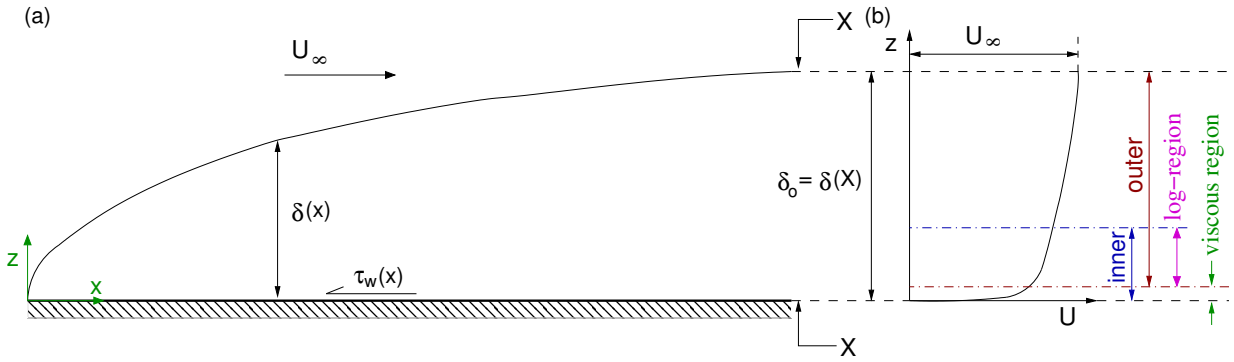

FIGURE 2.2: (a) Simplified schematic of a streamwise developing turbulent boundary layer over a flat plate with freestream velocity, U_∞. (b) Schematic showing the mean velocity profile at a particular streamwise position, X along with the different flow regions proposed for a turbulent boundary layer based on the scaling arguments.

velocity (U) are z, ν and the friction velocity, U_τ. Here, the friction velocity is by definition $U_\tau = \sqrt{\tau_w/\rho}$, where ρ is the fluid density. Application of the dimensional analysis yields the following relationship in the inner region:

$$\frac{U}{U_\tau} = f\left(\frac{zU_\tau}{\nu}\right), \tag{2.1}$$

which is referred to as the law of the wall. It suggests U_τ and ν/U_τ to be the characteristic velocity and length scales in the inner region, respectively. On the other hand, in the region away from the wall, which is referred to as the outer region, variables which influence U are z, U_τ, δ and the freestream velocity U_∞. The functional relationship between the mean velocity and these variables in the outer region was put forward by von Kármán (1930). This relationship, which is also known as the defect law, is given by:

$$\frac{U_\infty - U}{U_\tau} = F\left(\frac{z}{\delta}\right), \tag{2.2}$$

with δ and U_τ respectively the characteristic length and velocity scales in the outer region. While various forms of the outer velocity scale have been used previously (Zagarola and Smits, 1998), here the friction velocity (U_τ) is considered as the appropriate scale for the entire layer owing to its relevance in forming the inner boundary condition for the outer flow (Marusic et al., 2010c).

Millikan (1939) proposed the existence of an overlap region in the wall-normal range where both (2.1) and (2.2) would hold simultaneously. Consequently, in this overlap region, the

derivatives of these two equations should be equal, which leads to

$$z^+ \frac{\partial f}{\partial z^+} = -\eta\left(\frac{\partial F}{\partial \eta}\right) \tag{2.3}$$

where $z^+ = (zU_\tau/\nu)$ and $\eta = (z/\delta)$ represent the wall-normal distance normalized by the inner length scale (ν/U_τ) and the outer length scale (δ), respectively. Throughout the thesis, the superscript '+' has been used to denote normalization by either the inner length or velocity scale. The left- and right-hand-side of (2.3) are only a function of z^+ and η, respectively, meaning that both sides must equate to a constant. Integration of the two sides of (2.3) yields:

$$\frac{U}{U_\tau} = \frac{1}{\kappa}\ln\left(\frac{zU_\tau}{\nu}\right) + A, \text{ and} \tag{2.4}$$

$$\frac{U_\infty - U}{U_\tau} = -\frac{1}{\kappa}\ln\left(\frac{z}{\delta}\right) + B, \tag{2.5}$$

where both κ and A are universal constants while B is a parameter which depends on the flow geometry. For historical purposes, κ is referred to as the Kármán constant. Equations (2.4) and (2.5) represent the popular logarithmic law (or log-law), showcasing the logarithmic dependence of the mean streamwise velocity on the wall-normal height, due to which the overlap region is also known as the log-region (or the inertial layer). It is the most well-known analytical expression describing the wall-bounded turbulent flows, given that it has been corroborated by experiments over a wide range of flow conditions (Nickels et al., 2007). It should, however, be noted that the derivation of the log-law is not limited solely to the overlap arguments by Millikan (1939). The same relationship can also been derived using the mixing-length hypothesis of Prandtl (1925), the attached eddy hypothesis of Townsend (1976), as well as from the first principles (Oberlack, 2001; Fife et al., 2005).

Coles (1962), after surveying the available experimental data of the mean velocity profiles, suggested the values of $\kappa = 0.41$ and $A = 5.0$ for (2.4). There has, however, been substantial debate in the literature surrounding the value of κ, since its estimation depends on the wall-normal range considered to be the log-region, the 'true' bounds for which are still not universally accepted. While the classical arguments suggest the upper bound to be a fixed fraction of δ, and the lower bound fixed at a viscous-scaled wall-normal location (z^+), determining these bounds isn't straight-forward (Marusic et al., 2010c) due to the very slow deviation of the mean velocity profile from (2.4). Consequently, in the literature, one would come across a large variation in the estimates for the lower bound (in particular), with proposed values ranging from $z^+ \approx 30$ (Tennekes and Lumley, 1972) up to $z^+ \approx$

600 (Zagarola and Smits, 1998). Marusic et al. (2013) suggested that this difficulty may be overcome by imposing an additional criterion, in the form of a logarithmic variation of the streamwise variance ($\overline{u^2}$) with z for the overlap region. The latter is an analytical outcome from the attached eddy hypothesis of Townsend (1976), which will be discussed ahead in §2.4. By analyzing the experimental data over a wide range of friction Reynolds number Re_τ ($2 \times 10^4 < Re_\tau < 6 \times 10^5$), Marusic et al. (2013) proposed $3\sqrt{Re_\tau} \lesssim z^+ \lesssim 0.15Re_\tau$ to be a reasonable approximation for the bounds of the overlap region. Here, Re_τ is the Reynolds number based on the friction velocity, and is defined as $Re_\tau = zU_\tau/\nu$. This parameter reflects the ratio of the largest ($\sim \mathcal{O}(\delta)$) and the smallest ($\sim \mathcal{O}(\nu/U_\tau)$) energy-containing scales in the flow, with an increasing Re_τ suggestive of the increase in scale separation between the two. The Re_τ-dependence of the log-region lower bound is thus indicative of it being influenced also by the outer scales, which although contrary to classical arguments, has previously been argued based on first principles by Klewicki et al. (2009).

2.2.2 Townsend's local equilibrium hypothesis

In his seminal work widely respected for its original ideas, Townsend (1961, 1976) also developed scaling arguments for a part of the inner region away from the wall, where he noted that "*the local rates of energy production and dissipation are so large that aspects of the turbulent motion concerned with these processes are determined almost solely by the distribution of shear stress within the region and are independent of conditions outside it*". He called this region the *equilibrium layer* considering the "*energy equilibrium existing between local rates of energy production and dissipation*". To develop his scaling arguments, Townsend (1961) began by considering the turbulent kinetic energy budget, which as per the usual boundary layer approximations, is given by (Tennekes and Lumley, 1972):

$$\underbrace{U\frac{\partial \overline{q^2}/2}{\partial x} + W\frac{\partial \overline{q^2}/2}{\partial z}}_{\text{advection}} + \underbrace{\overline{uw}\frac{\partial U}{\partial z}}_{\text{production}} + \underbrace{\frac{\partial \overline{wq^2}/2}{\partial z} + \frac{\partial \overline{wp}}{\partial z}}_{\text{transport}} + \underbrace{\varepsilon}_{\text{dissipation}} = 0, \tag{2.6}$$

where $\overline{q^2} = \overline{u^2} + \overline{v^2} + \overline{w^2}$, p is the kinematic pressure and ε is the local rate of turbulent energy conversion to heat. As per the definition of the equilibrium layer, terms associated with the turbulent energy transport and advection in (2.6) should be negligible as compared to the rate of local energy production and dissipation. This reduces (2.6) to:

$$\overline{uw}\frac{\partial U}{\partial z} + \varepsilon \approx 0. \tag{2.7}$$

Townsend (1961) further assumed the equilibrium layer to coincide with a constant stress layer wherein the Reynolds shear stress, $\overline{uw}(z) \approx U_\tau^2$. This assumption modifies (2.7) further, such that all terms can be normalized by using U_τ and z as the relevant velocity and length scales. Thus, for an equilibrium layer,

$$\begin{aligned} \varepsilon &= \frac{U_\tau^3}{\kappa z}, \text{ and} \\ \frac{\partial U}{\partial z} &= \frac{U_\tau}{\kappa z}. \end{aligned} \tag{2.8}$$

On integration, equation (2.8) leads to the log-law given by 2.4, which conveys that the equilibrium layer essentially corresponds to the log-layer. It should be noted that in today's terminology, flows that adhere to (2.7) are described to be in a 'local equilibrium' (Morrison et al., 1992; McKeon and Morrison, 2007), to suggest the dissipation of energy at approximately the same location where it is generated. This was demonstrated by McKeon and Morrison (2007) to be increasingly accurate for high-Re_τ wall-bounded flows.

It is important to note here that the aforementioned arguments are applicable only to that part of the turbulent flow which is associated with production and dissipation of energy. Townsend (1961, 1976) defined the motions responsible for the generation of the Reynolds shear stress $\overline{uw}$ (and consequently also for turbulent production), at any z in the equilibrium layer, as 'active' motions, and described them as universal in the sense that they scale solely with U_τ and z. This characteristic is largely associated with the w-velocity signatures at z exhibiting a similar universal behaviour, as opposed to the wall-parallel velocity signatures, both of which were found to be Re_τ-dependent (Townsend, 1961, 1976). Thus, only a fraction of the u- and v-velocity signatures at z are associated with the Reynolds shear stress carrying (active) motions at z. The remaining aspects of the u- and v-velocity signatures (at z) were described as 'inactive' or non-universal features. As per Townsend (1961, 1976), these motions do not contribute to the local production (at z) but may be of significance further away from the wall.

2.2.3 Spectral scaling arguments

Owing to the multi-scale nature of the flow, spectral analysis of the signals recorded in turbulent flows has been the key analysis methodology adopted by many studies in the past, to develop insights into the statistical structure of the flow. Similar to the scaling exhibited by the mean velocity, Perry and Abell (1977) and Perry et al. (1986) demonstrated that the scale-specific energy in the three velocity components, which is reflected by the velocity

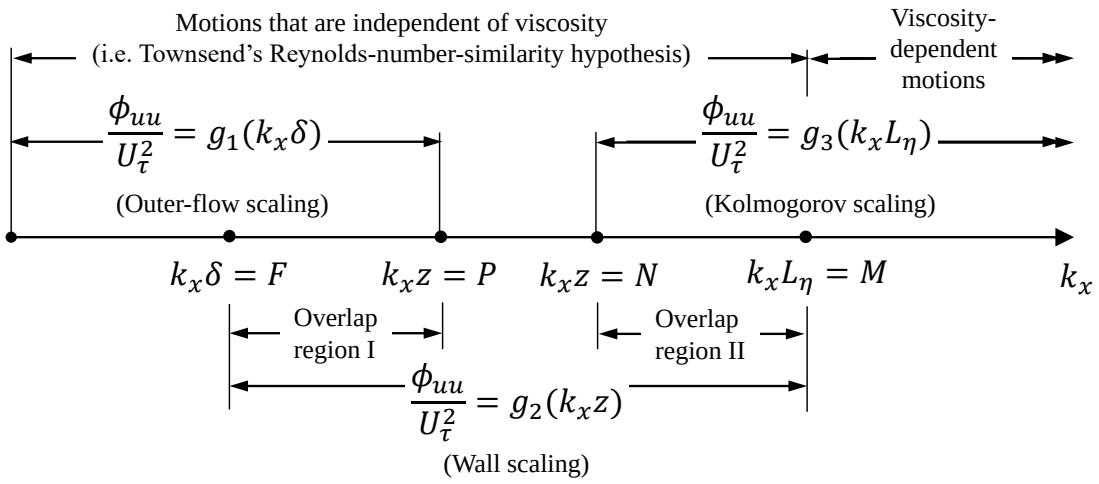

FIGURE 2.3: Summary of the scalings exhibited by various spectral regions in the 1-D streamwise u-spectra in the logarithmic region. Adapted from Perry et al. (1986).

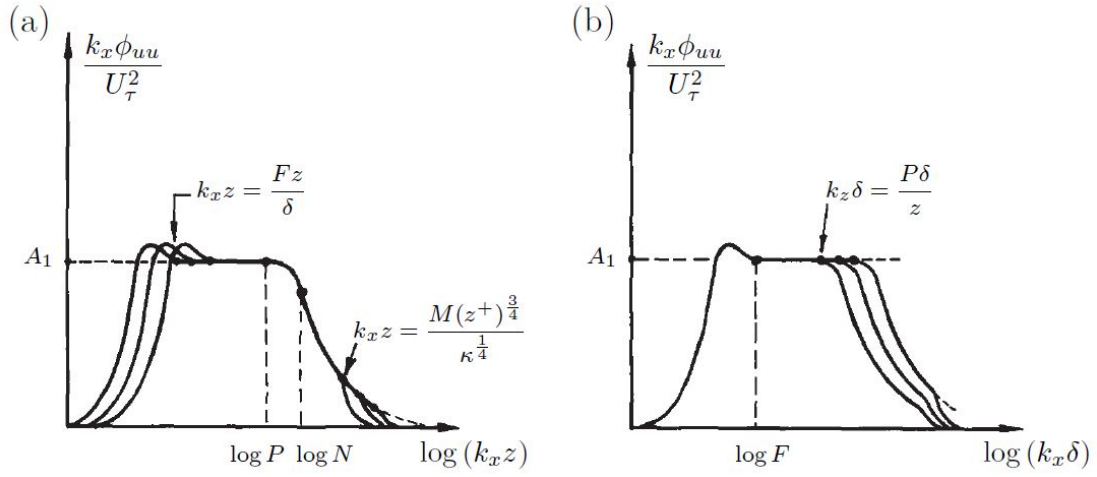

FIGURE 2.4: Schematic of the expected distributions of the premultiplied u-spectra with (a) inner-flow scaling and (b) outer-flow scaling. Adapted from Perry et al. (1986).

spectra, also conform to certain scaling arguments in the log-region (figures 2.3 and 2.5). In this thesis, we denote the one-dimensional (1-D) streamwise spectra by $\phi_{ij}(k_x)$, where i,j = u,v or w. By definition, $\int_0^\infty \phi_{ij}(k_x)\,d(k_x) = \overline{ij}$, where k_x is the streamwise wavenumber. For their arguments, Perry and co-workers considered the spectra in three spectral ranges: (i) the high wavenumber range covering viscosity dependent dissipative motions, (ii) the intermediate wavenumber range comprising of motions scaling with distance from the wall, and finally (iii) the low wavenumber range which represents δ-scaled motions. Of these, the low and intermediate range of wavenumbers correspond to the energy-containing inertial

motions (Perry et al., 1986), which are predominant in the log-region. Following the log-law relationship discussed in §2.2.1, the only important variables in this region are U_τ, k_x, z and δ. Considering first the streamwise velocity component (u) at any $z \ll \delta$, here, eddies of scale $O(\delta)$ will contribute to the low wavenumber end of $\phi_{uu}(z; k_x)$. This leads to an 'outer-flow' scaling as follows:

$$\frac{\phi_{uu}(k_x\delta)}{U_\tau^2} = \frac{\phi_{uu}(k_x)}{\delta U_\tau^2} = g_1(k_x\delta). \tag{2.9}$$

Similarly, eddies of scale $O(z)$ will contribute to motions at the intermediate and high waveneumber end of $\phi_{uu}(z; k_x)$, leading to 'inner-flow' scaling as follows:

$$\frac{\phi_{uu}(k_x z)}{U_\tau^2} = \frac{\phi_{uu}(k_x)}{z U_\tau^2} = g_2(k_x z). \tag{2.10}$$

Here, δ wasn't considered since eddies of that scale would make no contribution to the concerned wavenumber range at $z << \delta$. The very high-wavenumber motions coexisting at z, which are viscosity-dependant, can be expected to be locally isotropic in accordance to Kolmogorov's hypothesis (Kolmogorov, 1941). Thus, small-scale motions contributing to $\phi_{uu}(z; k_x)$ will follow the classical Kolmogorov viscosity dependant scaling law:

$$\frac{\phi_{uu}(k_x L_\eta)}{U_\eta^2} = \frac{\phi_{uu}(k_x)}{L_\eta U_\eta^2} = g_3(k_x L_\eta), \tag{2.11}$$

where L_η and U_η are the Kolmogorov length and velocity scales respectively. Both these quantities depend on the average turbulent energy dissipation ($\langle\varepsilon\rangle$) and the kinematic viscosity, and are defined as follows:

$$L_\eta = \left(\frac{\nu^3}{\langle\varepsilon\rangle}\right)^{\frac{1}{4}}, \text{ and } U_\eta = (\nu\langle\varepsilon\rangle)^{\frac{1}{4}}. \tag{2.12}$$

Equations (2.9), (2.10) and (2.11) thus summarize the scaling exhibited by the streamwise velocity spectra (ϕ_{uu}) at $z \ll \delta$ over a range of wavenumbers, k_x. Similar to the overlap argument for the mean flow (§2.2.1), Perry et al. (1986) proposed two overlap regions for the u-spectra between the scaling regions given by equations (2.9) - (2.11), as shown in figure 2.3. The boundaries of the spectral regions are denoted by constants F, M, N and P. In the region of overlap I, both equations (2.9) and (2.10) are valid, leading to a power law region of the form (Perry et al., 1986):

$$g_1(k_x\delta) = \frac{A_1}{k_x\delta} \text{ and } g_2(k_x z) = \frac{A_1}{k_x z}, \tag{2.13}$$

where A_1 is a universal constant and is also known as the Townsend-Perry constant. The expression in (2.13) can be used to rearrange (2.10) and (2.9) to obtain the form of the premultiplied spectra as:

$$\frac{k_x \phi_{uu}(k_x)}{U_\tau^2} = A_1, \tag{2.14}$$

which corresponds to the k_x^{-1}-scaling. Figure 2.4 adapted from Perry et al. (1986) depicts the plateau representing the k_x^{-1}-scaling in the premultiplied 1-D u-spectra, which has been a topic of considerable debate in the literature (Nickels et al., 2005; Rosenberg et al., 2013; Lee and Moser, 2015; Chandran et al., 2017; Baars and Marusic, 2020a; Yoon et al., 2020; Hwang et al., 2020).

The scaling laws for the spectra, such as the k_x^{-1} power law, are significant in the sense that they provide information regarding the geometry of the statistically representative structures in the turbulent flow, as well as their contribution to the total energy. For example, the k_x^{-1}-scaling indicated by (2.14) suggests the range of scales (represented by k_x) contribute equally ($\sim$ A$_1$) to the streamwise turbulent kinetic energy. Further discussion related to the empirical observations of this scaling, in the literature, will be continued in §2.5.

In region of overlap II (figure 2.3), similarly, (2.10) and (2.11) are valid simultaneously. Assuming that the motions in this wavenumber region are in 'local equilibrium' (§2.2.2), the Kolmogorov length and velocity scales (given in equation 2.12) can be expressed purely as a function of ν, U_τ and z using (2.8):

$$L_\eta = \left(\frac{\nu^3 \kappa z}{U_\tau^3}\right)^{\frac{1}{4}} \text{ and } U_\eta = \left(\frac{\nu U_\tau^3}{\kappa z}\right)^{\frac{1}{4}}. \tag{2.15}$$

Substituting these in (2.11) and comparing with (2.10), Perry et al. (1986) obtained:

$$\begin{aligned} g_2(k_x z) &= \frac{\phi_{uu}(k_x z)}{U_\tau^2} = \kappa^{\frac{-2}{3}} \frac{K_0}{(k_x z)^{\frac{5}{3}}} \text{ and,} \\ g_3(k_x L_\eta) &= \frac{\phi_{uu}(k_x z)}{U_\tau^2} = \frac{K_0}{(k_x L_\eta)^{\frac{5}{3}}}. \end{aligned} \tag{2.16}$$

The region of overlap II corresponds to the inertial subrange hypothesized by Kolmogorov (1941), where K_0 denotes the universal Kolmogorov constant. This scaling law, popularly known as Kolmogorov's $k^{-5/3}$-scaling, has received substantial empirical evidence in the literature (Saddoughi and Veeravalli, 1994; Samie et al., 2018). Based on the arguments of Townsend (1976) (discussed previously in §2.2.2), regarding both wall-parallel velocity

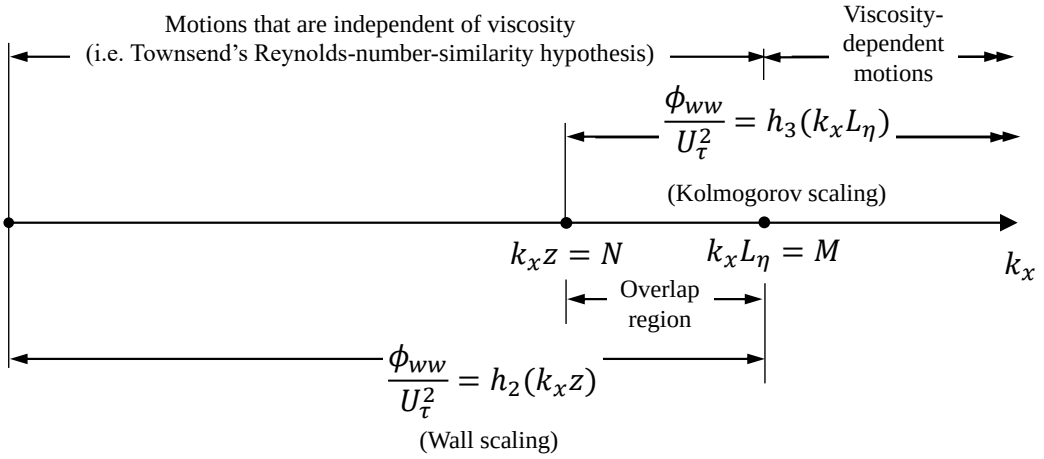

FIGURE 2.5: Summary of the scalings exhibited by various spectral regions in the 1-D streamwise w-spectra in the logarithmic region. Adapted from Perry et al. (1986).

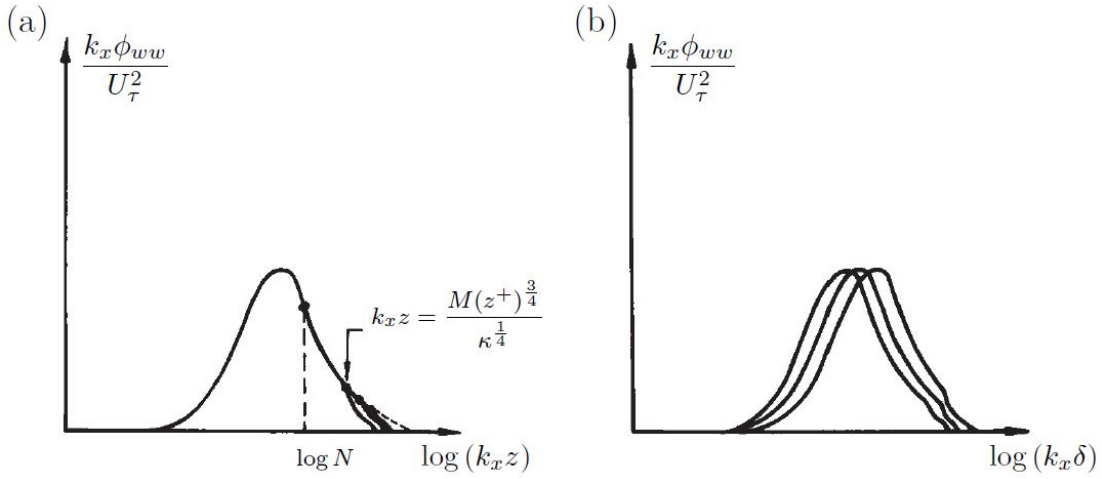

FIGURE 2.6: Schematic of the expected distributions of the premultiplied w-spectra with (a) inner-flow scaling and (b) outer-flow scaling. Adapted from Perry et al. (1986).

components exhibiting similar scaling behaviours in the log-region, Perry et al. (1986) argued that the spanwise spectra ϕ_{vv} follows scaling laws similar to ϕ_{uu}. The functional forms given in (2.13) thus indicate a k_x^{-1}-scaling for both the ϕ_{uu} and ϕ_{vv} spectra, with only the universal constant A_1 being replaced by A_2 for the latter.

For the wall-normal component at $z \ll \delta$, on the other hand, Townsend (1976) noted $w(z)$ to comprise velocity signatures localized at z, indicating no δ-scaled eddy contributions to the low-wavenumber range of $\phi_{ww}(k_x, z)$ (figure 2.5). Subsequently, only a single region of

overlap exists for ϕ_{ww}, where:

$$\begin{aligned} \frac{\phi_{ww}(k_x z)}{U_\tau^2} = \frac{\phi_{ww}(k_x)}{z U_\tau^2} &= h_2(k_x z) \text{ and,} \\ \frac{\phi_{ww}(k_x L_\eta)}{U_\eta^2} = \frac{\phi_{ww}(k_x)}{L_\eta U_\eta^2} &= h_3(k_x L_\eta) \end{aligned} \tag{2.17}$$

hold simultaneously. Subsequently, no k_x^{-1} scaling exists for the ϕ_{ww} spectra, which is illustrated by the sketch adapted from Perry et al. (1986) depicted in figure 2.6. Integration of the spectral scaling laws in equations (2.9) – (2.11), (2.13), (2.16) and (2.17), across the respective energetic wavenumber range, leads to the following analytical expressions for the variances of the three velocity components in the log-region (Perry et al., 1986):

$$\begin{aligned} \overline{u^2}^+ &= B_1 - A_1 \ln\left(\frac{z}{\delta}\right), \\ \overline{v^2}^+ &= B_2 - A_2 \ln\left(\frac{z}{\delta}\right), \text{ and} \\ \overline{w^2}^+ &= B_3, \end{aligned} \tag{2.18}$$

where A_1, A_2, B_1, B_2 and B_3 are constants. These expressions are the same as those obtained previously by Townsend (1976) based on his attached eddy arguments. Further discussion on these is continued in section §2.4, where the attached eddy model has been reviewed.

2.3 Coherent structures in wall-turbulence

Owing to the seminal studies of Brown and Roshko (1974) and Brown and Thomas (1977), it is now well accepted in the turbulence community that any turbulent shear flow is populated by recurrent and statistically-significant features, known as 'coherent motions'. This discovery was significant because it suggested the existence of an inherent organization in a flow which was previously deemed to be completely random and chaotic. Ever since, researchers have been able to associate various features of the flow, brought out by the flow statistics, with these motions. In the case of wall-bounded flow, for example, the log-law relationship given by (2.4) has been shown to be an artifact of the time-averaged signature of long streamwise momentum-containing coherent motions (Heisel et al., 2020) co-existing in the log-region. A coherent motion, however, is not limited to a specific flow variable; Robinson (1991) defined it to be "*a three-dimensional region of the flow over which at least one fundamental flow variable (velocity component, density, temperature, etc.) exhibits*

significant correlation with itself or with another variable over a range of space and/or time that is significantly larger than the smallest local scales of the flow". A vast amount of literature can be found associated with this topic, which has also been a subject of a number of reviews (Robinson, 1991; Panton, 2001; Adrian, 2007; Jiménez, 2018). These studies were primarily stimulated by the need to understand the production and inter-scale transfer of turbulent kinetic energy (Robinson, 1991), wherein these structures are known to play a crucial role (Ganapathisubramani et al., 2003; Lee and Moser, 2019). Here, we briefly review the coherent motions relevant to the work in the present thesis. Interested readers may refer to the comprehensive reviews stated above, or the individual references mentioned ahead, for an in-depth understanding. Throughout this thesis, the terminology 'eddies', 'structures' and 'motions' are used interchangeably to correspond to the definition of a coherent motion outlined by Robinson (1991).

Smits et al. (2011), in their review on wall turbulence, identified four characteristic elements of the organized flow, namely near-wall streaks (Kline et al., 1967), hairpin vortices (Theodorsen, 1952), large-scale motions (LSMs; Kim and Adrian (1999)) and very-large-scale motions (VLSMs; Kim and Adrian (1999), Hutchins and Marusic (2007)), with each being dominant in various regions of the shear flow. The near-wall streaks form part of a 'self-sustaining' or 'autonomous' cycle occurring at the small-scales in the near-wall region (Hamilton et al., 1995; Jeong et al., 1997; Jiménez and Pinelli, 1999). This cycle was found to work as follows: the streaks are created by the streamwise vortices, and become unstable and wavy with time. This waviness in the streaks stretches the streamwise vorticity which creates new vortices, which leads to new streaks, and so on. These processes are known to be directly associated with the intense local levels of turbulence production, as well as the generation of wall-shear stress in the near-wall region. While this kinetic energy production is crucial for a low Reynolds number flow, at high Reynolds numbers, the bulk of the turbulent kinetic energy production takes place in the outer region (Marusic et al., 2010b; Smits et al., 2011; Lee and Moser, 2019), particularly in the log-region. This is owing to the fact that the viscous-scaled location and intensity of the autonomous cycle remains fixed, while the log-region spans a larger wall-normal range with increase in Re_τ.

Hairpin vortices (also referred as horshoe vortices or Λ-vortices) have been described as the key structural entity of a wall-bounded flow (Adrian, 2007) and were first proposed by Theodorsen (1952) (figure 2.7(a)). This structure corresponds to a concentrated region of vorticity distributed in the shape of a hairpin, with its two legs comprising quasi-streamwise vorticity close to the wall while the head, which joins these two legs, primarily comprising of spanwise vorticity much farther from the wall. The first clear experimental evidence of

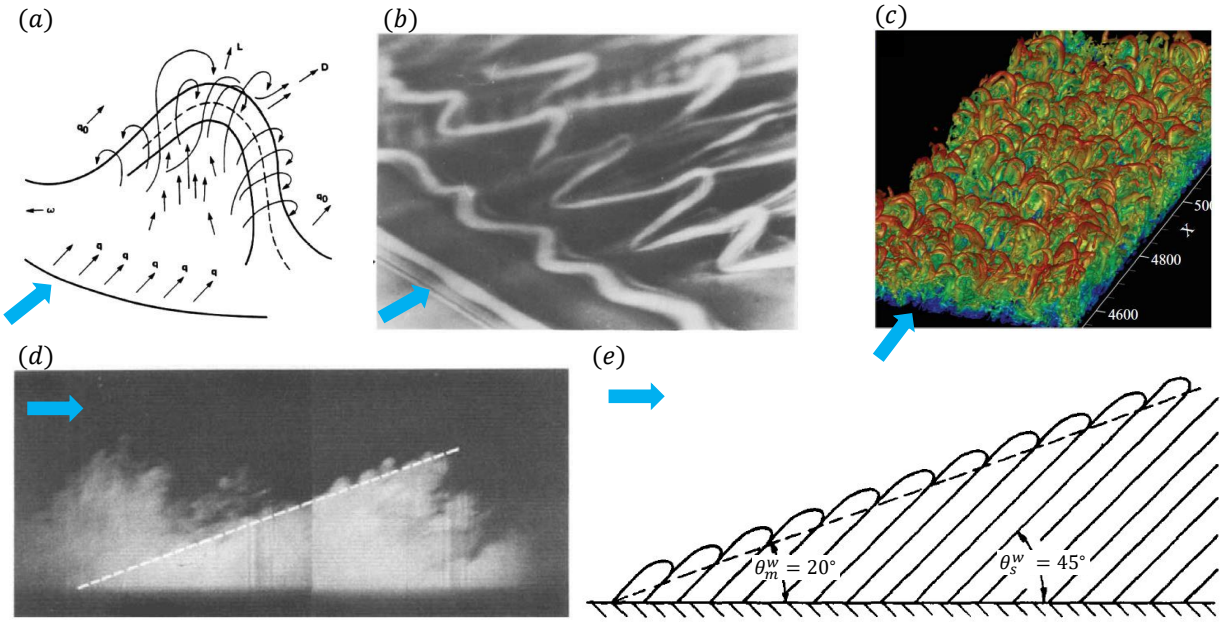

FIGURE 2.7: Hairpins as a dominant coherent structure in a wall-bounded flow: (a) Theodorsen's (1952) conceptualization of a horseshoe/hairpin vortex. (b) Hairpin vortices observed via flow visualization in a boundary layer (Perry and Chong, 1982). (c) Hairpin-shaped structures observed in the instantaneous field obtained from DNS of a ZPG TBL by Wu and Moin (2009). (d,e) Organization of hairpins as a packet to form larger 'ramp-like' structures conceptualized (in (e)) by Head and Bandyopadhyay (1981) based on their flow visualization in (d). Blue arrow indicates mean flow direction.

the presence of hairpins came from the seminal work of Head and Bandyopadhyay (1981) and Perry et al. (1981). These studies employed flow visualization techniques to reveal the omnipresence of the hairpin vortices in the shear flow, which is evident from the snapshot taken by Perry et al. (1981) shown as figure 2.7(b). These findings motivated the direct numerical simulation (DNS) studies in the channel and ZPG TBL geometry to quantitatively estimate the vortex strength in the hairpin vortices, along with its geometric characteristics. Figure 2.7(c) shows an instantaneous volume of ZPG TBL DNS by Wu and Moin (2009), with the flow comprising of a forest of hairpin eddies. A number of features of the hairpins, which were initially estimated via observation from experiments, were also confirmed by these simulations. For example, Head and Bandyopadhyay (1981) observed that individual hairpin structures were consistently oriented at $\theta_s^w = 45°$ relative to the mean flow direction (figure 2.7(e)), which was confirmed later by the channel DNS study of Moin and Kim (1985). Interestingly, on increasing the Re_τ, Head and Bandyopadhyay (1981) found the hairpin vortices coalesced to form large ramp-like structures (figure 2.7(d)), with a characteristic inclination angle (θ_m^w) of approximate 20° (figure 2.7(e)). It was hypothesized that the formation of these large structures, subsequently, obscures the geometric

features of an individual hairpin in high-Re_τ flows.

The unique vorticity distribution in a hairpin vortex, as depicted in figure 2.7(a), leads to the induction of low ($-u$) and high ($+u$) streamwise momentum in the region inside and outside the hairpin legs respectively, in accordance to the Biot-Savart law. Here, it should be noted that '-u' and '+u' events at z are relative to the mean streamwise velocity $U(z)$. In general, all motions in the wall-bounded flows have a mean convection velocity along $+x$. The three dimensional extent of these streamwise momentum zones, induced by a hairpin, depends on the relative positioning and speed of the individual hairpins in the flow, with those aligned along the streamwise direction subsequently coalescing to form 'packets' of hairpins with associated long momentum zones. While this notion of streamwise concatenation of the hairpin vortices was conjectured previously by Head and Bandyopadhyay (1981) and others (conceptualized in figure 2.7(e)), it was only confirmed after the quantitative analysis of a wall-bounded flow field conducted by Adrian and co-workers (Meinhart and Adrian, 1995; Kim and Adrian, 1999; Adrian et al., 2000; Tomkins and Adrian, 2003). By employing particle image velocimetry (PIV), Meinhart and Adrian (1995) investigated the instantaneous flow in the wall-normal plane of the ZPG TBL to find nested zones of quasi-streamwise momentum, which were segregated by thin layers of concentrated spanwise vorticity (representing the hairpin heads). These observations were explained in further detail with the help of a low-Re_τ numerical experiment conducted by Zhou et al. (1999), which suggested new hairpin vortices were created via interactions between $+u$ and $-u$ regions of older hairpin vortices. This time-dependent interaction was hypothesized as the mechanism inducing an array of aligned hairpins in the streamwise direction, and was later confirmed by the seminal work reported in Adrian et al. (2000). These experiments not only established hairpin vortices to be the key structural entity in the outer(wake)-region of the wall-bounded flow, but also showed that hairpins are more likely to appear as 'packets' of inclined coherent groups convecting at nearly the same streamwise velocity. Figure 2.8(a) summarizes these key findings from Adrian et al. (2000) in the form of a conceptual sketch, which depicts the flow dynamics occurring in the outer-region of a wall-bounded flow. Also indicated in the schematic is the streamwise inclination angle of the 'packet' of hairpins (θ_m^w), which is smaller in comparison to that of an individual hairpin, consistent with the hypothesis of Head and Bandyopadhyay (1981) given in figure 2.7(e).

The long streamwise momentum zones induced from the hairpin packets were termed as large-scale motions (LSMs; Kim and Adrian (1999)), which typically extend up to 2-3δ in streamwise length. These LSMs, and the associated hairpin packets, are known to

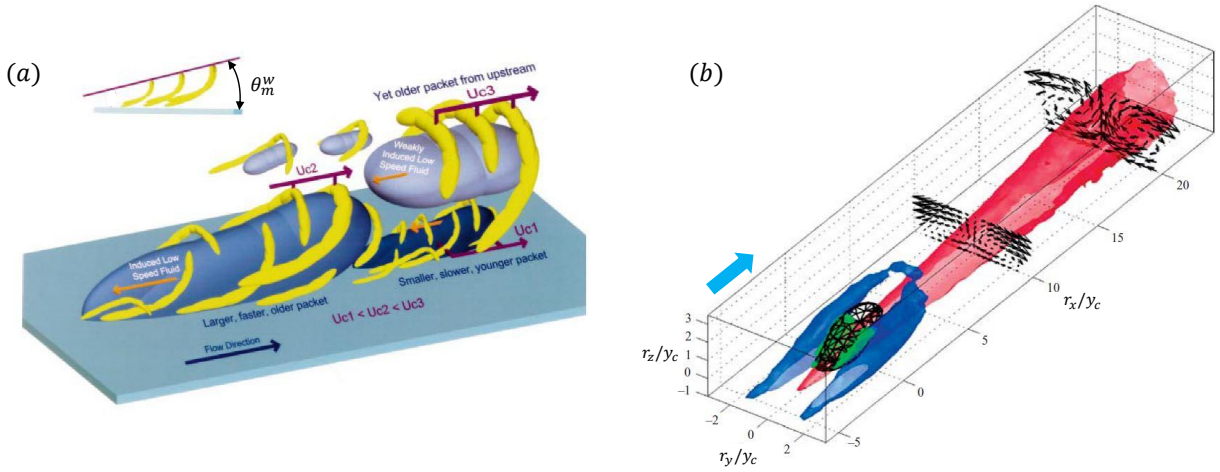

FIGURE 2.8: (a) Scenario of nested packets of hairpins (in yellow) in a boundary layer conceptualized and illustrated by Adrian et al. (2000). They hypothesized the packets to be aligning along streamwise direction to create long streamwise momentum zones (in blue), with speeds lower than the mean streamwise velocity. (b) Three-dimensional plot of the conditional-averaged velocity field obtained from a DNS of a turbulent channel flow by del Álamo et al. (2006). Red and blue isosurfaces represent low and high speed regions, while the green isosurface represents the discriminant of the velocity gradient tensor, which can be considered surrogate of the vorticity. Blue arrow indicates direction of the mean flow velocity.

constitute a majority percentage of turbulence production and turbulent kinetic energy (Ganapathisubramani et al., 2003; Balakumar and Adrian, 2007; Wu et al., 2012), a feature which is universal across all canonical wall-bounded flows. The relevance of these structures in the momentum transfer across the shear layer prompted the numerical investigation of the organization of these vortex clusters by del Álamo et al. (2006), who studied it for a turbulent channel flow. They identified two types of vortex clusters beyond the inner-region flow, one type are wall-coherent (i.e. structures with signatures extending down to the wall) and the other wall-incoherent, with the latter predominantly occupying the outer-region of the flow. Although none of these clusters resembled hairpin packets, as suggested otherwise by Adrian et al. (2000), the low (-u) and high (+u) momentum velocity field associated with the wall-coherent clusters (figure 2.8(b)) resembled the picture presented by the hairpin packet paradigm (figure 2.8(a)) given by Adrian et al. (2000). Interestingly, the wall-coherent clusters extracted by del Álamo et al. (2006) were found to exhibit geometric and kinematic self-similarities, akin to those noted previously in the case of the hairpin vortices by Tomkins and Adrian (2003).

The largest and most energetic motions, which dominate the log-region flow along with the LSMs, are the very-large-scale-motions (VLSMs; Kim and Adrian (1999)). These correspond to spanwise-alternatively arranged (Dennis and Nickels, 2011) very long structures

of low ($-u$) and high ($+u$) streamwise momentum (Hutchins and Marusic, 2007; Monty et al., 2007), noted to exhibit meandering and obey outer-scaling (figure 2.9). While these characteristics are found to be similar in both the external as well as internal flows, the lengths of these motions differ between the two flow types (Monty et al., 2009). Accordingly, these are commonly referred to as VLSMs in the case of internal flows (Monty et al., 2009) and superstructures (or SS) in the case of external flows (Hutchins and Marusic, 2007). It is worth mentioning here that there remains much disagreement in the literature concerning the true streamwise extent of the SS. For example, instantaneous planar (x-y) flow fields in the log-region, reconstructed from the hotwire rake data (by employing the Taylor's hypothesis), suggest SS to extend up to 20δ (Hutchins and Marusic, 2007), while estimates based on the one-dimensional (1-D) u-correlation suggest coherence of the order of 6δ (Lee and Sung, 2011). This difference has been associated with the spanwise meandering exhibited by these very large-scale motions (Hutchins and Marusic, 2007), which masks the true streamwise length of these motions in the flow statistics. The hairpin vortex packet paradigm given by Adrian and co-workers hypothesizes these very long motions to also be a consequence of the concatenation of the hairpin packets in a pseudo-streamwise manner. This explanation has found experimental support from the tomo-PIV reconstruction of the ZPG TBL flow by Dennis and Nickels (2011). They found majority of the long u-structures to be aligned in a quasi-streamwise manner, in turn giving an impression of a contiguous very long structure in the flow, consistent with the concatenation hypothesis of Adrian et al. (2000) and Tomkins and Adrian (2005). The same has also been confirmed based on a space-time analysis of high-fidelity DNS datasets in ZPG TBL (Lee and Sung, 2011), channel (Lee et al., 2014) as well as a pipe (Baltzer et al., 2013), although the mechanism encouraging this concatenation still remains unknown (Jiménez, 2012).

2.3.1 Inner-outer interactions

After the discovery of the LSMs and VLSMs, the emergence of which has been associated with the aggregation of hairpins of smaller scales, the initial belief in the community was that these motions cannot exist in the absence of smaller motions (Hwang and Cossu, 2011). There is now, however, sufficient evidence to show that the turbulent kinetic energy associated with the LSMs and VLSMs is produced in the outer-region (Ganapathisubramani et al., 2003; Lee and Moser, 2019). Essentially, it means that their existence is driven by a self-sustaining mechanism (Hwang and Cossu, 2010, 2011) independent of any input from the smaller scales. This, however, doesn't rule out the possibility of any interaction

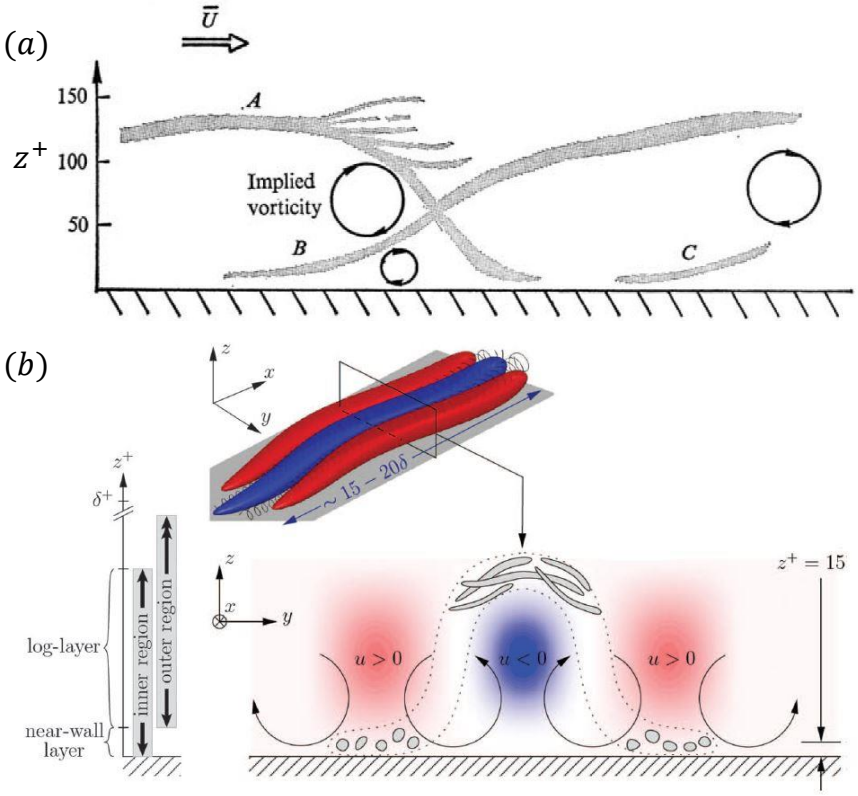

FIGURE 2.9: (a) Energy exchange cycle representing the 'bottom-up' transport of energy. A, B and C represent three successive ejections ($u < 0$, $w > 0$) carrying energy away from wall, which after a certain distance gives rise to a sweep ($u > 0$, $w < 0$) which moves towards the wall. (b) Schematic showing the very-large-scale-motions or superstructures extending from the log-region down to the wall, to superpose their signature as well as modulating the near-wall region. These regulate the 'top-down' transport of energy which is non-local. Figures (a) and (b) have been adapted from Offen and Kline (1975) and Marusic et al. (2010a), respectively.

between the small- and large-scales residing predominantly in the near-wall and outer-region, respectively. This interaction is manifested in the form of an energy transfer across the wall-normal direction, as well as across scales (Lee and Moser, 2019). Here, the focus is on the former, which is known to occur in either directions with respect to the wall: (i) the 'top-down' transport of energy to the wall from the outer-region, and (ii) 'bottom-up' transfer of energy produced in the near-wall region, away from the wall.

The VLSMs/SS, owing to their enormous size, are known to facilitate energy transfer from the outer to the near-wall region. This was first noted from the large-scale footprint in the energy spectra of the u-signal acquired in the near-wall region (Hutchins and Marusic, 2007; Hutchins et al., 2009). Apart from linear superposition of this energy onto the near-wall region, these large-scales were also known to modulate energy in the small-scales via non-linear interactions (Mathis et al., 2009; Marusic et al., 2010a; Ganapathisubramani et al.,

2012). This interaction is depicted schematically in figure 2.9(b) adapted from Marusic et al. (2010a). Mathis et al. (2009) noted this large-scale modulation of the small-scales in the inner-region to be increasing with Re_τ, effectively signaling the increase in large-scale contributions with Re_τ (in the near-wall region).

Apart from this 'top-down' transfer of energy, there is also considerable evidence of 'bottom-up' transfer of energy in a wall-bounded flow (del Álamo et al., 2006; Lee and Moser, 2019). This involves small-scale energy transferring through the 'lift-up' of streaks predominating the near-wall region. It is possible because the near-wall region comprises a plethora of Reynolds shear-stress carrying motions in the form of ejections ($u < 0$, $w > 0$) and sweeps ($u > 0$, $w < 0$), which are responsible for the intense local turbulent kinetic energy production ($uw < 0$). Offen and Kline (1975) hypothesized these ejections and sweeps to be a part of an energy-exchange cycle between the near-wall region and the log region, which they proposed to work as follows: the self-similar ejections (Morrison et al., 1992; del Álamo et al., 2006) 'lift-up' from the near-wall region and interact with the flow in the logarithmic region. This interaction produces sweeps which move toward the wall and generate new ejections further downstream. Figure 2.9(a), adapted from Offen and Kline (1975), illustrates this energy exchange cycle. Recently, Lee and Moser (2019) found this bottom-up energy transport to be 'localized' at a wall-normal location, in comparison to the top-down energy transfer by the VLSMs (figure 2.9(b)), which is clearly non-local (Hunt and Carlotti, 2001).

The overlap of both the 'bottom-up' and 'top-down' energy interactions, in the log-region, makes this region significant in the context of fundamental understanding of the mechanism of wall-turbulence. The research interest in this region is further substantiated by the fact that at high Re_τ, the log-region is also responsible for a major proportion of turbulence kinetic energy production (Smits et al., 2011). Adding to this, the geometric and kinematic self-similarity of flow phenomena dominating this region, noted in previous studies (Morrison et al., 1992; Tomkins and Adrian, 2003; del Álamo et al., 2006), makes a strong case in favour of phenomenological modelling of the log-region flow, capable of facilitating high Re_τ predictions. Consequently, the present thesis focuses predominantly on the structure and scaling in the log-region (or the inertial region) of a canonical turbulent boundary layer. Hence, discussions in the forthcoming sections will be mostly centered around the boundary layer phenomena in this region only.

2.3.2 Taylor's hypothesis

All coherent structures in a wall-bounded flow convect with a characteristic velocity in the positive streamwise direction. While it is possible to estimate these velocities via a well-resolved spatio-temporal analysis, in the majority of experiments, researchers are mostly limited to either a good temporally resolved acquisition system (hotwire anemometry) or a spatially-resolved system (particle image velocimetry; PIV). The present thesis investigates the turbulent boundary layers via stationary hotwire experiments, and subsequently lacks the adequate information to accurately convert the time series into spatial information. Taylor's hypothesis (Taylor, 1938) is useful in such circumstances, according to which the time-series of the velocity signal can be assumed to be the signature of a 'frozen' spatial feature of turbulence advecting beyond the probe with a constant mean speed of U_c. The term 'frozen' turbulence implies $u(x,t) = u(x - U_c t,0)$, meaning that temporal signals can be converted to spatial flow descriptions simply by using a characteristic convection velocity, U_c. As per Taylor's original hypothesis, $U_c = U(z)$, which has been demonstrated as a reasonable assumption in the log-region (Dennis and Nickels, 2008; de Silva et al., 2015) of a smooth-wall turbulent boundary layer. In other regions of the shear flow, however, particularly in the near-wall region, recent studies (Liu and Gayme, 2020) suggest convection velocities to be a function of scale as well as wall-normal location.

2.4 Attached eddy model of wall-turbulence

The previous section has brought out a picture of the wall-bounded flow as an amalgamation of organized coherent motions of various scales (Robinson, 1991). Given that this has been well-accepted in the turbulence community for quite some time, there have been several efforts in the past attempting to explain the flow physics based on coherent structure-based models (Grant, 1958; Townsend, 1976; Davidson and Krogstad, 2009). Notably, Townsend (1976) proposed a model for the structure of turbulent boundary layers based on his attached eddy hypothesis, wherein the flow is modelled using arrays of large 'eddies' or representative velocity fields, induced by characteristic vortex structures. The hypothesis was given by Townsend (1976) on noting the success of the log-law (§2.2.1,2.2.2) in estimating the mean velocity profile, and goes as follows: "*it is difficult to imagine how the presence of the wall could impose a dissipation length-scale proportional to distance from it unless the main eddies of the flow have diameters proportional to distance of their 'centres' from the wall, because their motion is directly influenced by its presence. In other*

words, the velocity fields of the main eddies, regarded as persistent, organized flow patterns, extend to the wall and, in a sense, they are attached to the wall". Hence, as per (Townsend, 1976), "*any eddy with a size that scales with its distance from the wall (z) may be considered 'attached' to the wall*". This means attached eddies which are farther from the wall, would be bigger in size, due to which their velocity field will persist closer to the wall. Townsend (1976) hypothesized that the inertial region of a wall-bounded turbulent flow can be statistically represented by a random superposition of such attached eddies of various sizes. Here, the various sized eddies reflect the range of scales existing in a turbulent flow.

To get quantitative estimates from the model, Townsend (1976) began by formulating an expression to account for the cumulative contribution from these random attached eddies to the correlation functions. Further, he also derived the distribution of eddy sizes, as a function of wall-normal distance, such that it would generate the observed invariance of the Reynolds shear stress ($\overline{uw}/U_\tau^2$) with z in the log-region (§2.2.2). This was solved for an inviscid flow system with slip allowed for the wall-parallel velocity components but a zero-penetration boundary condition imposed at the wall (i.e. u,$v \neq 0$ but $w = 0$ at $z = 0$). The solution revealed an eddy population density inversely proportional to their size and consequently, also with z. This facilitated the prediction of wall-normal variation of the normal Reynolds stress components, which were given by:

$$\begin{aligned} \overline{u^2}^+ &= B_1 - A_1 \ln\left(\frac{z}{\delta}\right), \\ \overline{v^2}^+ &= B_2 - A_2 \ln\left(\frac{z}{\delta}\right), \text{ and} \\ \overline{w^2}^+ &= B_3, \end{aligned} \tag{2.19}$$

Similar expressions were derived later by Perry et al. (1986), based on spectral overlap arguments, which have been reviewed in §2.2.3. The expressions in (2.19) have received substantial support from the experiments as well as simulations in recent years (Jimenez and Hoyas, 2008; Hultmark et al., 2012; Marusic et al., 2013; Baidya et al., 2014; Lee and Moser, 2015; Orlandi et al., 2015), extending empirical support to the attached eddy hypothesis. The noteworthy aspect of these expressions is that they are brought out from the model simply by the imposition of the invariance of Reynolds shear stress and the impermeability condition at the wall, without assuming a particular eddy geometry. These conditions make them applicable only to the inertial (or equilibrium) layer of a wall-bounded flow. The values of the constants, however, depend on the choice of the representative eddies.

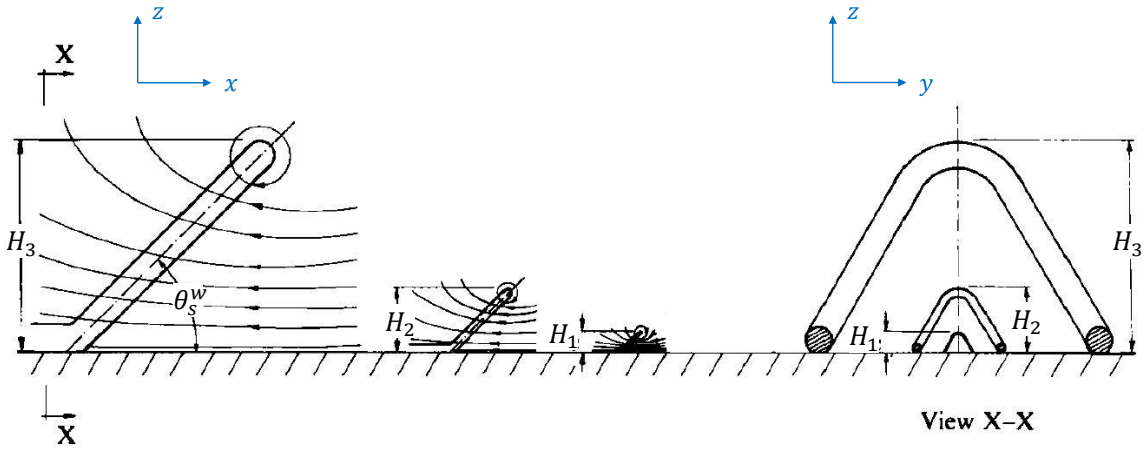

FIGURE 2.10: Schematic depicting three hairpin vortices as representative attached eddies of varying heights ($\mathcal{H}_i$), along with the associated streamline pattern generated by each eddy. Adapted from Perry et al. (1986).

The analytical expression for the wall-normal velocity variance in (2.19) reflects the same nature as that of the Reynolds shear stress, i.e. both equate to a constant value in the log-region. This can be related to the previous discussion in §2.2.2 regarding the w-velocity signatures (at z) exclusively associating with the (attached) eddies of height, $\mathcal{H} \sim \mathcal{O}(z)$, also referred as active motions by Townsend (1961, 1976). The streamwise and spanwise variances, on the other hand, are not universal and vary as a function of Re_τ. Townsend (1961, 1976) explained this behaviour to be owing to u- and v-fluctuations associated with the inactive motions with respect to z, which correspond to a range of attached eddies of height: $\mathcal{O}(z) \ll \mathcal{H} \lesssim \mathcal{O}(\delta)$. Hence, a larger range of eddies contribute to $\overline{u^2}$ and $\overline{v^2}$ with decrease in z, which explains why these stress components increase as z moves closer to the wall. This logarithmic increase, however, stops in the wall-normal range where the viscous effects are of the order of the inertial forces, and hence can no longer be neglected (as assumed by the attached eddy hypothesis).

2.4.1 Attached eddy model of Perry and Chong (1982)

To make further progress beyond the expressions given by (2.19), Townsend (1976) proposed that the statistically representative eddies may be considered conical in geometry (representing the streamwise vortices) as they yielded correlations in good agreement with those calculated directly from the measurements. This representative shape, however, did not predict the behaviour of the streamwise velocity successfully. Inspired by the hypothesis, Perry and Chong (1982) proposed a more detailed kinematic model of the wall-bounded

flow. For this, they considered hairpin eddies (or Λ-eddies) inclined with respect to the flow direction at $\theta_s^w = 45°$, which was based on the flow visualization observations of Head and Bandyopadhyay (1981) discussed earlier (§2.3). Figure 2.10 illustrates three such hairpin eddies with characteristic heights of $\mathcal{H}_1$, $\mathcal{H}_2$ and $\mathcal{H}_3$, along with their respective velocity fields (denoted by streamlines). The velocity field induced by each attached eddy, for all three velocity components, is consistent with the hypothesis of Townsend (1976) (§2.2.2), with the w-component induced by the eddy of height $\mathcal{H}_1$, for example, localized at $z \sim \mathcal{H}_1$, while the wall-parallel velocity signatures (from the same eddy) observed for $0 \leq z \lesssim \mathcal{H}_1$. A random array of these hairpin eddies, each with the same circulation but at differing stages of stretching, was referred to as a 'hierarchy' by Perry and Chong (1982). It is important to note that these eddies are simply statistically representative structures, and there may not even be a single eddy of this geometry in an actual wall-bounded turbulent flow.

After considering these randomly distributed eddies, Perry and Chong (1982) attempted to reproduce the log-law of the mean velocity (§2.2.1), which was possible after assuming a range of scales of geometrically self-similar hierarchies with a population density varying inversely with size. Due to its resemblance with Townsend's original model, the model of Perry and Chong (1982) also yielded the same expressions for the Reynolds stresses as in (2.19). Interestingly, the spectral behaviour from the model resulted in the k_x^{-1}-scaling for the 1-D spectra of the wall-parallel velocity components, which was also obtained later via spectral overlap arguments by Perry et al. (1986) (equation 2.14). Notably, the two studies found the k_x^{-1}-plateau of the premultiplied spectra, for the two wall-parallel velocity components (A_1, A_2), to be equivalent to the logarithmic decay rate of the respective Reynolds stresses with respect to z. This connection has, ever since, been used to test the notion of geometric self-similarity of the coherent motions in a real wall-bounded flow, which the attached eddy model of Perry and Chong (1982) proposes.

The availability of more high-Re_τ data over time has led to further improvements in the model to better predict the flow statistics (Marusic and Monty, 2019). For example, Perry and Marusic (1995) and Marusic and Perry (1995) extended the model of Perry and Chong (1982) to include contributions from the 'wake structures' in addition to the 'wall structures', in order to better resemble the Reynolds stresses and the energy spectra obtained from a zero-pressure as well as an adverse pressure gradient TBL. Inspired by the work of Adrian and coworkers (Zhou et al., 1999; Adrian et al., 2000), Marusic (2001) proposed the use of packets of hairpin eddies, instead of using simple Λ-vortices, to model the log-region flow. The proposal was substantiated by computing several statistics such as the two-point

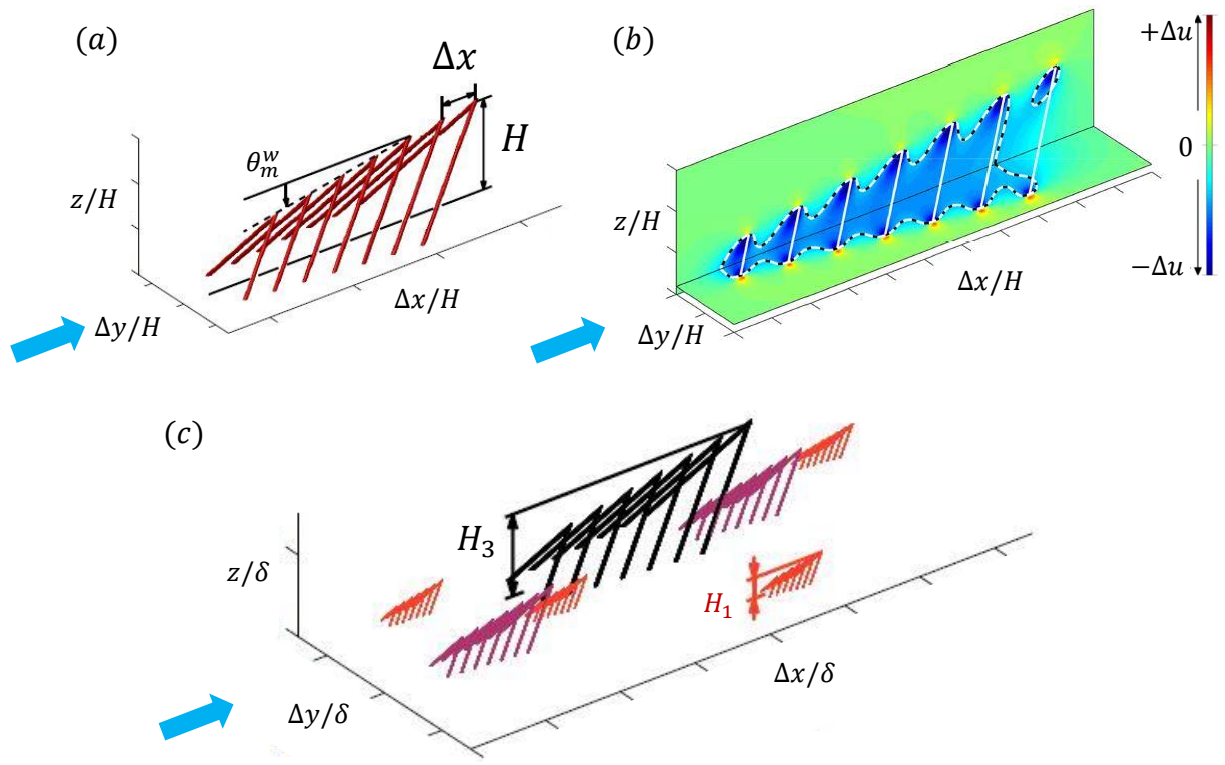

FIGURE 2.11: (a) Seven representative Λ-hairpin vortices arranged along the streamwise direction (with spacing Δx) to form a hairpin packet representative of an eddy of height, $\mathcal{H}$. Here, solid lines indicate vortex rods. (b) Streamwise velocity field induced by the vorticity in the representative packet-eddy shown in (a). (c) Three hierarchies of the representative packet-eddy considered to model the flow in a ZPG TBL. (a,c) have been adapted from Baidya et al. (2014) while (b) has been adapted from Baidya et al. (2017). Blue arrow indicates direction of the mean flow velocity.

correlations, the structure inclination angle, etc., which were found to be closer to the experimental estimates when a packet-eddy was used in the model. Figure 2.11(a) depicts a schematic of a packet-eddy, which essentially comprises of a series of Λ-vortices organized along the streamwise direction to maintain a packet inclination angle equivalent to that observed experimentally. Figure 2.11(b) shows the representative streamwise velocity field induced by the vorticity present in the Λ-vortices. Recent extensions to the model (Baidya et al., 2014; Woodcock and Marusic, 2015; de Silva et al., 2016; Eich et al., 2020; Chandran et al., 2020) utilize several hierarchies of such hairpin packets, depicted in figure 2.11(c), to model an idealized TBL with the total energy distributed over a range of scales. Interested readers may refer to Marusic and Monty (2019) where most of these developments have been discussed in terms of their significance in extending the original attached eddy model of Perry and Chong (1982).

2.5 Evidence of the geometric self-similarity in a wall-bounded flow

The attached eddy model is undoubtedly the most well known conceptual model for the inertially-dominated portion of wall-bounded turbulence in today's time. Its popularity lies in its simple conceptual description of an otherwise complex flow phenomena: it describes the inertial region as an amalgamation of geometrically self-similar attached eddies spanning a broad range of hierarchies dependent on the flow Reynolds number. While the expressions of the Reynolds stresses derived from the model (equation 2.19) have received good empirical support in the literature, support for the k_x^{-1}-spectral scaling (Perry and Chong, 1982; Perry et al., 1986), which relates to the geometry of the energetic motions, has been scant, unconvincing and of considerable debate. As per Nickels et al. (2007), relying simply on the empirical support for (2.19) as evidence for the validity of the model isn't sufficient since a precise k_x^{-1} law is not a necessary condition for observing the logarithmic decay of $\overline{u^2}$ (or $\overline{v^2}$). This is owing to the integral not being sensitive to small departures from the spectrum's behaviour, in turn calling for a rigorous testing of the turbulence spectra to substantiate the model. This section reviews the empirical evidence in the literature in support of the attached eddy model of wall-turbulence, with particular emphasis on the geometric aspects of the attached eddies brought out via spectral analysis.

2.5.1 k_x^{-1}-scaling law

Physically, the k_x^{-1}-scaling law indicates the range of scales which contribute equally to turbulent kinetic energy, and hence its empirical observation is deemed as a crucial evidence to support the notion of geometric and kinematic self-similarity of the energy-containing structures, as proposed by the attached eddy hypothesis. According to Perry and Chong (1982), the extraction of k_x^{-1}-scaling, via measurement, requires careful considerations of the experimental conditions. Primarily, the u- (or v-) signal needs to be measured in the inertially dominated region close to the wall in a high-Re_τ flow, in order to obtain contributions from a sufficiently large range of energetic scales which make up the plateau. The sufficiently large range of scales is an important requirement since as per Baidya et al. (2017), k_x^{-1}-scaling may not be observed for a low-Re_τ flow even if self-similarity is strictly enforced.

Consequently, most of the early empirical evidence on the k_x^{-1}-scaling of the u-spectrum was reported from the very high-Re_τ ($\sim 10^6$) atmospheric surface layer measurements

(Katul and Chu, 1998; Hunt and Morrison, 2000; Högström et al., 2002), which revealed a linear relationship between $\log(\phi_{uu})$ and $\log(k_x)$ with a slope approximately equal to -1. A shortcoming for the atmospheric measurements, however, is the limited signal sampling duration due to uncontrollable environment conditions. As a result, the wavenumbers in the low to intermediate-scale range, in which the k_x^{-1}-scaling is observed, are not very well converged, leading to large scatter in the data (Kunkel and Marusic, 2006). This makes discerning the true k_x^{-1}-scaling from these measurements very challenging.

Nickels et al. (2005) were one of the first groups to investigate the k_x^{-1}-scaling in a controlled laboratory environment, while also taking into consideration the recommendations of Perry and Chong (1982). From their measurements at $Re_\tau \approx 14\ 000$, they noted a k_x^{-1}-scaling in the wavelength range $\lambda_x/z \gtrsim 15.7$ and $\lambda_x/\delta \lesssim 0.3$ for the wall-normal locations $100 \lesssim z^+ \lesssim 0.019Re_\tau$. Here, λ_x is the streamwise wavelength, and is defined as $\lambda_x = 2\pi/k_x$. The plateau of their premultiplied spectra, however, did not match the logarithmic decay rate of $\overline{u^2}^+$, which is required as per the attached eddy arguments (Perry and Chong, 1982). In a recent study, Baars and Marusic (2020a) argued that the k_x^{-1} plateau observed by Nickels et al. (2005) relates to the 'saddle-type' topology formed due to a shift in the spectral energy dominance, from the lower wavelengths to higher wavelengths (Hutchins and Marusic, 2007), with increase in z. A similar challenge, associated with obtaining an unobscured view of k_x^{-1}-scaling for the premultiplied 1-D u-spectra, has been noted by many recent studies as well (Rosenberg et al., 2013; Baidya et al., 2017; Baars and Marusic, 2020a). On the other hand, the 1-D spanwise u-spectra ($k_y\phi_{uu}$) investigated by recent DNS studies (Pirozzoli and Bernardini, 2013; Lee and Moser, 2015) was found to reveal a more clear k_y^{-1}-scaling. The plateau for the premultiplied spectra observed in these studies, however, also isn't consistent with A_1 obtained from the corresponding $\overline{u^2}^+$ profiles. Hence, despite significant improvements in experimental resolution and availability of high Reynolds number facilities as well as high fidelity simulations, an unobscured view of the k^{-1}-scaling, consistent with the AEM, remains to be observed (Marusic et al., 2010b; Smits et al., 2011; Baars and Marusic, 2020a).

The wall-bounded flow comprises of a plethora of coherent structures coexisting in the log-region. These structures are anisotropic in nature and exhibit dissimilar scalings (Perry et al., 1986; Perry and Marusic, 1995; Baars and Marusic, 2020a; Yoon et al., 2020). Baars and Marusic (2020a) argued that this could obscure the true k_x^{-1}-scaling expected from the pure geometrically self-similar attached eddies, coexisting amongst other non-self-similar motions. Notable flow features corresponding to the latter include the δ-scaled motions

such as very-large-scale motions (or superstructures) which contribute to the low wavenumber (high wavelength) end of the spectrum (Perry and Marusic, 1995; Baars and Marusic, 2020a; Yoon et al., 2020). Testing the notion of self-similarity, in such circumstances, would first require the decomposition of the total energy into contributions from the various eddy types. One way of achieving this is by linear stochastic estimation, which will be discussed ahead in §2.5.3. In a separate study, Chandran et al. (2017) argued that coexisting energetic coherent motions have a characteristic wavelength (which is representative of its statistical geometry) in both wall-parallel directions (Tomkins and Adrian, 2005). Consequently, estimation of their spectral energy distribution via the 1-D streamwise spectra gives an inaccurate picture due to the spectral aliasing (Tennekes and Lumley, 1972; Davidson et al., 2006), which also can obscure the true k^{-1}-scaling. The problem of aliasing can be avoided by direct measurement of the two-dimensional energy spectrum, which maps the energy distribution across both streamwise and spanwise wavelengths. Discussion associated with how the 2-D spectra can be a better statistical tool to test for self-similarity is included next.

2.5.2 Two-dimensional energy spectrum

In the literature, 2-D energy spectrum has been predominantly used to interpret the relative energy distribution amongst wavelengths along the two wall-parallel directions (del Álamo et al., 2004; Jimenez and Hoyas, 2008; Lee and Moser, 2019). In addition, such an analysis has been mostly carried out on numerically simulated data, owing to the multi-point nature of the measurements required for experimentally reconstructing the 2-D spectra (Morrison and Kronauer, 1969; Tomkins and Adrian, 2005). The ability to use the 2-D spectra, as a tool to check for self-similarity, was demonstrated by Chung et al. (2015) via dimensional considerations. Figure 2.12(a), adapted from Chung et al. (2015), depicts a constant energy region in a 2-D spectrum, bounded by power laws (f_1,f_2) of the form:

$$\frac{\lambda_y}{z} = \frac{\lambda_L}{z} \sim f_1\left(\frac{\lambda_x}{z}\right), \text{ and } \frac{\lambda_y}{z} = \frac{\lambda_U}{z} \sim f_2\left(\frac{\lambda_x}{z}\right), \tag{2.20}$$

at the lower (λ_L) and upper (λ_U) spanwise wavelength range, respectively. f_1 and f_2 in (2.20) were considered to be power laws inspired from the findings of del Álamo et al. (2004). Here, the streamwise and spanwise wavelengths may be considered to be a surrogate of the geometric extent of the energetic motions along x and y, respectively. By definition, the 2-D spectrum can be integrated to obtain the 1-D spectrum by following (Chung et al.,

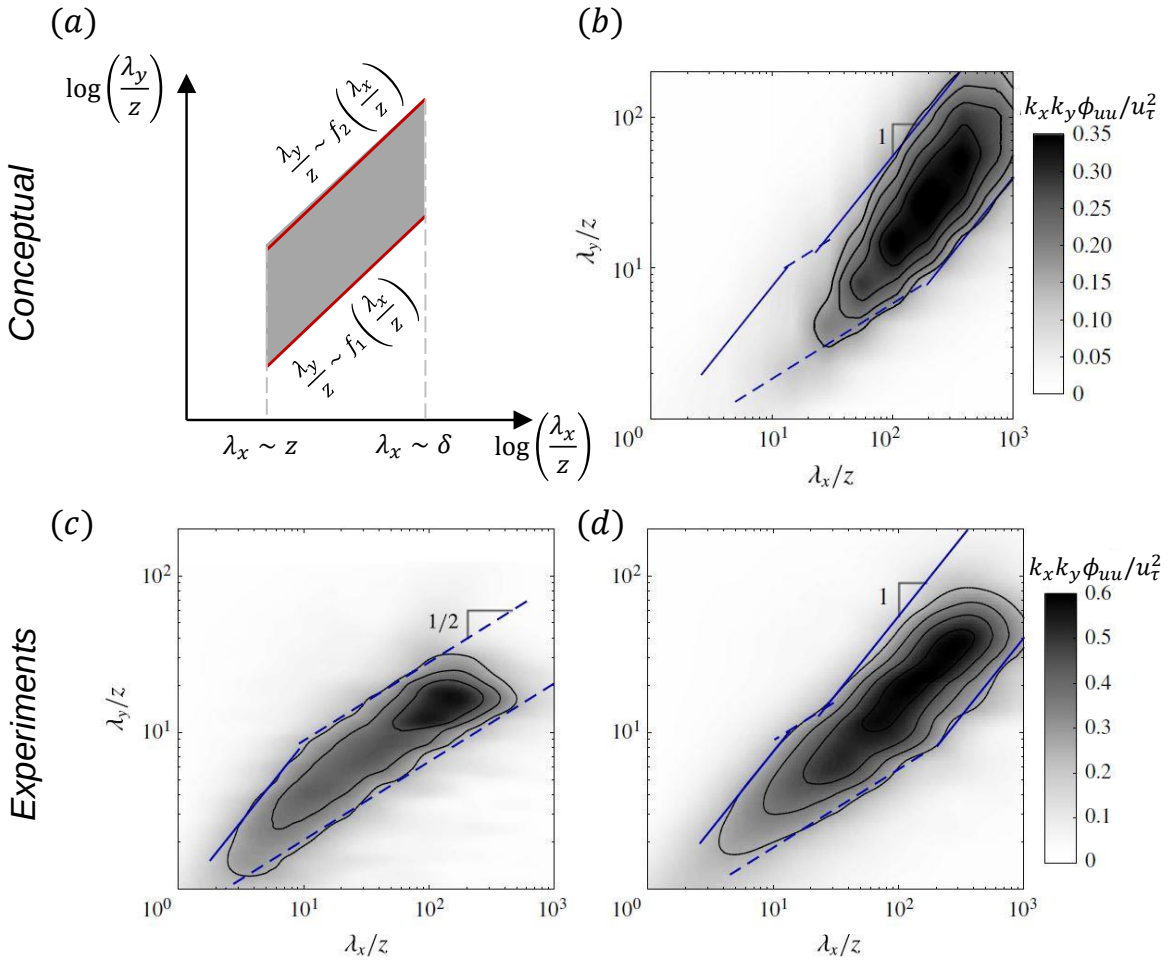

FIGURE 2.12: (a) An illustration of the two-dimensional (2-D) u-energy spectrum with the grey region, bounded by the two power laws (in red), representing a region of uniform energy. (b) 2-D u-spectrum at $z^+ \approx 2.6\sqrt{Re_\tau}$ computed from an attached eddy model for a ZPG TBL at $Re_\tau \approx 26\,000$. (c,d) 2-D u-spectra reconstructed experimentally at $z^+ \approx 2.6\sqrt{Re_\tau}$ in a ZPG TBL at (c) $Re_\tau \approx 2\,400$ and (d) $Re_\tau \approx 26\,000$. Solid and dashed blue lines in (b-d) denote $\lambda_y \sim \lambda_x$ and $\lambda_y \sim (\lambda_x)^{1/2}$ relationship, respectively. (a) has been adapted from Chung et al. (2015), while (b-d) has been adapted from Chandran et al. (2017).

2015; Chandran et al., 2017):

$$\frac{k_x \phi_{uu}(k_x)}{U_\tau^2} = \int_{\lambda_L}^{\lambda_U} \frac{k_x k_y \phi_{uu}(k_x, k_y)}{U_\tau^2} d\left(\ln\left(\frac{\lambda_y}{z}\right)\right). \tag{2.21}$$

By assuming $k_x k_y \phi_{uu}(k_x, k_y)/U_\tau^2 \approx 1$ for convenience in analysis, Chung et al. (2015) obtained:

$$\frac{k_x \phi_{uu}(k_x)}{U_\tau^2} = \ln\left(\frac{\lambda_U}{\lambda_L}\right). \tag{2.22}$$

When considering the above expression in the wavenumber range where the k_x^{-1}-scaling law would be applicable (§2.14), the right-hand-side of (2.22) must equate to a constant A_1 (Townsend-Perry constant), meaning that the two power laws (f_1, f_2) should be identical. Further, since k_x^{-1}-scaling is indicative of the geometric self-similarity, f_1 and f_2 would represent linear relationships of the form $\lambda_y/z \sim \lambda_x/z$ (del Álamo et al., 2004; Chandran et al., 2017), which suggests the span of the eddies to be growing at the same rate as their length. The same is reflected by the 2-D spectrum computed from a flow field represented by hierarchies of purely self-similar attached eddies (as shown in figure 2.11(c)), which is plotted in figure 2.12(b). The spectrum is obtained using the attached eddy model of Baidya et al. (2017), which simulates flow phenomena in the log-region at $Re_\tau \approx 26\,000$. The constant energy contours of the 2-D spectra can be observed to be clearly following the $\lambda_y/z \sim \lambda_x/z$ relationship, which is henceforth deemed as an indicator of geometric self-similarity in the remainder of this thesis.

To test the arguments made by Chung et al. (2015), Chandran et al. (2017) measured the 2-D u-spectra in the inertial region of a ZPG TBL over a decade of Re_τ ($2\,400 \lesssim Re_\tau \lesssim 26\,000$) via multi-point hotwire measurements. In the low-Re_τ range (figure 2.12(c)), they found the constant energy region of the 2-D spectra to be nominally bounded by power laws of the form: $\lambda_y/z \sim (\lambda_x/z)^{1/2}$. A similar behaviour was noted previously by del Álamo et al. (2004) in turbulent channel flows at $Re_\tau \lesssim 1\,900$ and was interpreted to be a failure of self-similarity, given that the motions do not grow along y at the same rate as they do along x. 2-D spectra results at $Re_\tau \approx 26\,000$ (figure 2.12(d)), however, indicated the large-scale behaviour deviating towards a linear relationship, hinting at the possibility of observing self-similarity at higher Re_τ. Such a trend was brought out quantitatively via computing the ratio (m) of the plateaus of the 1-D streamwise and spanwise u-spectra, obtained by integrating the 2-D spectra as per (2.21). According to Chandran et al. (2017), $m \approx 1$ is representative of a linear relationship for the power laws representing the constant energy contours, and hence indicates geometric self-similarity. Based on their asymptotic analysis, Chandran et al. (2017) conjectured $m \approx 1$ to be observed for a ZPG TBL at $Re_\tau \approx 60\,000$.

The analysis of Chandran et al. (2017) thus suggests that although the chances of obscuring the k^{-1}-scaling, via spectral aliasing, have been avoided by directly measuring the 2-D spectra, the effect of the coexistence of various structures, with differing scaling, remains significant even at $Re_\tau \approx 26\,000$. The next subsection discusses spectral decomposition techniques used recently by Baars and Marusic (2020a,b), which can be used to segregate these various contributions.

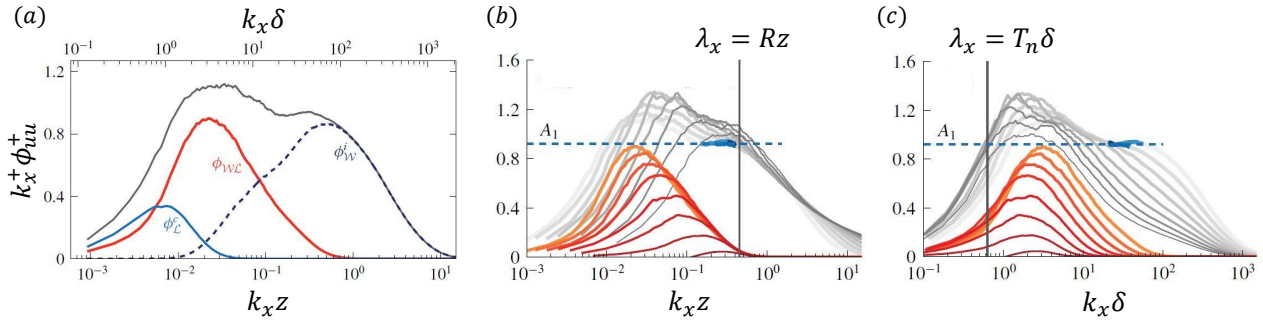

FIGURE 2.13: (a) Premultiplied 1-D u-spectra at $z^+ \approx 100$ for a ZPG TBL at $Re_\tau = 14\,000$ (solid grey line), triple decomposed via data-driven filters into Φ_W^i (dashed dark blue line), Φ_{WL} (solid red line) and Φ_L^c (solid light blue line). (b,c) Φ_{WL} and the premultiplied 1-D u-spectra estimated at z^+ across the log-region for the same dataset as in (a), plotted as a function of λ_x scaled with (b) z and (c) δ, respectively. Terminology has been discussed in §2.5.3. The figure has been adapted from Baars and Marusic (2020a).

2.5.3 Energy decomposition using linear stochastic estimation

The most likely reason behind why spectral self-similarity is conjectured to be more apparent in a flow at very large Re_τ (Nickels et al., 2005; Baidya et al., 2017; Chandran et al., 2017; Baars and Marusic, 2020a) is linked to increased scale separation. At low Re_τ, contributions from various eddy types existing in the log-region (which follow dissimilar scalings) closely overlap with one another (Perry and Marusic, 1995; Baars and Marusic, 2020a), subsequently obscuring the spectral characteristics associated with the geometrically self-similar structure ingrained in the flow. A possible manner in which these characteristics can be unravelled is by implementing a methodology which segregates or filters out energy associated with the different eddy types coexisting in the log-region. On segregation, each of these 'family' of structures can be checked for their independent spectral characteristics to determine the eddy-type representative of Townsend's attached eddies.

Two recent studies have shown promising results with respect to segregating the self-similar and non-self-similar energy contributions. The first is by Yoon et al. (2020), who inspired from the earlier works of del Álamo et al. (2006), Lozano-Durán et al. (2012) and Hwang and Sung (2018), decomposed the instantaneous ZPG TBL DNS fields (at $Re_\tau \approx 825$) into energetic u-motions coherent and incoherent with the wall. The terminology 'wall-coherent' here refers to motions with their velocity signatures extending all the way down to the wall. Yoon et al. (2020) detected and segregated these 'clusters' of streamwise motions, from individual instantaneous flow fields, by using the connectivity of neighbouring grid points (del Álamo et al., 2006). Each of the two motion types were found to have subsets

which were geometrically self-similar as well as non-self-similar. Amongst these, energy contributions from the self-similar wall-coherent motions led to the log-variation of $\overline{u^2}^+$ with z (equation 2.19), and the k_y^{-1}-scaling of the spanwise energy spectra, which led them to propose these motions as the principal candidates for Townsend's AEH.

The second study by Baars and Marusic (2020a,b) proposed a triple decomposition of the streamwise turbulent kinetic energy (figure 2.13(a)) into: (i) an inner-scaled, universal portion of $\overline{u^2}$ (Φ_W^i), (ii) the fraction of $\overline{u^2}$ consistent with the characteristics of Townsend's attached eddies (Φ_{WL}) and (iii) part of $\overline{u^2}$ contributed by the VLSMs/superstructures (Φ_L). The decomposition, in their case, was conducted via two data-driven universal filters based on spectral coherence analysis. These filters were generated from two-point hotwire measurements conducted in a high-Re_τ ZPG TBL, and were used to obtain a stochastic estimate of the per-scale energy contributions from the three eddy types. Hence. the decomposition approach of Baars and Marusic (2020a) is different than that of Yoon et al. (2020), who decomposed the total energy by physically identifying and segregating 3-D motions of various eddy-types in the instantaneous flow fields. In the case of Baars and Marusic (2020a), the experiments used to construct the filters were designed based on certain known characteristics of the three eddy-types listed above. For instance, Baars et al. (2017) had found previously via a linear coherence spectrum that a self-similar wall-coherent structure, with a streamwise/wall-normal aspect ratio of 14, was ingrained into the ZPG TBL flow. Based on this result, the spectral energy at wavelength smaller than $\lambda_x \approx 14z$ was deemed as wall-incoherent in a stochastic sense, and conforming to (i). However, not all wall-coherent motions, with wavelengths $\lambda_x > 14z$, depict self-similar characteristics. For example, the VLSMs or superstructures, which also belong to this subset, scale exclusively with δ. These motions, although coherent with the wall, are large and tall and consequently span across the entire log-region. The second filter exploits this feature of the superstructures and isolates energy contributions from these δ-scaled very large motions corresponding to (iii) mentioned above. The fraction of the streamwise turbulent kinetic energy remaining after removal of (i) and (iii) was associated predominantly with the self-similar attached eddies (Φ_{WL}). This was confirmed by checking Φ_{WL} for the spectral scaling arguments (figures 2.13(b,c)) of Perry et al. (1986) reviewed previously in section §2.2.3, with the small and large-scale ends of the spectrum exhibiting the z- and δ-scaling respectively. The k_x^{-1} plateau, however, was not observed at $Re_\tau \approx 14\,000$ and was conjectured to be evident only at $Re_\tau \gtrsim 80\,000$. Given that the present thesis deals predominantly with the high-Re_τ multi-point hotwire data, the more relevant energy decomposition methodology which can be used to test the notion of self-similarity is that of Baars and Marusic (2020a), and is reviewed in greater depth ahead.

2.5.3.1 Data-driven decomposition: spectral linear stochastic estimation

Baars and Marusic (2020a) obtained the stochastic estimate of the energy contributions from the three different eddy types, at a wall-normal location z_o, via cross-correlation analysis. The analysis was conducted on synchronously acquired u-signals at z_o, as well as another wall-height (z_r), the latter chosen dependent on the spatial coherence of the concerned eddy-type. The stochastic estimation techniques, as they are commonly known, have been used previously by Adrian (1979) and Adrian et al. (1987) to interpret the structural properties of turbulent flows. In the study by Baars and Marusic (2020a), however, the analysis was conducted in spectral space (instead of physical space) to facilitate decomposition of the energy spectra. One of the methodologies to estimate a subset of the u-energy spectrum at any z_o, associated with contributions from specific eddy-type coexisting across z_o and z_r, is the spectral linear stochastic estimation (SLSE) technique. Considering a scale-specific input ($\widetilde{u}(z_r;\lambda_x)$) and output ($\widetilde{u}(z_o;\lambda_x)$) of a linear time-invariant system (Bendat and Piersol, 1986; Tinney et al., 2006; Baars et al., 2016a), the SLSE of the output is given by:

$$\widetilde{u}^E(z_o;\lambda_x) = H_L(z_o,z_r;\lambda_x)\widetilde{u}(z_r;\lambda_x), \tag{2.23}$$

where $\tilde{u}(z_r;\lambda_x)$ represents the Fourier transform of $u(z_r)$ in x. Here, the superscript E represents the estimated quantity while H_L represents the scale-specific linear transfer kernel, with the latter computed from an ensemble of data following:

$$H_L(z_o,z_r;\lambda_x) = \frac{\langle\widetilde{u}(z_o;\lambda_x)\widetilde{u}^*(z_r;\lambda_x)\rangle}{\langle\widetilde{u}(z_r;\lambda_x)\widetilde{u}^*(z_r;\lambda_x)\rangle} = \mid H_L(z_o,z_r;\lambda_x)\mid e^{i\psi(z_o,z_r;\lambda_x)}, \tag{2.24}$$

with ψ and $\mid H_L \mid$ the scale-specific phase and gain respectively, and the angle brackets ($\langle\rangle$), asterisk ($*$) and vertical bars ($||$) denoting the ensemble averaging, complex conjugate and modulus, respectively. Hence, (2.23) indicates how the SLSE estimates a conditional output by transforming an unconditional input (all in spectral domain) via one multiplication step. It should be noted that the stochastic estimate of the output can also be obtained in the physical space simply by inverse Fourier transforming (2.23). The equation can also be used to estimate the energy spectrum at z_o following:

$$\phi^E_{uu}(z_o;\lambda_x) = \mid H_L(z_o,z_r;\lambda_x)\mid^2\phi_{uu}(z_r;\lambda_x). \tag{2.25}$$

Here, ϕ^E may be interpreted as the scale-specific energy at z_o, comprising only those scales which are coherent across z_o and z_r. The same procedure (equations (2.23) - (2.25)) can

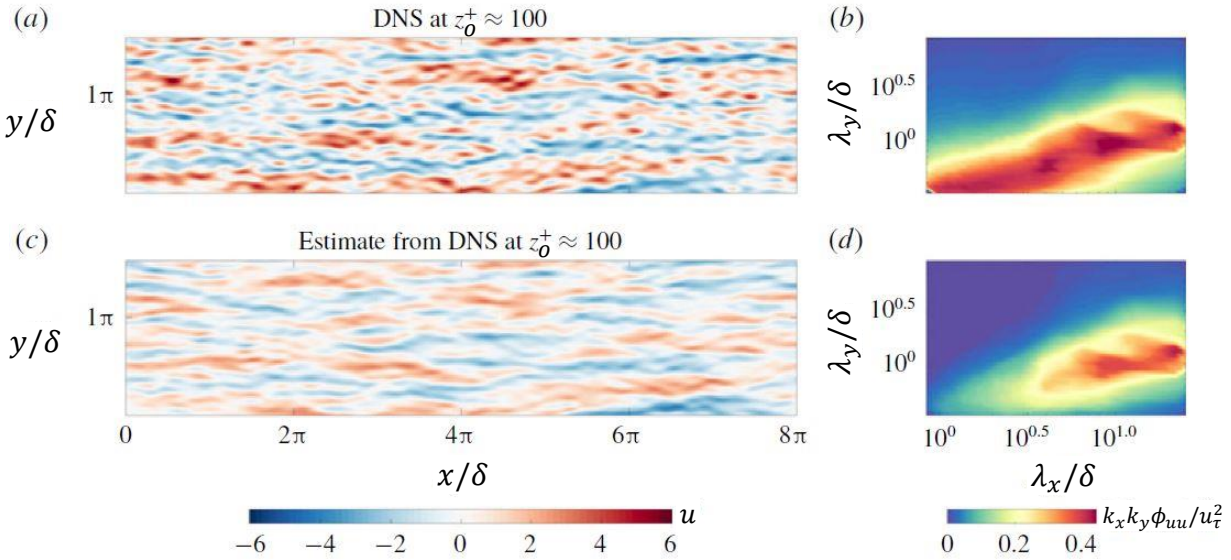

FIGURE 2.14: (a) Wall-parallel flow field of instantaneous u-fluctuations and (b) the associated two-dimensional u-spectrum at $z_o^+ \approx 100$ computed from the $Re_\tau \approx 2000$ Channel dataset of Encinar et al. (2018). (c) Wall-parallel flow field of instantaneous u-fluctuations and (d) the associated two-dimensional u-spectrum estimated at $z_o^+ \approx 100$ via SLSE technique with $z_r^+ \approx 300$. Adapted from Madhusudanan et al. (2019).

be extended to be a function of both wall-parallel wavelengths, λ_x and λ_y. Madhusudanan et al. (2019) applied this methodology to wall-parallel DNS flow fields, to estimate the subset of the instantaneous flow fields as well as the 2-D energy spectrum in the log-region (at $z_o^+ \approx 100$), which has been shown in figure 2.14. Figures 2.14(a,b) respectively show the instantaneous u-field and the 2-D u-spectra at $z_o^+ \approx 100$, consisting of contributions from all coexisting eddies at z_o. Figures 2.14(c,d) show the same statistics obtained from SLSE, comprising contributions from only those motions which are coherent across $z_o^+ \approx 100$ and $z_r^+ \approx 300$, thus corresponding to predominantly the large-scale structures.

2.5.3.2 Data driven filter: linear coherence spectrum

The previous discussion highlights the ability to obtain spectral stochastic estimates based on construction of a scale-by-scale coupling using two-point datasets. In order to construct universal filters, which could be employed for energy decomposition at various Re_τ, Baars and Marusic (2020a) utilized the linear coherence spectrum (LCS) to compute the normalized quantitative estimate of the scale-by-scale coupling. The LCS can be computed for

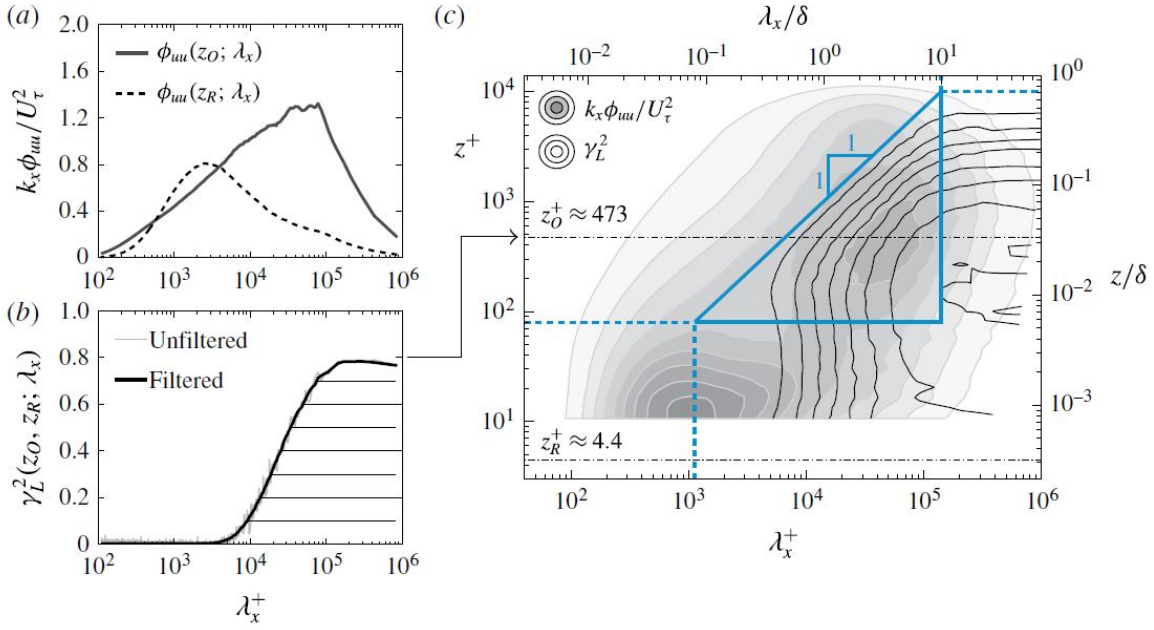

FIGURE 2.15: (a) Premultiplied 1-D u-energy spectra at $z_r^+ \approx 4.4$ (dashed line) and $z_o^+ \approx 473$ (solid line) for a ZPG TBL at $Re_\tau = 14\,000$. (b) γ_L^2 corresponding to the u-spectra considered in (a). (c) Energy spectrogram of the u-velocity component (in colour) for the same ZPG TBL dataset as in (a), with the corresponding coherence spectrogram (denoted by solid lines) overlaid on top of it. Solid lines denote γ_L^2 contour levels 0.1:0.1:0.9. Adapted from Baars et al. (2017).

the u-signals, at any z_o and z_r, following (Bendat and Piersol, 1986; Baars et al., 2017):

$$\gamma_L^2(z_o, z_r; \lambda_x) = \frac{|\,\langle \widetilde{u}(z_o;\lambda_x)\widetilde{u}^*(z_r;\lambda_x)\rangle\,|^2}{\langle|\,\widetilde{u}(z_o;\lambda_x)\,|^2\rangle\langle|\,\widetilde{u}(z_r;\lambda_x)\,|^2\rangle} = \frac{|\,\phi_{u_o u_r}(z_o, z_r;\lambda_x)\,|^2}{\phi_{uu}(z_o;\lambda_x)\phi_{uu}(z_r;\lambda_x)}, \tag{2.26}$$

where $\phi_{u_o u_r}$ represents the complex-valued cross-spectrum across z_o and z_r. Physically, γ_L^2 may be "*interpreted as the square of a scale-specific correlation coefficient*" (Baars et al., 2017), and represents the fraction of streamwise turbulence intensity ($\overline{u^2}$) shared, per scale, by $u(z_o)$ and $u(z_r)$. Hence by definition, $0 \leq \gamma_L^2 \leq 1$. While (2.26) only considers the magnitude of the complex-valued cross-spectrum, the γ_L^2 is implicitly influenced by the phase between the two velocity signals during the ensembling procedure. That is, $\gamma_L^2(\lambda_x) \rightarrow 0$ for a λ_x which has a non-consistent phase across various ensembles, deeming it as stochastically incoherent across z_o and z_r. Figures 2.15(a,b) adapted from Baars et al. (2017) graphically illustrates γ_L^2 (figure 2.15(b)) computed from u-signals at wall-normal locations, $z_o^+ \approx 473$ and $z_r^+ \approx 4$ (figure 2.15(a)), using (2.26). Contours for γ_L^2 computed in a similar way for various z_o^+ are shown in figure 2.15(c), overlaid on top of the 1-D u-energy spectrogram. The comparison reveals the scale-specific energy at various z_o^+ coherent with the wall ($z_r^+ \approx 4$), which understandably is dominated mostly by the large-scales.

Considering equations (2.24) and (2.26), H_L and γ_L^2 can be related via the expression (Baars et al., 2016a):

$$\mid H_L(z_o, z_r; \lambda_x) \mid = \sqrt{\gamma_L^2(z_o, z_r; \lambda_x) \frac{\langle \mid \widetilde{u}(z_o; \lambda_x) \mid^2 \rangle}{\langle \mid \widetilde{u}(z_r; \lambda_x) \mid^2 \rangle}}. \tag{2.27}$$

Based on this relationship, (2.25) can be reorganized as (Baars and Marusic, 2020a):

$$\phi_{uu}^E(z_o; \lambda_x) = \mid H_L(z_o, z_r; \lambda_x) \mid^2 \phi_{uu}(z_r; \lambda_x) = \gamma_L^2(z_o, z_r; \lambda_x) \phi_{uu}(z_o; \lambda_x). \tag{2.28}$$

Hence, the energy at z_o, reconstructed via SLSE using an input at z_r, can be simply estimated by multiplying the total energy at z_o (i.e. $\phi_{uu}(z_o;\lambda_x)$) with $\gamma_L^2(z_o, z_r)$. This enables $\gamma_L^2(z_o, z_r)$ to be used as a scale-specific filter to decompose $\phi_{uu}(z_o;\lambda_x)$ into a stochastically coherent and incoherent fraction with respect to z_r, following:

$$\phi_{uu}(z_o; \lambda_x) = \underbrace{(\gamma_L^2)\phi_{uu}(z_o; \lambda_x)}_{\text{scales coherent with respect to } z_r} + \underbrace{(1 - \gamma_L^2)\phi_{uu}(z_o; \lambda_x)}_{\text{scales incoherent with respect to } z_r}. \tag{2.29}$$

The two filters used by Baars and Marusic (2020a,b), to decompose $\phi_{uu}(z_o;\lambda_x)$ into contributions from three different eddy-types as plotted in figure 2.13, were based on the LCS computed with respect to two different z_r. It is important to note here that using a linear methodology for stochastic estimation (Guezennec, 1989) was sufficient for Baars and Marusic (2020a) since they were only focused on velocity-velocity coupling. Previous studies (Naguib et al., 2001) have, however, shown that higher order terms may also have to be included in case of pressure-velocity couplings, for example.

Chapter 3

Experimental details

In this thesis, all measurements were conducted via hotwire anemometry. Two types of measurements were conducted, each with a different probe type, which are classified here as: (i) single-point measurements with an X-wire probe, and (ii) multi-point measurements with single-wire probes. These measurements were conducted in two different wind tunnel facilities housed in the Walter Bassett Aerodynamics Laboratory at the University of Melbourne: the Channel flow facility and the High Reynolds Number Boundary Layer Wind Tunnel (HRNBLWT). While the channel facility was used exclusively for the single-point measurements, both types of measurements were conducted in HRNBLWT. §3.1 of this chapter provides details of these two wind tunnel facilities, along with the instrumentation used to acquire the necessary flow statistics for the two types of measurements listed above. This is then followed by individual sections giving experimental details of the multi-point (§3.2) and single-point (§3.3) measurements. Specific details related to processing of the data and subsequent analysis, however, have been described in the subsequent chapters discussing the results as per necessity.

3.1 Wind tunnel facilities

3.1.1 HRNBLWT

All high Re_τ experiments for this thesis ($Re_\tau \gtrsim \mathcal{O}(10^4)$) were conducted in the HRNBLWT. It is an open-return blower type wind tunnel, with a working section of 27 m $\times$ 1.89 m $\times$ 0.92 m. Figure 3.1 depicts a schematic of the facility, and highlights the key features of

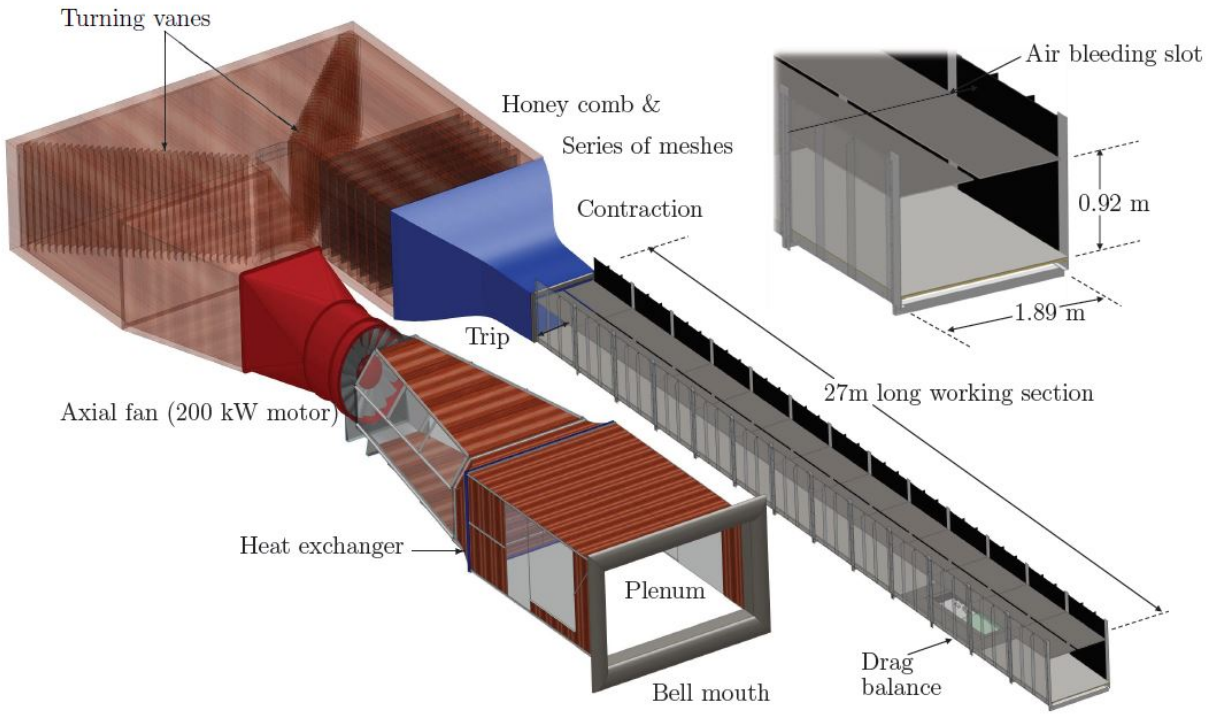

FIGURE 3.1: Schematic of the large Melbourne wind tunnel facility (HRNBLWT) housed inside the Walter Bassett Aerodynamics Laboratory at the University of Melbourne. Adapted from Kulandaivelu (2012).

the wind tunnel, which serve the following purposes (listed in the direction of wind flow): The air enters the facility first via the bell mouth, which ensures a smooth transition in the flow by reducing the flow unsteadiness, consequently avoiding flow separation and the associated acoustic noise. After this, the flow passes through a plenum which leads it to the heat exchanger, following which the rectangular cross-section changes gradually to a circular one at the intake of the axial fan. The fan, which is driven by a 250 kW DC motor, is capable of generating flow rates high enough to deliver a freestream speed of up to 45 ms^{-1} in the working section. The flow from the fan then expands into a rectangular chamber, housing two guide vane cascades, which gradually turn the flow orientation from 0° to 90°, and finally from 90° to 180°, before passing it into the settling chamber. This chamber comprises of a honeycomb screen and a cascade of six fine meshes. While the honeycomb straightens the flow by reducing the lateral velocity fluctuations, the series of meshes reduce fluctuations in the streamwise velocity. This combination is successful in reducing the free-stream turbulence intensity ($\sqrt{u^2}/U_\infty$) in the working section below 0.3% for a prominent range of freestream velocities (10 ms^{-1} - 40 ms^{-1}). This 'clean' flow then enters a two-dimensional contraction, with an area ratio of 6.25:1, which smoothly accelerates it into the working section. At the entrance of the working section (considered

at $x = 0$ for reference), the flow is tripped by a coarse 40 grit sand paper, 35 mm wide, to generate a 'canonical' turbulent boundary layer farther downstream (Marusic et al., 2015).

The floor of the 27 m long working section is made up of individually polished aluminium plates with a root-mean-squared surface roughness less than 1.5 μm (Nickels et al., 2007). These plates are joined together via an epoxy filler to form the 'wall' of the turbulent boundary layer, with the epoxy ensuring a smooth transition of the flow moving over the plates. The ceiling, on the other hand, is made up of a series of medium-density fibre board panels arranged in order to leave a gap along the centreline of the working section. These streamwise gaps permit air bleeding, and thereby facilitate setting up a nominally zero pressure gradient (ZPG) flow ($C_P \approx \pm 0.87\%$) along the entire 27 m long working section (Marusic et al., 2015). The tunnel flow speeds are set using a 0 - 10 V DC voltage input for the DC motor of the fan, which is controlled via a dedicated computer for the facility. This permits full automation of the wind tunnel testing procedure, including the hotwire calibration at different air speeds, etc.

The unique feature of this facility is its long working section, which permits investigation of a high Reynolds number flow with a physically thick boundary layer ($\approx$ 0.36 m at $x \approx$ 27 m). The facility is designed based on a *big and slow approach*, which recommends attaining a high Reynolds number boundary layer flow such that the smallest length scale ($\nu/U_\tau = \delta/Re_\tau$) can be resolved via conventional measurement techniques. Of the two types of measurements conducted in the facility, the single point measurements (with an X-probe) were conducted at $x \approx 13$ m from the beginning of the test section, at a tunnel freestream speed (U_∞) of 15 ms^{-1}. The thickness of the boundary layer, for these conditions, is $\delta \approx 0.32$ m, resulting in a $Re_\tau \approx 10\,000$. Here, the U_τ and δ are estimated via the composite fit of Chauhan et al. (2009). The multi-point measurements were conducted with help from a multi-traverse system (§3.1.1.1) which could be positioned only at $x \approx$ 21 m. This region of the working section comprises the drag balance (figure 3.1), which is made up of nine interchangeable aluminium plates of dimension 0.3 m $\times$ 0.7 m. The traverse system was installed into the working section by removing one of these plates at $x \approx 21$ m. All multi-point measurements were conducted at $U_\infty \approx 20$ ms^{-1}, which results in a ZPG TBL of thickness $\delta = 0.36$ m, yielding a $Re_\tau \approx 15\,000$ for the flow.

3.1.1.1 Sensor traversing systems used for measurements

For the single-point measurements across the TBL profile, the same traversing system as that used previously by Kulandaivelu (2012) and Baidya (2016) was employed in the

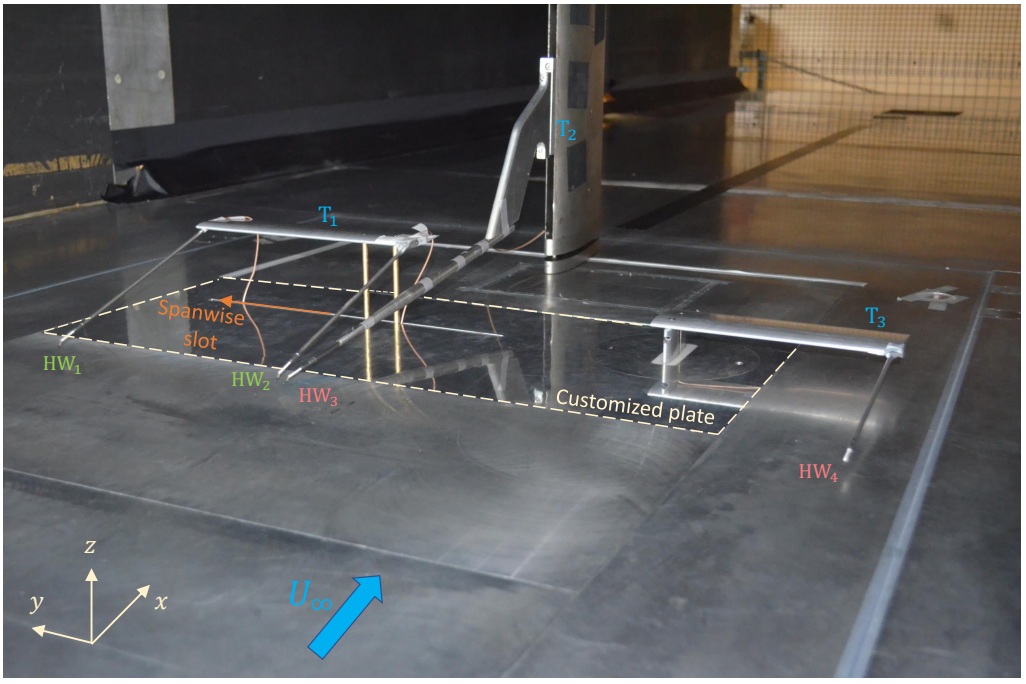

FIGURE 3.2: A photograph showcasing the multi-traverse system (T_{1-3}), which facilitates the movement of the four hotwire probes (HW_{1-4}), installed inside the working section of the HRNBLWT.

present study (see figure 3.2 of Kulandaivelu (2012)). This traverse can be moved along the entire streamwise length of the working section, courtesy of the streamwise slot present in the ceiling of the working section, and is controlled via the same computer monitoring the tunnel speed. The shape of the traverse system resembles that of a streamlined body (NACA 0016) with a chord length of 180 mm, ensuring minimum blockage effects and vortex shedding from the body (labelled as T_2 in figure 3.2). During measurement at a specific streamwise location, the traverse body is anchored to the tunnel floor using a retractable pneumatic foot to avoid any flow-induced vibrations. A ball-screw driven plate, which is also numerically controlled, is fitted inside the traverse body to facilitate movement in the wall-normal direction. This movement is regulated by a *Renishaw* RGH24 linear optical encoder, giving a positional accuracy of ± 0.5 μm, which is critical for the hotwire measurements in the near-wall region. During measurement, the hotwire probe is held by a long arm, approximately 0.5 m upstream of the traverse body, to minimize the blockage effect on the velocity measurements.

For the multi-point measurements, two other traverse systems (T_1,T_3) are used in conjunction with the main traverse of HRNBLWT (T_2 described above) to facilitate the positioning of the four hotwire probes (HW_{1-4}) in the shear flow. Figure 3.2 shows a photograph of the

entire experimental setup for the multi-point measurements in the HRNBLWT working section, which has also been employed previously by Chandran (2019) for their experiments. The entire setup is designed to facilitate synchronous acquisition of the u-signals spaced as far as 1 m apart (approximately) in the spanwise direction. The use of four hotwires, as opposed to the conventional two hotwires in such measurements, permits covering this large spanwise offset range (during measurement) in a much shorter time duration. As is evident from figure 3.2, while T_2 is held by the airfoil-shaped body extending up to the tunnel ceiling, T_1 and T_3 extend down to the wall, where they are housed on a customized aluminium plate flushed with the tunnel floor. Each of the three traverse systems have their own unique traversing capabilities – given that they are attached onto the aluminium plate, T_1 and T_3 cannot traverse along the streamwise direction, unlike the case of T_2 which carries HW_3. T_1, however, is capable of traversing HW_1 and HW_2 along the spanwise direction as well as the wall-normal direction. T_3, on the other hand, is designed to traverse HW_4 only in the wall-normal direction.

Similar to T_2, all exposed portions of T_1 and T_3 have an airfoil cross-section to avoid flow-induced vibrations of the setup. The only exception is the support-system holding the airfoil in T_1, which comprises a pair of 8 mm diameter rods which are suitable to slide along the spanwise-oriented slot provided on the customized plate (figure 3.2). This dimension was optimally chosen by Chandran (2019) so as to minimize (i) the effect of blockage due to the rods, (ii) the width of the spanwise slot and (iii) the flow-induced vibrations of the system. (iii) was experimentally verified by Chandran (2019) via estimation of the horizontal and vertical displacements of the hotwire probes, which were monitored by high-resolution cameras during a test run in the tunnel at $U_\infty \approx 20\ \mathrm{ms}^{-1}$. The viscous-scaled root-mean-square displacement of the tip of the hotwire probes was calculated via image processing, and was found to be nominally 1. Further details regarding how the three traverses were used during the measurement will continue in §3.2.

3.1.1.2 Sensor positioning

The varying traversing capabilities of the three traverse systems, used for the multi-point measurements, meant that appropriate positioning of the sensors had to be ensured before the beginning of the experiment. The details of the desired positioning, and the manner in which it was checked, are outlined below in the order followed while setting up the experiment:

1. Streamwise positioning: All hotwire sensors had to be positioned at nominally the same streamwise position with respect to the start of the working section ($x \approx 21$ m). While HW_{1-2} and HW_4 were constrained in x due to their respective T_1 and T_3 traverses, T_2 had to be traversed in order to position HW_3 at the same streamwise location as the other three hotwires. This alignment was checked via a FatMax cross line laser level.

2. Spanwise positioning and orientation with respect to the wall: After ensuring the alignment of the four probes at nominally the same x, the relative spanwise positioning of the four sensors had to be recorded. Owing to the constraints imposed on the respective traverses, the spanwise offset between the hotwire pairs HW_1-HW_2 and HW_3-HW_4 was always fixed and known from the design of the setup. Hence, recording only the offset between HW_2 and HW_3, at the start of the experiment, was sufficient to estimate relative spanwise offsets for all possible hotwire pairs (total six possible). The initial spanwise spacing between HW_2 and HW_3 was recorded via a microscope with its eyepiece oriented in the streamwise direction. The microscope was in turn connected to a digital camera (AmScope), which projected the view on a laptop. The spacing between the two probes, which is estimated in pixels from the microscope, was converted to physical units based on a pixel to length calibration conducted before each such measurement. On recording the initial spanwise offset between HW_2 and HW_3, the two probes were brought together as close as practically possible in terms of their spanwise offset (denoted by $(\Delta y_1)_{min}$), which was in turn dependent on their final wall-normal position.

   The same microscope plus camera combination was also used to ensure that all four hotwire probes were parallel to the wall at the start of the measurement. This was achieved by comparing the orientation of the actual hotwire sensor against its image on the aluminium wall below, which was also captured by the microscope. The sensor was considered to be appropriately oriented only if the sensor and its image were found to be parallel to one another.

3. Wall-normal positioning: During the multi-point measurements, the wall-normal positions of the four probes did not change during a particular experiment, but were different for each experiment (refer table 3.1). Hence, the wall-normal positions for the four probes had to be set individually to the required values before the start of each experiment. This was made possible via a displacement microscope from Titan tool supply, which also was connected to the AmScope digital camera for viewing the real-time image on a laptop. The special characteristic of this microscope is its

shallow depth of focus, of approximately 30 μm, along with the capability to record its vertical shift via a digital indicator, with a very fine resolution of 1 μm. To measure the wall-normal position of a sensor, the microscope was first focused on the wall surface, and the reading of the dial indicator noted. After this, the focus was shifted to the sensor, and the difference between the two dial readings indicated the wall-normal location of the sensor. With the initial position as the reference, the sensor could be finally traversed to the desired position by moving the numerically controlled traverse.

In the case of single-point measurements, only the wall-normal position of the X-wire probe (installed on traverse T_2) had to be ensured. The probe was positioned at a near-wall location at the start of the measurement, from where it was traversed to 40 different wall-normal locations across the boundary layer, for measurement. For this, the same procedure as that described in (iii) above, for a single-wire probe, was followed. The procedure, however, had to be repeated for both the sensors, in a manner dependant on the X-probe type. In case of a *uv* X-probe, wherein both the sensors are parallel to the tunnel floor, the distance from the wall of both the sensors is estimated first. The average of the two is considered the centre of the X-probe (Baidya, 2016). In case of a *uw* X-probe, on the other hand, no sensor is visible via the microscope since the sensor plane is perpendicular to the tunnel wall. In such a scenario, the distance from the wall to the prong tips (which hold the sensors) is estimated and used to determine the wall-normal location of the centre of the X-probe. The nearest possible wall-normal position of the X-probe centre was $z \approx 1.1$ mm (corresponding to $z^+ \sim 35$ at $Re_\tau \approx 10\,000$).

3.1.1.3 Pressure measurement

The dynamic pressure was measured in the working section, at the streamwise location corresponding to the measurement, to facilitate: (i) hotwire sensor calibration and (ii) setting the required tunnel speed during the experiments. It was measured by a pitot-static tube mounted on the body of the traverse T_2, approximately 0.5 m from the wall. The flow at this height is always at the free-stream velocity, irrespective of the streamwise position of the traverse or the tunnel freestream speed, meaning that the pitot's position never requires adjustment. The tube itself is 0.5 m long, which ensures that the pressure estimation is not influenced by the blockage effects due to the traverse body. The pressure difference between the total and static tubes (i.e. the dynamic pressure) was measured using a 10 Torr 698A Baratron differential pressure transducer combined with a MKS

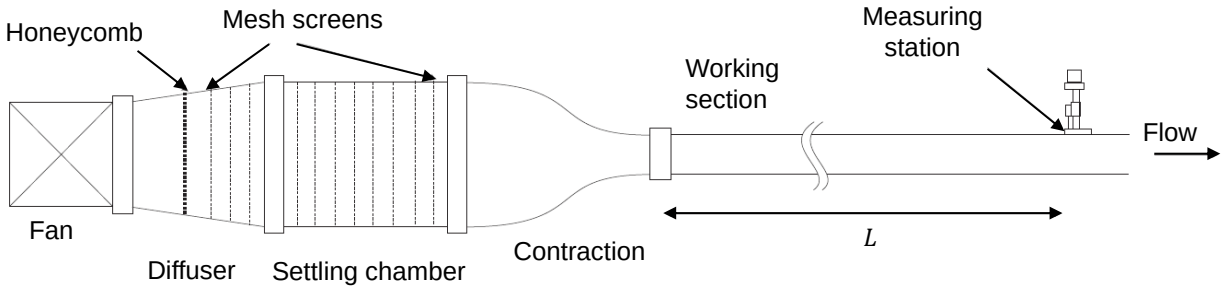

FIGURE 3.3: Schematic of the channel flow facility in the Walter Bassett Aerodynamics Laboratory of the University of Melbourne. Adapted from Ng (2011).

type 270 signal conditioner. This conditioner is linked with a digital controller, which controls the sensitivity of the pressure transducer in an automated manner. This feature is especially useful in improving the measurement accuracy during hotwire calibration, when the freestream velocities vary over a significant range. For example, the sensitivity of the transducer is increased by ten- and hundred-fold for freestream speeds 12 ms^{-1} and 3 ms^{-1}, respectively, as compared to that existing for $U_\infty \approx 20$ ms^{-1}.

Obtaining the freestream speed from the dynamic pressure also requires estimation of the ambient air density and viscosity, which can be calculated if the ambient pressure and temperature are known. In HRNBLWT, the atmospheric pressure is measured by a Sensor Technique 144S-BARO digital barometer while the working section temperature is measured by an Omega OL series linear thermistor linked with a DP25 controller. The measured values are then used in the perfect gas law and Sutherland's correlation equation to estimate the density and viscosity, respectively.

3.1.2 Channel flow facility

Figure 3.3 gives the layout of the Channel flow facility, used exclusively for single-point X-probe measurements. This facility is a blower-type wind tunnel comprising a fan driven by a DC motor and a DC controller capable of providing an air mass flow rate of $3.6m^3s^{-1}$, equivalent to a bulk velocity, $U_b \approx 30$ ms^{-1} in the test section. Once downstream of the fan, the flow is made to pass through a honeycomb screen which is at the entrance of the diffuser for straightening purposes. After this, the flow passes via several mesh screens in the settling chamber and the diffuser, after which, it encounters a two-dimensional contraction with an area ratio of 9:1, which uniformly accelerates the flow into the working section. The degree of flow uniformity was estimated by Monty (2005) to be within $\pm 0.5\%$ of the

centreline velocity (U_{cl}) in the region $y = \pm 4.5h$ relative to the spanwise midpoint. h, here, refers to the channel half-height. At the inlet of the working section ($x = 0$), the incoming flow is tripped with 80 *grit* sandpaper surrounding the entire perimeter and extending 100 mm in the x-direction. Complete details of the construction and characterization of this facility can be found in Monty (2005).

The channel test section has a cross-sectional area (width by height) of 1170 mm X 100 mm and is 22 m in length. The half-height of the channel is thus, $h = 50$ mm. The cross-section design is as per the recommendations of Dean (1978), according to whom, a 11.7:1 width-to-height ratio is satisfactory to ensure the two-dimensionality of the flow. The facility has six pressure taps installed at $x = 7.29$, 9.73, 12.17, 14.61, 17.04 and 19.48 metres, from the beginning of the working section, to measure the pressure gradient. In the present work, all measurements were carried out at $L = 20.5$ m ($\approx 410h$) from the beginning of the working section (figure 3.3), using a measuring station located at the spanwise midpoint, at $U_{cl} \approx 6.5$ ms^{-1}. This corresponds to a turbulent channel flow at $Re_\tau \approx 1000$, allowing a one-to-one comparison of the experimental data with the publicly available DNS results of del Álamo et al. (2004) at $Re_\tau = 934$.

3.1.2.1 Traversing and sensor alignments

During the single-point measurements, the X-probe was traversed in the wall-normal direction using the same traversing mechanism as used by Hutchins et al. (2011). The mechanism consisted of a sting in an airfoil profile (NACA0012) mounted to a linear rail actuated by a ball screw and stepper motor arrangement. To avoid errors due to backlash, a *Renishaw* linear encoder, installed on the linear rail, was used to provide accurate measurements of all incremental traverse movements with a resolution of approximately 0.5 μm. The traverse was long enough to allow the vertical movement of an X-probe outside of the channel working section, from the top access plate, which was required for conducting the 2-D calibration of the probe using a jet calibrator.

During velocity profile measurements, the probe was traversed across the fully developed turbulent channel profile at 28 logarithmically spaced points within the range 3 mm $< z <$ 50 mm ($= h$). In terms of inner-scaling, this corresponds to the distance from the wall of $z^+ \approx 60$. This spacing was limited by the 6 mm diameter of the *Dantec* $55H25$ X-probe holder, which was held at zero degree inclination with respect to the horizontal, to avoid errors due to sensor misalignment (Baidya et al., 2019b). Before each measurement, the exact wall-normal position of the centre of the X-probe was determined by using a traversable

microscope, in a manner similar to that conducted during experiments in HRNBLWT (§3.1.1.2).

3.1.2.2 Pressure measurement

In the case of the channel flow experiments, pressure measurements were required to facilitate the following: (i) static pressure measurements for the determination of pressure drop in the channel, and (ii) measurement of the dynamic pressure, at the channel centreline, to determine U_{cl} during calibration and wall-normal profile measurement. All the pressure measurements were carried out using an MKS Baratron 698A11TRA differential pressure transducer and the signals sampled from MKS Type 270D signal conditioner. To facilitate (i), stainless steel inserts, with an outer diameter of 1.6 mm, were used as pressure taps in the channel working section to measure the static pressure drop. These individual pressure tappings were connected to the pressure transducer via spaghetti tubes. The tap farthest upstream (closest to the beginning of the working section) was used as the reference pressure when determining the pressure gradient. The static pressure gradient was measured prior to each hot-wire velocity profile measurement, with the readings sampled at $50kHz$ for a time of 90 seconds. The long time duration was required since the magnitudes of the static pressure were low. On the other hand, to facilitate (ii), the facility has a pitot tube attached from the top portion of the working section, in a manner such that its centre is always aligned with the channel centreline to measure U_{cl}. The tube is located at a spanwise offset of $\Delta y \approx 2h$ from the X-probe location to avoid blockage effects from the pitot influencing the velocity measurement.

3.2 Multi-point single-wire measurements

3.2.1 Hotwire sensors and anemometry details

All four hotwire probes (HW_{1-4}) used for the multi-point experiment (as shown in figure 3.2) were boundary layer type miniature probes (55P15) purchased from *Dantec*. They were prepared by soldering Wollaston wires, of diameter $d = 2.5\ \mu$m, onto the stainless steel prong tips. The wire is then etched by following the procedure outlined in Perry (1982) to expose the Platinum-Rhodium sensor length of 0.5 mm. This allows the length-to-diameter ratio of the sensors to be kept at 200, which is long enough to avoid significant heat loss owing to end conduction (Ligrani and Bradshaw, 1987; Hutchins et al., 2009).

During the experiment, the hotwires were operated using a Melbourne University Constant Temperature Anemometry (MUCTA) circuit. For all the measurements, an overheat ratio (OHR) of 1.8 was used. Here, OHR is defined as:

$$\text{OHR} = \frac{R_w - R_0}{R_0}, \tag{3.1}$$

where R_w is the wire resistance when heated and R_0 is the wire resistance at ambient temperature. Before use in the experiment, the exposed wire was annealed to stabilize its sensor properties, by operating the wire at the desired OHR for more than seven hours (Perry, 1982). After the annealing procedure, the frequency response of the combined system, which included the hotwire plus the anemometer circuit, was recorded by following the square-wave test procedure suggested by Perry (1982). In this, the hotwire anemometer circuit is perturbed by a square-wave voltage, a feature included in the MUCTA, to measure the dynamic response of the combined system. To avoid any additional perturbation from the turbulent fluid, the square-wave test was performed with the probe positioned in the freestream. The freestream speed, however, was maintained at $U_\infty/3$ to approximately match the mean speed at $z^+ \approx 15$, as per the recommendations of Baidya (2016). Here, U_∞ corresponds to the desired freestream velocity during the experiment and $z^+ \approx 15$ corresponds to the wall-normal location at which the streamwise velocity variance is maximum. The frequency response for the 0.5 mm length hotwire sensor was found to be approximately 25 kHz, meaning the normalized cut-off frequency in viscous units, for the current measurements, was approximately $f_c^+ = f_c\nu/U_\tau^2 \approx 0.9$. This is greater than $f_{max}^+ \approx 0.33$ found by Hutchins et al. (2009) as the approximate limit for the maximum energetic frequencies in turbulent boundary layers.

For data acquisition, a *Data Translation* analogue to digital converter (DT9836), having 16 bit resolution across ± 10 V, was used to sample as well as convert the voltages from the sensors to binary format. The data from the sensors was sampled at 50 kHz during all muli-point measurements. On acquisition, the signals from the anemometer system were passed through a low pass filter (USBPGF-S1 from *Alligator Technologies*) programmed to allow only frequencies below 25 kHz, to avoid temporal aliasing. Before beginning each measurement, the noise levels in the hot-wire signal were also checked. This is owing to a previous observation (Baidya, 2016) of electronic noise from other equipment getting introduced into the hot-wire signal, in cases where both share a common power line. Hence, a measurement was conducted only when the voltage fluctuations from the hot-wire, for zero freestream velocity, remained within ± 10 mV. Further, in order to ensure that the measurement is not influenced by the unpredictable voltage fluctuations in the power lines,

the anemometer and the signal conditioner were powered by an uninterruptible power supply (UPS) system. For the main experiment, the total data sampling duration (T) at each measurement location was chosen to be 360 seconds in order to have a boundary layer turnover time ($= TU_\infty/\delta$) of approximately 20 000. The long time duration ensures that a sufficient number of cycles corresponding to the large-scale structures in the boundary layer (of the order of δ) are captured by the hot-wire to provide converged turbulence statistics, as well as a partially converged spectra at the large scales.

3.2.2 Probe calibration

A voltage-velocity map is required to be generated empirically for each hotwire, to convert the voltages acquired during an experiment to a velocity time series. This mapping, commonly known as the 1-D calibration, is conducted by varying the freestream speeds and recording the corresponding mean sensor voltages. Since hotwire probes are prone to drift over time, all four hotwire probes used in the experiment were calibrated both before and after each measurement. Ideally, all sensors need to be calibrated in the freestream, where the turbulence intensity is minimum. However, in case of multi-point measurements, HW_{1-2} and HW_4, which were attached to traverses T_1 and T_3 respectively, could not be extended up to the freestream. Hence, only HW_3 which was attached to T_2, could be traversed up to $z \approx 0.5$ m from the wall and calibrated with the help of the pitot static tube at that location (§3.1.1.3). Calibration for HW_3 was conducted by sampling the hotwire voltages, for varying mean speeds of the freestream, for 60 seconds. Once HW_3 was calibrated, it was traversed closer to the wall, to the same wall-normal location at which HW_{1-2} and HW_4 were maintained. These three wires were, subsequently calibrated inside the TBL, by using the mean velocity at that height estimated from the HW_3. Given that the hotwires are exposed to much stronger turbulent fluctuations within the shear layer, the sampling time (T_c) during this calibration was maintained at $T_c U_\infty/\delta \approx 10\,000$ to ensure the convergence of the mean velocity. This calibration procedure, for the present multi-traverse setup, has been previously validated by Chandran (2019).

3.2.3 The measurement campaign

One of the main aims of the present thesis is to reconstruct the 2-D spectra of the streamwise velocity. Since this has been previously investigated by Chandran et al. (2017, 2020) by utilizing the same experiental setup, the same experimental methodology as that of

Arrangement	z_o^+	z_r^+	$U_\infty(ms^{-1})$	$\delta\ (m)$	TU_∞/δ	l^+	$(\Delta y_1)_{min}$	$(\Delta y_4)_{max}$
1	100	100	20	0.36	19 500	22	0.01δ	2.7δ
1	200	200	20	0.36	19 500	22	0.01δ	2.7δ
1	318	318	20	0.36	19 500	22	0.01δ	2.7δ
1	477	477	20	0.36	19 500	22	0.01δ	2.7δ
1	750	750	20	0.36	19 500	22	0.01δ	2.7δ
1	1 025	1 025	20	0.36	19 500	22	0.01δ	2.7δ
1	**2 250**	**2 250**	20	0.36	19500	22	0.01δ	2.7δ
2	15	15	20	0.36	19 500	22	0.01δ	2.7δ
3	100	15	20	0.36	19 500	22	0	2.5δ
3	200	15	20	0.36	19 500	22	0	2.5δ
3	318	15	20	0.36	19 500	22	0	2.5δ
3	477	15	20	0.36	19 500	22	0	2.5δ
3	750	15	20	0.36	19 500	22	0	2.5δ
3	1 025	15	20	0.36	19 500	22	0	2.5δ
3	**2 250**	15	20	0.36	19 500	22	0	2.5δ
4	100	**2 250**	20	0.36	19 500	22	0	2.5δ
4	200	**2 250**	20	0.36	19 500	22	0	2.5δ
4	318	**2 250**	20	0.36	19 500	22	0	2.5δ

TABLE 3.1: A summary of the various multi-point measurements conducted in HRNBLWT, classified into four different arrangements based on the relative wall-normal positioning of the hotwire probes. Terminology has been described in §3.2.3 and figure 3.4. Values highlighted in bold represent the upper limit of the log-region, $z^+ \approx 0.15\delta^+$ (Marusic et al., 2013).

Chandran et al. (2017) was adopted here. They, however, obtained the spectra by reconstructing the 2-D cross-correlation of the streamwise velocity fluctuations acquired in the same wall-parallel plane, which consequently reflects the 2-D spatial signatures of all coherent structures coexisting in that plane. The experiments in this thesis extend this investigation to reconstruct the statistical picture along all three dimensions. They were inspired based on the work of both Chandran et al. (2017) as well as Baars and Marusic (2020a), discussed previously in §2.5, and were aimed at extracting spatial signatures of large 3-D coherent structures in the turbulent boundary layer.

Table 3.1 lists all the multi-point measurements utilized in part or whole in the subsequent chapters of this thesis. All these measurements were carried out at HRNBLWT, at a nominal freestream of $U_\infty \approx 20\ \mathrm{ms}^{-1}$, to attain a $Re_\tau \approx 15\ 000$. In the table, z_o refers to the wall-normal position of HW_{1-2}, while z_r refers to that for HW_{3-4}. In certain

experiments, $z_o \approx z_r$, which led to reconstruction of the 2-D cross-correlation similar to that done previously by Chandran et al. (2017). While, the experiments for which $z_o \neq z_r$ reconstruct the 3-D statistical picture of the flow. The variation of z_o and z_r listed in table 3.1 can be used as the basis to classify all the measurements into four general 'arrangements' of the hotwire probes, which have been schematically depicted in figure 3.4.

While the relative wall-normal positioning of the four probes is different in each arrangement, the manner in which the experiment is conducted is the same for all these cases. The measurement begins with HW_2 and HW_3 kept as near as practically possible to one other, indicated by $(\Delta y_1)_{min}$, which varies depending on the relative wall-normal positioning of HW_2 with respect to HW_3. Owing to $z_o \approx z_r$ for both arrangements 1 and 2, $(\Delta y_1)_{min}$ was limited by the diameter of the probe holders, which is approximately 0.01δ. On the other hand, $(\Delta y_1)_{min}$ was ensured to be zero for cases where $z_o \neq z_r$, by aligning HW_2 vertically above or below HW_3 in case of arrangements 3 and 4, respectively. Next, to build the cross-correlation in the spanwise direction, T_1 carrying HW_{1-2} is traversed in the spanwise direction (but maintaining the same wall-normal position), while HW_{3-4} remain at a fixed spanwise and wall-normal location throughout the measurement. u-signals are simultaneously acquired by all hotwire probes after every spanwise traverse of T_1. The traversing is programmed such that the spanwise offset between HW_2 and HW_3 varies logarithmically, ensuring more data acquisition at smaller offsets as compared to that at larger spanwise offsets. This procedure goes on until the spanwise spacing between HW_1 and HW_4 reaches $(\Delta y_4)_{max}$, which has also been recorded for each measurement in table 3.1. Figure 3.5(a) depicts the 1-D spanwise cross-correlation coefficient ($\widetilde{\mathcal{R}}_{u_o u_r}$) reconstructed from the multi-point measurements for each of the four arrangements depicted in figure 3.4, with $z_o^+ \approx 318$ for arrangements 1, 2 and 4. Here, $\widetilde{\mathcal{R}}_{u_o u_r}$ is defined as:

$$\begin{aligned} R_{u_o u_r}(\Delta y; z_o, z_r) &= \overline{u(y; z_r) u(y + \Delta y; z_o)}, \\ \text{with } \widetilde{\mathcal{R}}_{u_o u_r} &= R_{u_o u_r} / (\sqrt{u^2(z_o)} \sqrt{u^2(z_r)}), \end{aligned} \tag{3.2}$$

where the overbar indicates ensemble time average. A 1-D Fourier transform of $R_{u_o u_r}$ gives the 1-D spectra as a function of spanwise wavelengths, $\phi_{uu}(k_y)$ which is defined as:

$$\phi_{u_o u_r}(k_y; z_o, z_r) = \int_{-\infty}^{\infty} R_{u_o u_r}(\Delta y; z_o, z_r) e^{-j2\pi(k_y \Delta y)} d(\Delta y), \tag{3.3}$$

where j is a unit imaginary number. Figure 3.5(b) plots the absolute form of the premultiplied 1-D spanwise spectra ($\mid k_y^+ \phi_{uu}^+ \mid$) corresponding to each of the cross-correlations in

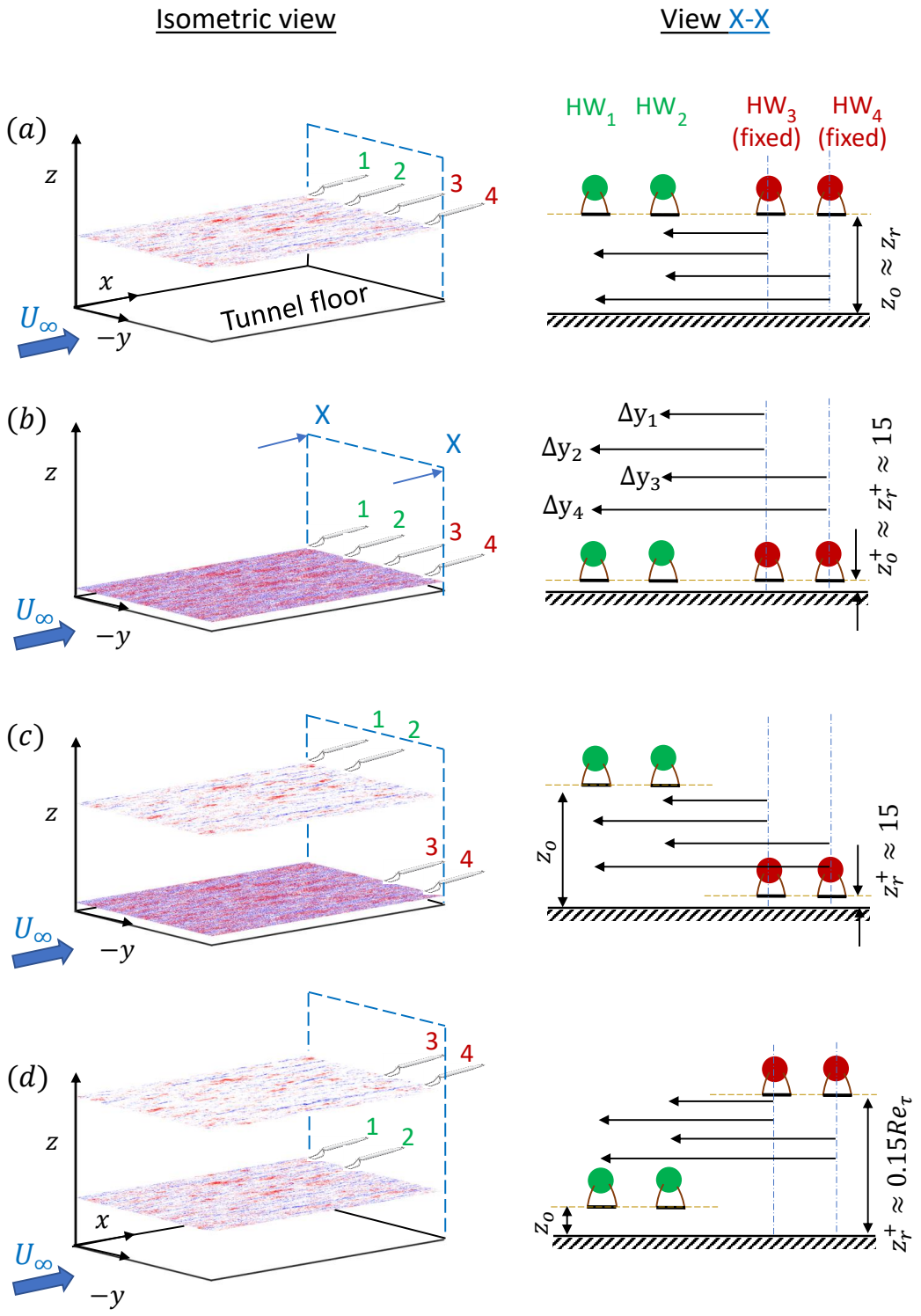

FIGURE 3.4: Schematic depicting the relative positioning and movement of the four hotwire probes (HW_{1-4}) during the multi-point measurements in the HRNBLWT. (a-d) Four specific arrangements have been classified based on the relative wall-normal locations of the HW_{1-2} (at z_o) and HW_{3-4} (at z_r) in the various experiments (table 3.1), with (a) Arrangement 1 corresponding to $100 \lesssim z_o^+ \approx z_r^+ \lesssim 0.15Re_\tau$, (b) Arrangement 2 corresponding to $z_o^+ \approx z_r^+ \approx 15$, (c) Arrangement 3 corresponding to $100 \lesssim z_o^+ \lesssim 0.15Re_\tau$, $z_r^+ \approx 15$ and (d) Arrangement 4 corresponding to $100 \lesssim z_o^+ \lesssim 318$, $z_r^+ \approx 0.15Re_\tau$. Blue arrows indicate direction of the mean flow velocity along x. The instantaneous u-fluctuations plotted in the isometric view have been extracted from the ZPG TBL DNS dataset of Sillero et al. (2013) and are used simply for representative purposes. In these representative flow fields, blue and red contours correspond to low and high streamwise momentum motions, respectively.

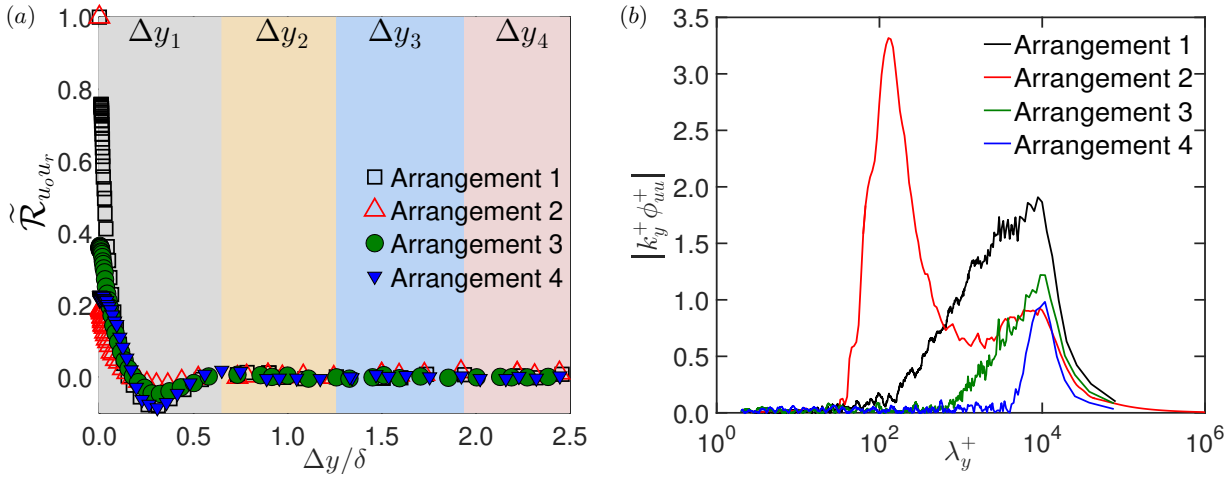

FIGURE 3.5: (a) Cross-correlation coefficient ($\widetilde{\mathcal{R}}_{u_o u_r}$) reconstructed from the u-signals acquired at various spanwise offsets during the multi-point measurements. Here, a measurement corresponding to each of the four different arrangements classified in figure 3.4 has been considered as an example, with $z_o^+ \approx 318$ in case of Arrangements 1, 2 and 4. (b) Premultiplied 1-D spanwise u-spectra corresponding to each of the $\widetilde{\mathcal{R}}_{u_o u_r}$ profiles shown in (a).

figure 3.5(a). It should be noted that the spanwise spectra plotted in figure 3.5(b) has been corrected to account for the inaccurate $R_{u_o u_r}$ estimated for $0 < \Delta y < (\Delta y_1)_{min}$ (by assuming linear interpolation) via implementation of the correction scheme proposed by Chandran et al. (2016). The spectra plotted in figure 3.5 may be considered representative of the range of scales (λ_y^+) influencing the cross-correlations reconstructed in the four different arrangements. In the case of arrangement 1 (figure 3.4(a)), $100 \lesssim z_o^+ \lesssim 0.15 Re_\tau$, which corresponds to the inertial region of the TBL. $\widetilde{\mathcal{R}}_{u_o u_r}$ reconstructed from this measurement would be influenced by all the energetic inertial motions coexisting in the wall-parallel plane at z_o, as indicated by the representative flow field from the DNS of Sillero et al. (2014) in figure 3.4(a). The same is also reflected in the corresponding spanwise spectra in figure 3.5(b), which encompasses a considerable range of scales and hence is broadband in nature as compared to the other spectra.

Arrangement 2 depicted in figure 3.4(b) is similar to arrangement 1 in the sense that $z_o \approx z_r$, but all four probes in this case were positioned close to the wall at $z_o^+ \approx z_r^+ \approx 15$, which translates to a wall-normal location of approximately 0.3 mm in physical units. Owing to this, the spanwise traverse of HW_{1-2} had to be conducted in a slightly different manner to prevent breakage of the sensor. After acquiring u-signals for $(\Delta y_1)_{min}$, T_1 (carrying HW_{1-2}) was first moved away from the wall by 0.5 mm, then traversed to the required spanwise offset Δy_1, and finally traversed towards the wall by 0.5 mm. Before acquiring the long u-signals for 360 seconds at the new Δy_1, the position of the HW_{1-2} was first

verified by computing the 1-D streamwise u-spectra by acquiring data for 120 seconds. This spectra was compared with the near-wall spectra acquired previosuly by Hutchins et al. (2009), in the same facility at similar tunnel conditions, to confirm the wall-normal location of the HW_{1-2} after the spanwise traverse. Figure 3.6(a) plots these 1-D streamwise u-spectra computed from the u-signals acquired by HW_{1-2} after each spanwise traverse. By comparing with the reference spectra in the wall-normal range: $10.6 \lesssim z^+ \lesssim 17.5$, it was established that the HW_{1-2} were maintained in the given wall-normal range throughout the measurement. While this variation in the probe wall-normal location can lead to certain inaccuracies in the cross-correlation being reconstructed at $z_o \approx z_r \approx 15$, as per the earlier findings of Chandran (2019), the influence on the correlation isn't significant for a mismatch in the range $\Delta z^+ < 10$. The spanwise spectra subsequently obtained from the reconstructed cross-correlation is plotted in figure 3.5(b), and reflects the flow features related to the near-wall cycle ($\lambda_y^+ \approx 100$; Kline et al. (1967)), as well as the footprints of the large-scales from the outer region (Hutchins and Marusic, 2007).

In case of arrangement 3, HW_{3-4} were positioned at the same near-wall wall-normal location as in arrangement 2 (i.e. $z_r^+ \approx 15$), while HW_{1-2} were positioned in the inertial region ($100 \lesssim z_o^+ \lesssim 0.15Re_\tau$). The cross-correlation reconstructed from this arrangement is a reflection of 3-D large structures coherent with the wall and extending beyond z_o in terms of their wall-normal coherence (Baars and Marusic, 2020a). This is evident from the spanwise spectra (figure 3.5(b)) corresponding to this arrangement, wherein the energy is concentrated at only the relatively large wavelengths, in comparison to spectra obtained from arrangement 1. Finally, in case of arrangement 4, HW_{3-4} were moved to the upper bound of the log-region ($z_r^+ \approx 0.15Re_\tau$) while HW_{1-2} were maintained in the inertial region, similar to arrangement 3. u-signals cross-correlated in such an arrangement are influenced by the velocity signatures of predominantly the very large-scale motions, which are coherent across the inertial region and beyond (Baars and Marusic, 2020a). Accordingly, the spanwise spectra obtained from such an arrangement is predominantly concentrated at $\lambda_y \sim \mathcal{O}(\delta)$, which is suggestive of the VLSM contributions.

For both these arrangements 3 and 4, $\Delta y_1 \approx 0$ had to be ensured at the start of the experiment, given that a non-zero spanwise offset results in the inaccurate estimation of energy in the small spanwise scales (Chandran et al., 2016). This was verified by computing the linear coherence spectrum (§2.5.3.2) defined as:

$$\gamma_L^2(z_o, z_r, \Delta y = 0; \lambda_x) = \frac{\mid \langle \widetilde{u}(z_o, \Delta y = 0; \lambda_x) \widetilde{u}^*(z_r; \lambda_x) \rangle \mid^2}{\langle \mid \widetilde{u}(z_o, \Delta y = 0; \lambda_x) \mid^2 \rangle \langle \mid \widetilde{u}(z_r; \lambda_x) \mid^2 \rangle}, \tag{3.4}$$

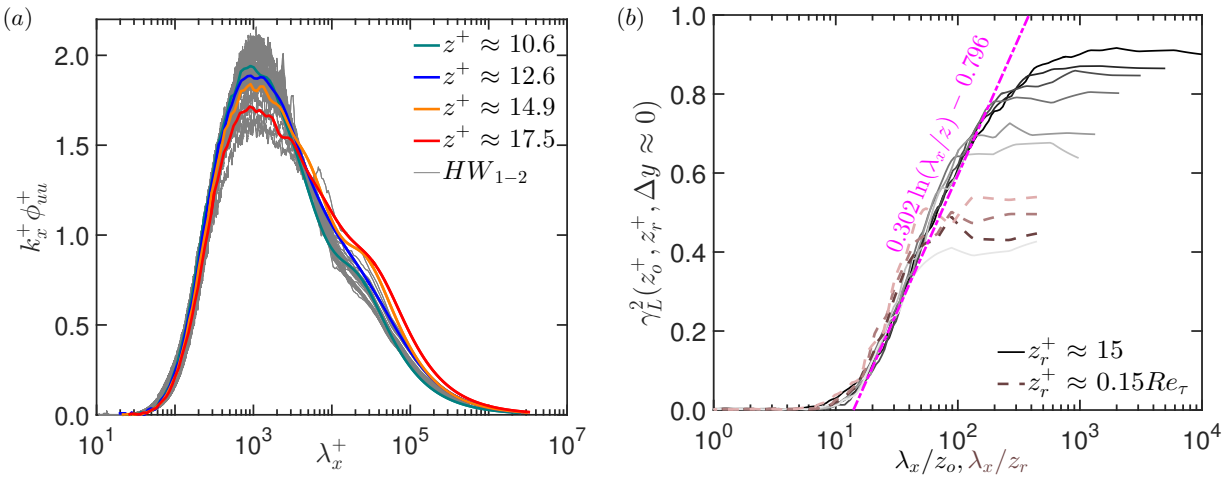

FIGURE 3.6: Premultiplied 1-D streamwise spectra computed from u-signals acquired by HW_{1-2} (in grey) at all spanwise offsets (Δy_{1-4}) during the multi-point experiment corresponding to $z_o^+ \approx z_r^+ \approx 15$ (Arrangement 2). These spectra are compared with the near-wall spectra (denoted by solid lines of other colours) obtained previously by Hutchins et al. (2009) in the same facility at similar flow conditions. (b) 1-D γ_L^2 computed from the u-signals acquired by HW_2 (at z_o) and HW_3 (at z_r) at the start of the multi-point measurements (i.e. $\Delta y_1 \approx 0$) corresponding to Arrangements 3 (solid lines) and 4 (dashed lines). Dark to light shading denotes the increase in z_o. Dash-dotted magenta line represents the empirical fit for γ_L^2 proposed by Baars et al. (2017).

from the u-signals acquired by HW_2 (at z_o) and HW_3 (at z_r) in a test run before the start of the experiment. γ_L^2 computed from the present data is plotted in figure 3.6(b), where it is compared against the empirical fit given by Baars et al. (2017) for the range of wavelengths at which $\gamma_L^2(z_o,z_r,\Delta y = 0;\lambda_x)$ exhibits z_o-scaling. Given that γ_L^2 is known to be sensitive to small changes in Δy (Baidya et al., 2019a), good comparison between the empirical fit and the present experimental data verifies the claim that $\Delta y_1 \approx 0$ at the start of the experiment.

3.3 Single-point X-probe measurements

3.3.1 X-wire probe

This section gives a brief introduction to X-wire probes (or X-probes), the principles governing their operation, and also discusses the calibration scheme used to process data acquired from the same. The hot-wire sensors are operated using an anemometer circuit which maintains the sensors at a constant temperature (and thus a constant resistance) through a feedback mechanism. When exposed to a flow, the heated wire loses heat to

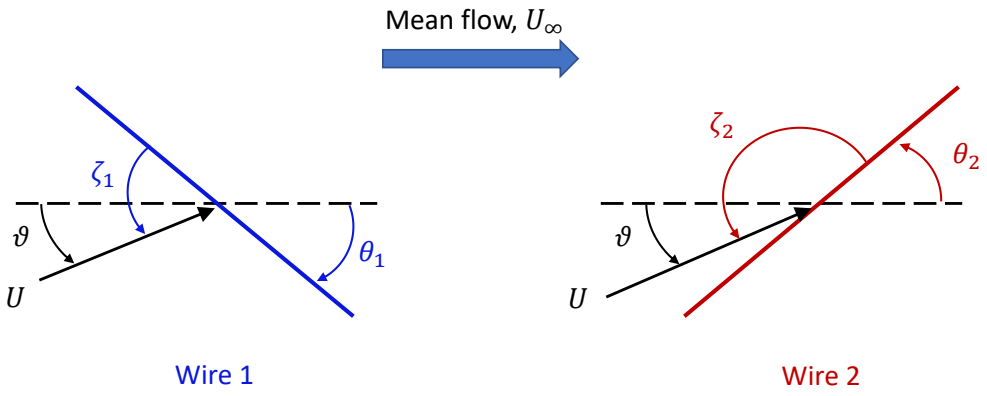

FIGURE 3.7: Schematic of a typical X-wire configuration used to measure two velocity components in the same plane as the plane parallel to both the wires. The two wires are shown separately in the schematic for clarity. U is the instantaneous velocity vector which is inclined at ϑ with respect to the mean flow (U_∞) direction, x. ζ_i denotes the angle between the instantaneous flow vector and the wire i, with $i = 1$ or 2. Adapted from Bruun (1996).

the surroundings via convection (King, 1914) and is almost immediately reheated to the desired temperature by the circuit. The heat lost by the wire can thus be estimated from the energy required to re-heat the wire. King (1914) showed analytically that the supplied current by the anemometer to keep the hot-wire at a constant temperature can be related to the instantaneous flow velocity. He analyzed such a problem for an infinitely long wire and came up with a power law relationship between the anemometer voltage and the flow velocity. Considering the fact that in reality hot-wires are of finite length, Bruun (1996) found that a modified power law or polynomial fit describes the measured velocity-voltage relationship in a better manner.

In case of a single hot-wire measurement which is restricted to measuring only the streamwise velocity component, a 1-D calibration is sufficient to get a unique relation between the streamwise velocity and hot-wire voltage. The 1-D calibration, which involves recording sensor voltages over varying flow velocities, is generally conducted in the free-stream (in case of a boundary layer flow) or at the channel centreline where the turbulence intensity is the minimum. Due to the simple nature of the 1-D calibration, it can be performed by varying the speeds at various intervals dependent on the application. Subsequently, the functional form of the velocity-voltage relationship, for this calibration, doesn't influence the final outcome (Bruun, 1996).

For the X-probes, however, which are used to acquire the streamwise velocity as well as one of the two lateral velocity components, a 2-D calibration is required wherein the flow

velocity as well as the angle is varied. The probe is calibrated using a jet facility, capable of releasing a low turbulent flow at varied angles. An X-probe consists of two wires (wires 1 and 2) oriented at an angle (θ_1 or θ_2) with respect to the streamwise direction (figure 3.7), unlike the single wire where the sensing element is normal to the flow direction. The two wires are kept at a certain spacing (Δs_j), where j corresponds to the direction normal to the sensor plane. Both these wires are kept in the same plane (hereafter referred to as the sensor plane) and the choice of plane depends on the desired lateral velocity component v or w. The voltages from the X-probe, measured during calibration, may be described as follows:

$$\begin{aligned} E_1 &= P_1(\mid U \mid, \vartheta) \\ E_2 &= P_2(\mid U \mid, \vartheta), \end{aligned} \tag{3.5}$$

where E_1 and E_2 denote the mean output voltages from the two hot-wires while ϑ and $\mid U \mid$ respectively correspond to the mean flow angle (relative to x) and velocity magnitude. Considering N to be the number of velocities considered for both the 1-D and 2-D calibration, and also the number of jet orientation angles, the total number of calibration points required increases from N (for 1-D calibration) to N^2 (for 2-D calibration). A number of calibration schemes have been proposed in the past to generate the velocity-voltage map and can be categorized into three types (Baidya, 2016): (i) full calibration, (ii) dynamic calibration and (iii) effective angle method. In the present study, we use the effective angle method and hence limit our discussion only to this method.

3.3.1.1 Effective angle method

The nature of the hot-wire measurement technique is such that the voltage recorded by the anemometer cannot be uniquely assigned to a particular velocity component (say u) impacting the wire, but to the resultant magnitude of the flow velocity over the wire. This very fact is utilized in the implementation of the effective velocity method. Indeed, the velocity component normal to the wire is the one which influences the convective heat transfer the most. However, contribution from the velocity components tangential and bi-normal to the wire is not negligible. Suppose a hot-wire sensor outputs a voltage E_1 for a particular instantaneous velocity vector. The effective velocity, U_{eff} is defined such that the same voltage E_1 is produced for U_{eff} 'normal' to the wire. This allows E-$\mid U \mid$ calibration curves, at various flow angles ϑ, to collapse on to a single E-U_{eff} curve for each sensing element. The mean effective cooling angle, ζ_{eff} is defined as the angle which

satisfies the following:

$$| U |f(\zeta_{eff}) = U_{eff}. \tag{3.6}$$

The mean effective angle, ζ_{eff} is approximately equal to the angle between the velocity vector and the wire ζ shown in figure 3.7. If ζ_{eff} is assumed to be a function of only the flow angle ϑ, the voltage-velocity mapping function can be constructed by performing two 1-D calibrations where only one variable, amongst the jet flow velocity or the angle of the jet flow, is varied while the other is kept constant. This creates a possibility of reducing the minimum points required from 2-D calibration, from N^2 to $2N$.

Previously, many researchers have proposed functional forms for $f(\zeta_{eff})$ to relate $| U |$ and U_{eff}. One of the most commonly used expressions is the one proposed by Hinze (1975):

$$f(\zeta_{eff}) = \sqrt{sin^2\zeta + k^2 cos^2\zeta} \tag{3.7}$$

where k is known as the tangential cooling coefficient. On applying equation 3.6 to the two wires shown in figure 3.7, we get the following:

$$\begin{aligned} | U |f(\vartheta_{eff} + \theta_1) &= U_{eff1}, \\ | U |f(\vartheta_{eff} - \theta_2) &= U_{eff2} \end{aligned} \tag{3.8}$$

where θ_1 and θ_2 correspond to the inclination angles of the two wires relative to the mean flow direction, while the ϑ_{eff} corresponds to the angle between the flow velocity vector and streamwise direction. Equations 3.6 and 3.8 are used to solve for the two unknowns $| U |$ and ϑ_{eff} during measurements, after determining the mapping functions describing E-U_{eff} relation and the angle sensitivity for the wires, $f(\vartheta)$ from the 2-D calibration.

3.3.2 The measurement campaign

The single-point X-probe measurements were performed both in the channel flow (§3.1.2) and the high Reynolds number boundary layer (§3.1.1) facility. Table 3.2 gives details of these experiments conducted via various X-probes, which differ in terms of their viscous-scaled measuring volumes. Figure 3.8 illustrates the definition of the geometric parameters used to define the measurement volume for the two X-probe types, uv and uw X-probe. Here, Δs_i^+ and l_i^+ refers to the spacing between the two sensors and lengths of the individual sensing elements, respectively. The subscript 'i' indicates the direction along which the distance is measured, which varies depending on the probe type (uv or uw). For instance, in case of a uv X-probe (figure 3.8(a)), the geometry of the full sensor is indicated by l_x^+

Probe	Ref.	Re_τ	Probe type	Facility	h or δ (in m)	ν/U_τ (in μm)	θ_w (in deg)	l_x^+, l_y^+ or l_z^+	Δs_y^+ or Δs_z^+	l/d
Auspex A55P51	$AX1$	1 000	uv,uw	Channel	0.05	50	45	14	10	200
Auspex A55P61	$AX2$	1 000	uv,uw	Channel	0.05	50	45	7	10	200
Custom	CX	1 000	uv,uw	Channel	0.05	50	45	7	4	200
		10 000	uv,uw	HRNBLWT	0.32	32	45	12	7	200

TABLE 3.2: A summary of the various single-point measurements conducted using various X-probes. Terminology has been described in § 3.3.2.

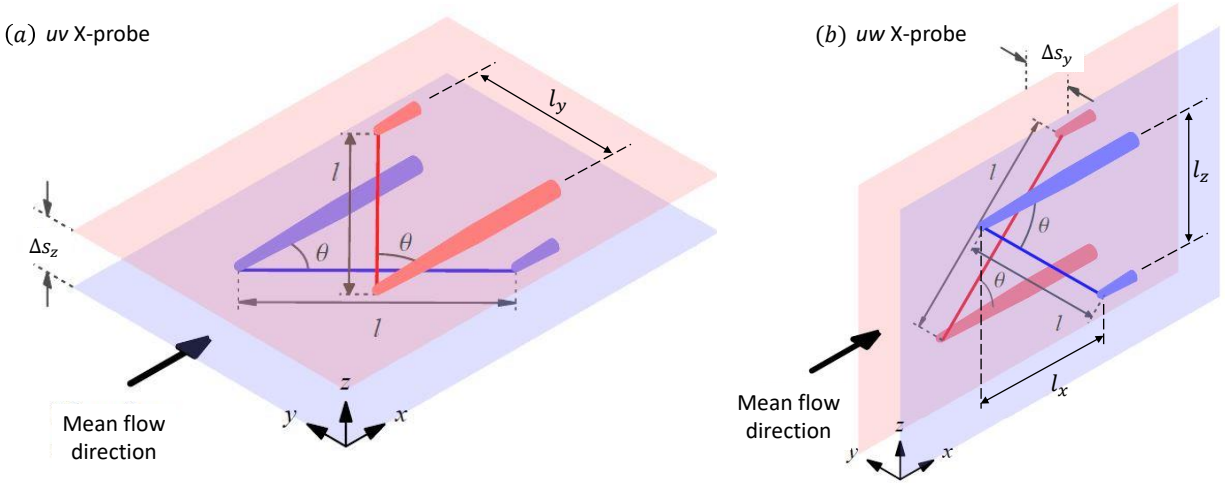

FIGURE 3.8: Schematic of a (a) *uv* and (b) *uw* X-probe depicting the various geometric parameters (l_i, Δs_i, θ) used to define the measurement volume of an X-probe, with i representing the direction of measurement. The two sensors are indicated by red and blue lines, with the light shaded planes of the same colour denoting the respective sensor planes. Adapted from Baidya (2016).

$\times\ l_y^+ \times \Delta s_z^+$. Further, the angle made by the two sensors, with the freestream direction x, is given by θ while 'd' is the diameter of the wire.

Of the three X-probes used (table 3.2), two probes with relatively large measuring volume ($AX1$ and $AX2$) were purchased off-the-shelf from *Auspex Corporation*. While, the probe with the smallest measuring volume (CX-probe) was manufactured in-house to reduce errors associated with spatial resolution. The methodology adopted to fabricate this probe was inspired from that detailed previously by Baidya (2016). The CX-probe was fabricated using four 330 μm diameter stainless steel prongs, which were selected to approximately match the prong diameter of 350 μm in the standard *Auspex* X-probes. The prong tips were sharpened using a grinding wheel so that the tip diameter tapers down to approximately 80 μm, to facilitate the soldering of Wollaston wire on these tips during probe preparation. Finally, these prongs were held rigidly in a ceramic tube using epoxy resins to get the desired probe geometry. The diameter of the ceramic tube is approximately 2 mm, similar to the ceramic tubing in the *Auspex* X-probes, making it compatible to connect with the *Dantec* X-probe holder (55H25).

There are, however, certain differences in the X-probe designed for the present study and that used previously by Baidya (2016). The CX-probe is designed such that the sensing elements are not directly connected to the prong tips, i.e. the hot-wire is stubbed. The presence of stubs decreases end conduction, which increases the possibility of a uniform

temperature profile along the hot-wire sensor (Tropea and Yarin, 2007). Considering a stubbed X-probe also allows the CX-probe to be prepared for measurement in the same way as for the *Auspex* probes, using Wollaston wires as the sensing elements (the same procedure, as outlined in Perry (1982), was followed for soldering and subsequently etching the Wollaston wires). Subsequently, the preparation time for a stubbed probe is also much shorter than that required to prepare stubless probes (Baidya, 2016). For the present measurements, the Wollaston wires in every X-probe were etched to the point such that the length to diameter ratio (l/d) of the sensors would equal approximately 200 (Ligrani and Bradshaw, 1987; Hutchins et al., 2009).

3.3.3 Hotwire anemometry details

All X-probes were operated using the Melbourne University Constant Temperature Anemometer (MUCTA), and the overheat ratio (OHR) for these probes was selected to be 1.8, same as that chosen for the single-wire probes. Since the spacing between the two wires is very small ($\approx$ 0.2 mm) in case of the CX-probe, the OHR was selected only after ensuring that there was no thermal cross-talk between the two wires for mean streamwise velocities relevant to the measurement. On preparation of an X-probe, the wires were annealed to stabilize the sensors by operating at the desired OHR for more than seven hours (Perry, 1982). A square wave test was also conducted, in a manner similar to that discussed in §3.2.1, to adjust the anemometer settings in order to have a similar frequency response from both the wires of the X-probe. A frequency response of 7 kHz and 25 kHz was noted for the sensors with 5 μm and 2.5 μm diameter wire, respectively.

A *Data Translation* analogue to digital converter (DT9836), having 16 bit resolution across $\pm$ 10 V, was used to sample as well as convert the data from the X-probe to binary format for all the experiments. The data from the X-probe was sampled at 30 kHz for the channel measurements and 50 kHz for the ZPG TBL measurements. The signals from the anemometer system were passed through a low pass filter (9002-LP00 from *Frequency Devices*) set at 15 kHz for channel measurements ($\sim$ 25 kHz for the TBL measurements) to avoid temporal aliasing. This frequency cut-off is significantly greater than the maximum frequency of the energetic turbulent motions in the shear layer (Hutchins et al., 2009). The total sampling duration (T) at each wall location, in case of the channel measurements, was chosen to be 180 seconds in order to have a boundary layer turnover time ($= TU_\infty/\delta$) of the order of 10^4. In the case of the TBL measurements, the sampling duration had to be increased to 330 seconds to obtain a turnover time of the same order.

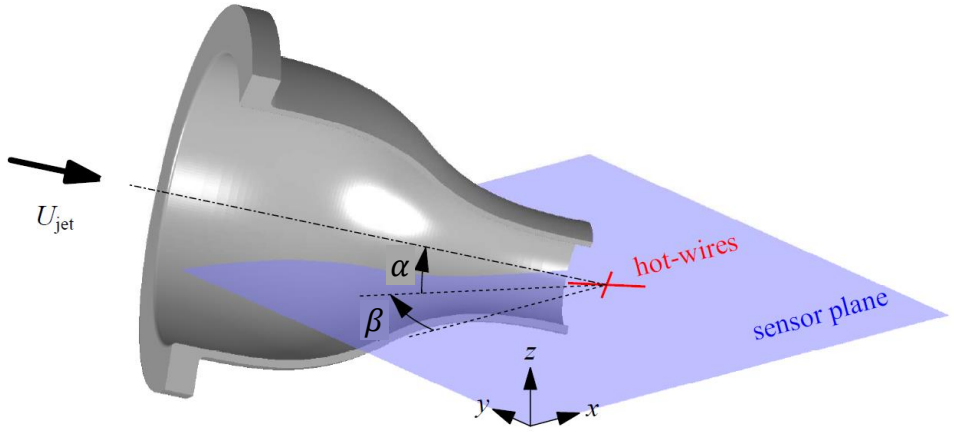

FIGURE 3.9: Schematic of the jet orientation relative to a uv X-probe (indicated by the sensor plane). β corresponds to rotation in the sensor plane, while α corresponds to rotation normal to the sensor plane. Adapted from Baidya (2016).

Similar to the single-wire experiment, the noise levels in the hot-wire signal were checked before beginning each measurement. Notably, in the case of the X-probe measurements in the channel, it was observed that the noise levels in the hot-wire signal increased significantly when the 2-D jet calibrator was powered from the same line as the hotwire anemometer. Hence, it was made sure that the calibrator was disconnected from the power lines once the 2-D calibration was done. A measurement was conducted only when the voltage fluctuations from both the hot-wire sensors, for zero flow velocity, remained within $\pm$ 10 mV. Since the electronic noise only alters the fluctuations of a voltage signal and not its mean, the mean statistics obtained during the 2-D calibration weren't influenced by the electronic noise.

3.3.4 2-D calibration

In order to use X-probes for turbulence measurements, a 2-D calibration is required to account for both the streamwise (u) and the lateral (v or w) velocity components. To this end, a custom made jet facility was used to perform in-situ 2-D calibration of the X-probe. This is achieved by varying the jet exit speeds U_{jet} and angles α and β corresponding to the rotation of the jet about the y and z axis, respectively. Figure 3.9 shows a schematic illustrating the orientation of the jet with respect to the X-probe sensor plane. The jet calibrator system has been designed to be compact and light, allowing it to be placed at the

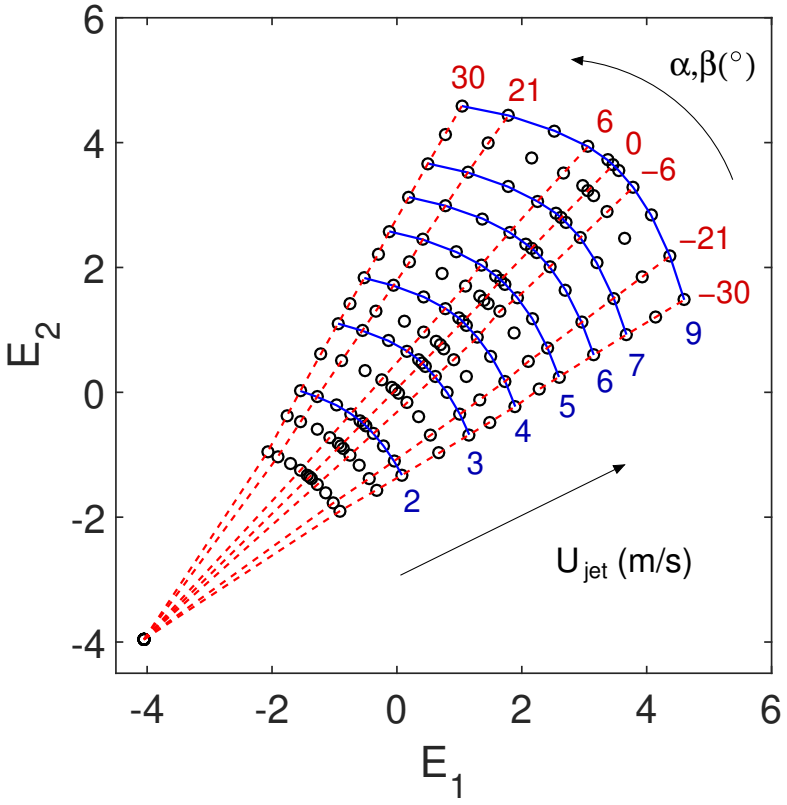

FIGURE 3.10: X-probe voltage pairs (E_1, E_2) acquired from a typical 2-D calibration. ◯ represents the mean voltage pair estimated from the calibration for various jet velocities (U_{jet}) and jet angles (α or β depending on the X-probe type) with respect to the freestream direction. (–) lines represents the constant jet velocity lines and (- -) represents the constant jet angle lines at which the 2-D calibration was conducted.

top of the channel working section, in the case of the channel flow measurements. Hence, in order to conduct a 2-D calibration, the X-probe was required to be vertically traversed approximately 0.45 m above the channel centreline. This vertical traversing was facilitated by the presence of an access plate above the measuring station in the working section. For the TBL measurements, on the other hand, the jet could be placed inside the HRNBLWT working section, directly in front of the traverse T_2 holding the sensor to conduct an 'in-situ' calibration. Complete details regarding the construction and characterization of the jet facility may be found in Baidya (2016).

The jet is powered by compressed air to achieve an exit velocity as high as 30 ms^{-1}. The pitch and yaw inclination of the jet, with respect to the probe, is restricted to the range -30° $< \beta <$ 30° and -30° $< \alpha <$ 30° due to physical restrictions. Since this study is focused on using only two wires in a hotwire probe, the rotation of the jet is restricted to within the sensor plane during the calibration. For example, for the *uv* X-probe, the

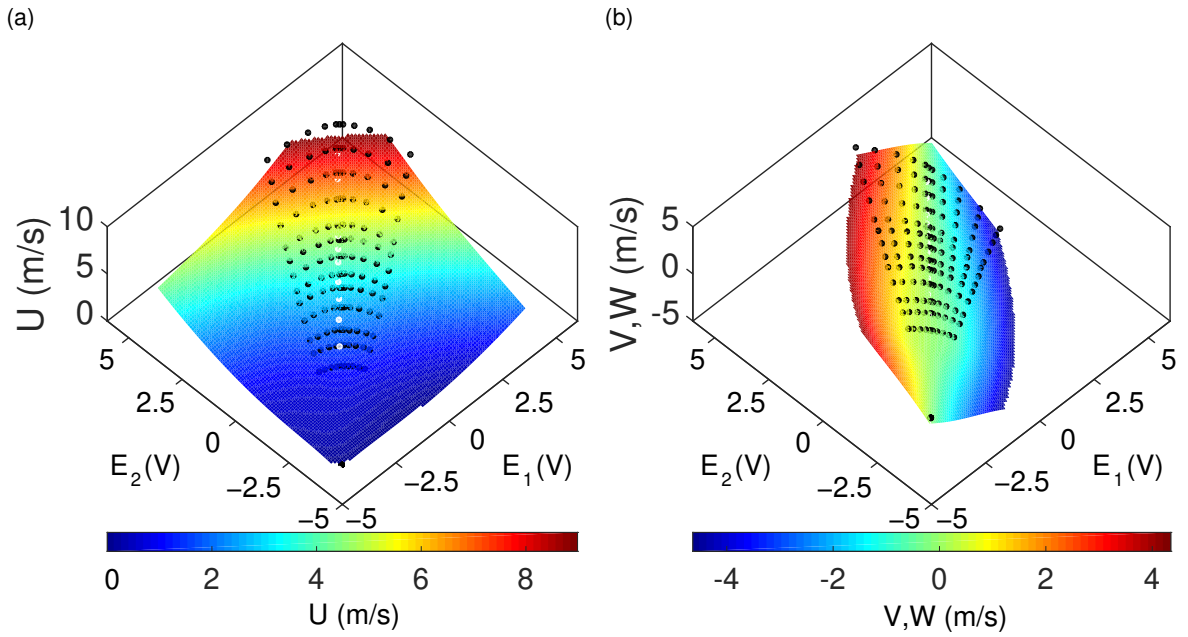

FIGURE 3.11: The velocity-voltage surface plot fitted from the 2-D calibration for the (a) streamwise (U) and (b) lateral velocity (V or W) component. Black dots indicate the 2-D calibration points while the white dots indicate the 1-D calibration points.

x–y plane is the sensor plane (figure 3.9) while the x–z plane is the sensor plane for the uw X-probe. Consequently, the jet is rotated about the z and y axis for the uv and uw X-probes, respectively.

To obtain a one-to-one mapping between the voltage and velocity pairs, the jet is rotated (about an axis) between its two extremes at various speeds, U_{jet}. Figure 3.10 shows the voltages recorded from the two wires at various jet velocities (U_{jet}) and jet angle (β) combinations during a typical 2-D calibration of a uv X-probe. The calibration was done at 11 different angles for 14 different jet velocities respectively. Amongst the 14 velocities, lower velocities were incremented by smaller intervals to account for relatively severe non-linearities in the velocity-voltage relationship at these speeds. Similarly, the increments in the angles were small close to β,$\alpha = 0$, which corresponds to the majority of the velocity vectors existing in the boundary layer. The effective angle method, discussed in §3.3.1.1, is used to find the velocity-voltage map for the streamwise (U) and the lateral velocity (V and W) component by essentially following the same methodology as that adopted previously by Baidya (2016). The final velocity-voltage maps, processed for the 2-D calibration shown in figure 3.10, are depicted as an example in figure 3.11. Such a map is used to convert the voltage time series, acquired during experiments from the two sensors, to the two-component velocity time series.

Chapter 4

Two-dimensional cross-spectrum of the streamwise velocity in turbulent boundary layers

[Published paper I[1]]

4.1 Preface to the chapter

This chapter is an article published in the *Journal of Fluid Mechanics*, titled "Two-dimensional cross-spectrum of the streamwise velocity in turbulent boundary layers" (Deshpande et al., 2020a). This study tests the notion of geometric self-similarity, along both the streamwise and spanwise directions, for the energetic wall-coherent motions of the streamwise velocity (u) coexisting in the log-region. This is achieved by reconstructing, for the first time, the 2-D cross-spectrum of u from the multi-point dataset acquired in the high-Re_τ TBL (§3.2). The spectrum is representative of the energy contributions from the wall-coherent motions coexisting in the inertial (log) region, and is tested for self-similarity arguments in accordance to the attached eddy model of Perry and Chong (1982) and Perry et al. (1986).

Readers should take note that the terminology '*wall-attached/wall-detached structures*', used in the original published manuscript, has been replaced by '*wall-coherent/wall-incoherent*

[1]Deshpande, R., Chandran, D., Monty, J.P. & Marusic, I. (2020). Two-dimensional cross-spectrum of the streamwise velocity in turbulent boundary layers. *Journal of Fluid Mechanics* 890, R2. DOI: https://doi.org/10.1017/jfm.2020.139

structures' across this entire chapter to maintain a consistent terminology across the thesis, and also to avoid indication of any one-to-one linkage with Townsend's definition of 'attached' eddies. The 2-D cross-spectrum of the i-velocity component (where $i = u$, v or w), reconstructed using the i-component measured at wall-normal locations z_o and z_r, has been referred as $\Phi_{ii}^{cross}(z_o^+,z_r^+)$ across this thesis. However, since this particular chapter is focused on the wall-coherent motions, which would only show up in case of $\Phi_{ii}^{cross}(z_o^+,z_r^+ \lesssim 15)$, we refer them as $\Phi_{ii}^{cross,w}$ for convenience in discussion, and to differentiate it from $\Phi_{ii}^{cross}(z_o^+,z_r^+ > 15)$. In the remainder of the thesis (especially chapters 7 and 8), all 2-D cross-spectra are simply referred as $\Phi_{ii}^{cross}(z_o^+,z_r^+)$.

4.2 Abstract

In this chapter, we present two-dimensional (2-D) energy cross-spectrum of the streamwise velocity (u) component and use it to test the notion of self-similarity in turbulent boundary layers. Primary focus is on the cross-spectrum ($\Phi_{uu}^{cross,w}$) measured across the logarithmic (z_o) and near-wall (z_r) wall-normal locations, providing the energy distribution across the range of streamwise (λ_x) and spanwise (λ_y) wavelengths (or length scales) that are coherent across the wall-normal distance. $\Phi_{uu}^{cross,w}$ may thus be interpreted as a *wall*-filtered subset of the full 2-D u-spectrum (Φ_{uu}), the latter providing information on all co-existing eddies at z_o. To this end, datasets comprising synchronized two-point u-signals at z_o and z_r, across the friction Reynolds number range $Re_\tau \sim \mathcal{O}(10^3)$ - $\mathcal{O}(10^4)$, are analyzed. The published direct numerical simulation (DNS) dataset of Sillero et al. (2014) is considered for low-Re_τ analysis, while the high-Re_τ dataset is obtained by conducting synchronous multi-point hot-wire measurements. High-Re_τ cross-spectra reveals that the wall-coherent large scales follow a $\lambda_y/z_o \sim \lambda_x/z_o$ relationship more closely than seen for Φ_{uu}, where this self-similar trend is obscured by co-existing scales. The present analysis reaffirms that a self-similar structure, conforming to Townsend's attached eddy hypothesis, is ingrained in the flow.

4.3 Introduction and motivation

Modelling turbulent boundary layers (TBL) has been an increasingly active area of research, leading to proposals of various reduced-order as well as conceptual models. Amongst the latter, the attached eddy model that has evolved from the attached eddy hypothesis

(AEH) of Townsend (1976) is well-known and provides a kinematic description of the logarithmic (log) region of wall-turbulence. It assumes the TBL as an assemblage of randomly distributed geometrically self-similar attached eddies or structures, with their population density inversely proportional to their size (see Marusic and Monty (2019) for a comprehensive review). Throughout this article, the words 'structures', 'eddies' and 'motions' are used interchangeably and essentially refer to the definition of a *coherent eddy* given by Robinson (1991). Coherent eddies can be *self-similar* or *non-self-similar* (Perry et al., 1986; Perry and Marusic, 1995). A self-similar eddy refers to a flow structure whose geometric lengths and velocity field scale with distance from the wall (z) and friction velocity (U_τ), respectively. A non-self-similar eddy, on the other hand, does not exhibit these characteristics.

Based on the attached eddy model, Perry et al. (1986) showed using spectral-overlap arguments that self-similarity leads to a k_x^{-1} scaling in the premultiplied one-dimensional (1-D) u-spectra. Here, k_x is the streamwise wavenumber and u, v and w would refer to the streamwise, spanwise and wall-normal velocity fluctuations respectively, associated with the coordinate system x, y and z. The true k_x^{-1} scaling for the u-spectra, representative of the contributions from purely self-similar eddies, however has been obscured in the previously reported experiments and simulations due to various reasons, namely: (i) spectral aliasing (Davidson et al., 2006; Chandran et al., 2017) and (ii) overlapping contributions from various eddy types at finite Re_τ (Perry et al., 1986; Perry and Marusic, 1995; Baars and Marusic, 2020a). The present study tests the notion of self-similarity by bypassing both the aforementioned scenarios through a methodology discussed ahead.

The 1-D spectra represents the average energy contribution over the entire range of k_y, for a particular k_x, making it susceptible to spectral aliasing (Tennekes and Lumley, 1972). In that respect, a better alternative to the 1-D u-spectra is the direct measurement of the 2-D u-spectra as a function of both k_x ($=2\pi/\lambda_x$) and k_y ($=2\pi/\lambda_y$). The 2-D spectra, however, is difficult to measure experimentally at high Re_τ. Chandran et al. (2017) were able to measure 2-D u-spectra at $2\,400 \lesssim Re_\tau \lesssim 26\,000$, in the log-region of a zero pressure gradient (ZPG) TBL, by first reconstructing the 2-D two-point correlation:

$$\begin{aligned} R_{u_o u_r}(\Delta x, \Delta y; z_o, z_r) &= \overline{u(x, y, z_r) u(x + \Delta x, y + \Delta y, z_o)}, \\ \text{with } \widetilde{\mathcal{R}}_{u_o u_r} &= R_{u_o u_r} / (\sqrt{u^2(z_o)}\, \sqrt{u^2(z_r)}). \end{aligned} \tag{4.1}$$

Subsequently, the 2-D spectrum was computed by taking the 2-D Fourier transformation of $R_{u_o u_r}$ as:

$$\phi_{u_o u_r}(k_x, k_y; z_o, z_r) = \int\int_{-\infty}^{\infty} R_{u_o u_r}(\Delta x, \Delta y; z_o, z_r) e^{-j2\pi(k_x \Delta x + k_y \Delta y)} d(\Delta x) d(\Delta y), \quad (4.2)$$

where j is a unit imaginary number and overbar denotes ensemble time average. Throughout this article, the 2-D spectrum refers to the modulus of the premultiplied form of $\phi_{u_o u_r}$ normalized by the friction velocity, i.e. $\mid k_x^+ k_y^+ \phi_{u_o u_r}/U_\tau^2 \mid$. For convenience, 2-D spectrum for $z_r = z_o$ will be referred to as Φ_{uu}, while that for $z_r \neq z_o$ will be referred to as Φ_{uu}^{cross}. In agreement with del Álamo et al. (2004), at $Re_\tau \approx 2\ 400$, Chandran et al. (2017) observed the constant energy region of Φ_{uu} to be nominally bounded by power laws $\lambda_y/z_o \sim (\lambda_x/z_o)^{1/2}$ in the large scale range: λ_x/z_o,$\lambda_y/z_o > 10$. Here, the wavelengths λ_x and λ_y were interpreted as the surrogate length and width of the energetic eddies in the TBL. Therefore, the observation of a square-root relationship suggested a failure of self-similarity at low Re_τ since it indicates that the eddies do not grow wider (with z) at the same rate as they grow longer. At $Re_\tau \approx 26\ 000$, however, they found that the large scales deviate away from the square-root relationship *towards* a linear behaviour ($\lambda_y/z_o \sim \lambda_x/z_o$), which is representative of the self-similarity. The large-scale range where this change occurs was referred to as the *large-eddy region*, existing in the nominal range $\lambda_x > 10z_o$ and $\lambda_x < 7\delta$ (Chandran et al., 2017; Chandran, 2019).

Chandran et al. (2017) conjectured that clear evidence of self-similarity would be observed only for a TBL at $Re_\tau \gtrsim 60\ 000$, due to $\Phi_{uu}(z_o)$ comprising energy contributions from various eddy-types coexisting at z_o, which obey different scalings (Baars and Marusic, 2020a). These contributions overlap with one another at relatively lower Re_τ ($\lesssim 60\ 000$), due to the limited scale separation, obscuring any $\lambda_y/z_o \sim \lambda_x/z_o$ relationship that may be present. The issue relates to the second reason ((ii) mentioned above) responsible for obscuring self-similar trends in previous studies and we attempt to resolve it here by 'filtering' out the energy contribution from the non-self-similar structures to bring out the self-similarity unequivocally. Here, the term 'filter' is used to refer, in general, the methodology adopted to extract flow statistics at z_o contributed by structures coherent across a specified wall-normal range, say z_r-z_o. Different studies have adopted different approaches to 'filter' out these non-self-similar contributions, with some making use of the *wall*-filter. Here, the prefix 'wall' before 'filter' refers to the methodology utilized for extracting flow features (at z_o) contributed by eddies extending all the way down to the wall ($z_r \to 0$). These are referred to as the *wall-coherent* structures in the present manuscript.

Similarly, structures which physically do not extend to the wall will be referred as *wall-incoherent structures*.

Two recent studies, utilizing the *wall*-filter, have shown promising results with respect to removing the non-self-similar contributions. The first is by Hwang and Sung (2018), who following the works of del Álamo et al. (2006) and Lozano-Durán et al. (2012), implemented a *wall*-filter in their instantaneous ZPG TBL DNS fields at $Re_\tau \approx 1\,000$ to extract only those energetic motions which were physically attached to the wall. Analysis of these filtered fields revealed a linear relationship between the streamwise and spanwise length scales for the large wall-coherent structures. This evidence led them to conclude that the extracted structures were principal candidates for Townsend's AEH. The structures from the $Re_\tau \approx 1\,000$ DNS, however, are likely not statistically dominant in the log-region due to an insufficient scale separation (Hwang and Sung, 2018), encouraging a similar analysis at higher Re_τ. The second study, by Baars et al. (2017), involved computing the 1-D linear coherence spectrum from synchronized two-point u-signals acquired at a near-wall and log-region reference location. They identified the characteristic lengths of the energetic wall-coherent structures to be scaling self-similarly with z_o, as $\lambda_x/z_o \approx 14$. The analysis, which spanned datasets across three decades of Re_τ, led to the conclusion that a "self-similar attached eddy structure is ingrained within the TBL flow". Agostini and Leschziner (2017) made similar observations for structures in the mesolayer. The present study may be viewed as a first step towards the extension of the work by Baars et al. (2017) to 2-D. Here, we study the 2-D cross-spectrum, $\Phi_{uu}^{cross,w}$ (i.e. $z_r \neq z_o$; superscript 'w' used when $z_r^+ \lesssim 15$) by considering z_r in the near-wall region and z_o in the log-region. Therefore, $\Phi_{uu}^{cross,w}(z_o,z_r)$ shows the 2-D distribution of energy contributed purely by the wall-coherent eddies that extend up to z_o and beyond (with $z_o \gg z_r$) and is investigated here to test the notion of self-similarity. Throughout the article, superscript '+' indicates normalization by viscous length (ν/U_τ) and velocity (U_τ) scales.

4.4 Experimental and numerical data

Two TBL datasets across a decade of Re_τ are considered for analysis in the present study (table 4.1). The high-Re_τ dataset ($\mathcal{E}_1$) includes 2-D u-spectra (Φ_{uu}) and first measurements of 2-D u-cross-spectra ($\Phi_{uu}^{cross,w}$) at $Re_\tau \approx 15\,000$. This dataset was obtained via synchronized multi-point hot-wire measurements in the large Melbourne wind tunnel (HRNBLWT) and the details of these experiments are provided in table 4.1. Here, l, U_∞ and T denote the hot-wire sensor length, free-stream velocity and total sampling duration, respectively.

	ZPG TBL dataset acquired at HRNBLWT, $Re_\tau \approx 15\,000$ ($\mathcal{E}_1$):							
Set-up	z_o^+	z_r^+	$U_\infty(ms^{-1})\delta\ (m)$	TU_∞/δ		l^+	$(\Delta y_1)_{min}$	$(\Delta y_4)_{max}$
Φ_{uu}	**318**	**318**	20	0.36	19500	22	0.01δ	2.7δ
Φ_{uu}	477	477	20	0.36	19500	22	0.01δ	2.7δ
Φ_{uu}	750	750	20	0.36	19500	22	0.01δ	2.7δ
Φ_{uu}	1025	1025	20	0.36	19500	22	0.01δ	2.7δ
Φ_{uu}	2250*	2250*	20	0.36	19500	22	0.01δ	2.7δ
$\Phi_{uu}^{cross,w}$	**318**	15	20	0.36	19500	22	0	2.5δ
$\Phi_{uu}^{cross,w}$	477	15	20	0.36	19500	22	0	2.5δ
$\Phi_{uu}^{cross,w}$	750	15	20	0.36	19500	22	0	2.5δ
$\Phi_{uu}^{cross,w}$	1025	15	20	0.36	19500	22	0	2.5δ
$\Phi_{uu}^{cross,w}$	2250*	15	20	0.36	19500	22	0	2.5δ
	ZPG TBL DNS (Sillero et al., 2014), $Re_\tau \approx 2\,000$ ($\mathcal{S}_1$):							
	z_o^+	z_r^+	x_{start}	x_{end}	$(\Delta x)_{max}$	$(\Delta x^+)_{min}$	$(\Delta y^+)_{min}$	$(\Delta y)_{max}$
Φ_{uu}	**120**	**120**	28.4δ	40.3δ	11.9δ	6.5	3.7	7.6δ
Φ_{uu}^{cross}	**120**	15 - 77	28.4δ	40.3δ	11.9δ	6.5	3.7	7.6δ

TABLE 4.1: A summary of the various datasets containing synchronized multi-point u-signals at z_r and z_o for various spanwise offsets, Δy. Terminology has been described in §4.4. Values highlighted in bold indicate the approximate z^+-location for the beginning of the log-region, $2.6\sqrt{Re_\tau}$ (Klewicki et al., 2009), underlined represent $z^+ \approx 3.9\sqrt{Re_\tau}$ and the ones with superscript (*) represent the upper limit of the log-region, $z^+ \approx 0.15\delta^+$ (Marusic et al., 2013).

Boundary layer thickness, δ, and the friction velocity, U_τ, are estimated via the composite fit proposed by Chauhan et al. (2009). 2.5μm diameter Wollaston hot-wire probes were used for all measurements, which were operated using an in-house Melbourne University Constant Temperature Anemometer at a rate of $\Delta T^+ \equiv U_\tau^2/(\nu f_s) \approx 0.5$, where f_s refers to sampling frequency.

First, two-point measurements with $z_r^+ \approx z_o^+$ were conducted with the aim to obtain Φ_{uu} at five wall-normal locations in the log-region, by employing the same experimental set-up and methodology of Chandran et al. (2017). Figure 4.1(a)(i) shows the schematic of the experimental set-up used to reconstruct the corresponding $R_{u_o u_r}$, with four hot-wire probes (HW_{1-4}) located at z_o. Following the calibration procedure adopted by Chandran et al.

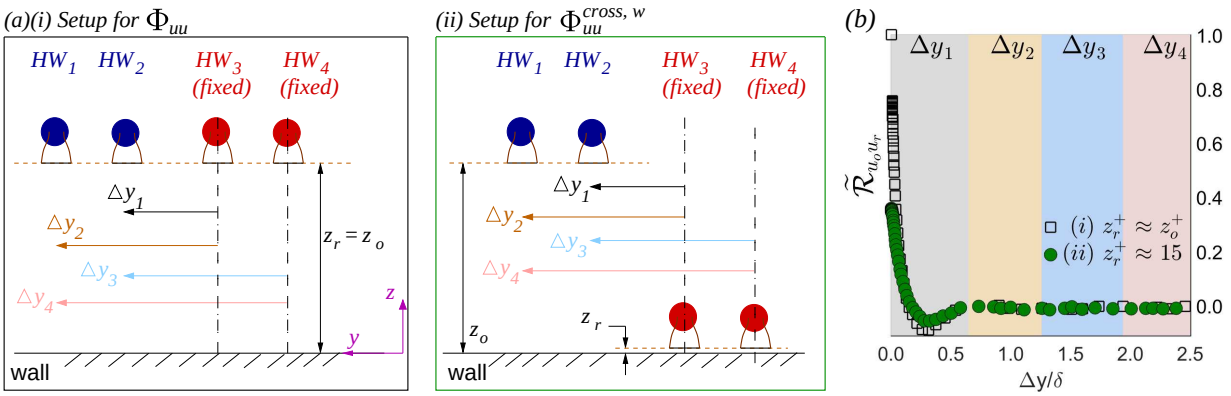

FIGURE 4.1: (a) Schematic of the experimental set-up in HRNBLWT showing relative positioning and movement of the four hot-wire probes (HW_1-HW_4) for reconstructing the 2-D correlation corresponding to (i) Φ_{uu} and (ii) $\Phi_{uu}^{cross,w}$. Mean flow direction is along x. (b) Correlation coefficients ($\widetilde{\mathcal{R}}_{u_o u_r}$) as a function of spanwise separation $\Delta y/\delta$, computed for $z_o^+ \approx 2.6\sqrt{Re_\tau}$ and $\Delta x = 0$.

(2017), HW_1, HW_2 and HW_4 were calibrated at z_o by using the free-stream calibrated HW_3 as reference. During experiments, HW_3 and HW_4 remained stationary at a fixed spanwise location while HW_1 and HW_2 were traversed together in the spanwise direction with logarithmic spacing. u-velocity time series acquired from a pair of hot-wires is cross-correlated to obtain the correlation coefficient ($\widetilde{\mathcal{R}}_{u_o u_r}$; equation 4.1) as a function of the spanwise spacing Δy (figure 4.1(b)). At the start of the measurement, HW_2 and HW_3 were kept as close as practicably possible, at $(\Delta y_1)_{min} \approx 0.01\delta$. Thereafter, every step movement of the traverse gives $\widetilde{\mathcal{R}}_{u_o u_r}$ at four distinct spanwise spacings: Δy_1 (HW_2-HW_3), Δy_2 (HW_1-HW_3), Δy_3 (HW_2-HW_4) and Δy_4 (HW_1-HW_4). Figure 4.1(b) highlights the Δy range covered by each of these hot-wire pairs with different background colors. The experiment continues up to $(\Delta y_4)_{max} \approx 2.7\delta$, enabling computation of $\widetilde{\mathcal{R}}_{u_o u_r}$ for $\Delta y = 0$ and $(\Delta y_1)_{min} \leq \Delta y \leq (\Delta y_4)_{max}$. Taylor's hypothesis, with the mean streamwise velocity at z_o considered as the convection velocity, is employed to construct $\widetilde{\mathcal{R}}_{u_o u_r}$ at different streamwise spacings (Δx) for the temporal data set, $\mathcal{E}_1$. $\Phi_{uu}(z_o)$ is finally obtained from $R_{u_o u_r}$ via equation 4.2. It should be noted that $(\Delta y_1)_{min}$ is limited to 0.01δ for the setup in figure 4.1(a)(i), which leads to energy redistribution in Φ_{uu} at small spanwise scales (Chandran et al., 2017). To account for this, the DNS-based correction scheme proposed by Chandran et al. (2016) has been implemented to correct Φ_{uu} using 2-D $\widetilde{\mathcal{R}}_{u_o u_r}$ obtained from the dataset of Sillero et al. (2014).

To obtain $R_{u_o u_r}$ corresponding to $\Phi_{uu}^{cross,w}$, HW_3 and HW_4 were fixed at $z_r^+ \approx 15$ while HW_1 and HW_2 were positioned at the same z_o^+ (figure 4.1(a)(ii)) as in the measurements for Φ_{uu}. Since the wall-coherence analysis remains largely unaffected for $0 \leq z_r^+ \lesssim 15$

(Baars et al., 2017), the positioning of the wall-reference probe at $z_r^+ \approx 15$ was considered appropriate. Except for the difference in the wall-normal locations of HW_3 and HW_4, the measurement technique to compute $R_{u_o u_r}$ is similar to the previous case. However, for this set-up, $(\Delta y_1)_{min}$ was reduced to zero by vertically aligning HW_2 above HW_3. The 1-D linear coherence spectrum (Baars et al., 2017) computed from the u-signals acquired by these two probes, at $\Delta y_1 \approx 0$, agreed with its empirical fit proposed by Baars et al. (2017), confirming the vertical alignment. Hence, as opposed to Φ_{uu}, no small-scale correction was required for $\Phi_{uu}^{cross,w}$. A part of this data set has also been used recently by Deshpande et al. (2019a), wherein the sensitivity of the 1-D linear coherence spectrum to Δy has been showcased.

The low-Re_τ dataset ($\mathcal{S}_1$) considered in the present study is that of Sillero et al. (2014). Thirteen raw DNS time blocks are considered, each of which is a subset of the full computational domain between x_{start} and x_{end} (see table 4.1) to ensure a limited Re_τ increase along x. Table 4.1 gives more details regarding the spatial resolution and size of the flow fields considered. In the case of $\mathcal{S}_1$, Φ_{uu} and $\Phi_{uu}^{cross,w}$ are computed with $z_o^+ \approx 2.6\sqrt{Re_\tau}$ in order to correspond with $\mathcal{E}_1$. Since we get access to synchronous $u(x,y)$ data at various z in the case of DNS, we also selected several z_r^+ in the range $15 < z_r^+ < z_o^+$ to study the variation in $R_{u_o u_r}$ and the corresponding Φ_{uu}^{cross}.

4.5 Results and discussions

4.5.1 Physical interpretation of $\Phi_{uu}^{cross,w}$ and how it differs from Φ_{uu}

While $\Phi_{uu}(z_o)$ gives the energy distribution of all co-existing eddies at z_o, $\Phi_{uu}^{cross,w}(z_o,z_r)$ indicates the energy contributed by only those eddies at z_o that have coherence at the wall, i.e. are 'wall-coherent'. We attempt to explain this difference by first investigating the cross-correlations, $\widetilde{\mathcal{R}}_{u_o u_r}$. Figure 4.2(a) shows the positive and negative isosurfaces of $\widetilde{\mathcal{R}}_{u_o u_r}$ considered from a correlation volume, $\widetilde{\mathcal{R}}_{u_o u_r}(\Delta x,\Delta y,z_r;z_o)$ obtained for $z_o^+ \approx 2.6\sqrt{Re_\tau}$ and $15 \lesssim z_r^+ < 150$ for dataset $\mathcal{S}_1$. The plot is essentially similar in concept to figure 1 of Sillero et al. (2014). Considering a wall-parallel plane at $z_r = z_o$ in this correlation volume gives a 2-D $\widetilde{\mathcal{R}}_{u_o u_r}$ map which is analogous to the experimental 2-D correlation obtained via the probe arrangement shown in figure 4.1(a)(i) and plotted at $z_r^+ \approx 2.6\sqrt{Re_\tau}$ in figure 4.2(b). Now, by considering a wall-parallel plane at $z_r^+ \approx 15$ in figure

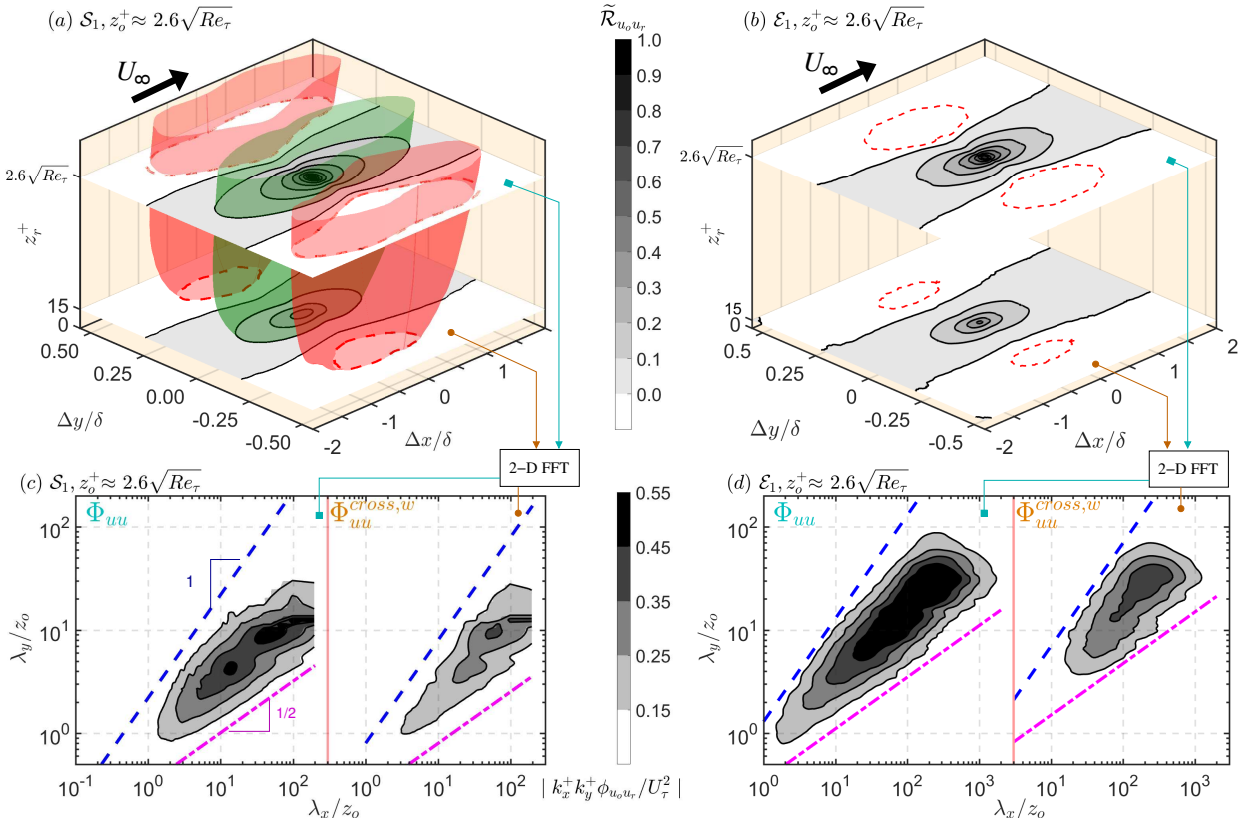

FIGURE 4.2: (a) 3-D representation of $\widetilde{\mathcal{R}}_{u_o u_r}$ for dataset $\mathcal{S}_1$ with $z_o^+ \approx 2.6\sqrt{Re_\tau}$ (=120) as a reference and $15 \lesssim z_r^+ < 150$ to plot isosurfaces for $\widetilde{\mathcal{R}}_{u_o u_r} = 0.1$ (green) and -0.04 (red). Wall-parallel planes at $z_r^+ \approx 2.6\sqrt{Re_\tau}$ and 15 have positive $\widetilde{\mathcal{R}}_{u_o u_r}$ contours as solid lines at levels 0.0:0.1:1.0 and a dashed red contour for -0.04. (b) Experimentally ($\mathcal{E}_1$) reconstructed $\widetilde{\mathcal{R}}_{u_o u_r}$ at equivalent z_o^+ and z_r^+ as in (a) and the same contour levels. (c,d) Φ_{uu} and $\Phi_{uu}^{cross,w}$ for datasets (c) $\mathcal{S}_1$ and (d) $\mathcal{E}_1$ obtained on computing 2-D FFT of corresponding 2-D $\widetilde{\mathcal{R}}_{u_o u_r}$ plotted in (a) and (b). Contours in (c) and (d) represent energy levels 0.15:0.10:0.55. Dot-dashed magenta and dashed blue lines represent the square-root and linear relationship, respectively.

4.2(a), we get a 2-D map of u-correlation between the log ($z_o^+ \approx 2.6\sqrt{Re_\tau}$) and the near-wall ($z_r^+ \approx 15$) region. An experimental analogue of such a correlation is reconstructed with the probe arrangement shown in figure 4.1(a)(ii) and is plotted in figure 4.2(b) at $z_r^+ \approx 15$. A qualitative comparison between the respective $\widetilde{\mathcal{R}}_{u_o u_r}$ maps from the two data sets shows good consistency: (i) The length and width of a particular $\widetilde{\mathcal{R}}_{u_o u_r}$ contour level reduces as z_r^+ is varied from z_o^+ towards the wall. This is consistent with the observations of del Álamo et al. (2004), who attributed this decrease to the absence of the contributions from wall-incoherent eddies as $z_r^+ \to 0$. (ii) The positive u correlations at the spanwise centre ($\Delta y = 0$) are flanked by the negative correlations on either side, which extend all the way from the log-region to the wall. This is representative of the adjacent wall-coherent low- and high-momentum zones responsible for the streaky pattern in the TBL (Hutchins

and Marusic, 2007; Hwang and Sung, 2018).

A 2-D Fourier transform of the respective wall-parallel $\widetilde{\mathcal{R}}_{u_o u_r}$ planes in figures 4.2(a,b), following equation 4.2, gives the corresponding 2-D spectral energy distribution plotted in figures 4.2(c,d). In each of these plots, Φ_{uu} and $\Phi_{uu}^{cross,w}$ as a function of the wavelengths scaled with z_o are plotted on the left and right panels, respectively. The energy distribution in $\Phi_{uu}^{cross,w}$ is restricted to the large λ_x and λ_y with negligible energy in the small scales: $\lambda_x \lesssim 14z_o$, $\lambda_y \lesssim 2z_o$, which is unlike the scenario observed for Φ_{uu}. This can be explained by $z_o^+ \gg z_r^+$, meaning that only physically large wall-coherent eddies would appear in $\Phi_{uu}^{cross,w}(z_o)$. In the forthcoming sub-section, we compare $\Phi_{uu}(z_o)$ and $\Phi_{uu}^{cross}(z_o,z_r)$ obtained from the two datasets.

4.5.2 Low versus high Re_τ 2-D spectra

Figure 4.3(a) shows the energy spectra for $z_o^+ \approx 2.6\sqrt{Re_\tau}$ and various z_r^+ at a constant energy level of 0.2 for the low-Re_τ dataset ($\mathcal{S}_1$). Also shown are dot-dashed magenta and dashed blue lines which represent the square-root and linear relationship, respectively. As discussed by del Álamo et al. (2004) and Chandran et al. (2017), constant energy contours of Φ_{uu} follow a linear relationship ($\lambda_y \sim \lambda_x$) only in the small-scale region: λ_x/z_o,$\lambda_y/z_o < 10$. It changes to a square-root relationship ($\lambda_y \sim {\lambda_x}^{1/2}$) at larger scales, suggesting a failure of self-similarity at low Re_τ. On the other hand, if we consider the cross-spectra, the constant energy contours in the same large scale range depart from the square-root *towards* a linear behaviour as z_r approaches the wall (i.e. for $\Phi_{uu}^{cross,w}$). This suggests that the energetic wall-coherent eddies are predominantly self-similar. Further, this self-similar trend is obscured in Φ_{uu} by energy contributions from the wall-incoherent eddies. It is obvious, however, that a larger scale-separation (i.e. higher Re_τ) would better highlight the changing trend with z_r.

Figure 4.3(b) shows constant energy contours (~ 0.2) of Φ_{uu} and $\Phi_{uu}^{cross,w}$ from the high-Re_τ dataset, $\mathcal{E}_1$ with the range of scales increased by almost a decade. Consistent with the observations made by Chandran et al. (2017), for the 2-D spectrum Φ_{uu}, the square-root relationship for the intermediate range of scales deviates towards a relatively higher power law at $\lambda_x \sim 100z_o$ and $\lambda_y \sim 15z_o$, with the large scales having an average aspect ratio of $\lambda_x/\lambda_y \approx 7$ (indicated by a dark yellow line). According to Chandran et al. (2017), this ratio is significant since the large-scale energetic structures in a ZPG TBL become self-similar only after evolving into such large aspect ratios. As opposed to Φ_{uu}, the energetic ridge of $\Phi_{uu}^{cross,w}$ is seen to follow $\lambda_x/\lambda_y = 7$ along its entire stretch with negligible

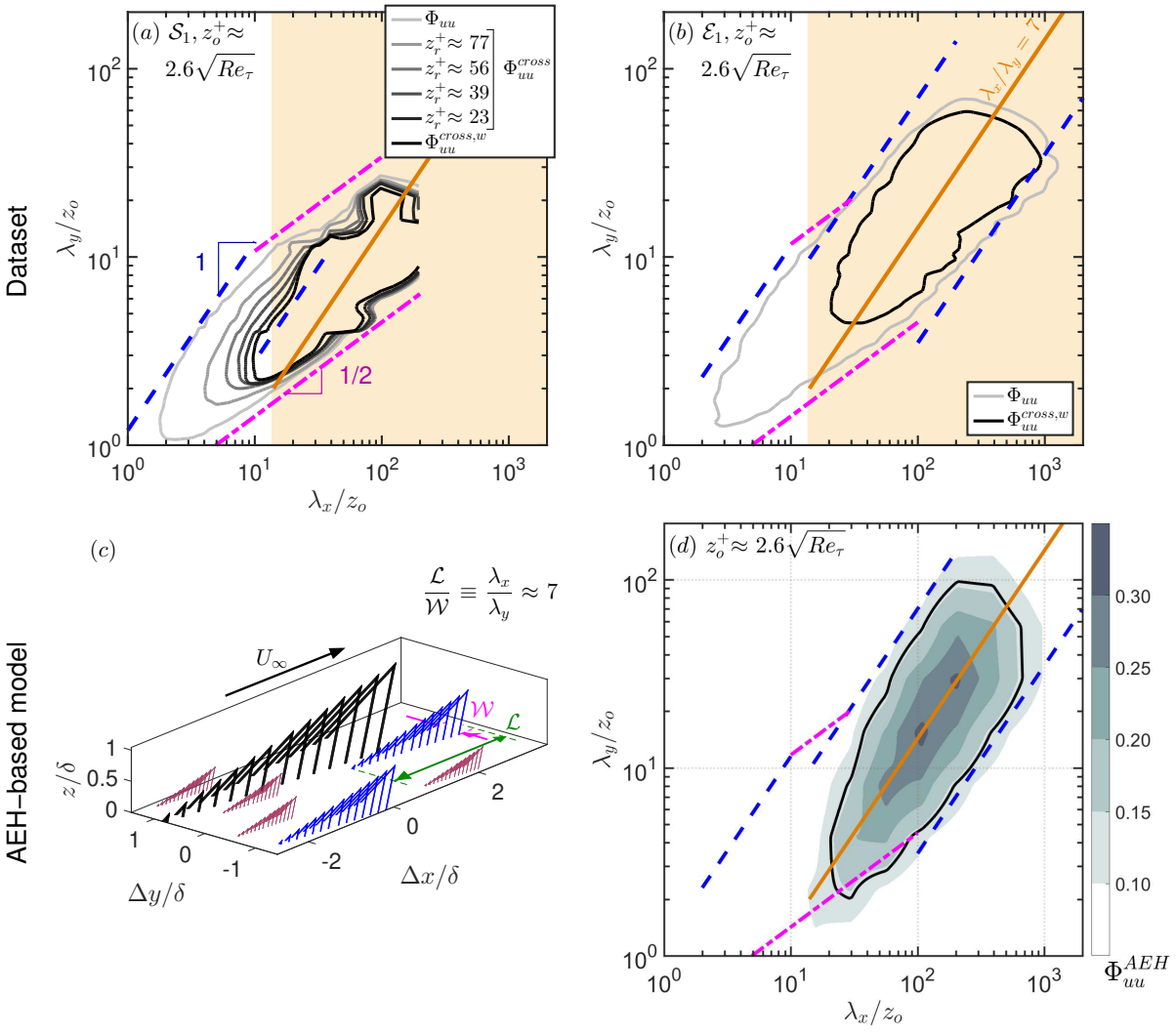

FIGURE 4.3: (a,b) 2-D energy spectra for $z_o^+ \approx 2.6\sqrt{Re_\tau}$ and various z_r^+ at constant energy level of 0.2 for datasets (a) $\mathcal{S}_1$ and (b) $\mathcal{E}_1$. Light yellow background indicates $\lambda_x/z_o > 14$. (c) Schematic of the AEH-based model considered, shown here having three distinct hierarchies of self-similar wall-coherent eddies with the largest eddy (in black) of the order of δ. $\mathcal{L}$ and $\mathcal{W}$ denote the length and width of an eddy hierarchy, respectively. (d) 2-D spectrum obtained from the AEH-based model for $Re_\tau \approx 15\,000$ and $z_o^+ \approx 2.6\sqrt{Re_\tau}$. Solid black contour is qualitatively equivalent ($\sim 0.5(\Phi_{uu}^{AEH})_{max}$) to the one in (b). In (a,b,d), dot-dashed magenta, dashed blue and solid yellow lines denote $\lambda_y/z_o \sim (\lambda_x/z_o)^{1/2}$, $\lambda_y/z_o \sim \lambda_x/z_o$ and $\lambda_x/\lambda_y = 7$ relationships, respectively.

energy distribution in the scale range where Φ_{uu} contours vary as $\lambda_y/z_o \sim (\lambda_x/z_o)^{1/2}$. The high-$Re_\tau$ $\Phi_{uu}^{cross,w}$ hence provides convincing evidence of the self-similarity of wall-coherent eddies. The fact that the energetic structures contributing to $\Phi_{uu}^{cross,w}$ are restricted to $\lambda_x > 14z_o$ (highlighted by yellow background), which is consistent with the streamwise inner-scaling limit of self-similar wall-coherent structures (Baars et al., 2017), further adds credence to our claim. Given that $\Phi_{uu}^{cross,w}$ contours follow $\lambda_x/\lambda_y \approx 7$ and $\lambda_x > 14z_o$, present analysis suggests $\lambda_y > 2z_o$ as the plausible spanwise inner-scaling limit for the wall-coherent self-similar eddies.

The experimentally obtained $\Phi_{uu}^{cross,w}$ is qualitatively similar to the 2-D energy spectrum (Φ_{uu}^{AEH}) computed from a flow field consisting purely of self-similar wall-coherent eddies, as shown in figure 4.3(d). Φ_{uu}^{AEH}, here, is obtained using an AEH-based model (Perry et al., 1986; Baidya et al., 2017; Chandran et al., 2017) where the log-region is statistically represented by continuous hierarchies of representative eddies whose geometric sizes scale with z_o and their probability density varies inversely with z_o. The idea is illustrated in figure 4.3(c) where, for clarity, the model is depicted in a discretized form with three distinct hierarchies. Heights of the smallest and largest eddies are taken as 100 viscous units and δ, respectively with each eddy inclined with respect to x at 45° (Deshpande et al., 2019a). The aspect ratio of the eddy hierarchy is roughly equivalent to the ratio of the large scales observed in the high-Re_τ results. Figure 4.3(d) plots the 2-D spectrum generated from this model at conditions similar to dataset $\mathcal{E}_1$: $Re_\tau \approx 15\,000$ and $z_o^+ = 2.6\sqrt{Re_\tau}$. It can be noted that the high Re_τ $\Phi_{uu}^{cross,w}$ contours show a good correspondence with Φ_{uu}^{AEH} contours, which follow the $\lambda_y/z_o \sim \lambda_x/z_o$ relation given the imposition of self-similarity.

We extend this qualitative comparison between $\Phi_{uu}^{cross,w}$ and Φ_{uu}^{AEH} to investigate their scaling in the context of spectral overlap arguments of Perry et al. (1986). According to their arguments, the energy contribution from self-similar eddies would follow both outer-flow scaling (δ-scaling) and inner-flow scaling (z_o-scaling) in the wavelength range corresponding to $\sim \mathcal{O}(\delta)$ and $\mathcal{O}(z_o)$, respectively. These scaling arguments are illustrated in figure 4.4 using $\Phi_{uu}^{cross,w}$ and Φ_{uu}^{AEH}, for all z_o^+ corresponding to $\mathcal{E}_1$ (table 4.1), wherein the wavelengths are scaled with δ (figure 4.4a) and z_o (figure 4.4b) respectively. $\Phi_{uu}(z_o)$ is also plotted at the same z_o^+ to demonstrate the effectiveness of the *wall*-filter. A noteworthy observation from figure 4.4 is that both Φ_{uu}^{AEH} and $\Phi_{uu}^{cross,w}$ contours exhibit the δ- and z_o-scalings in similar wavelength range. This is suggested by the overlapping constant energy contours for the respective spectra at various z_o^+. Further, these contours indicate energy distribution predominantly in the *large eddy region* (Chandran et al., 2017) where they closely follow the $\lambda_y/z_o \sim \lambda_x/z_o$ relationship. This supports the claim that

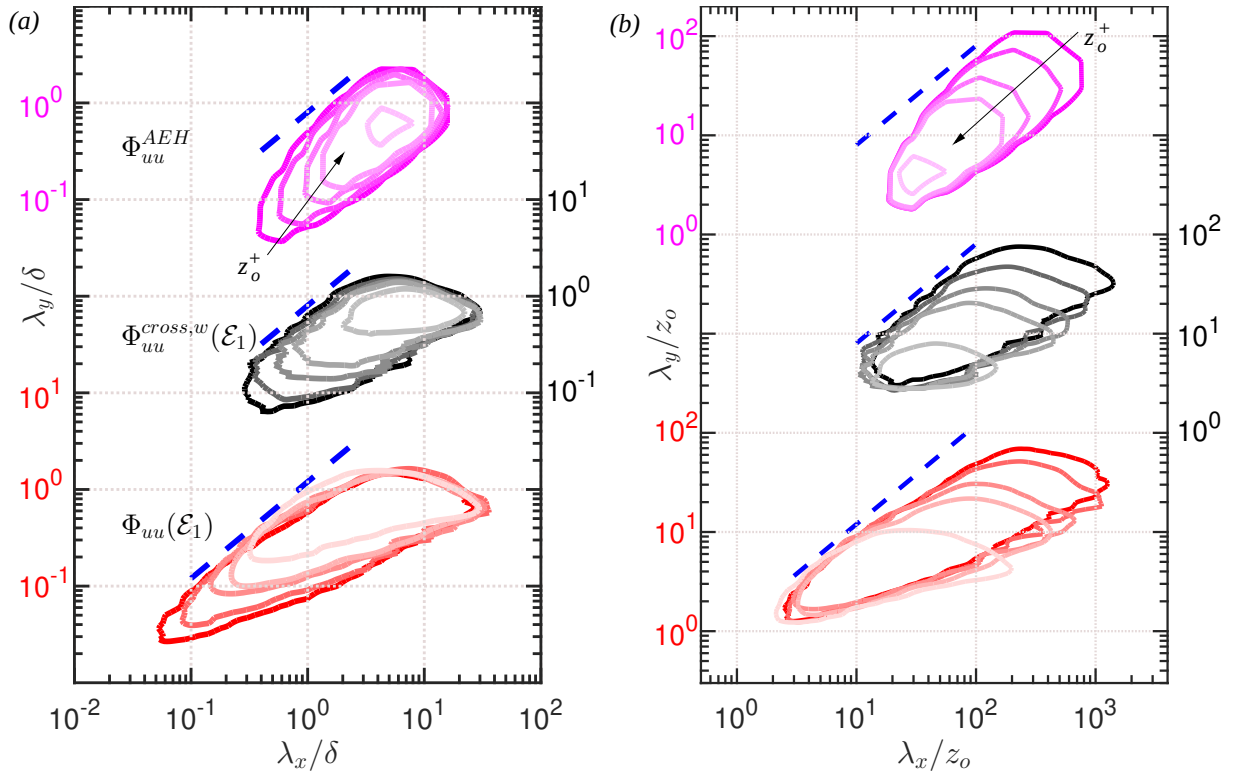

FIGURE 4.4: (a,b) Contours at a constant energy level of $0.35(\Phi_{uu}^{AEH})_{max}$, $0.35(\Phi_{uu}^{cross,w})_{max}$ (dataset $\mathcal{E}_1$) and $0.35(\Phi_{uu})_{max}$ (dataset $\mathcal{E}_1$) for z_o^+ across the log-region (table 4.1) plotted as a function of wavelengths scaled with (a) δ and (b) z_o. Dark to light shade indicates increase in z_o^+. For each of the respective spectrum, maximum value at $z_o^+ \approx 2.6\sqrt{Re_\tau}$ was considered as a reference to normalize the energy spectra at all z_o^+. Dashed blue lines represent the linear power law relationship for respective spectra.

$\Phi_{uu}^{cross,w}$ predominantly consists of contribution from the self-similar eddies that comply with Townsend's AEH. This contribution can be seen to decrease for both Φ_{uu}^{AEH} and $\Phi_{uu}^{cross,w}$ as distance from the wall increases, with energy at $z_o^+ \approx 0.15\delta^+$ (light shaded contours) effectively representing contribution only from the tall wall-coherent structures extending beyond the log-region. In case of Φ_{uu}, on the other hand, the z_o-scaling is also observed in the small scales which are predominantly wall-incoherent and hence do not show up in $\Phi_{uu}^{cross,w}$. While, the wavelength range exhibiting δ-scaling is similar to that observed for $\Phi_{uu}^{cross,w}$.

4.5.3 Is a wall-filter sufficient to extract purely self-similar structures?

Referring to the discussion in §4.3, on the studies by Baars et al. (2017) and Hwang and Sung (2018), $\Phi_{uu}^{cross,w}(z_o)$ may be interpreted as the *wall*-filtered subset of $\Phi_{uu}(z_o)$. Recent studies by Baars and Marusic (2020a) and Yoon et al. (2020) show that not all wall-coherent structures exhibit self-similarity and some of them may be geometrically non-self-similar. Given the qualitative resemblance between $\Phi_{uu}^{cross,w}$ and Φ_{uu}^{AEH} (§4.5.2), it is worth investigating here if the energy contributions isolated via the *wall*-filter correspond purely to self-similar structures, or also has contributions from the non-self-similar structures. To this end, we probe the energetic-ridges (Chandran et al., 2017) of Φ_{uu} and $\Phi_{uu}^{cross,w}$, as self-similarity requires the slope (m) of the ridge to be equal to one ($\lambda_y \sim \lambda_x$). Here, the energetic ridge of the spectrum is computed by identifying the spanwise wavelength, λ_y corresponding to the maximum value of the spectrum at each streamwise wavelength, λ_x. Additionally, Chandran et al. (2017) has shown that the slope of the ridge translates as the ratio of the plateaus in the 1-D streamwise u-spectra to that in the 1-D spanwise u-spectra. Here, the 1-D streamwise and spanwise spectra are obtained by integrating the 2-D spectrum along λ_y and λ_x, respectively.

Figure 4.5(a) shows the energetic ridges of Φ_{uu} and $\Phi_{uu}^{cross,w}$ for $z_o^+ \approx 2.6\sqrt{Re_\tau}$, while figure 4.5(b) shows the respective 1-D spectra. A'_{1x} and A'_{1y} denote the peaks in the 1-D streamwise and spanwise spectra respectively, while A^w_{1x} and A^w_{1y} refer to the peaks in the 1-D streamwise and spanwise cross-spectra, respectively. These peaks conform to the scale range where the 1-D spectra is expected to plateau at very high Re_τ (Chandran et al., 2017) and is hence used as a reference over here for analysis purposes. Direct computation of m, from the ratio of the 1-D spectra peaks, shows a difference from 0.7 (for Φ_{uu}) to 0.85 for $\Phi_{uu}^{cross,w}$, suggesting a relatively greater contribution from self-similar structures to $\Phi_{uu}^{cross,w}$. A change in slope is also evident from the comparison between the energetic-ridges of Φ_{uu} and $\Phi_{uu}^{cross,w}$. Figure 5(c) plots m, directly computed from $\frac{A'_{1x}}{A'_{1y}}$ and $\frac{A^w_{1x}}{A^w_{1y}}$ for Φ_{uu} and $\Phi_{uu}^{cross,w}$ respectively, at all z_o^+ corresponding to $\mathcal{E}_1$ (table 4.1). Here, $\frac{A'_{1x}}{A'_{1y}}$ can be seen decreasing with increase in z_o^+. This is consistent with the observations of Chandran et al. (2017), who linked this trend with the AEH prediction on the decrease in self-similar eddy population with distance from the wall (Townsend, 1976). Interestingly, $\frac{A^w_{1x}}{A^w_{1y}}$ on the other hand remains approximately constant (≈ 0.85) at all z_o^+. This suggests that the variation of $\frac{A'_{1x}}{A'_{1y}}$ with z_o^+ is most likely dictated by the contributions from the wall-incoherent eddies,

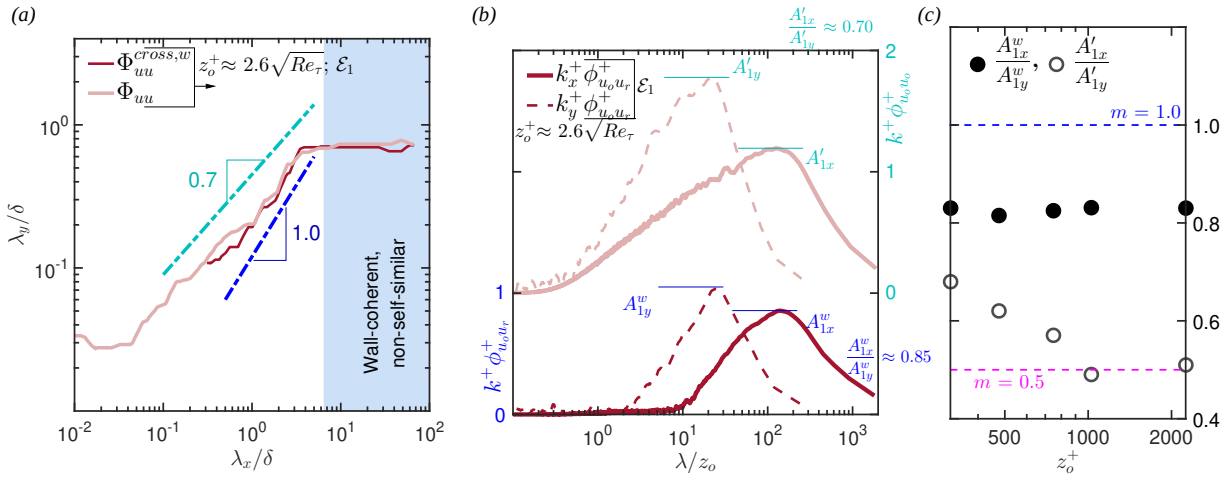

FIGURE 4.5: (a) Energetic ridges of Φ_{uu} (light shaded) and $\Phi_{uu}^{cross,w}$ (dark shaded) for $z_o^+ \approx 2.6\sqrt{Re_\tau}$ from dataset $\mathcal{E}_1$, plotted against δ-scaled wavelengths alongside power laws indicated by dot-dashed lines. (b) 1-D spanwise and streamwise (cross-)spectrum obtained on integrating corresponding Φ_{uu} ($\Phi_{uu}^{cross,w}$) for $z_o^+ \approx 2.6\sqrt{Re_\tau}$ from $\mathcal{E}_1$. Also highlighted are the peaks of the 1-D spectrum (A'_{1x}, A'_{1y}) and cross-spectrum (A^w_{1x}, A^w_{1y}). (c) $\frac{A'_{1x}}{A'_{1y}}$ and $\frac{A^w_{1x}}{A^w_{1y}}$ estimated at all z_o^+ corresponding to $\mathcal{E}_1$ (table 4.1) by following the methodology shown in (b).

which are predominantly small but can be either self-similar or non-self-similar (Marusic and Monty, 2019; Yoon et al., 2020).

The increment in m *towards* 1.0, when comparing Φ_{uu} and $\Phi_{uu}^{cross,w}$, confirms that the *wall*-filter does indeed filter out energy contributions from the non-self-similar structures which are wall-incoherent. However, the fact that $m \approx 0.85$ and not 1.0 suggests that $\Phi_{uu}^{cross,w}$ still consists of contributions from wall-coherent non-self-similar structures. This can be better understood on investigating the ridge for Φ_{uu} and $\Phi_{uu}^{cross,w}$ (figure 4.5(a)) in the scale range: $\lambda_x \gtrsim 7\delta$, $\lambda_y \sim \delta$, where it appears to plateau at a constant λ_y and grows only in λ_x for both the spectra. The energetic ridge in this scale range is representative of the energy contribution from the δ-scaled superstructures (Hutchins and Marusic, 2007; Chandran, 2019), which are known to have $(\lambda_x)_{max}$ up to 20δ but spanwise width restricted to $\lambda_y \sim \delta$. The overlap suggests that $\Phi_{uu}^{cross,w}$, like Φ_{uu}, also consists of energy contributions from the superstructures which, although wall-coherent, cannot be categorized as self-similar structures. The presence of these δ-scaled wall-coherent structures has been noted previously by Baars et al. (2017) as well as very recently by Yoon et al. (2020), who also described these structures to be tall and reminiscent of the superstructures. $\Phi_{uu}^{cross,w}$ contour for $z_o^+ = 0.15\delta^+$ (figure 4(a)), which is centered at $\lambda_x \sim 7\delta$ and $\lambda_y \sim \delta$, can be considered *representative* of the energy contributions from these tall non-self-similar structures. The present analysis thus suggests that this contribution would have

to be 'filtered' out from the wall-coherent energy (at lower z_o^+) to obtain a 2-D spectral distribution purely from the self-similar eddies. Our conclusion aligns with the recent work of Baars and Marusic (2020a), who in addition to a *wall*-filter, also proposed a *log*-filter in order to isolate the energy contributions from the wall-coherent self-similar eddies to the 1-D streamwise spectra. Construction of a robust *log*-filter, however, is challenging since it requires measurements to be conducted in a physically thick boundary layer and/or at even higher Re_τ than reported in the present study (Baars and Marusic, 2020a).

4.6 Concluding remarks

The present study investigates the 2-D cross-spectrum of u in a ZPG TBL for Re_τ spanning $\mathcal{O}(10^3)$ - $\mathcal{O}(10^4)$. Special emphasis is laid on the cross-spectrum ($\Phi_{uu}^{cross,w}$) representing coherence between a log (z_o) and a near-wall reference, which depicts the energy distribution across a range of wall-coherent eddies existing at z_o and hence is a subset of the full 2-D spectrum $\Phi_{uu}(z_o)$. Removal of the energy contributions from wall-incoherent eddies results in $\Phi_{uu}^{cross,w}$, at high Re_τ, having negligible energy contribution in the scale range where otherwise a $\lambda_y/z_o \sim (\lambda_x/z_o)^{1/2}$ behaviour is noted for Φ_{uu}. Further, the energetic large scales contributing to $\Phi_{uu}^{cross,w}$ follow $\lambda_y/z_o \sim \lambda_x/z_o$ power law more closely than seen for Φ_{uu}. This supports the hypothesis on the obscured view of the self-similar trend for Φ_{uu}, at finite Re_τ, being a result of limited scale separation between various eddies following dissimilar scalings. Further, $\Phi_{uu}^{cross,w}$ closely resembles the qualitative 2-D spectrum obtained from an AEH-based model (Φ_{uu}^{AEH}), in terms of scale-specific energy distribution as well as obeyance of the self-similar scaling laws, giving strong evidence of self-similarity ingrained in the TBL. It is shown, however, that $\Phi_{uu}^{cross,w}$ does not represent energy contributions purely from self-similar eddies. At least one more filter is required to remove the contributions from wall-coherent non-self-similar structures.

Acknowledgement

The authors wish to acknowledge the Australian Research Council for financial support and thank the authors of Sillero et al. (2014) for making their DNS data available. The authors are also grateful to the anonymous reviewers for their helpful comments which improved the quality of the manuscript.

Chapter 5

Large-scale spanwise periodicity in a canonical turbulent boundary layer

[Published paper II[1]]

5.1 Preface to the chapter

This chapter is based on an article published in the *Proceedings of 22nd Australasian Fluid Mechanics Conference*, titled "Large-scale spanwise periodicity in a canonical turbulent boundary layer" (Deshpande et al., 2020b), with minor updates to the original text. This study investigates the spanwise geometry and organization of wall-coherent motions of the streamwise velocity in the log-region. It is achieved by performing a scale-specific coherence analysis on the multi-point high Re_τ dataset described in §3.2. An understanding of the flow organization of the energetic coherent motions can facilitate development of a semi-empirical attached eddy model, wherein the sizes and relative positioning of the representative vortex structures are defined based on the estimates from the high-Re_τ experiments in the TBL.

[1]Deshpande, R., Monty, J.P. & Marusic, I. (2020). Large-scale spanwise periodicity in a canonical turbulent boundary layer. In *Proceedings of 22nd Australasian Fluid Mechanics Conference, Brisbane, Australia*. DOI: https://doi.org/10.14264/933c23f

5.2 Abstract

The present study reports empirical evidence for periodic organization of very large-scale motions (also known as superstructures), along the spanwise direction, in a zero pressure gradient turbulent boundary layer. This is made possible by performing a scale-specific coherence analysis on datasets comprising streamwise velocity fluctuations, synchronously measured at multiple locations across large spanwise and wall-normal separations within the shear flow. Datasets considered include published low-Re_τ direct numerical simulation and high-Re_τ experimental datasets across a friction Reynolds number range, $Re_\tau \sim \mathcal{O}(10^3)$ – $\mathcal{O}(10^4)$. The present analysis reveals that the intermediate and large-scale motions exhibit geometric self-similarity over a range of scales, up to a characteristic spanwise width equivalent to that of the superstructures, which scale in outer-units.

5.3 Introduction

Since the discovery of 'coherent' structures in a wall-bounded turbulent shear flow, a significant number of studies have been conducted to understand the mechanism associated with their formation and organization (Smits et al., 2011). One of the earliest efforts in this respect was the seminal work of Kline et al. (1967), who observed the near-wall streaky structures to be organized along the spanwise direction, at a characteristic viscous-scaled wavelength of 100, which is common to all three canonical wall-bounded turbulent flows (Monty et al., 2009) – the zero pressure gradient turbulent boundary layer (ZPG TBL), the fully developed turbulent channel and pipe flow. Studies conducted over the past two decades (Tomkins and Adrian, 2005; de Silva et al., 2020) have reported a similar organization even for the energetic large coherent structures existing in the outer region of the wall-bounded flow, albeit at much larger spacings. The existence of such an 'order within chaos' is particularly exciting from the perspective of developing conceptual models for these complex flows (for example, the attached eddy model based on the attached eddy hypothesis (AEH) of Townsend (1976)).The present study investigates the organization as well as the geometric characteristics of the energetic motions in a ZPG TBL, in the hope to facilitate the AEH-based modelling for this flow type (Marusic and Monty, 2019).

Recent modelling efforts have primarily concentrated on the logarithmic (log) region of a wall-bounded shear flow (Marusic and Monty, 2019), which comprises a major proportion of the turbulence production at practically relevant Reynolds numbers (Smits et al., 2011).

This region is predominated by the so-called large-scale motions (LSMs;Smits et al. (2011)) and very-large-scale motions or superstructures (SS;Hutchins and Marusic (2007); Monty et al. (2009)) carrying streamwise (u) momentum, which together constitute a significant portion of the Reynolds shear stress and turbulent kinetic energy (Smits et al., 2011) of the flow, making them the primary focus of this study. The LSMs correspond to u-motions with streamwise (x) lengths of the order of 2-3δ, and are induced by hairpin packets formed via coalescence of multiple hairpin vortices along x (Smits et al., 2011). δ, here, refers to the boundary layer thickness of a ZPG TBL. Recent direct numerical simulations (DNS) have revealed via space-time analysis (Lee and Sung, 2011; Baltzer et al., 2013; Lee et al., 2014) that it is these LSMs which concatenate along the streamwise direction to form the SS, an idea earlier hypothesized by Tomkins and Adrian (2005). The SS correspond to spanwise-alternatively arranged very long structures ($> 20\delta$) of low ($-u$) and high ($+u$) momentum (Hutchins and Marusic, 2007; Monty et al., 2009), extending down to the wall (i.e. they are wall-coherent (Deshpande et al., 2020a)), subsequently influencing the near-wall dynamics via superposition and modulation (Hutchins and Marusic, 2007; Mathis et al., 2009). While their spanwise periodicity has been noted previously via Fourier analysis (Tomkins and Adrian, 2005; de Silva et al., 2020), these estimates should however, be treated with caution given that the associated wavelengths essentially correspond to Fourier wavelengths (Baltzer et al., 2013), which inherently assumes periodicity along the concerned direction.

Consequently, here we re-investigate published datasets, spanning across a decade of Re_τ, to look for a direct evidence of the periodic organization of the SS along the spanwise direction. To this end, experimental and numerical datasets comprising multi-point u-fluctuations measured synchronously across large spanwise (Δy) and wall-normal ($\Delta z = z_o$ - z_r) spacings are considered to compute the scale-specific u-coherence over space and/or time. The unique aspect of the present analysis is the consideration of one of the reference u-velocity signals (to investigate coherence) from the near-wall region, which ensures that the estimates are solely influenced by the wall-coherent motions (Deshpande et al., 2020a, 2019a). Given that the SS are formed via concatenation of the LSMs (Lee and Sung, 2011; Baltzer et al., 2013; Lee et al., 2014), the present analysis also facilitates investigation of these relatively smaller wall-coherent motions acting as the constituent elements for the former. The associated findings would be useful to model the SS, while developing the framework of an AEH-based conceptual model for the ZPG TBL flow (Marusic and Monty, 2019). Throughout this article, superscript '+' indicates normalization by viscous length (ν/U_τ) and velocity (U_τ) scales, the latter defined mathematically by $U_\tau = (\frac{\tau_w}{\rho})^{1/2}$, with τ_w and ρ the mean wall-shear stress and fluid density, respectively.

Study	Deshpande et al. (2020a)		Sillero et al. (2014)	
Facility	HRNBLWT (Exp)		DNS	
$Re_\tau \approx$	15 000		2 000	
Sensor ref.	z_o^+	z_r^+	z_o^+	z_r^+
Location	$2.6\sqrt{Re_\tau}$	$\approx z_o^+$	$2.6\sqrt{Re_\tau}$	$= z_o^+$
Location	$2.6\sqrt{Re_\tau}$, $0.15Re_\tau$	15	$2.6\sqrt{Re_\tau}$	15
$l^+ \approx$	22	22	3.7	3.7
$\Delta y/\delta \approx$	0.0 - 2.5	–	0.0 - 2.5	–

TABLE 5.1: A summary of the data sets containing synchronized multipoint u-measurements at z_r^+ and z_o^+, which are separated by various spanwise offsets, Δy. l^+ represents the spatial resolution of the sensor/grid along the spanwise direction. $z_o^+ \approx 2.6\sqrt{Re_\tau}$ and $0.15Re_\tau$ corresponds to the lower and upper bound of the log-region, respectively (Deshpande et al., 2020a).

5.4 Experimental and numerical data

The flow organization is investigated by conducting a coherence analysis on published datasets (Sillero et al. (2014), Deshpande et al. (2020a); table 5.1) ranging over a decade of friction Reynolds number, $Re_\tau \sim \mathcal{O}(10^3)$ – $\mathcal{O}(10^4)$. Here, $Re_\tau = U_\tau\delta/\nu$, which is the ratio of the inner and outer length scales of the wall-bounded flow. The experimental dataset essentially comprises of the time series of the u-fluctuations (with the mean subtracted from the instantaneous signal) synchronously acquired via hotwire anemometry at multiple locations across the shear flow, specific details of which are given in table 5.1. The dataset is obtained from one of the largest state-of-the-art facilities available for investigating the ZPG TBL – the Melbourne High Reynolds Number Boundary Layer Wind Tunnel (HRNBLWT) facility at the University of Melbourne. The facility is designed on the 'big and slow' approach, i.e. it allows the TBL to grow along the streamwise direction (x), producing a high Reynolds number flow which is physically thick (meaning a large δ) while keeping the smallest energetic viscous scale within $\mathcal{O}(10\ \mu\text{m})$. This permits accessibility to the near-wall region of the high Reynolds number flows, which scales in viscous units, while also ensuring that the entire spectrum of the energetic scales can be resolved by conventional hotwire sensors.

In HRNBLWT, the TBL is allowed to develop over a very long flat plate from the start of the test section ($x = 0$), with the multi-point hotwire measurements conducted at $x \approx 20\ m$, where $\delta \approx 0.36\ m$. To facilitate the study of the spanwise organization of the energetic wall-coherent motions, u-fluctuations were acquired simultaneously at locations in the near-wall ($z_r^+ \approx 15$) as well as at the start of the log-region ($z_o^+ \approx 2.6\sqrt{Re_\tau}$). These two probes were separated by a spanwise offset Δy, which was varied by physically traversing the probe at z_o (along the span y) for every measurement while keeping the other probe (at z_r) fixed. Figure 5.1(a) schematically depicts this probe arrangement. The same experiment was also conducted to investigate the tall wall-coherent motions extending up to the upper bound of the log-region, by choosing $z_o^+ \approx 0.15Re_\tau$, the schematic for which has been given in figure 5.1(b). The cumulative observations from these two measurements, thus, can be deemed representative of the flow phenomena in the entire log-region.

Apart from the arrangement where $z_o^+ \neq z_r^+ \approx 15$ (table 5.1), a similar two-point measurement but with $z_o^+ \approx z_r^+ \approx 2.6\sqrt{Re_\tau}$ was also conducted to estimate the u-coherence influenced by all motions coexisting at z_o, to compare with the former experiment. Full details of the setup as well as the methodology adopted to conduct both these measurements can be found in Deshpande et al. (2020a). Apart from these experimental data, a low Re_τ dataset of Sillero et al. (2014) is also selected from their published DNS database for a ZPG TBL. Thirteen raw DNS volumes, comprising instantaneous streamwise velocity fluctuations, are considered in total to investigate the large-scale coherence. Sensor locations, z_o^+ and z_r^+ for this dataset were selected to be compatible with the experimental dataset and have been specified in table 5.1.

5.5 Results

Here, the spatial coherence of the u-motions is quantified by computing the scale-specific coherence function (Bailey et al., 2008), Γ:

$$\Gamma(z_o, z_r, \Delta y; \lambda_x) = \frac{\Re[\langle \widetilde{u}(z_o, \Delta y; \lambda_x)\widetilde{u}^*(z_r; \lambda_x)\rangle]}{\sqrt{\langle \mid \widetilde{u}(z_o, \Delta y; \lambda_x) \mid^2\rangle}\sqrt{\langle \mid \widetilde{u}(z_r; \lambda_x) \mid^2\rangle}}, \tag{5.1}$$

where $\tilde{u}(z_o, \Delta y; \lambda_x)$ indicates the Fourier transform of $u(z_o, \Delta y)$ in either time or x, depending on the data set. Here, λ_x is the streamwise wavelength and is equal to $2\pi/k_x$, with k_x the streamwise wavenumber. The asterisk ($*$), angle brackets ($\langle\rangle$) and vertical bars ($||$) indicate the complex conjugate, ensemble averaging in time and modulus, respectively

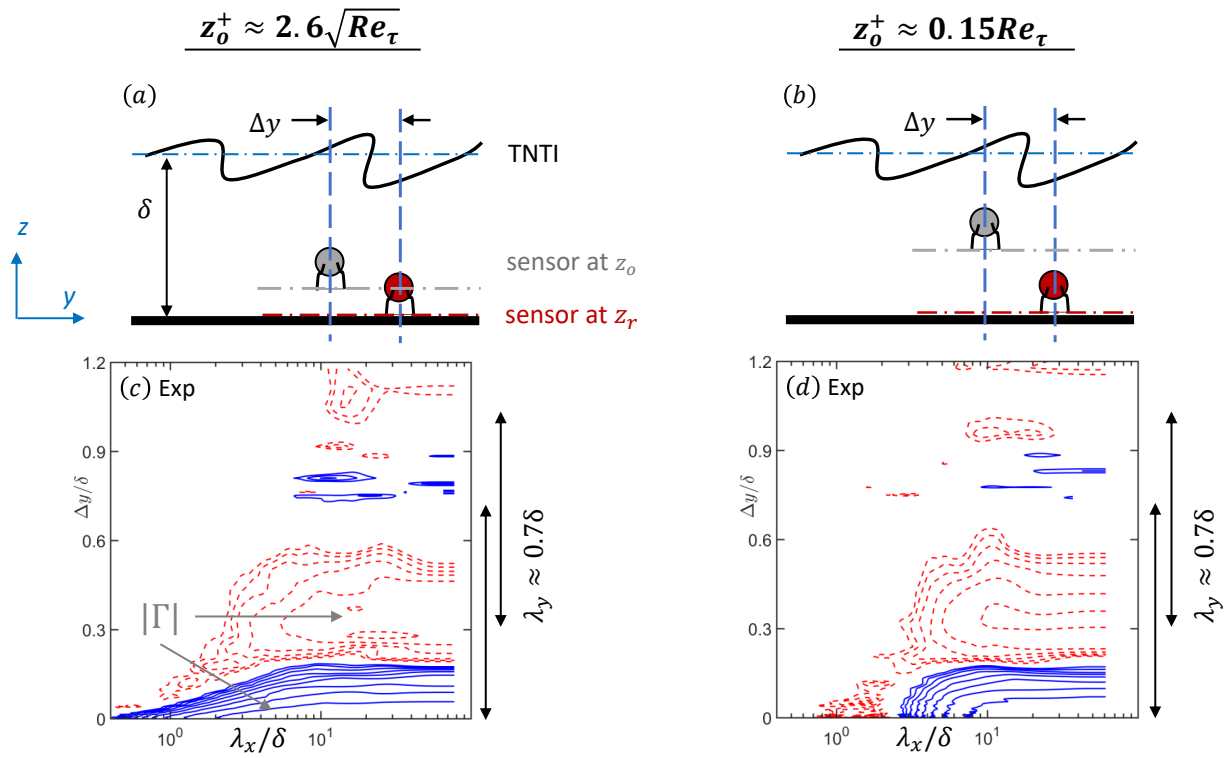

FIGURE 5.1: Contours of the coherence function, Γ calculated for the experimental dataset for (c) $z_o^+ \approx 2.6\sqrt{Re_\tau}$, $z_r^+ \approx 15$ and (d) $z_o^+ \approx 0.15Re_\tau$, $z_r^+ \approx 15$, as depicted in the respective schematics of the hotwire setup (a,b). Solid blue and dashed red contours respectively indicate Γ contours with values varying logarithmically in the range (0.05,0.95) and (-0.22,-0.02), in the direction of the arrows shown in (c). The spanwise wavelength estimates (λ_y) denoted in (c,d) correspond to the dominant spanwise Fourier mode noted for the ZPG TBL in the literature (Tomkins and Adrian, 2005; de Silva et al., 2020).

while $\Re$ denotes the real component. It is noted, that by definition -1 $\leq \Gamma \leq$ 1, with +1 and −1 representing perfect correlation and anti-correlation respectively, analogous to the correlation coefficient which has been widely used in the literature (Hutchins and Marusic, 2007; Monty et al., 2009) to study spatial coherence. The present study, however, uses Γ as the preferred metric since it allows contributions from the small and large motions to be compared individually, yielding information which is otherwise lost due to ensemble averaging in case of the correlations (Bailey et al., 2008; Deshpande et al., 2019a). It can be noted that, when $z_r^+ \approx 15$, Γ would be solely influenced by the wall-coherent motions (Deshpande et al., 2019a, 2020a) at z_o, which is of primary interest to us in this study.

In the case of the experimental dataset, which is limited only to having the u-time series at various Δy, the streamwise coherence in equation 5.1 is obtained by using the Taylor's frozen turbulence hypothesis, which assumes all large-scale motions to be convecting along x at a common velocity (U_c) throughout the shear flow (Bailey et al., 2008; Smits et al.,

2011). Since the present study focuses on investigating the SS in a ZPG TBL, we choose $U_c = 0.75U_\infty$ (where U_∞ is the free-stream velocity) based on their convective velocities estimated in the literature (Lee and Sung, 2011).

5.5.1 Large-scale spanwise periodicity

Figure 5.1 plots the constant energy contours for Γ, as a function of λ_x and Δy scaled with respect to δ, for the high-Re_τ experimental dataset. Here, Γ is estimated for both: $z_o^+ \approx 2.6\sqrt{Re_\tau}$ (figure 5.1(c)) and $z_o^+ \approx 0.15Re_\tau$ (figure 5.1(d)), while maintaining $z_r^+ \approx 15$, so that the two plots cumulatively denote scale-specific coherence of the wall-coherent u-motions across the log-region. For discussion, $+\Gamma$ and -Γ contours are interpreted here as being representative of the statistically averaged $+u$ and -u motions, respectively and are indicated by solid blue and dashed red contours in the plot. High magnitudes for both $+\Gamma$ and -Γ are seen for small spanwise offsets at large λ_x, which is representative of a $+u$ superstructure flanked on either sides (along y) by a -u superstructure, given the flow symmetry in the spanwise direction. Such an organization is consistent with the observations reported previously in the literature (Hutchins and Marusic, 2007; Monty et al., 2009; Lee and Sung, 2011).

This arrangement of alternatively arranged very-large-scale u-motions can be noted to be existing even at larger spans, $\Delta y \sim \mathcal{O}(\delta)$, albeit represented by relatively weaker contour levels. The low contour levels may be attributed to the fact that the coherence at such large Δy is due to the very large scales (Baltzer et al., 2013), which is evident from the positioning of the contours at $\lambda_x \sim \mathcal{O}(10\delta)$, corresponding to the SS. The Γ contours in figures 5.1(c,d), thus, provide direct empirical evidence in support of $+u$ and -u SS statistically organized in a spanwise periodic manner across the log-region of a ZPG TBL. Such a flow organization is brought out only after consideration of the scale-specific coherence over very large spatial offsets, which would be otherwise obscured if the ensemble-averaged correlation coefficient was considered instead. The present interpretation is further substantiated by comparing the centre-to-centre distance between the subsequent peaks (troughs) of $+\Gamma$ (-Γ) with the dominant spanwise wavelength ($\lambda_y \approx 0.7\delta$) reported in the literature based on Fourier analysis (Tomkins and Adrian, 2005; de Silva et al., 2020). The two values are consistent across the log-region, as has been highlighted in figures 5.1(c,d).

Apart from spanwise periodicity, the Γ-contours for the two different z_o^+ also bring out differences in the relatively small-scale contributions ($\lambda_x < 2\delta$), which do not show up in figure 5.1(d). It signifies that the tall wall-coherent motions are predominantly large in

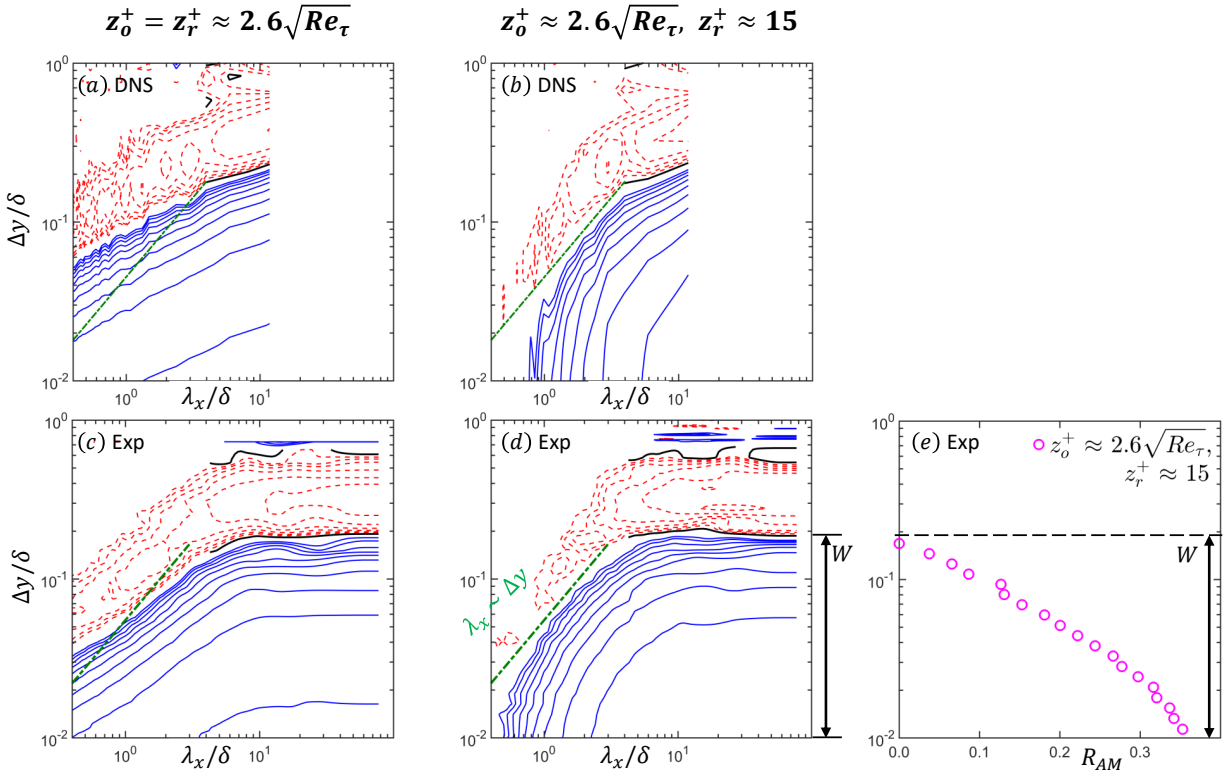

FIGURE 5.2: Contours of the coherence function, Γ calculated for the (a,b) DNS and (c,d) experimental datasets for (a,c) $z_o^+ \approx z_r^+ \approx 2.6\sqrt{Re_\tau}$ and (b,d) $z_o^+ \approx 2.6\sqrt{Re_\tau}$, $z_r^+ \approx 15$. Solid blue, dashed red and solid black contours indicate $+\Gamma$, $-\Gamma$ and $\Gamma \approx 0$, respectively while the dash-dotted green line represents the linear relationship, $\lambda_x \sim \Delta y$, representative of the self-similarity. Magnitude of Γ, for both the blue and red contours, increases in the same manner as shown in figures 5.1(c,d). (e) Two-point amplitude modulation coefficient ($\mathcal{R}_{AM}$) calculated from the experimental dataset for various Δy following (5.2).

size along both the streamwise and spanwise direction. Figure 5.1(c), on the other hand, depicts significant coherence in the relatively small λ_x-Δy range at the lower bound of the log-region. Given that the SS are a consequence of the streamwise concatenation of relatively smaller u-motions (Lee and Sung, 2011; Baltzer et al., 2013; Lee et al., 2014), we now focus on the Γ contours at $z_o^+ \approx 2.6\sqrt{Re_\tau}$, in this λ_x-Δy range, to understand the geometric characteristics of the latter.

5.5.2 Self-similarity of the wall-coherent motions

Figures 5.2(b,d) depicts Γ contours (with $z_r^+ \approx 15$) for both the experimental and DNS ZPG TBL datasets, with the y-axis plotted on a logarithmic scale to investigate coherence over shorter $\Delta y/\delta$. The contours can be noted to be following the linear trend, $\lambda_x \sim \Delta y$ at spanwise widths $\sim \mathcal{O}(0.01\delta)$ for both the datasets, spanning across a decade of

Re_τ. This trend is representative of the self-similar variation of the spanwise widths of the wall-coherent u-motions with respect to their streamwise extents (λ_x), consistent with Townsend's AEH (Townsend, 1976; Deshpande et al., 2020a). This linear growth, however, ceases at a characteristic width, $W \sim 0.17\delta$, in case of both datasets, which can be described as the average spanwise half-width of the largest self-similar structure coherent to the wall. Beyond this point, Γ contours vary only along λ_x, suggesting these large self-similar motions to be having similar spanwise widths as the SS (Bailey et al., 2008). This can be confirmed by calculating the two-point amplitude modulation coefficient, $\mathcal{R}_{AM}$, to measure the spanwise extent up to which the wall-coherent SS modulate (Hutchins and Marusic, 2007; Mathis et al., 2009) the small-scales in the near-wall region. To this end, u-time series (from the experimental dataset) synchronously acquired at $z_o^+ \approx 2.6\sqrt{Re_\tau}$ and $z_r^+ \approx 15$ is used to compute $\mathcal{R}_{AM}$ plotted in figure 5.2(e) following:

$$\mathcal{R}_{AM}(z_o, z_r, \Delta y) = \frac{\overline{u_C(z_o, \Delta y; t) E_C(u_I(z_r; t - \Delta t))}}{\sqrt{\overline{u_C^2(z_o, \Delta y)}}\sqrt{\overline{E_C(u_I(z_r))^2}}}, \tag{5.2}$$

where subscripts C and I respectively represent filtered u-signals comprising the wavelength range corresponding to the wall-coherent and incoherent scales, while E represents the envelope returned by the Hilbert transform (Mathis et al., 2009). Overbar indicates the estimate averaged over time, t. The wall-coherent and incoherent components of the u-signal are obtained via the linear coherence spectrum-based procedure described in Deshpande et al. (2019a), conducted for the same experimental dataset. To get the maximum correlation in equation (5.2), a time shift Δt (Mathis et al., 2009) is also applied to the u-signal at z_r to account for the inclination angle of the averaged structure with respect to $u(z_o,\Delta y)$. Interested readers may refer to Deshpande et al. (2019a) for complete information regarding the methodology employed to find this inclination angle.

As explained by Mathis et al. (2009), $\mathcal{R}_{AM}$ quantifies the intensity with which the SS (at z_o) modulate the near-wall fluctuations, meaning it would drop to zero at $\Delta y/\delta$ extending beyond the average spanwise half-width of the SS. Interestingly, $\mathcal{R}_{AM} \to 0$ at the same characteristic half-width (W) where the Γ contours deviate away from the self-similar trend to grow only along λ_x in figures 5.2(b,d). This is evidence that the spanwise width of the largest motions in the self-similar hierarchy is nominally equal to that of the SS. It should be noted here, that the self-similarity of the intermediate-scaled wall-coherent motions is brought out due to the choice of z_r^+ in the near-wall region (while estimating Γ). For the case of $z_r^+ \approx z_o^+$, which has been plotted in figures 5.1(a,c), Γ would also be influenced by the wall-incoherent motions at z_o, owing to which the contours no longer follow the linear

relationship representative of the self-similarity.

5.6 Conclusions

The study investigates the spanwise organization of the energetic large-scale u-motions in a ZPG TBL across a decade of Re_τ. This is facilitated by a scale-specific coherence analysis of the u-fluctuations synchronously acquired over large wall-normal and spanwise spacings across the shear flow. The wall-coherent u-motions in the intermediate-scale range exhibit geometric self-similarity up to a characteristic δ-scaled spanwise half-width (W), equivalent to that of the SS. A clear evidence of the spanwise periodicity of the SS is also reported. The present findings, thus, have direct ramifications towards future AEH-based conceptual modelling of the ZPG TBL flow. The organized state of the energetic large-scale motions, found in the present study, can also facilitate flow-control strategies aimed towards manipulating these motions to achieve drag reduction.

5.7 Acknowledgements

The authors wish to acknowledge the Australian Research Council for financial support, and are thankful to the authors of Sillero et al. (2014) for making their DNS data available.

Chapter 6

Streamwise inclination angle of large wall-coherent structures in turbulent boundary layers

[Published paper III[1]]

6.1 Preface to the chapter

This chapter is an article published in the *Journal of Fluid Mechanics*, titled "Streamwise inclination angle of large wall-attached structures in turbulent boundary layers" (Deshpande et al., 2019a). This study proposes a methodology to estimate the streamwise inclination angle of the large wall-coherent motions of the streamwise velocity, by physically isolating them from the influence of the relatively smaller motions coexisting in the log-region. It is made possible by conducting a spectral coherence analysis on the multi-point high-Re_τ dataset described in §3.2. A data-driven estimation of the streamwise inclination angle facilitates definition of the same for the representative vortex structures in the attached eddy-based modelling of the high-Re_τ TBL.

Readers should take note that the terminology '*wall-attached structures*', used in the original published manuscript, has been replaced by '*wall-coherent structures*' across this entire

[1]Deshpande, R., Monty, J.P. & Marusic, I. (2019). Streamwise inclination angle of large wall-attached structures in turbulent boundary layers. *Journal of Fluid Mechanics* 877, R4. DOI: https://doi.org/10.1017/jfm.2019.663

chapter to maintain a consistent terminology across the thesis, and also to avoid indication of any one-to-one linkage with Townsend's definition of 'attached' eddies.

6.2 Abstract

The streamwise inclination angle of large wall-coherent structures, in the log region of a canonical turbulent boundary layer, is estimated via spectral coherence analysis, and is found to be approximately 45°. This is consistent with assumptions used in prior attached eddy model-based simulations. Given that the inclination angle obtained via standard two-point correlations is influenced by the range of scales in the turbulent flow (Marusic, 2001), the present result is obtained by isolating the large wall-coherent structures from the rest of the turbulence. This is achieved by introducing a spanwise offset between two hot-wire probes, synchronously measuring the streamwise velocity at a near-wall and log region reference location, to assess the wall-coherence. The methodology is shown to be effective by applying it to data sets across Reynolds numbers, $Re_\tau \sim \mathcal{O}(10^3)$–$\mathcal{O}(10^6)$.

6.3 Introduction

The turbulent boundary layer (TBL) consists of an ensemble of coherent motions (Robinson, 1991) which are responsible for the production and dissipation of turbulence. Previous studies have found the majority of these motions to be inclined forward in the direction of the mean flow. Table 6.1 lists a small selection of the many studies that have reported the streamwise inclination angle of these motions in a zero pressure gradient (ZPG) TBL at various Reynolds numbers. As is evident from the table, the value of the angle varies significantly depending on the type of structure it is defined for, with subscript 'm' and 's' referring to inclination angle of a *mean* and *individual* flow structure, respectively (terminology inspired from Adrian et al. (2000) who also noted this difference). The superscript 'w' is considered when referring to wall-coherent structures only. Throughout this article, the words 'motions', 'structures' and 'eddies' are used interchangeably and essentially follow the definition of a coherent motion given by Robinson (1991).

The information on the structure inclination angle is important from a wall-turbulence modeller's perspective, be it developing a model of the near-wall region for a large eddy simulation (LES; Piomelli and Balaras (2002)) or to predict the TBL velocity statistics by

θ_s in the outer region of wall-bounded flow			θ_s^w assumed for AEH simulations		θ_m^w in the log region of wall-bounded flow		
Reference	Re_θ	θ_s	Reference	θ_s^w	Reference	Re_τ	θ_m^w
Head and Bandyopadhyay (1981)	500-10000	45°	Perry and Marusic (1995)	45°	Brown and Thomas (1977)	3413	18°
Moin and Kim (1985)#	13800	45°	Baidya et al. (2014, 2017)	45°	Marusic and Heuer (2007)	1350	14°
Adrian et al. (2000)	930-6845	3°-35°	Chandran et al. (2017)	45°	Marusic and Heuer (2007)‡	1.4×10^6	14°

TABLE 6.1: A summary of the streamwise inclination angles of coherent motions in a ZPG TBL, estimated (θ_s, θ_m^w) or assumed (θ_s^w) in various studies. Friction Reynolds number, Re_τ is defined based on friction velocity (u_τ) and TBL thickness (δ). While, Re_θ is based on free-stream velocity (U_∞) and momentum thickness. Terminology for angles has been described in §6.3. #This study was for a fully developed turbulent channel flow and their Reynolds number is defined based on channel centreline velocity and half-width.
‡ Results are for atmospheric surface layer under neutrally buoyant conditions.

modeling the flow based on attached eddy hypothesis (AEH; Marusic and Monty (2019)). The latter approach has gained popularity for investigating the kinematics in the logarithmic (log) region of a TBL by representing it with an assemblage of self-similar wall-coherent vortex structures. Researchers who have utilized the AEH approach previously (table 6.1) assumed θ_s^w for these statistically-representative structures to be equivalent to θ_s recorded by identifying structures via flow visualization, vortex identification techniques, etc. θ_s estimated in these studies, however, was based on structures clearly discernible only in the outer region of the boundary layer (Moin and Kim, 1985) with no evidence of these being wall-coherent (hence not referred here as θ_s^w). Notwithstanding, the AEH simulations yield results consistent with experimental observations, suggesting $\theta_s^w \approx 45°$ is a good assumption. Theoretical support towards θ_s^w being nominally 45° is obtained on investigating the mean-strain-rate and rotation tensor, the two components of the velocity gradient tensor, for a ZPG TBL which is two-dimensional in the mean. As pointed out by Perry et al. (1992) and Moin and Kim (1985), it is more likely for eddies in such a flow to assume the direction of the principal rate of mean strain since the rotation field has no preferred direction. If we consider ψ to correspond to the inclination of the principal rate of mean strain

with the streamwise direction (x) and z to be the wall-normal direction, it was deduced by Perry et al. (1992) that:

$$\psi = \frac{1}{2} atan\left(\frac{\frac{\partial U}{\partial z}}{2\frac{\partial U}{\partial x}}\right), \tag{6.1}$$

from which $\psi = 45°$ for a ZPG TBL, where $\frac{\partial U}{\partial x} = 0$ with U being the mean streamwise velocity. In spite of these arguments, there is still a lack of empirical evidence to support the claim of $\theta_s^w \approx 45°$.

Apart from direct visualization of *individual* structures, experimentalists (table 6.1) have statistically estimated the inclination angle of a *mean* wall-coherent structure (θ_m^w) in the log region via cross-correlating simultaneously acquired wall-shear stress (τ) and u velocity fluctuations. This is achieved through probes on the wall ($z = 0$) and in the log-region ($z = z_o$), respectively following:

$$R_{\tau u}(\Delta t) = \frac{\langle \tau(t) u(z_o; t + \Delta t) \rangle}{\sqrt{\langle \tau^2 \rangle} \sqrt{\langle u^2(z_o) \rangle}} \tag{6.2}$$

where angle brackets ($\langle\rangle$) denote ensemble time-average with t being the time. Here, u, v and w refer to the streamwise, spanwise and wall-normal velocity fluctuations respectively, associated with the coordinate system x, y and z. To estimate θ_m^w, the temporal delay (Δt_p) corresponding to the peak in $R_{\tau u}$ is identified (Marusic and Heuer, 2007) and then $\theta_m^w = \text{atan}(z_o/(\Delta t_p U_c))$, where U_c is the convection velocity. The stark difference between θ_m^w and expected θ_s^w exists due to θ_m^w being a function of the distribution and the range of scales of eddies convecting past the two probes (Marusic, 2001), hence giving it the name of a *mean* structure angle (figure 6.1 differentiates θ_m^w and θ_s^w; see also figure 13 in Head and Bandyopadhyay (1981)). Marusic (2001) demonstrated this via attached eddy simulations by considering individual eddies (with $\theta_s^w \approx 45°$) of various length scales in an organized manner, analogous to a spatially correlated packet of vortices observed experimentally by Adrian et al. (2000). It was shown that θ_m, estimated from the cross-correlations obtained from these simulated fields, closely resembles the experimentally obtained inclination angles. On the other hand, it was found that $\theta_m \approx \theta_s$ when eddies of only specific length scales were considered in the simulation. In a real turbulent boundary layer experiment, it is possible to isolate structures of specific length scale from the rest in post-processing. In the present study, we draw inspiration from the recent work of Baidya et al. (2019a) to isolate large wall-coherent structures in a TBL by imposing a spanwise offset between the log region and wall-probe to find θ_s^w.

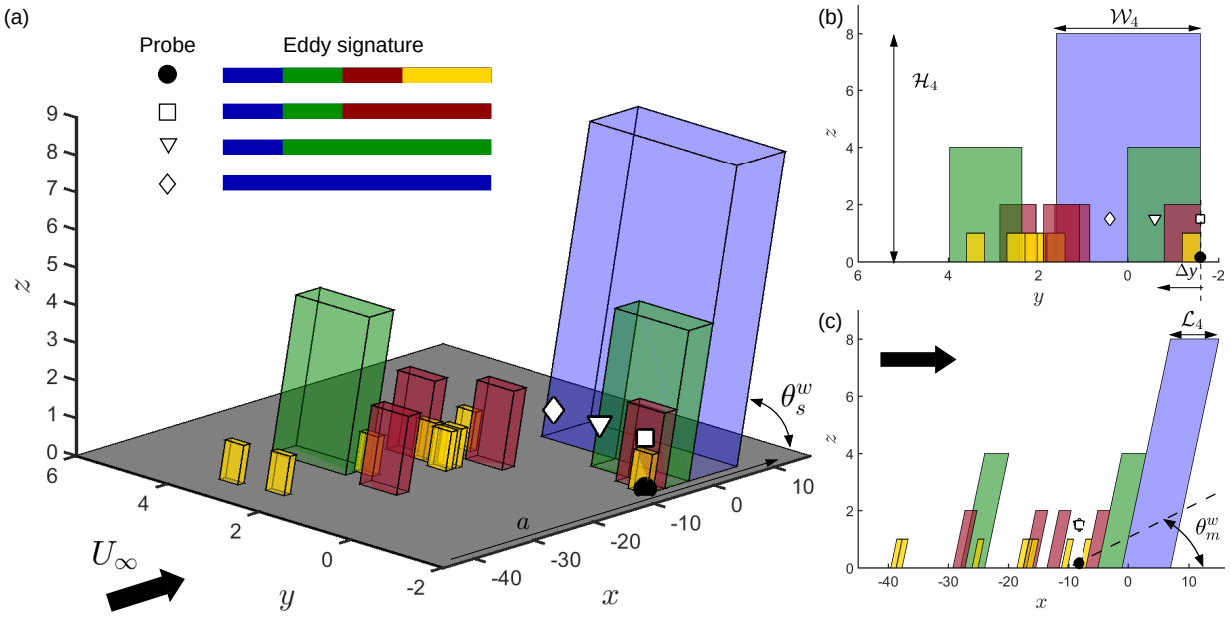

FIGURE 6.1: Schematic showing the (a) isometric, (b) y-z plane and (c) x-z plane view of a hierarchy of self-similar wall-coherent eddies (shown as simplified cuboids) representing the log region of a ZPG TBL. Four hierarchy levels are considered each represented by different colours. Symbols represent various probe locations. Eddy signatures identified by respective probes, over a streamwise distance of a, are shown in (a). L_i, W_i and H_i denote the streamwise, spanwise and wall-normal extent of a hierarchy level. θ_m^w and θ_s^w denote mean and individual structure angles, respectively. Figure concept adopted from Baidya et al. (2019a).

6.4 Methodology adopted to isolate large wall-coherent structures

We begin by demonstrating the methodology adopted to isolate large wall-coherent structures via a conceptual reconstruction of a TBL from an AEH view point. Figures 6.1(a)-(c) shows a schematic with a hierarchy of self-similar wall-coherent structures representing the log region of a TBL (Marusic and Monty, 2019; Baidya et al., 2019a). Apart from these preferentially forward-inclined structures, which represent the majority, a real TBL will invariably also consist of additional randomly oriented structures (Perry et al., 1992) that influence the flow statistics. These, however, are not considered in AEH-based simulations. Here, four hierarchy levels of randomly positioned attached eddies are considered with each hierarchy shown in a different colour. Starting from the hierarchy with the smallest eddies (yellow), the eddy size in each consecutive hierarchy is doubled in a self-similar manner and the number of eddies is quartered in three-dimensional space. For simplicity, we consider the volume of influence of eddies, in each level, to be characterized by $\mathcal{L}_i$, $\mathcal{W}_i$ and $\mathcal{H}_i$ in

the x, y and z directions, respectively with i = 1-4 denoting the hierarchy level. A spectral analysis of the flow field consisting of such eddies would lead to their lengths and spans showing up as wavelengths, $\lambda_x \sim 2\mathcal{L}_i$ and $\lambda_y \sim 2\mathcal{W}_i$ (Baidya et al., 2019a). Here, $\lambda_x = 2\pi/k_x$ where k_x is the streamwise wavenumber. θ_s^w represents the streamwise inclination of the individual eddies.

The solid and empty symbols represent probes placed on the wall and in the log region, respectively to synchronously record the signature of the convecting eddies, shown in figure 6.1(a). The □ probe is able to record all except the smallest hierarchy in comparison to the wall probe (•). Accordingly, the correlation between u fluctuations from □ and • probes (following equation 6.2) represents a *mean* structure of the wall-coherent flow influenced by the hierarchy levels 2, 3 and 4 (Marusic, 2001). The inclination angle of this mean structure is given by θ_m^w (figure 6.1(c)). Increasing the relative spanwise offset (Δy) between the log-region and wall probes means that only the hierarchy levels with the large eddies correlate between the two probes. For example, considering probe ◊ placed at $W_3 < \Delta y < W_4$, only eddies belonging to the fourth hierarchy remain correlated with the wall probe, effectively isolating these eddies from the others. Following Marusic (2001), we hypothesize that the streamwise inclination angle obtained on correlating the u fluctuations from • and ◊ probes should reflect the angle for a large *individual* wall-coherent structure θ_s^w in this simplified flow model. We consider experimental as well as numerical data sets which allow us to work along this hypothesis in the following sections. It is to be noted that the relative offset, Δy, can be obtained on moving either the wall- or log region probe along y owing to the spanwise homogeneity of the TBL.

6.5 Experimental and numerical data

To test the hypothesis proposed in the previous section, we consider three data sets (table 6.2) each comprising synchronized two-point u velocity signals at a near-wall (z_r) and a log region (z_o) reference location for various spanwise offsets, Δy. One of these is the DNS by Sillero et al. (2013) ($\mathcal{S}_1$). Thirteen raw DNS time blocks, spanning up to 11.9δ in x, were considered such that the Reynolds number increases nominally across the domain. This is the same block size considered by Baars et al. (2017) for their linear coherence spectrum (LCS) analysis with $Re_\tau \approx 1992$ at the streamwise centre of the domain. Here, values of δ for both data sets $\mathcal{S}_1$ and $\mathcal{E}_1$ were calculated by a modified Coles law of the wake fit (Jones et al., 2001). Both z_r^+ and z_o^+ (viscous-scaled) in $\mathcal{S}_1$ were chosen to correspond with the experimental data set, $\mathcal{E}_1$ (described next).

Dataset:			
Label	$\mathcal{S}_1$	$\mathcal{E}_1$	$\mathcal{E}_2$
Facility	DNS(raw)	HRNBLWT	SLTEST atm.
Study	Sillero et al. (2013)	present study	Hutchins et al. (2012)
$Re_\tau \approx$	2 000	15 000	7.7×10^5
Near-wall sensor:			
Sensor	–	Hot-wire	Sonic
$z_r^+ \approx$	14.6	15	$0.036Re_\tau$
$l^+ \approx$	3.7	22	1000
Log-region sensor:			
Sensor	–	Hot-wire	Sonic
$z_o^+ \approx$	$2.6\sqrt{Re_\tau}$	$2.6\sqrt{Re_\tau}$, $3.9\sqrt{Re_\tau}$	$0.05Re_\tau$
$l^+ \approx$	3.7	22	1000
$\Delta y/\delta \approx$	0.00 - 0.15	0.00 - 0.15	0.00 - 0.15

TABLE 6.2: A summary of the various data sets containing synchronized multipoint measurements at a near-wall (z_r) and log region (z_o) reference location at various spanwise offsets, Δy. l^+ represents the spatial resolution of the sensor/grid along the spanwise direction.

The high-Re_τ laboratory measurements ($\mathcal{E}_1$) were conducted in the large Melbourne wind tunnel (HRNBLWT). They were made possible by employing the same experimental set-up used by Chandran et al. (2017). Figure 6.2(a) shows a schematic of how the experiment was conducted. The set-up comprised of two 2.5μm diameter Wollaston hot-wire probes - HW_r and HW_o at wall-normal heights z_r and z_o, respectively. They were operated using an in-house Melbourne University Constant Temperature Anemometer (MUCTA) at a viscous-scaled sampling rate ~ 0.5. The same calibration procedure, as employed by Chandran et al. (2017), was followed wherein the HW_o was calibrated in the TBL using the free-stream calibrated HW_r as a reference. The measurement began with both probes vertically aligned (figure 6.2(a)(i)), which was ensured by viewing the arrangement via a traversable microscope. Long velocity signals were acquired with a length of $TU_\infty/\delta \approx 20\ 000$ (T is the total sampling duration) to obtain converged statistics at the largest energetic wavelengths. As the experiment progressed, HW_r always remained at a fixed spanwise location while HW_o was traversed in the spanwise direction (with log spacing)

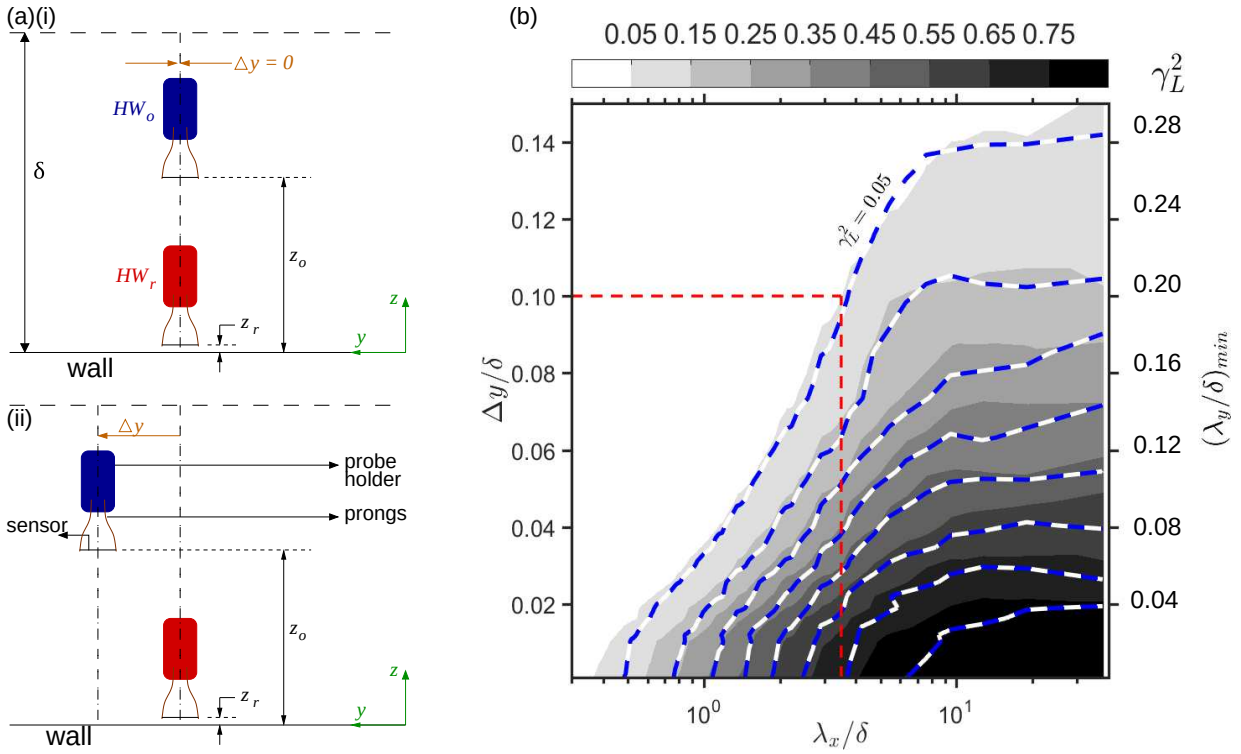

FIGURE 6.2: (a) Schematic of the experimental set-up in HRNBLWT showing locations of the near-wall (HW_r) and log region (HW_o) reference probe. Mean flow direction is along x. The experiment begins with HW_o placed vertically above HW_r ($\Delta y = 0$;(i)) and is followed by the spanwise traverse ($\Delta y > 0$;(ii)) of HW_o. (b) γ_L^2 computed as a function of λ_x and Δy on correlating u from HW_o and HW_r for data set $\mathcal{E}_1$. The grey scale and line contours correspond to γ_L^2 for $z_o^+ \approx 2.6\sqrt{Re_\tau}$ and $3.9\sqrt{Re_\tau}$, respectively. Both contours are at levels 0.05:0.1:0.85. The red dashed line is used to highlight the streamwise spectral cut-off $\lambda_{x,c}$ corresponding to $\Delta y/\delta = 0.1$.

as shown in figure 6.2(a)(ii). HW_o was traversed only up to $\Delta y/\delta \approx 0.15$ since the cross-correlation tends to 0 at such spans (Baidya et al., 2019a). Although the present study focuses on inclination angles of wall-coherent structures, a hot-wire probe positioned at $z_r^+ \approx 15$ was preferred over a wall-mounted shear stress sensor (hotfilm) owing to spatial resolution and frequency response issues (Baars et al., 2017). This was possible due to the observation made by Baars et al. (2017) on the wall-coherence analysis being unaffected for $0 < z_r^+ \lesssim 15$. The data set $\mathcal{E}_1$ consists of two cases of z_o^+ (table 6.2), both lying within the log region of the TBL (Baars et al., 2017).

The data set at the highest Reynolds number, $Re_\tau \approx 7.7\times10^5$ ($\mathcal{E}_2$) consists of one hour of synchronously acquired u fluctuations in the atmospheric surface layer (under near-neutral buoyant conditions) by a spanwise and wall-normal array of 18 sonic anemometers at the SLTEST facility. Here, we consider the sonic located at 4.26m from the ground ($t4$; refer figure 1 of Hutchins et al. (2012)) as the log region reference. Of the 10 sonics

in the spanwise array, each of which were separated by approximately 3m and fixed at approximately 2.14m from ground, we consider only four sonics ($s1$-$s4$) to obtain relative spanwise offsets, $0 \lesssim \Delta y/\delta \lesssim 0.15$ ($\delta = 60$m for $\mathcal{E}_2$) and to act as the near-wall reference. Given that z_r is significantly far from the wall, the structure inclination angle obtained through data set $\mathcal{E}_2$ cannot be associated with a wall-coherent structure. This data set is used here merely to demonstrate the feasibility of isolating large structures by introduction of a spanwise offset between the two reference probes. For the case of both temporal data sets $\mathcal{E}_1$ and $\mathcal{E}_2$, Taylor's frozen turbulence hypothesis is used to construct cross-correlation functions between z_o and z_r, at different streamwise (Δx) spacings, by assuming the local mean velocity at z_o (i.e. $U(z_o)$) to be the convection speed (U_c) of the flow structures (Baars et al., 2017). We expect the effects due to this assumption to be minimal since the present analysis is restricted to the log region where this assumption has been shown to perform reasonably well for estimating streamwise velocity correlations (Uddin, 1994; de Silva et al., 2015). Further, as noted by Alving et al. (1990), even the choice of U_c does not significantly influence the estimation of the structure inclination angle.

6.6 Results and discussions

6.6.1 Variation in scale-specific wall-coherence with spanwise offset

Quantitative support towards the idea of isolating large wall-coherent structures in the log region (proposed in §6.4) should come by analysing the one-dimensional (1-D) LCS (Baars et al., 2017; Baidya et al., 2019a). We employ it here to represent the streamwise-scale (λ_x) based linear coupling between z_o and z_r by considering u fluctuations acquired from the probes at these two locations, for various Δy, following:

$$\gamma_L^2(z_o, z_r, \Delta y; \lambda_x) = \frac{\mid \langle \widetilde{u}(z_o, \Delta y; \lambda_x)\widetilde{u}^*(z_r; \lambda_x)\rangle \mid^2}{\langle \mid \widetilde{u}(z_o, \Delta y; \lambda_x) \mid^2\rangle\langle \mid \widetilde{u}(z_r; \lambda_x) \mid^2\rangle} = \frac{\mid \phi_{u_o u_r}(z_o, z_r, \Delta y; \lambda_x) \mid^2}{\phi_{uu}(z_o, \Delta y; \lambda_x)\phi_{uu}(z_r; \lambda_x)} \quad (6.3)$$

where $\tilde{u}(z_o, \Delta y; \lambda_x) = \mathcal{F}[u(z_o, \Delta y)]$ is the Fourier transform of $u(z_o, \Delta y)$ in either time or x depending on the data set. The asterisk ($*$), angle brackets ($\langle\rangle$) and vertical bars ($||$) indicate the complex conjugate, ensemble averaging and modulus, respectively. Thus, $\phi_{u_o u_r}$ is the 1-D cross-spectrum between $u(z_o, \Delta y)$ and $u(z_r)$, while $\phi_{uu}(z_o)$ and $\phi_{uu}(z_r)$ are the energy spectra at z_o and z_r, respectively. γ_L^2 may be interpreted as the spectral

domain equivalent of a physical two-point correlation and varies between $0 \leq \gamma_L^2 \leq 1$ owing to the normalization defined in equation 6.3.

Figure 6.2(b) plots the γ_L^2 contours for $z_o^+ \approx 2.6\sqrt{Re_\tau}$ and $3.9\sqrt{Re_\tau}$ for the $\mathcal{E}_1$ data set. Following Baars et al. (2016a), we consider a coherence threshold of $\gamma_{filt}^2 = 0.05$ to identify a streamwise spectral cut-off $\lambda_{x,c}(z_o, z_r, \Delta y)$ to classify structures with $\lambda_x > \lambda_{x,c}(z_o, z_r, \Delta y)$ as being coherent between z_r and z_o for a specific Δy. As discussed in §6.4, it is observed that an increase in Δy leads to reduction in the range of scales correlated between the two probes (i.e. an increase in $\lambda_{x,c}$). While γ_{filt}^2 is used to identify relevant streamwise wavelengths, the spanwise offset between probes inherently filters out the possible range of spanwise wavelengths (λ_y) for coherent structures, i.e. $\lambda_y > \lambda_{y,c}$ where $\lambda_{y,c}/\delta \sim 2(\Delta y/\delta)$ (this has been highlighted as $(\lambda_y/\delta)_{min}$ on the secondary y-axis in figure 6.2(b)). It implies that on increasing $\Delta y/\delta$ to 0.1, for example, only structures with $\lambda_x/\delta > 3.5$ and $\lambda_y/\delta > 0.2$ are correlated between the two probes. This means that these wall-coherent structures, which are large both in length and span, have been *isolated* from the remaining assemblage of eddies. Hence, the corresponding cross-correlation shouldn't be influenced by the smaller structures.

It is noted that γ_L^2 contours for the two cases of z_o tend to overlap at large $\Delta y/\delta$, suggesting that a similar range of large wall-coherent structures (on an average) are correlated between probes at z_o and z_r, for any z_o lying in the log region (also observed by Baidya et al. (2019a)). Conclusions drawn from forthcoming discussions, focusing on these structures, are thus applicable across this region. Interestingly, figure 6.2(b) shows that superstructures ($\lambda_x/\delta > 10$; Hutchins and Marusic (2007)) remain correlated between the two probes up to $\Delta y/\delta \approx 0.14$. Such large structures, however, would be absent while analysing the data set $\mathcal{S}_1$ due to the limited streamwise domain ($\approx 11.9\delta$) considered.

6.6.2 Variation of mean structure inclination angle with spanwise offset

Having verified that large wall-coherent structures are isolated on increasing Δy between probes at z_r and z_o, we now investigate the variation of θ_m (with Δy) by locating the peak (Marusic and Heuer, 2007) in the correlation coefficient ($R_{u_o u_r}$) obtained on cross-correlating raw (unfiltered) velocity data from the two probes as follows:

$$R_{u_o u_r}(\Delta x, \Delta y) = \frac{\langle u(z_r; x, y) u(z_o; x + \Delta x, y + \Delta y) \rangle}{\sqrt{\langle u^2(z_r) \rangle} \sqrt{\langle u^2(z_o) \rangle}}. \tag{6.4}$$

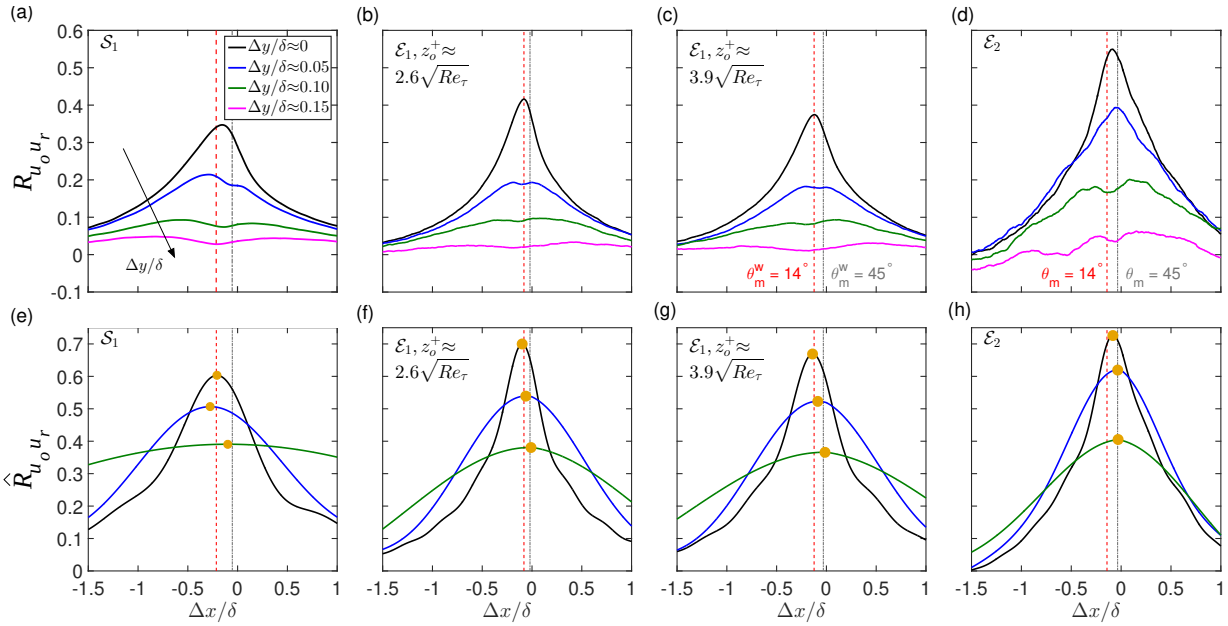

FIGURE 6.3: Cross-correlation of u measured at z_r and z_o, for various $\Delta y/\delta$, for data sets listed in table 6.2. (a)-(d) and (e)-(h) are correlations obtained from raw and large-wavelength pass filtered velocity time series, respectively with filter cut-off $\lambda_{x,c}(z_o,z_r,\Delta y)$ based on $\gamma_L^2(z_o,z_r,\Delta y) = 0.05$ computed for respective data sets. Red dashed and grey dot-dashed lines indicate $\Delta x/\delta$ corresponding to $\theta_m^w = 14°$ and $45°$ respectively for datasets $\mathcal{E}_1$ and $\mathcal{S}_1$, and $\theta_m = 14°$ and $45°$ respectively for dataset $\mathcal{E}_2$. Here, $\theta_m = \text{atan}((z_o\text{-}z_r)/\Delta x_p)$. Yellow bullets in (e)-(h) highlight the peak in the cross-correlation.

$R_{u_o u_r}(\Delta x)$ for the three data sets, at selected Δy, is plotted in figures 6.3(a-d). It may be observed that the correlation curve changes from having a clear distinct peak at $\Delta y \approx 0$ to one exhibiting a bi-modal behaviour as Δy increases, for all data sets. The magnitude of the peak also drops significantly, making it difficult to locate a unique peak and associate it with the streamwise delay (Δx_p) corresponding to the inclination of the *mean* structure. It is interesting to note that one of these two peaks in $R_{u_o u_r}$ is consistently close to $\Delta x \sim 0$ for all the datasets. Since $\Delta x \sim 0$ corresponds to $\theta_m^w \sim 90°$, this peak may be associated with the randomly oriented structures, for example isotropic structures, which are known (Alving et al., 1990) to bias the cross-correlation towards $\theta_m^w \sim 90°$ and negligibly contribute to the covariance (i.e. numerator in equation 6.4). It is quite possible that some of these structures, which have no preferred inclination angle, may also be coherent across the two probes, apart from the majority forward-inclined structures (Perry et al., 1992). To make things clearer, the velocity data at both z_o and z_r is passed through a long-wavelength pass filter with a filter bound, $\lambda_{x,c}(z_o,z_r,\Delta y)$ obtained from the corresponding $\gamma_{filt}^2(z_o,z_r,\Delta y) = 0.05$ for the three data sets (refer §6.6.1). Application of this filter ensures that only those streamwise wavelengths are considered which have been stochastically found to be

coherent between the two probes for various Δy (i.e. wall-coherent).

On filtering the velocity data, the new cross-correlation coefficient ($\hat{R}_{u_o u_r}$) is computed by replacing $u(z_o)$ and $u(z_r)$ with their filtered counterparts, $\hat{u}(z_o)$ and $\hat{u}(z_r)$ in equation 6.4 and is plotted in figures 6.3(e)-(h). Since $\lambda_{x,c}$ increases with Δy, $\hat{R}_{u_o u_r}$ becomes wider about the peak with increasing Δy. It is evident that the filtering aids in identification of a clear peak (highlighted by a yellow bullet) of the cross-correlation, with the associated correlation coefficient also having a significant value. The peak can be seen deviating from $\Delta x/\delta$ corresponding to $\theta_m = 14°$ (observed by Marusic and Heuer (2007)) towards that for 45° with increasing Δy. This observation supports our hypothesis proposed in §6.4 that $\theta_m \to \theta_s$ on increasing the spanwise offset between the two probes.

θ_m^w obtained from $\hat{R}_{u_o u_r}$ for data sets $\mathcal{E}_1$ and $\mathcal{S}_1$, at various Δy, is plotted in figure 6.4(a). Indeed, θ_m^w increases from approximately 14° at $\Delta y \approx 0$ with increasing Δy, reaching close to 50° at $\Delta y/\delta \approx 0.1$, after which it jumps abruptly to 90° for larger offsets. This jump to 90° suggests that eddies with an inherent forward inclination do not span across such large offsets and the coherence, $\gamma_L^2 \lesssim 0.1$ may be due to the randomly oriented eddies (Perry et al., 1992) co-existing in the TBL. These eddies tend to bias the cross-correlation peak towards $\Delta x \sim 0$ (Alving et al., 1990), which represents $\theta_m^w \sim 90°$ and has been observed in $R_{u_o u_r}$ plotted in figure 6.3. Taking this into consideration, the largest physically realistic values of θ_m^w are found to be approximately 35° and 50° at $\Delta y/\delta \approx 0.08$ and 0.10 respectively, which are both close to the theoretically supported angle of 45° (§6.1). This encourages us to conclude that θ_s^w is indeed nominally 45° for a large isolated flow structure. A similar trend of increasing θ_m^w, with increasing Δy, is also observed for the $\mathcal{S}_1$ data set (not shown completely for brevity), but the increment rate is relatively slow probably due to the limited streamwise scale range owing to the domain size selected for the analysis (discussed in §6.6.1). Since the coherence becomes lower than the threshold ($\gamma_L^2 \lesssim 0.05$) across all λ_x for $\Delta y/\delta \gtrsim 0.15$, no cross-correlation (and θ_m) is obtained for such spans after filtering.

6.6.3 Scale-specific inclination angle of wall-coherent structures

Analysing the cross-correlation yields θ_m which is influenced by a range of scales (Marusic, 2001). Since we see an increase in θ_m^w towards 45° with increase in Δy (figure 6.4(a)), it would be interesting to see how a streamwise-scale specific inclination angle ($\theta^w(\lambda_x)$) varies with Δy. Following Baars et al. (2016a), θ^w is obtained from the scale-dependant phase information embedded in the cross-spectrum ($\phi_{u_o u_r}$). $\phi_{u_o u_r}(\Delta y;\lambda_x) = \mathcal{F}[R_{u_o u_r}(\Delta y;\Delta x)]$

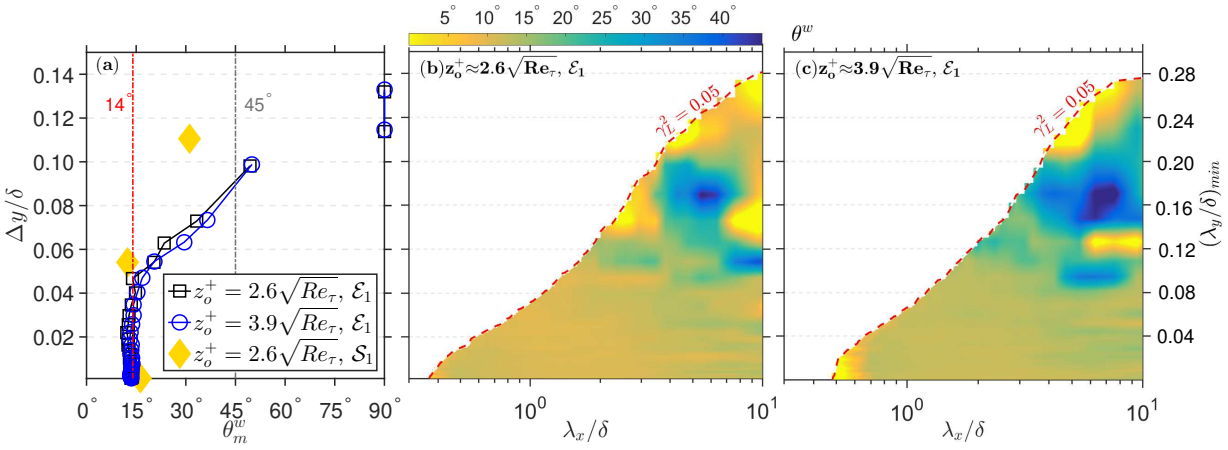

FIGURE 6.4: (a) Average structure inclination angle (θ_m^w) as a function of $\Delta y/\delta$ obtained by locating the peak of $\hat{R}_{u_o u_r}$ for data sets $\mathcal{E}_1$ and $\mathcal{S}_1$. (b,c) Scale-specific phase (Ψ) of the cross-spectra ($\phi_{u_o u_r}$), computed at various Δy, expressed as a physical inclination angle (θ^w) for $z_o^+ \approx$ (b) $2.6\sqrt{Re_\tau}$ and (c) $3.9\sqrt{Re_\tau}$ for data set $\mathcal{E}_1$.

has already been computed to find γ_L^2 in equation 6.3 and is complex-valued. The scale-specific phase (Ψ) is estimated from $\phi_{u_o u_r}$ as follows:

$$\Psi(\Delta y; \lambda_x) = atan\Big\{\frac{\Im[\phi_{u_o u_r}(\Delta y; \lambda_x)]}{\Re[\phi_{u_o u_r}(\Delta y; \lambda_x)]}\Big\} \tag{6.5}$$

where $\Im$ and $\Re$ denote the imaginary and real components of $\phi_{u_o u_r}$. Ψ essentially records the shift of each Fourier mode, λ_x owing to the correlation of u measured at two different wall-normal locations. A streamwise shift ($\mathrm{L}(\Delta y; \lambda_x)$) is obtained from the phase (which is in radians) by pre-multiplying it with the respective Fourier mode, i.e. $\mathrm{L}(\Delta y;\lambda_x) = \lambda_x \Psi(\Delta y; \lambda_x)/(2\pi)$. A scale-specific physical inclination angle is then computed at each Δy following:

$$\theta^w(\Delta y; \lambda_x) = atan\Big\{\frac{(z_o - z_r)}{\mathrm{L}(\Delta y; \lambda_x)}\Big\}. \tag{6.6}$$

$\theta^w(\lambda_x, \Delta y)$ is plotted in figures 6.4(b) and (c) for $z_o^+ \approx 2.6\sqrt{Re_\tau}$ and $3.9\sqrt{Re_\tau}$, respectively for data set $\mathcal{E}_1$. Here, we restrict our attention to streamwise wavelengths $\lambda_x/\delta \leq 10$ so that the interpretation of θ^w isn't influenced by the assumption of Taylor's hypothesis (de Silva et al., 2015).

It can be seen in both figures 6.4(b,c) that θ^w, in general, increases with Δy and corresponds well with the variation of θ_m^w shown in figure 6.4(a). At $\Delta y \approx 0$, all the wall-coherent scales agree to an almost constant angle of $\theta^w \approx 14°$, even at large λ_x (Baars et al., 2016a). This is because θ^w, here, is influenced by structures with $0 < \lambda_y < \infty$ meaning that not all

the influencing structures are large in the two-dimensional sense. As $\Delta y/\delta > 0.04$, θ^w increases across all $\lambda_x > \lambda_{x,c}$ since only structures of spanwise wavelength, $\lambda_y/\delta > 0.08$ influence the estimation. It is around this $\Delta y/\delta$ range where θ^w_m starts deviating from 14° (figure 6.4(a)). On increasing $\Delta y/\delta$ to 0.08, we are effectively considering only the large structures ($\lambda_x/\delta > 2$, $\lambda_y/\delta > 0.16$) for which $\theta^w \gtrsim 30°$, which aligns well with the previous estimations (θ_s; table 6.1) made via visualising individual structures. It also explains the average estimation, $\theta^w_m \approx 45°$ at similar offsets. The qualitatively similar variation of $\theta^w(\Delta y; \lambda_x)$ for both z_o^+, especially at high Δy (figures 6.4(b,c)), reinforces the fact that our conclusions should be applicable for all z_o^+ in the log region. It is difficult to physically interpret θ^w for $\Delta y/\delta > 0.11$ given that θ^w_m abruptly jumps to 90° for these offsets (figure 6.4(a)), suggesting contribution from randomly oriented structures to the cross-correlation.

6.6.4 Implications on LES and AEH-based simulations

Having empirically established that $\theta^w_s \approx 45°$ (nominally) for isolated large wall-coherent eddies, we now discuss possible implications of the findings of the present study on LES and AEH-based simulations. In recent AEH-based simulations (Baidya et al., 2014, 2017; Chandran et al., 2017), Λ-vortices organized in a packet are typically used as representative structures to statistically model the log region of a ZPG TBL. Simulation results reported by Marusic (2001) clearly indicate that the size, shape as well as the orientation of the eddies significantly influence the statistics yielded by the model. Over the years, researchers have attempted to improvise on the size and shape of the representative eddies (Marusic and Monty, 2019), via trial and error, to mimic the experimental trends. However, in the case of the orientation of the individual eddies (θ^w_s), considering support from the theory (§6.1) as well as flow visualizations reported in the seminal studies of Head and Bandyopadhyay (1981) and others, θ^w_s has always been assumed to be nominally 45°. This trend has continued over the years without any concrete empirical evidence, which this study has attempted to address. Here, via physical and statistical filters, we have isolated the large wall-coherent eddies and have empirically shown that θ^w_s is nominally 45° for these eddies, suggesting it to be a reasonable assumption for the orientation of the individual Λ-vortices considered for an AEH-based simulation.

Moving to the implication on LES simulations, due to limitations in computational power, high Re_τ LES simulations typically only compute the outer layer of the TBL (Piomelli and Balaras, 2002). The grid resolution for the simulation is thus chosen based on the outer layer eddies, making it incapable of resolving the relatively small eddies existing in

the inner layer of the TBL, in turn also limiting estimation of the wall shear stress (τ_w). In such a scenario, information from the computed outer flow is utilized to estimate τ_w (Marusic et al., 2001), wherein the inclination of the elongated eddies in the inner layer needs to be accounted for. Earlier studies (Carper and Porte-Agel, 2004; Piomelli et al., 1989) have used the experimentally obtained value of $\theta_m^w \approx 14^\circ$ as the mean inclination of these eddies. However, the empirical observations in the present study (figure 6.4(a)) in conjunction with the simulations of Marusic (2001) strongly suggest that θ_m^w depends on the range of scales being considered in the flow. Since the inclination angle of solely the unresolved structures in the inner layer needs to be taken into account while estimating τ_w, θ_m^w for these selective range of scales may be a function of the grid resolution and consequently may differ from 14°.

6.7 Concluding remarks

The streamwise inclination angle of large wall-coherent structures, in the log region of a TBL, is estimated statistically to be nominally 45°. This result was estimated by isolating these structures from the remaining assemblage of eddies by introducing a spanwise offset between the near-wall and log region reference probe, a methodology which was shown to be effective for TBL data sets across $Re_\tau \sim \mathcal{O}(10^3)$–$\mathcal{O}(10^6)$. The angle obtained closely resembles the inclination of individual 'hairpin'-type structures considered to be the dominant feature of a wall-bounded turbulent flow (Moin and Kim, 1985), suggesting wall-coherent structures to be of similar type. The present findings also provide empirical evidence in support of the eddy inclination angles considered when simulating a TBL with AEH model-based simulations. Although the empirical result, $\theta_s^w \approx 45^\circ$ may be limited to large wall-coherent structures, theoretical arguments discussed in §6.3 give a strong indication of what the approximate θ_s^w of relatively smaller wall-coherent structures would be. The present findings may also have implications for the wall-layer models employed in high Re_τ LES simulations of a TBL, which utilize experimentally determined θ_m^w to correlate wall-shear stress with the velocity estimated at the near-wall grid point. The present analysis reveals that θ_m^w is a function of the range of scales considered for its estimation, and this range would vary with the grid size considered for the LES simulation.

Acknowledgement

The authors wish to acknowledge the Australian Research Council for financial support and appreciate the publicly available DNS data of Sillero et al. (2013).

Chapter 7

Active and inactive components of the streamwise velocity in wall-bounded turbulence

[Published paper IV[1]]

7.1 Preface to the chapter

This chapter is an article published in the *Journal of Fluid Mechanics*, titled "Active and inactive components of the streamwise velocity in wall-bounded turbulence" (Deshpande et al., 2021). The study proposes a methodology to segregate the energy contributions associated with the active and inactive components (§2.2.2) in the inertial region of wall-bounded turbulent flows (Townsend, 1976). The efficacy of the proposed decomposition methodology is tested here for the streamwise velocity component by implementing it on the multi-point experimental dataset described in chapter 3. The methodology is based upon utilizing the two types of 2-D spectra, analyzed previously in chapter 4, as an input to decompose the total energy in the inertial region into two sub-components, associated with the active and inactive motions.

[1]Deshpande, R., Monty, J.P. & Marusic, I. (2021). Active and inactive components of the streamwise velocity in wall-bounded turbulence. *Journal of Fluid Mechanics* 914, A5. DOI: https://doi.org/10.1017/jfm.2020.884

7.2 Abstract

Townsend (1961) introduced the concept of active and inactive motions for wall-bounded turbulent flows, where the active motions are solely responsible for producing the Reynolds shear stress, the key momentum transport term in these flows. While the wall-normal component of velocity is associated exclusively with the active motions, the wall-parallel components of velocity are associated with both active and inactive motions. In this chapter, we propose a method to segregate the active and inactive components of the 2-D energy spectrum of the streamwise velocity, thereby allowing us to test the self-similarity characteristics of the former which are central to theoretical models for wall-turbulence. The approach is based on analyzing datasets comprising two-point streamwise velocity signals coupled with a spectral linear stochastic estimation (SLSE) based procedure. The data considered span a friction Reynolds number range $Re_\tau \sim \mathcal{O}(10^3)$ – $\mathcal{O}(10^4)$. The procedure linearly decomposes the full 2-D spectrum (Φ_{uu}) into two components, Φ^{ia}_{uu} and Φ^{a}_{uu}, comprising contributions predominantly from the inactive and active motions, respectively. This is confirmed by Φ^{a}_{uu} exhibiting wall-scaling, for both streamwise and spanwise wavelengths, corresponding well with the Reynolds shear stress cospectra reported in the literature. Both Φ^{a}_{uu} and Φ^{ia}_{uu} are found to depict prominent self-similar characteristics in the inertially dominated region close to the wall, suggestive of contributions from Townsend's attached eddies. Inactive contributions from the attached eddies reveal pure k^{-1}-scaling for the associated 1-D spectra (where k is the streamwise/spanwise wavenumber), lending empirical support to the attached eddy model of Perry and Chong (1982).

7.3 Introduction and motivation

The attached eddy model (Perry and Chong, 1982; Marusic and Monty, 2019), based on Townsend's attached eddy hypothesis (Townsend, 1976), is a conceptual model through which the kinematics in a wall-bounded flow can be statistically represented by a hierarchy of geometrically self-similar attached eddies that are inertially dominated (inviscid), and randomly distributed in the flow field. Here, the term 'attached' refers to a flow structure whose geometric extent, i.e. the size of its velocity field, scales with its distance from the wall (z) and mean friction velocity (U_τ), respectively. As per Townsend (1976), the attached eddies have a population density inversely proportional to their height ($\mathcal{H}$), which ranges between $\mathcal{O}(z_{min}) \lesssim \mathcal{H} \lesssim \mathcal{O}(\delta)$, where z_{min} corresponds to the start of the inertial region, while δ is the boundary layer thickness. At any $z \gtrsim z_{min}$, the cumulative contribution from

the range of attached eddies results in the streamwise and spanwise turbulence intensities varying logarithmically as a function of z, while the wall-normal variance is a constant following:

$$\begin{aligned} \overline{u^2}^+ &= B_1 - A_1 \ \ln(\frac{z}{\delta}), \\ \overline{v^2}^+ &= B_2 - A_2 \ \ln(\frac{z}{\delta}), \\ \overline{w^2}^+ &= B_3, \text{ and } \overline{uw}^+ = B_4, \end{aligned} \tag{7.1}$$

where A_1, A_2, B_1, B_2, B_3 and B_4 are constants. Here, u, v and w are the velocity fluctuations along the streamwise (x), spanwise (y) and wall-normal (z) directions, respectively, while superscript '+' denotes normalization by U_τ and kinematic viscosity (ν). Recent literature (Jimenez and Hoyas, 2008; Baidya et al., 2014; Lee and Moser, 2015; Orlandi et al., 2015) has reported substantial support for expressions corresponding to the lateral velocity statistics in (7.1), from experimental as well as simulation data, down to as low as $z^+ \sim 100$. Support for a log law for $\overline{u^2}^+$ has been more convincing from high-Re_τ experimental datasets (Hultmark et al., 2012; Marusic et al., 2013) in comparison to low-Re_τ simulations (Jimenez and Hoyas, 2008; Lee and Moser, 2015), likely owing to the lack of scale separation resulting in the self-similar contributions becoming obscured by the non-self-similar contributions at the same scale (Jimenez and Hoyas, 2008; Rosenberg et al., 2013; Baars and Marusic, 2020b). Recently, Baars and Marusic (2020b) were able to segregate these two contributions, consequently revealing the near-wall logarithmic growth (of $\overline{u^2}^+$) due to self-similar contributions down to $z^+ \sim 80$, with a slope of 0.98 ($= A_1$; also known as the Townsend-Perry constant).

Given that the turbulence intensities in (7.1) equate to the integrated spectral energy in the respective velocity fluctuations (that is, $\overline{u^2} = \int_0^\infty \phi_{uu} dk_x$, where ϕ_{uu} is the one-dimensional (1-D) streamwise velocity spectrum and k_x is the streamwise wavenumber), the contribution from the hierarchy of attached eddies also manifests itself in the energy spectra of the two wall-parallel velocity components; in the form of the so-called k_x^{-1}-scaling (Perry and Chong, 1982). This scaling has been predicted previously via dimensional analysis and other theoretical arguments (Perry and Abell, 1977; Perry et al., 1986; Nikora, 1999; Katul et al., 2012), with Perry et al. (1986) further arguing that the respective premultiplied spectra ($k_x^+\phi_{uu}^+$, $k_x^+\phi_{vv}^+$) should plateau at a constant value equal to the rate of logarithmic decay (A_1 and A_2) for $\overline{u^2}^+$ and $\overline{v^2}^+$. These predictions, however, are rarely observed at finite Re_τ, likely due to the flow containing a mixture of self-similar attached eddies and other non-self-similar flow structures. The difficulty in separating the two contributions may explain the lack of convincing empirical evidence of the k_x^{-1}-scaling for ϕ_{uu}, and its

association with A_1, in the literature (Nickels et al., 2005; Rosenberg et al., 2013; Baars and Marusic, 2020a,b).

Noting that experiments show that $\overline{u^2}^+$ and $\overline{v^2}^+$ varies with Reynolds number in the inertial region while $\overline{uw}^+$ does not (as per equations 7.1), Townsend (1961) commented that "*it is difficult to reconcile these observations without supposing that the motion at any point consists of two components, an active component responsible for turbulent transfer and determined by the stress distribution and an inactive component which does not transfer momentum or interact with the universal component.*" He further elaborated "*that the inactive motion is a meandering or swirling motion made up from attached eddies of large size which contribute to the Reynolds stress much further from the wall than the point of observation.*" This definition of active and inactive motions, however, seems to have been interpreted differently by some in the literature. Therefore, we attempt to clarify here our (and Townsend's) interpretation and emphasise its consistency with the attached eddy hypothesis (AEH).

7.3.1 Active and inactive motions

In the simplest attached eddy model, attached eddies are the only eddying motions present in the boundary layer, and they lead to 'active' and 'inactive' contributions. The key reason for this is the nature of the velocity signature from individual attached eddies in this inviscid model. The impermeability boundary condition at the wall enforces $w = 0$ at the wall, but allows slip (and hence finite u and v at the wall). This is achieved by producing attached eddy velocity fields using a vortex structure with image vortex pairs in the plane of the wall. The result is a spatially localised w-velocity signature from the attached eddies - this is well illustrated in figure 1 of Perry et al. (1986). Consequently, at any wall-normal location z in the inertial region, active motions are solely due to the velocity fields of the attached eddies of height, $\mathcal{H} \sim \mathcal{O}(z)$, and these contribute to $u(z)$, $v(z)$, $w(z)$ and hence $\overline{uw}(z)$. The inactive motions, however, are caused by the velocity fields from relatively large and taller attached eddies of height $\mathcal{O}(z) \ll \mathcal{H} \lesssim \mathcal{O}(\delta)$, and while these eddies contribute to $u(z)$ and $v(z)$, they make no significant contribution to $w(z)$. Hence, the inactive motions do not contribute to $\overline{uw}(z)$ (or $\overline{w^2}(z)$). Therefore, while both active and inactive motions contribute to $\overline{u^2(z)}$ (and $\overline{v^2(z)}$), there are only active contributions to $\overline{uw}(z)$ (or $\overline{w^2}(z)$). The consequence of this is that active motions are the component of attached-eddy contributions that have pure wall-scaling (z and U_τ). The remaining attached eddy contributions are the relatively large scale inactive motions

which, together with the inverse probability distribution of scales as per AEH, lead to the logarithmic decay of $\overline{u^2}^+$ and $\overline{v^2}^+$ (equation 7.1) with z.

Given the above, the resulting attached eddy velocity fields can thus be decomposed following Panton (2007):

$$\begin{aligned} u &= u_{\text{active}} + u_{\text{inactive}}, \\ v &= v_{\text{active}} + v_{\text{inactive}}, \\ w &= w_{\text{active}}, \end{aligned} \tag{7.2}$$

and as the active and inactive velocity fields are uncorrelated (Townsend, 1961; Bradshaw, 1967), the Reynolds stresses in equation (7.1) can also be decomposed as:

$$\begin{aligned} \overline{u^2} &= \overline{u^2}_{\text{active}} + \overline{u^2}_{\text{inactive}}, \\ \overline{v^2} &= \overline{v^2}_{\text{active}} + \overline{v^2}_{\text{inactive}}, \\ \overline{w^2} &= \overline{w^2}_{\text{active}}, \\ \overline{uw} &= \overline{(u_{\text{active}})(w_{\text{active}})}. \end{aligned} \tag{7.3}$$

Here, the active and inactive motions can be deemed uncorrelated only if we ignore the non-linear interactions across these motions, such as modulation, which have been shown to exist previously (Morrison, 2007; Mathis et al., 2009; Marusic et al., 2010a; Chernyshenko et al., 2012; Wu et al., 2019). However, such interactions will not contribute significantly to second-order velocity statistics (equation 7.3), which we restrict this chapter to. Modelling of skewness and higher-order statistics would, however, require modulation effects to be incorporated.

In real turbulent boundary layers, both self-similar and non-self-similar motions exist and contribute to the individual Reynolds stress components (Baars and Marusic, 2020a,b; Deshpande et al., 2020a; Yoon et al., 2020). Therefore, these additional non-self-similar contributions need to be recognized and appropriately accounted for while considering the decomposition in (7.3). They include the fine dissipative scales, as well as those corresponding to the inertial sub-range (Perry et al., 1986; Saddoughi and Veeravalli, 1994). These contributions, however, are small relative to those from the inertial motions (Perry et al., 1986), and may thus be deemed insignificant for a wall-bounded flow in the limit of $Re_\tau \to \infty$, which the inviscid AEH models. Other contributions include those from the very-large-scale-motions or superstructures (SS), which are associated with tall and large δ-scaled eddies spanning across the inertial region and contributing substantively to $\overline{u^2}$ and $\overline{v^2}$ (Baars and Marusic, 2020a,b; Deshpande et al., 2020a; Yoon et al., 2020). Evidence from the literature suggests that superstructures, however, do not contribute to $\overline{w^2}$, which

is confirmed by the wall-scaling exhibited by the 1-D w-spectra (Bradshaw, 1967; Morrison et al., 1992; Katul and Vidakovic, 1996; Kunkel and Marusic, 2006; Baidya et al., 2017). Given the aforementioned characteristics, when considering these superstructures in the context of active and inactive contributions, the motions would also have an inactive signature in $\overline{u^2}$ and $\overline{v^2}$ in the inertial region. The total inactive contributions can thus be segregated as:

$$\begin{aligned} \overline{u^2}_{\text{inactive}} &= \overline{u^2}_{\text{inactive,AE}} + \overline{u^2}_{\text{inactive,SS}}, \text{ and} \\ \overline{v^2}_{\text{inactive}} &= \overline{v^2}_{\text{inactive,AE}} + \overline{v^2}_{\text{inactive,SS}}, \end{aligned} \tag{7.4}$$

where $\overline{u^2}_{\text{inactive,SS}}$ and $\overline{u^2}_{\text{inactive,AE}}$ represent inactive contributions from the δ-scaled superstructures and self-similar attached eddies, respectively. It is the presence of the former, which obscures the pure logarithmic decay of $\overline{u^2}_{\text{inactive}}$ with z, as well as the true k_x^{-1}-scaling in the associated 1-D spectra (Jimenez and Hoyas, 2008; Rosenberg et al., 2013; Baars and Marusic, 2020a,b).

7.3.2 Present contributions

The present study first proposes a methodology to estimate $\overline{u^2}_{\text{active}}$ and $\overline{u^2}_{\text{inactive}}$ in the inertially-dominated region of a canonical wall-bounded flow. Developing this capability of segregating the active from the inactive component, especially for u, is of use to the wall-turbulence modelling community, since it is u_{active} which contributes to the momentum transfer (equation 7.3). The present methodology exploits the characteristic of the inactive motions (say at a given wall-normal distance z_o in the inertial region) being chiefly created by large eddies relative to the active motions at z_o; these inactive motions are coherent across a significant wall-normal distance (Townsend, 1976; Baars et al., 2017). For instance, Townsend (1961, 1976) describes the inactive motions at z_o as 'swirling' motions that influence the velocity field at all wall heights below z_o, including the wall-shear stress, via low frequency variations (see also §5.3 in Hwang (2015)). Such motions have their spectral signatures reflected in the u-signals recorded at z_o and below, down to the wall (say at a reference wall-normal location z_r). Recent work on the 1-D linear coherence spectrum by Baars et al. (2017) and Deshpande et al. (2019a) has shown that a scale-by-scale cross-correlation of the synchronously acquired u-signals, at z_o and z_r, isolates the energetic motions coherent across z_o and z_r, which may be deemed as inactive for the case of $z_r \ll z_o$. Following (7.3), the isolated energy contribution from the inactive motions ($\overline{u^2}_{\text{inactive}}$) can simply be subtracted from the total u-energy at z_o ($\overline{u^2}$) to yield contributions predominated by the active motions at z_o. This makes the present approach different to

previous analytical efforts, such as Panton (2007), wherein the active contributions were simply assumed to be proportional to the Reynolds shear stress to estimate the inactive contributions.

The methodology adopted here to segregate the active and inactive contributions, based on direct measurements, is also implemented later to separate the inactive motions into contributions from the self-similar attached eddies ($\overline{u^2}_{\text{inactive,AE}}$) and from the δ-scaled superstructures ($\overline{u^2}_{\text{inactive,SS}}$). While contributions from the latter are known to be predominant across the inertial region, the self-similar attached eddy contributions to the inactive motions reduce significantly beyond the δ-scaled upper bound of the logarithmic (log) region (Baars and Marusic, 2020a,b). By choosing the reference wall-normal location at this upper bound, say at a $z_r \gg z_o$, the scale-by-scale cross-correlation of the synchronously acquired u-signals at these z_o and z_r would isolate $\overline{u^2}_{\text{inactive,SS}}$, which following (7.4) can be used to estimate $\overline{u^2}_{\text{inactive,AE}}$.

To this end, two zero-pressure gradient turbulent boundary layer (ZPG TBL) datasets, comprising multi-point u-fluctuations measured synchronously across a wide range of wall-normal ($\Delta z = \mid z_o \text{ - } z_r \mid$) and spanwise ($\Delta y$) spacings, are considered. The datasets include measurements across the inertially-dominated (log) region, and the TBLs span a decade of Re_τ, permitting us to test for: (i) the universal wall-scaling of the u-spectra associated with the active motions at z_o, and (ii) the k_x^{-1}-scaling of the u-spectra associated with the self-similar attached eddies inactive with respect to z_o. These data are first used to directly compute the 2-D u-spectrum (Chandran et al., 2017, 2020), which gives a map of the energy contributions from eddies of various streamwise ($\lambda_x = 2\pi/k_x$) and spanwise ($\lambda_y = 2\pi/k_y$) wavelengths coherent across z_o and z_r (Deshpande et al., 2020a). The two-point statistics are then used as an input to a spectral linear stochastic estimation (SLSE; Tinney et al. (2006), Baars et al. (2016a)) based procedure, which estimates the subset of the 2-D u-energy spectrum at z_o, associated with specific coherent motions coexisting at z_o.

7.4 ZPG TBL datasets

Two ZPG TBL datasets, consisting of synchronous multi-point u-velocity fluctuations, are considered for analysis in the present study. One is the $Re_\tau \approx 2\,000$ DNS dataset of Sillero et al. (2014), while the other is the $Re_\tau \approx 15\,000$ experimental dataset, a part of which has been reported previously in Deshpande et al. (2020a). A brief description of the two datasets is presented below.

	$Re_\tau \approx 15\,000$ (Deshpande et al., 2020a)				$Re_\tau \approx 2\,000$ (Sillero et al., 2014)			
Set-up	z_o^+	z_r^+	TU_∞/δ	$(\Delta y)_{max}$	z_o^+	z_r^+	$(\Delta x)_{max}$	$(\Delta y)_{max}$
Φ_{uu}	**15**, 100, 200, 318, 477, 750, 1025, <u>2250</u>	$\approx z_o^+$	19 500	2.7δ	**15**, 120 – <u>250</u>	$= z_o^+$	11.9δ	7.6δ
Φ_{uu}^{cross}	100, 200, 318, 477, 750, 1025, <u>2250</u>	**15**	19 500	2.5δ	120 – <u>250</u>	**15**	11.9δ	7.6δ
Φ_{uu}^{cross}	100, 200, 318	<u>2250</u>	19 500	2.5δ	–	–	–	–

TABLE 7.1: A summary of the ZPG TBL datasets comprising synchronized multi-point u-signals at z_r^+ and z_o^+ used to compute two types of 2-D u-spectra, Φ_{uu} and Φ_{uu}^{cross}. The terminology has been described in §7.4.1 and figure 7.1. Underlined values represent the approximate upper bound of the log-region ($0.15Re_\tau$; Marusic et al. (2013)), while the values in bold represent the near-wall reference location. Superscript '+' denotes normalization in viscous units.

7.4.1 Multi-point measurements at $Re_\tau \approx 14\,000$

The high-Re_τ dataset was acquired in the large Melbourne wind tunnel (HRNBLWT) under nominal ZPG conditions and low free-stream turbulence levels (Marusic et al., 2015) across its working section dimensions of $\simeq 0.92$ m $\times$ 1.89 m $\times$ 27 m. The very long length (27 m), and capability to generate free-stream speeds of up to 45 ms^{-1}, permit ZPG TBL measurements to the order of Re_τ $(= \delta U_\tau/\nu) \approx 26\,000$ in this facility. In the present study, all measurements were conducted at a location approximately 20 m from the start of the working section, at a free-stream speed of $U_\infty \approx 20$ ms^{-1}, resulting in a ZPG TBL at $Re_\tau \approx 15\,000$. The TBL thickness δ here is estimated via the modified Coles law of the wake fit (Jones et al., 2001) for both datasets. The multi-point measurements were made possible by a unique experimental set-up (Chandran et al., 2017) employing four hotwire probes (HW_{1-4}), the arrangement of which is depicted in figure 7.1(a). Wollaston hotwire probes of diameter, $d \approx 2.5\,\mu$m and exposed sensor length, $l \approx 0.5$ mm were used for all the measurements, resulting in an acceptable length-to-diameter ratio of approximately 200 (Hutchins et al., 2009) and a viscous-scaled sampling length, l^+ $(= lU_\tau/\nu) \approx 22$ for the

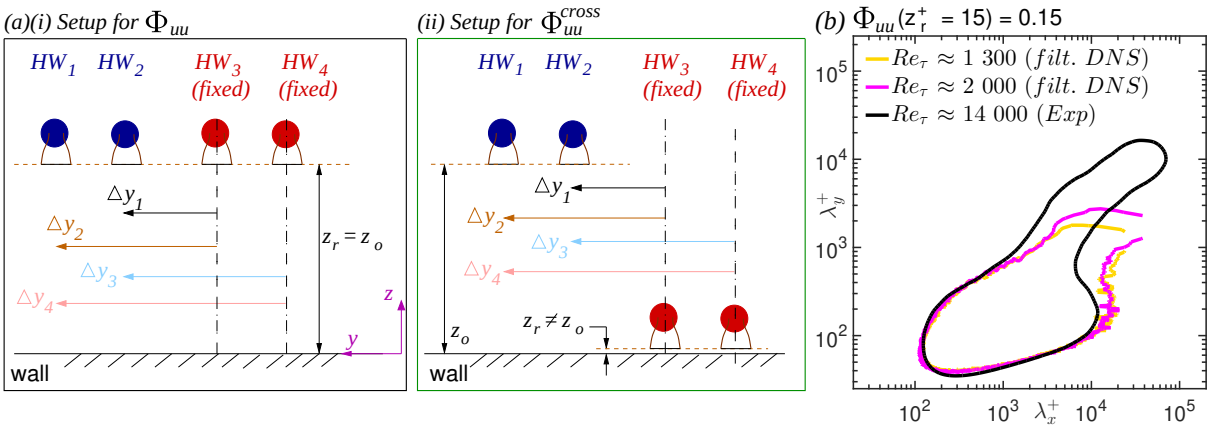

FIGURE 7.1: (a) Schematic of the experimental set-up in HRNBLWT showing relative positioning and movement of the four hot-wire probes (HW_{1-4}) for reconstructing the 2-D correlation corresponding to (i) Φ_{uu} and (ii) Φ_{uu}^{cross}. Mean flow direction is along x. In the case of (ii), HW_{3-4} are positioned at either $z_r \ll z_o$ or $z_r \gg z_o$, depending on the desired experiment (table 7.1). (b) Constant energy contours for $\Phi_{uu}(z_o^+ = z_r^+ \approx 15) = 0.15$, computed from the present experimental and the converged DNS dataset of Sillero et al. (2014), plotted as a function of viscous-scaled wavelengths. Estimates from the DNS are box-filtered along y to mimic the spatial resolution of the hotwire sensors. Figure concept for (a) has been adopted from Deshpande et al. (2020a).

given measurements. This hotwire length is sufficiently small compared to the energetic spanwise wavelengths in the inertial region, which can be inferred from the spanwise spectra of the u-velocity component from any published DNS dataset (for instance, see figure 9 of Lee and Moser (2015)). The sensors were operated in a constant temperature mode using an in-house Melbourne University Constant Temperature Anemometer (MUCTA) at an overheat ratio of 1.8 and at a viscous-scaled sampling rate, $\Delta T^+ \equiv U_\tau^2/(\nu f_s) \approx 0.5$, where f_s refers to sampling frequency.

The experimental set-up, as depicted in figure 1, allows HW_{1-2} to be traversed in the spanwise direction at a consistent wall-normal distance of z_o, while HW_{3-4} remain stationary at a fixed spanwise and wall-normal (z_r) location throughout the measurement. To calibrate the probes, the same procedure as that employed by Chandran et al. (2017) was implemented with HW_1, HW_2 and HW_4 simultaneously calibrated at a common wall-normal location by using the free-stream calibrated HW_3 as a reference. Simultaneously acquired u-signals from the four hotwires are used to reconstruct the two-point correlation:

$$R_{u_o u_r}(z_o, z_r; \Delta x, \Delta y) = \overline{u(z_r; x, y)u(z_o; x + \Delta x, y + \Delta y)} \tag{7.5}$$

for the Δy range, $0 \leq \Delta y \leq (\Delta y)_{max}$ and the total sampling duration (T) of the u-signals listed in table 7.1, with the overbar denoting ensemble time average. Taylor's frozen

turbulence hypothesis, which considers all the coherent structures coexisting at z_o to be convecting at the mean velocity at z_o (i.e. $U_c = U(z_o)$), is used to convert $R_{u_o u_r}$ from a function of time to that of Δx, with U_c denoting the convection velocity assumed at z_o. Following this, the 2-D Fourier transform of $R_{u_o u_r}$ is computed to obtain the 2-D spectrum as:

$$\phi_{u_o u_r}(z_o, z_r; k_x, k_y) = \int\int_{-\infty}^{\infty} R_{u_o u_r}(z_o, z_r; \Delta x, \Delta y) e^{-j2\pi(k_x \Delta x + k_y \Delta y)} d(\Delta x) d(\Delta y), \quad (7.6)$$

with j a unit imaginary number.

For this study, we are only concerned with two types of 2-D spectra, Φ_{uu} and Φ_{uu}^{cross} which are defined as:

$$\begin{aligned} \Phi_{uu}(z_o^+; \lambda_x, \lambda_y) &= |k_x^+ k_y^+ \phi_{uu}^+(z_o^+; \lambda_x, \lambda_y)| \text{ and} \\ \Phi_{uu}^{cross}(z_o^+, z_r^+; \lambda_x, \lambda_y) &= |k_x^+ k_y^+ \phi_{u_o u_r}^+(z_o^+, z_r^+; \lambda_x, \lambda_y)|, \end{aligned} \quad (7.7)$$

with the $R_{u_o u_r}$ corresponding to the former and latter, reconstructed via hotwire arrangements depicted in figure 7.1(a,i) and 7.1(a,ii), respectively. Here, $z_o^+ = \frac{z_o U_\tau}{\nu}$ and $k_x^+ = \frac{k_x \nu}{U_\tau}$ (with similar definitions for other associated terms), where the superscript '+' indicates normalization in viscous units. Table 7.1 details the exact wall-normal locations for which Φ_{uu} and Φ_{uu}^{cross} are computed, with (||) referring to the modulus operation. The present analysis is focused in the inertially-dominated region, considered nominally to exist beyond $z_o^+ \gtrsim 100$ (Nickels et al., 2005; Lee and Moser, 2015; Chandran et al., 2017; Baars and Marusic, 2020a), based on the empirical evidence discussed in §7.3. While Φ_{uu} represents contributions from all coexisting motions at z_o, Φ_{uu}^{cross} consists of contributions from only those motions that are coherent across z_o and z_r (Deshpande et al., 2020a). Both these spectra are used as an input to the SLSE methodology (§7.5) to estimate subsets of $\Phi_{uu}(z_o)$ representing contributions from a specific family of coherent motions coexisting at z_o. Φ_{uu}^{cross} has been estimated for two different reference wall-normal positions (z_r; table 7.1), each targeted at isolating specific contributions. The measurements to obtain $\Phi_{uu}^{cross}(z_o^+, z_r^+ \approx 0.15 Re_\tau)$, however, were conducted following the same methodology as that adopted for $\Phi_{uu}^{cross}(z_o^+, z_r^+ \approx 15)$, which have been reported previously in Deshpande et al. (2020a) and may be consulted for further details.

The present study also reports the first measurements of Φ_{uu} in the near-wall region ($z_o^+ = z_r^+ \approx 15$), which is required as per the SLSE methodology (§7.5) being adopted in the present study. Figure 7.1(b) compares the constant energy contour for this experimentally estimated Φ_{uu} against the same computed from the converged 2-D u-correlations

available from the DNS dataset of Sillero et al. (2014). While a reasonable overlap of contours is observed in the small-scale range (figure 7.1(b)), when plotted as a function of viscous-scaled wavelengths, a prominent 'footprint' can be noted appearing for the large scales with increase in Re_τ. This is representative of the increasing influence of the large scales in the near-wall region with increase in Re_τ, as discussed by Hutchins and Marusic (2007) and Hutchins et al. (2009). Here, the spectra from the DNS are box-filtered for better one-to-one comparison with the experimental spectrum, wherein the energy in the small-scales is underestimated due to the spatial resolution of the hotwire sensor (Hutchins et al., 2009). The box-filtering is carried out along the y-direction, by following the same methodology as outlined in Chin et al. (2009), taking into consideration the viscous-scaled hotwire sensor length corresponding to the measurements ($l^+ \approx 22$). Another thing to note here is that the contour corresponding to the experimental spectrum deviates significantly from the low-Re_τ DNS estimates at large wavelengths. This is possibly due to the failure of Taylor's hypothesis for these large-scales in the near-wall region (del Álamo and Jiménez, 2009; Monty and Chong, 2009). This inconsistency, however, doesn't affect any of the forthcoming analysis since all the calculations (§7.5) for the experimental dataset are carried out in the frequency domain before converting to λ_x via Taylor's hypothesis.

7.4.2 DNS dataset

A low-Re_τ dataset from the ZPG TBL DNS of Sillero et al. (2014) is also considered in the present study. Thirteen raw DNS volumes, each of which is a subset of their full computational domain between $x \approx 28.4\delta$ and $x \approx 40.3\delta$, are selected to ensure a limited Re_τ increase along x. Streamwise velocities $u(z_o^+;x,y)$ extracted from these fields are used to compute $\Phi_{uu}(z_o^+)$ and $\Phi_{uu}^{cross}(z_o^+, z_r^+ \approx 15)$ following (7.5) – (7.7), at z_o^+ and z_r^+ consistent with the experimental dataset (table 7.1). A similar analysis is also conducted using the instantaneous wall-normal velocity fluctuations, $w(z_o^+;x,y)$ extracted from this dataset. It is used to establish the efficacy of the SLSE-based methodology being implemented here to segregate active and inactive contributions, the results from which are discussed in appendix 1.

7.5 Energy decomposition into active and inactive contributions

As discussed in §7.3, the inactive motions at z_o are predominantly large motions (with respect to z_o) that are coherent across a significant wall-normal distance. This forms the basis for decomposing $\Phi_{uu}(z_o)$. Classically, the size and scaling of the coherent structures have been interpreted via two-point cross-correlations (Ganapathisubramani et al., 2005; Hutchins and Marusic, 2007). Correlations represent contributions from a wide range of scales which, during the ensemble averaging procedure, do not distinguish the individual contributions from the small and large motions (Baars et al., 2017; Deshpande et al., 2019a). Therefore, the present investigation has been conducted entirely in the spectral domain. Previous studies (Balakumar and Adrian, 2007) employing the spectral approach have utilized a sharp streamwise spectral cut-off to segregate the large motions from the rest of the turbulence, which inherently comes with a drawback that the estimates are cut-off dependent.

Here, the intention is to perform an unconditional linear decomposition of $\Phi_{uu}(z_o)$ into its inactive and residual component (figure 7.2) by utilizing the scale-by-scale coupling between u-signals simultaneously measured at two wall-normal locations, z_o^+ (in the inertially-dominated region) and $z_r^+ \approx 15$, ensuring $z_r^+ \ll z_o^+$. A linear decomposition was deemed sufficient for this purpose given the fact that the coupling has been computed between velocity signals at both ends (Guezennec, 1989; Baars et al., 2016a), and that the present interests are limited to the second-order velocity statistics (§7.3). $\Phi_{uu}^{cross}(z_o^+, z_r^+ \approx 15)$, which is considered here at various z_o^+ for both the experimental and DNS datasets, represents this scale-by-scale coupling. On comparing $\Phi_{uu}^{cross}(z_o^+, z_r^+ \approx 15)$ and $\Phi_{uu}(z_o^+)$ contours from the two datasets at various z_o^+ in figures 7.2(a,c), the former is representative of energetic large-scales that can be associated with the motions inactive at z_o^+. It is evident that $\Phi_{uu}^{cross}(z_o^+, z_r^+ \approx 15)$ also inherently comprises energy contributions from the δ-scaled superstructures ($\lambda_x \gtrsim 6\delta$), which are known to extend from the wall and span across the inertial region (Baars and Marusic, 2020a,b; Deshpande et al., 2020a; Yoon et al., 2020). We use Φ_{uu}^{cross} in conjunction with the SLSE (Tinney et al., 2006; Baars et al., 2016a) to obtain a linear stochastic estimate of the spectrum (Φ_{uu}^{ia}) associated with the inactive motions at z_o following:

$$\Phi_{uu}^{ia}(z_o^+; \lambda_x, \lambda_y) = \frac{\left[\Phi_{uu}^{cross}(z_o^+, z_r^+ \approx 15; \lambda_x, \lambda_y)\right]^2}{\Phi_{uu}(z_r^+ \approx 15; \lambda_x, \lambda_y)}. \tag{7.8}$$

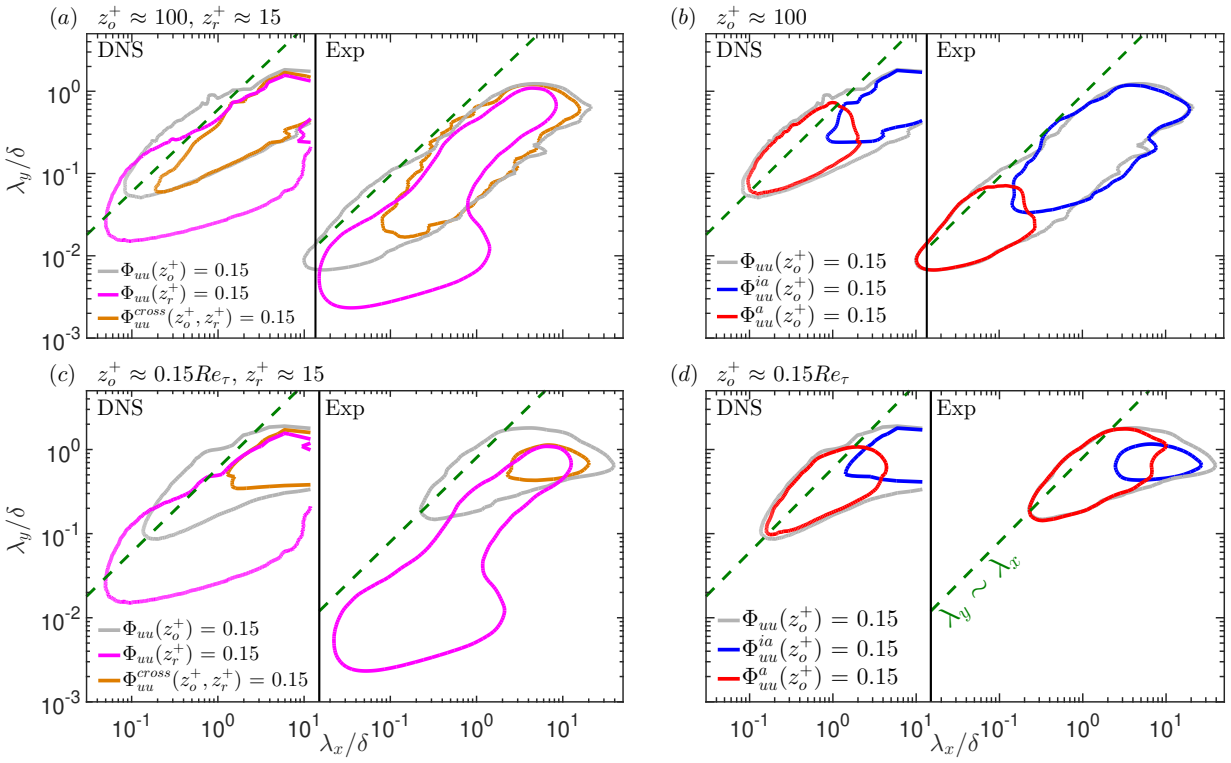

FIGURE 7.2: (a,c) Constant energy contours for $\Phi_{uu}(z_o^+)$, $\Phi_{uu}^{cross}(z_o^+, z_r^+ \approx 15)$ and $\Phi_{uu}(z_r^+ \approx 15)$ at energy level of 0.15 plotted for (a) $z_o^+ \approx 100$ and (c) $z_o^+ \approx 0.15Re_\tau$. (b,d) Constant energy contours for $\Phi_{uu}^{ia}(z_o^+)$ and $\Phi_{uu}^{a}(z_o^+)$, computed via (7.8) and (7.9), plotted at the same energy level and z_o^+ as in (a,c), respectively. In (a-d), contours on the left side correspond to those computed from the DNS data while those on the right are from the experimental data. Dashed green lines represent the linear relationship, $\lambda_y \sim \lambda_x$.

Interested readers may refer to appendix 1 to see the step-by-step procedure to arrive at the expression in (7.8). The mathematical operation in the above equation suggests $\Phi_{uu}^{ia}(z_o^+)$ to be essentially a normalized version of $\Phi_{uu}^{cross}(z_o^+, z_r^+ \approx 15)$, with the scale-by-scale normalization done by $\Phi_{uu}(z_r^+ \approx 15)$, the contours for which are also plotted in figures 7.2(a,c). It should be noted here that the calculations in (7.8) are carried out in the frequency domain for the experimental dataset, with the conversion to λ_x by invoking Taylor's hypothesis, using $U_c = U(z_o)$ (Baars et al., 2016a, 2017). Following the linear superposition assumption in (7.3), Φ_{uu}^{ia} can be simply subtracted from Φ_{uu} to leave a residual:

$$\Phi_{uu}^{a}(z_o^+; \lambda_x, \lambda_y) = \Phi_{uu}(z_o^+; \lambda_x, \lambda_y) - \Phi_{uu}^{ia}(z_o^+; \lambda_x, \lambda_y), \tag{7.9}$$

with Φ_{uu}, Φ_{uu}^{ia} and Φ_{uu}^{a} representative of $\overline{u^2}^+$, $\overline{u^2}^+_{\text{inactive}}$ and $\overline{u^2}^+_{\text{active}}$, respectively. If the flow consisted of only active and inactive inertial motions, Φ_{uu}^{a} and Φ_{uu}^{ia} would be the active and inactive component, respectively. However, we refer to Φ_{uu}^{a} as the residual spectrum,

given that it also comprises small contributions from the fine dissipative scales as well as those corresponding to the inertial sub-range (§7.3). We limit their influence in the present analysis by focusing our investigation on the high energy contours of Φ^{a}_{uu}, which are associated predominantly with the inertial active motions.

Figures 7.2(b,d) show the constant energy contours for the two components $\Phi^{ia}_{uu}(z_o^+)$ and $\Phi^{a}_{uu}(z_o^+)$, computed via (7.8) and (7.9), using the corresponding inputs plotted in figures 7.2(a,c), respectively. While Φ^{ia}_{uu} takes up the large-scale portion of Φ_{uu}, Φ^{a}_{uu} is restricted to the small-scale end of the spectrum. This is in spite of the fact that $\Phi^{cross}_{uu}(z_o^+, z_r^+ \approx 15)$ also comprises contributions from relatively small scales at $z_o^+ \approx 100$ (figure 7.2(a)) and can be explained by the linear transfer kernel (equations 7.15 and 7.16), which has been computed at various z_o^+ for the DNS dataset and shown in figure 7.8(a) in appendix 1. Interestingly, at $z_o^+ \approx 100$ (figure 7.2(b)), both $\Phi^{a}_{uu}(z_o^+)$ and $\Phi^{ia}_{uu}(z_o^+)$ can be seen to follow the $\lambda_y \sim \lambda_x$ relationship representative of geometric self-similarity, which is otherwise obscured for Φ_{uu} in the intermediate and large-scale range (Chandran et al., 2017, 2020; Deshpande et al., 2020a). The self-similar characteristic of Φ^{ia}_{uu} and Φ^{a}_{uu} is consistent with the hypothesis of Townsend (1961, 1976), who originally described both the active and inactive motions to be associated purely with the attached eddy contributions, but conforming to a different range of scales: the active motions at z_o^+ conform to the attached eddies with height, $\mathcal{H} \sim \mathcal{O}(z_o)$, while the inactive motions conform to relatively large eddies with $\mathcal{O}(z_o) \ll \mathcal{H} \lesssim \mathcal{O}(\delta)$ (see §7.3). Consequently, the contribution from the attached eddies to Φ^{ia}_{uu} reduces with increase in z_o^+, with energy contours at $z_o^+ \approx 0.15Re_\tau$ (figure 7.2(d)) corresponding predominantly to the tall δ-scaled superstructures coexisting across the inertial region. This likely explains why Φ^{ia}_{uu} contours do not align along $\lambda_y \sim \lambda_x$ at z_o^+ farthest from the wall. It also forms the basis for choosing $z_r^+ \approx 0.15Re_\tau$ as a reference wall height while implementing the SLSE methodology to isolate the superstructure contributions, which will be discussed later in §7.7.1. Φ^{a}_{uu}, on the other hand, comprises a significant range of scales irrespective of the change in z_o^+, with the contours simply shifting to relatively larger scales, which is suggestive of its distance-from-the-wall (z_o) scaling. Having defined the procedure to obtain Φ^{a}_{uu} and Φ^{ia}_{uu}, next we test for z_o- and δ-scaling to verify the extent to which the respective spectra can be associated with the active and inactive motions.

7.6 Active component of the streamwise velocity spectrum

Figures 7.3(a,b) show the constant energy contours of Φ^a_{uu} (= 0.15), computed from both DNS and experimental datasets, plotted as a function of wavelengths scaled with z_o and δ, respectively. The contours are plotted for Φ^a_{uu} across $100 \lesssim z_o^+ \lesssim 0.15Re_\tau$ and are seen to reasonably follow wall-scaling, that is, when the wavelengths are normalized by z_o. In contrast, no such collapse is observed when the wavelengths are scaled with δ. It is noted that this behaviour is only apparent after separating Φ^a_{uu} from Φ_{uu}. For comparison, figure 7.4 in §7.7 shows the corresponding Φ_{uu} results which exhibit both z_o- and δ-scaling in the intermediate and large-scale wavelength ranges, respectively (due to the wall-parallel velocity field associated with both the active and inactive motions (Bradshaw, 1967; Baidya et al., 2017)).

The z_o-scaling behaviour noted for Φ^a_{uu} is consistent with active motions. This can be seen by comparing the scaling behaviour of 1D w-spectra and 1D uw-cospectra, which have been shown to follow wall-scaling and exhibit a behaviour exclusively associated with active motions (Bradshaw, 1967; Morrison et al., 1992; Baidya et al., 2017). To this end, Φ^a_{uu} is integrated along λ_y and λ_x to obtain the corresponding premultiplied 1-D spectra as a function of λ_x ($\Phi^a_{uu,x}$; figure 7.3(c)) and λ_y ($\Phi^a_{uu,y}$; figure 7.3(d)), respectively. Also plotted, are the pre-multiplied 1-D w-spectra (figure 7.3(f)) and uw-cospectra (figure 7.3(e)) at $100 \lesssim z_o^+ \lesssim 0.15Re_\tau$ from the $Re_\tau \approx 10\,000$ dataset of Baidya et al. (2017), measured at the same experimental facility as Deshpande et al. (2020a). When the wavelengths are scaled with z_o, the 1-D spectra in figures 7.3(c-f) are observed to collapse for $\lambda \gtrsim z_o$, in-line with the characteristics of active motions. Further, both $\Phi^a_{uu,x}$ and $k_x^+\phi^+_{uw}$ peak at $\lambda_x \sim 10z_o$, supporting the argument that the motions associated with Φ^a_{uu} contribute to the Reynolds shear stress and can hence be deemed active in the sense of Townsend (1961, 1976). The efficacy of the present SLSE-based methodology, to extract energetic contributions from the active motions, can also be tested by implementing it on similar two-point statistics computed for the w-velocity component. Given that the w-component is associated exclusively with the active motions (§7.3), the present methodology can be deemed effective if it reveals negligible energy contributions from the inactive spectrum for the w-component. Interested readers may refer to appendix 1 where the SLSE analysis conducted on the w-component has been discussed.

Small scales ($\lambda \ll z_o$), which correspond to the viscous dissipative scales or those following the inertial sub-range scaling, do not scale with distance from the wall, explaining the

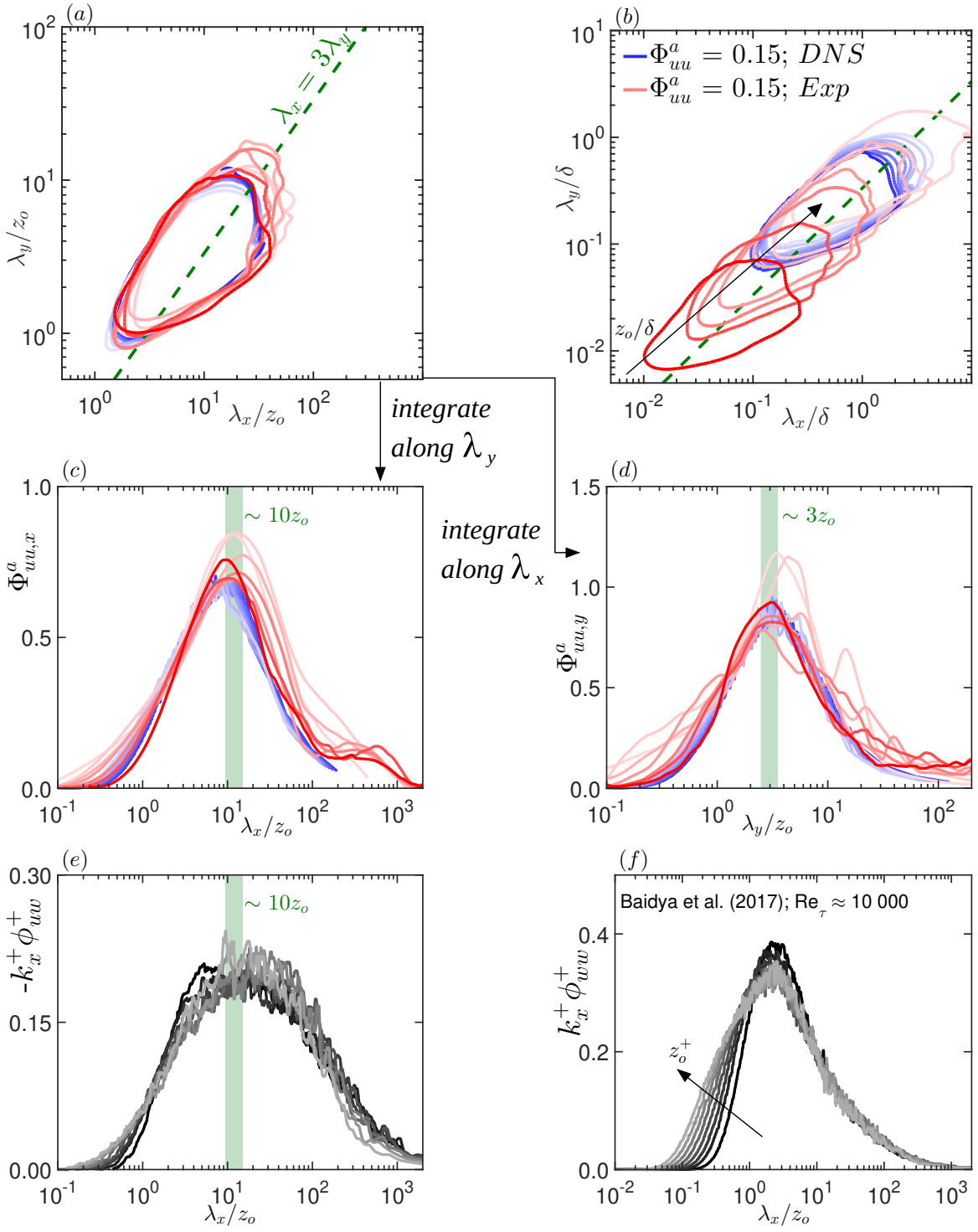

FIGURE 7.3: (a,b) Constant energy contours for $\Phi^a_{uu}(z_o^+)$ at energy level of 0.15 plotted for various z_o^+ as a function of wavelengths scaled with (a) z_o and (b) δ. Contours in red and blue correspond to Φ^a_{uu} estimated for the experimental and DNS datasets respectively (table 7.1), with dark to light shading indicating an increase in z_o^+ following $100 \lesssim z_o^+ \lesssim 0.15Re_\tau$ for Re_τ corresponding to respective datasets. Dashed green lines represent the linear relationship, $\lambda_x = 3\lambda_y$. (c,d) $\Phi^a_{uu}(z_o^+)$ integrated across λ_y and λ_x to obtain its corresponding 1-D version as a function of (c) λ_x and (d) λ_y respectively, each plotted with wavelengths scaled by z_o. Same colour coding is followed as that described for (a,b). (e,f) Pre-multiplied streamwise 1-D cospectra/spectra for the (e) Reynolds shear stress and (f) wall-normal velocity plotted as a function of λ_x scaled with z_o. This data is from the $Re_\tau \approx 10\,000$ dataset of Baidya et al. (2017) for various z_o^+. Dark to light shading corresponds to the increase in z_o^+ following $100 \lesssim z_o^+ \lesssim 0.15Re_\tau$, where $Re_\tau \approx 10\,000$.

deviation from the collapse of the 1-D spectra in figures 3(c,d,f). A similar deviation, although at a much smaller magnitude, is also observed for the Reynolds shear stress cospectra, which eventually drops to zero at $\lambda_x/z_o \lesssim 0.2$ owing to the approximate isotropy of these fine scales (Saddoughi and Veeravalli, 1994). On a side note, the reasonable agreement between $\Phi^a_{uu,x}$ estimated from the DNS and experimental datasets also validates the use of the local mean velocity as the convection velocity ($U_c = U(z_o)$) for the active motions, which seems intuitive given these are localized at z_o.

The present analysis, which is conducted along both the x and y directions, also reveals the dominant spanwise wavelength corresponding to the active motions, i.e. $\lambda_y \sim 3z_o$ (figure 7.3(d)). This yields the dominant streamwise/spanwise aspect ratio of $\lambda_x/\lambda_y \sim$ 3-4 for these motions, which is found to be true across a decade of Re_τ (indicated by dashed line in figures 7.3(a,b)). A similar SLSE-based analysis, as implemented here for the u-velocity spectrum, was conducted on the DNS dataset to analyze the active component of the v- and w-velocity spectrum (not shown here for brevity). These components were also found to exhibit wall-scaling, across the inertially-dominated region, with the contours of the spectrum following the self-similar relationship, $\lambda_x/\lambda_y \sim 1$ and $\lambda_x/\lambda_y \sim 1.4$ for the v and w-velocity spectrum, respectively (see Deshpande et al. (2020c)). Interestingly, the aspect ratio found for the active u-spectrum matches that of the self-similar wall-coherent vortex clusters ($\lambda_x \sim$ 2-$3\lambda_y$) investigated by del Álamo et al. (2006), Hwang (2015) as well as very recently by Hwang et al. (2020), revealing information which may be useful for modelling the active motions in future works. The close agreement with Hwang (2015) further suggests Φ^a_{uu} and Φ^{ia}_{uu}, both of which comprise of prominent self-similar contributions (figures 7.2,7.3,7.4), correspond well with the two component attached eddy structure proposed by Hwang (2015) for a wall-bounded turbulent flow. In their case, Hwang (2015) defined motions at a given spanwise scale to be composed of two distinct components: the first is the long streaky flow structure, attached to the wall and having significant turbulent kinetic energy, but inactive in the inner-region. The energy contributions from these motions are represented by Φ^{ia}_{uu}. While, the second component corresponds to the short and tall self-similar vortex packets which are active in the inner-region, and hence would contribute to Φ^a_{uu}.

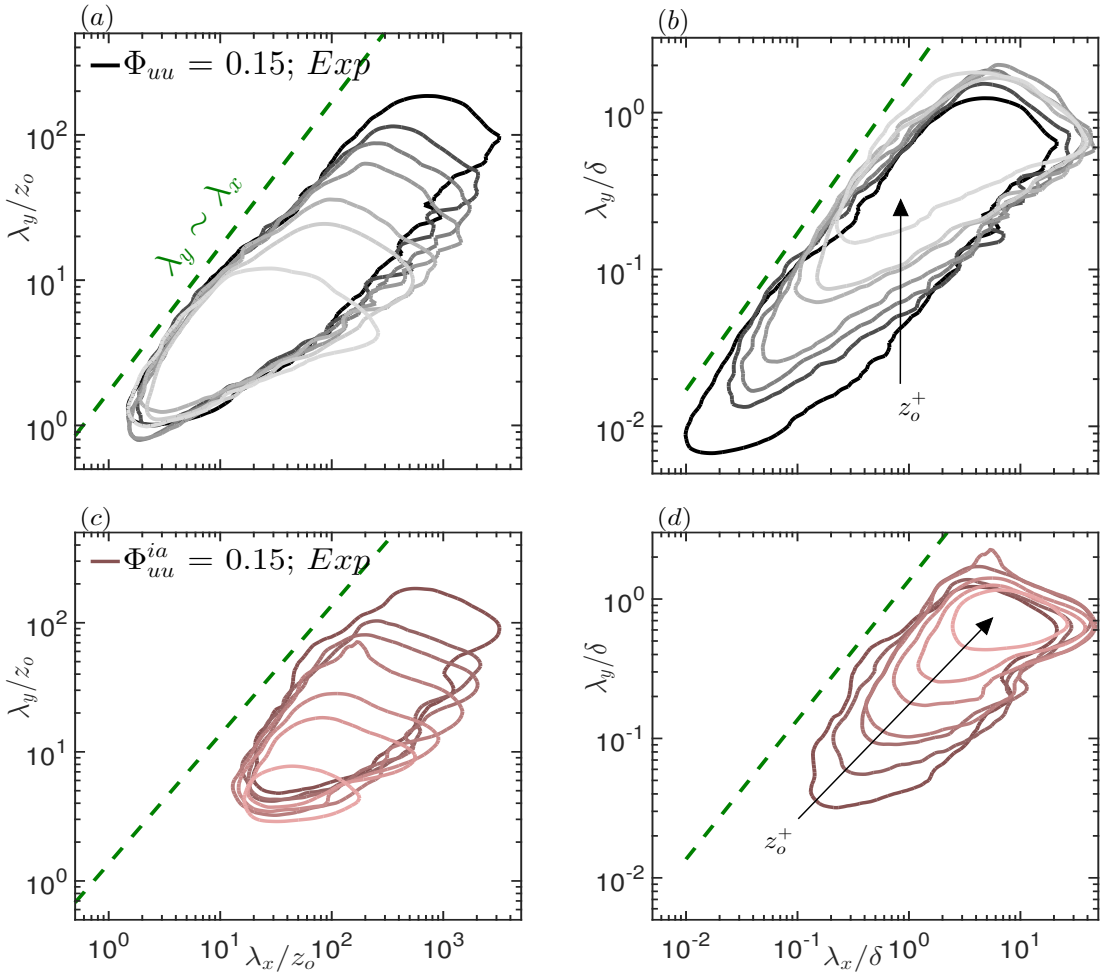

FIGURE 7.4: Constant energy contours for (a,b) $\Phi_{uu}(z_o^+)$ and (c,d) $\Phi_{uu}^{ia}(z_o^+)$ at energy level of 0.15 plotted for various z_o^+ as a function of wavelengths scaled with (a,c) z_o and (b,d) δ, respectively. All data in (a-d) corresponds to the high-Re_τ experimental dataset reported in table 7.1, with dark to light shading indicating an increase in z_o^+ following $100 \lesssim z_o^+ \lesssim 0.15Re_\tau$. Dashed green lines represent the linear relationship, $\lambda_y \sim \lambda_x$.

7.7 Inactive component of the streamwise velocity spectrum

Figure 7.4 shows the constant energy contours of Φ_{uu} (figures 7.4(a,b)) and Φ_{uu}^{ia} (figures 7.4(c,d)), computed for the experimental dataset, plotted as a function of wavelengths scaled with z_o (figures 7.4(a,c)) and δ (figures 7.4(b,d)). These contours are plotted at the same energy level and for the same z_o^+, as in figures 7.3(a,b). Consistent with the observations of Bradshaw (1967) and Baidya et al. (2017) for the 1-D u-spectra, Φ_{uu} contours can be observed to be exhibiting z_o-scaling in the intermediate scales ($\mathcal{O}(1) \lesssim$

$\lambda/z_o \lesssim \mathcal{O}(10)$) and δ-scaling for the large scales ($\lambda \gtrsim \mathcal{O}(\delta)$). This is due to contributions from both the active as well as the inactive motions to Φ_{uu}.

Φ^{ia}_{uu} also exhibits both z_o- and δ-scaling, with the scale range for z_o-scaling, however, much narrower than that observed for Φ_{uu}. This can be attributed to the fact that $\Phi^{ia}_{uu}(z_o)$ comprises contributions from the attached eddies of height, $\mathcal{O}(z_o) \ll \mathcal{H} \lesssim \mathcal{O}(\delta)$, as well as the δ-scaled superstructures (§7.3,§7.5). It means that the attached eddy contributions form a considerable portion of the total inactive contributions at any z_o close to the wall, due to which a clear $\lambda_y \sim \lambda_x$ trend is discernible in $\Phi^{ia}_{uu}(z_o)$. Townsend (1976), however, described the classification of an eddy as 'active' or 'inactive' to be a relative concept, dependent on the wall-normal location under consideration. Hence, the tall attached eddies which are inactive relative to $z_o^+ \approx 100$ may qualify as active at greater wall-heights. This explains the narrowing down of the $\Phi^{ia}_{uu}(z_o)$ contours to the largest scales with increase in z_o^+ (figure 7.4(d)), until only the superstructure contributions remain at $z_o^+ \approx 0.15Re_\tau$. The latter explains the deviation of the contours from the linear relationship, as z_o^+ moves away from the wall.

The reduction in the attached eddy contributions, with increase in z_o^+, translates into a drop of the cumulative streamwise turbulence intensity, i.e. $\iint_0^\infty \Phi^{ia}_{uu} d(\ln\lambda_x) d(\ln\lambda_y)$, plotted in figure 7.5(b) for the experimental dataset. Also shown alongside in figure 7.5(a) are cumulative contributions obtained by integrating Φ_{uu} and Φ^a_{uu} for $100 \lesssim z_o^+ \lesssim 0.15Re_\tau$. Figure 7.5 also includes, for reference, the well-resolved $\overline{u^2}^+$ profile of Samie et al. (2018) across the entire boundary layer, as well as a log law with $A_1 = 0.98$ proposed by (Baars and Marusic, 2020b). As is evident from the plot, the contributions from both Φ_{uu} and Φ^{ia}_{uu} decay with z/δ very similarly, however, they only approximately follow the $A_1 = 0.98$ log law. This disagreement can be associated with the δ-scaled superstructure contributions existing in both Φ_{uu} and Φ^{ia}_{uu} (Jimenez and Hoyas, 2008; Baars and Marusic, 2020b), given that the expressions in (7.1) are valid strictly for self-similar attached eddy contributions alone (§7.3). An attempt is thus made to remove this superstructure contribution from Φ^{ia}_{uu} in the next sub-section, by following the same SLSE-based methodology discussed previously in §7.5. Returning to figure 7.5, a similar variation for both the profiles obtained on integrating Φ_{uu} and Φ^{ia}_{uu} leads to the cumulative energy contributions from Φ^a_{uu} (≈ 2.7) being nearly constant across the inertial region (figure 7.5(a)). Such a trend is consistent with the statistical properties of the active motions scaling universally with U_τ and z (Townsend, 1961; Bradshaw, 1967).

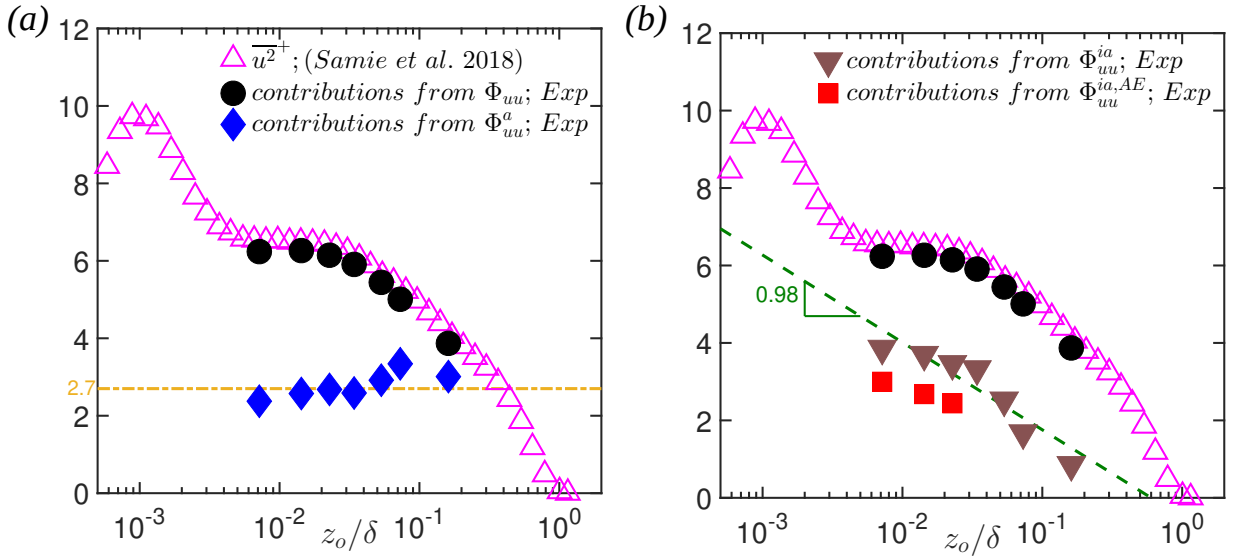

FIGURE 7.5: Comparison of the normalized streamwise turbulence intensities obtained by integrating Φ_{uu} ($= \overline{u^2}^+$), Φ^a_{uu} ($\approx \overline{u^2}^+_{\text{active}}$), Φ^{ia}_{uu} ($\approx \overline{u^2}^+_{\text{inactive}}$) and $\Phi^{ia,AE}_{uu}$ ($\approx \overline{u^2}^+_{\text{inactive,AE}}$) for the high-$Re_\tau$ experimental dataset described in table 7.1. Also plotted for comparison is the well-resolved $\overline{u^2}^+$ measured by Samie et al. (2018) across a ZPG TBL maintained at an Re_τ comparable to the present experimental dataset. The dashed green line in (b) represents the logarithmic decay of $\overline{u^2}^+$ described by (7.1) with $A_1 = 0.98$ (Baars and Marusic, 2020b), while the dash-dotted golden line in (a) represents a constant $\overline{u^2}^+ = 2.7$.

7.7.1 Inactive contributions from the self-similar attached eddies

Here, we consider isolating the inactive contributions from the self-similar attached eddies, by first estimating the δ-scaled superstructure contributions to $\Phi_{uu}(z_o)$. As discussed previously in §7.3 and observed from the experimental data in figures 7.2 and 7.4, the superstructures extend from the wall and span across the entire inertial region, while contribution from the tallest attached eddies is insignificant beyond the upper bound of the log-region ($z^+ \sim 0.15Re_\tau$). This is supported by the scale-by-scale coupling (Φ^{cross}_{uu}) computed from the u-signals simultaneously measured at z_o^+ ($\approx$ 100, 200 or 318) and $z_r^+ \approx 0.15Re_\tau$ plotted in figure 7.6(a), where the energy contours can be seen to be restricted only to the very large scale end of Φ_{uu}, indicative of the superstructure signature. The choice of $z_r^+ \approx 0.15Re_\tau$ is also consistent with Baars and Marusic (2020a,b), who also used it as a reference location to extract the superstructure contribution. They recommended keeping $z_o^+ \lesssim z_r^+/8$ to meet the requirement of $z_r^+ \gg z_o^+$, which explains the present $\Phi^{cross}_{uu}(z_o^+, z_r^+ \approx 0.15Re_\tau)$ measurements conducted at only three wall-normal locations (z_o^+) in the inertially dominated region. It is worth noting here that owing to this condition, the cross-spectrum

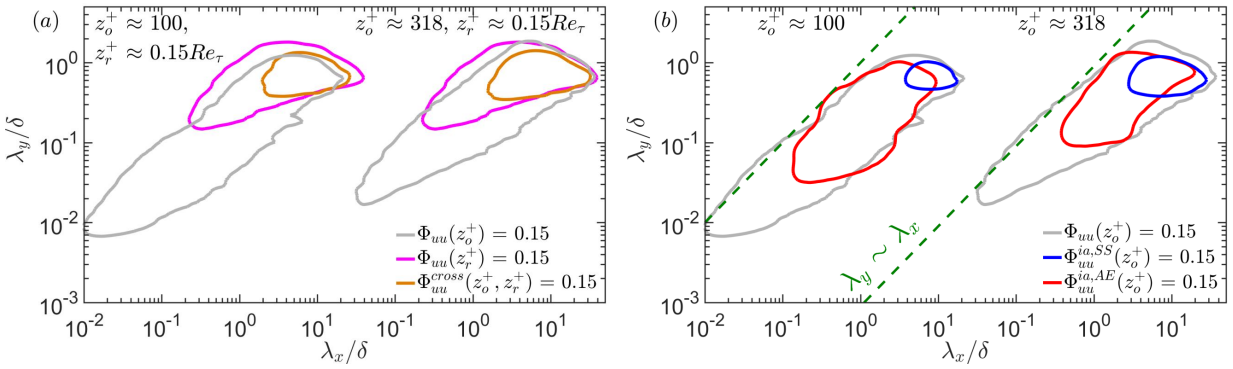

FIGURE 7.6: (a) Constant energy contours for $\Phi_{uu}(z_o^+)$, $\Phi_{uu}^{cross}(z_o^+, z_r^+ \approx 0.15Re_\tau)$ and $\Phi_{uu}(z_r^+ \approx 0.15Re_\tau)$ at energy level of 0.15 plotted for $z_o^+ \approx 100$ and 318. (b) Constant energy contours for $\Phi_{uu}^{ia,AE}(z_o^+)$ and $\Phi_{uu}^{ia,SS}(z_o^+)$, computed via (7.10) and (7.11), plotted at the same energy level and z_o^+ as in (a). All contours in (a,b) are computed from the high-Re_τ experimental data. Dashed green lines represent the linear relationship, $\lambda_y \sim \lambda_x$.

analysis to isolate the superstructure contribution is only possible on the high-Re_τ experimental dataset. On computing $\Phi_{uu}^{cross}(z_o^+, z_r^+ \approx 0.15Re_\tau)$ from the experimental data, it is used in conjunction with the SLSE (appendix 1) to obtain a linear stochastic estimate of the spectrum ($\Phi_{uu}^{ia,SS}$) associated with the superstructure contributions at z_o following:

$$\Phi_{uu}^{ia,SS}(z_o^+; \lambda_x, \lambda_y) = \frac{\left[\Phi_{uu}^{cross}(z_o^+, z_r^+ \approx 0.15Re_\tau; \lambda_x, \lambda_y)\right]^2}{\Phi_{uu}(z_r^+ \approx 0.15Re_\tau; \lambda_x, \lambda_y)}. \tag{7.10}$$

The above expression is similar to (7.8) discussed in §7.5, with the calculations in (7.10) also carried out first in the frequency domain, followed by the conversion to λ_x done by invoking Taylor's hypothesis using $U_c = U(z_r^+ \approx 0.15Re_\tau)$ (Baars and Marusic, 2020a,b). The choice of U_c in (7.10) is based on the 'global' nature and high convection speeds of the δ-scaled superstructures (Jimenez and Hoyas, 2008; del Álamo and Jiménez, 2009; Monty and Chong, 2009).

Contours associated with all the energy spectra in (7.10) have been plotted in figure 7.6(b), with $\Phi_{uu}^{ia,SS}$ centred around a δ-scaled location of $\lambda_x \sim 7\delta$, $\lambda_y \sim 0.7\delta$, representative of the superstructures. Following the linear superposition assumption in (7.4), $\Phi_{uu}^{ia,SS}(z_o)$ can be simply subtracted from $\Phi_{uu}^{ia}(z_o)$ to estimate the inactive contributions from the attached eddies at z_o ($\Phi_{uu}^{ia,AE}$):

$$\Phi_{uu}^{ia,AE}(z_o^+; \lambda_x, \lambda_y) = \Phi_{uu}^{ia}(z_o^+; \lambda_x, \lambda_y) - \Phi_{uu}^{ia,SS}(z_o^+; \lambda_x, \lambda_y), \tag{7.11}$$

with $\Phi_{uu}^{ia,SS}$ and $\Phi_{uu}^{ia,AE}$ representative of $\overline{u^2}^+_{\text{inactive,SS}}$ and $\overline{u^2}^+_{\text{inactive,AE}}$, respectively. The

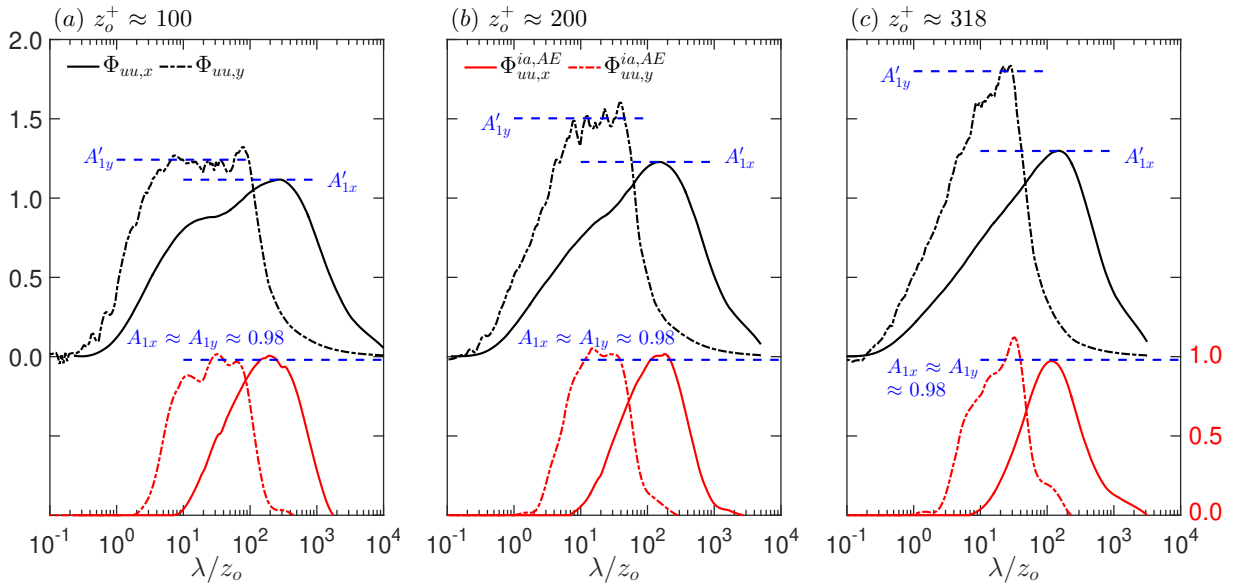

FIGURE 7.7: $\Phi_{uu}(z_o^+)$ and $\Phi_{uu}^{ia,AE}(z_o^+)$ integrated across λ_y and λ_x to obtain their corresponding premultiplied 1-D version as a function of λ_x ($\Phi_{uu,x}$, $\Phi_{uu,x}^{ia,AE}$; in solid line) and λ_y ($\Phi_{uu,y}$, $\Phi_{uu,y}^{ia,AE}$; in dash-dotted line), respectively, for $z_o^+ \approx$ (a) 100, (a) 200 and (c) 318. Also highlighted are the peaks/plateaus of $\Phi_{uu,x}^{ia,AE}$ and $\Phi_{uu,y}^{ia,AE}$ (A_{1x}, A_{1y}), along with those of $\Phi_{uu,x}$ and $\Phi_{uu,y}$ (A'_{1x}, A'_{1y}).

claim is also supported by the $\Phi_{uu}^{ia,AE}$ contours plotted in figure 7.6(b), which are seen to follow the $\lambda_y \sim \lambda_x$ relationship representing geometric self-similarity. $\overline{u^2}^+_{\text{inactive,AE}}$, obtained via integrating $\Phi_{uu}^{ia,AE}$ at the three z_o^+, has also been plotted in figure 7.5(b). While the trend looks promising when compared with the $\overline{u^2}^+$ expression in (7.1), three data points are not sufficient to firmly establish the present claim (for this additional data at even higher Reynolds number would be required). However, to confirm the association of $\Phi_{uu}^{ia,AE}$ with pure attached eddy contributions, we check for the constant energy plateau (representative of the k_x^{-1}-scaling) in the corresponding premultiplied 1-D spectra. In this respect, the parameters in the present analysis align well with the necessary conditions proposed by Perry and Chong (1982) and Nickels et al. (2005) to observe a clear k_x^{-1} region, i.e. to measure sufficiently close to the wall in a high Re_τ wall-bounded flow.

To this end, $\Phi_{uu}^{ia,AE}$ is integrated along λ_y and λ_x to obtain the corresponding premultiplied 1-D spectra as a function of λ_x ($\Phi_{uu,x}^{ia,AE}$) and λ_y ($\Phi_{uu,y}^{ia,AE}$), respectively, which has been plotted for the three z_o^+ in figure 7.7. Also plotted for reference in the same figure are the premultiplied 1-D spectra ($\Phi_{uu,x}$,$\Phi_{uu,y}$) obtained by integrating Φ_{uu} in the same manner. Indeed, $\Phi_{uu,x}^{ia,AE}$ can be observed to be plateauing at $A_{1x} \approx 0.98$ (nominally) for all three z_o^+, which is consistent with the Townsend-Perry constant (A_1) estimated by Baars and Marusic (2020b) from the streamwise turbulence intensity profile. The span of the $\Phi_{uu,x}^{ia,AE}$ plateau,

however, shrinks in size with the increase in z_o^+, likely due to decrease in the hierarchy of attached eddies inactive at z_o (Perry and Chong, 1982). To the best of the authors' knowledge, the present result is the first empirical evidence that establishes consistency between the logarithmic decay rate of the streamwise turbulence intensity and the constant energy plateau from the premultiplied 1-D u-spectrum, as argued by Perry et al. (1986) in the case of pure attached eddy contributions. This consistency, however, was not observed in the recent effort by Baars and Marusic (2020a,b) due to the energy decomposition conducted directly for the 1-D u-spectra in their case. That analysis neglected the scale-specific coherence over the spanwise direction, which has been duly considered in the present study using the new experimental data.

The present analysis also reveals the plateau, A_{1y} in the premultiplied spanwise 1-D spectra ($\Phi_{uu,y}^{ia,AE}$), which is found to be nominally equal to A_{1x} for all z_o^+. $A_{1y} \approx A_{1x}$ obtained here, thus satisfies the necessary condition proposed by Chandran et al. (2017) to associate the 2-D spectrum, $\Phi_{uu}^{ia,AE}$ with purely self-similar contributions. This condition was also recently confirmed by Hwang et al. (2020), by conducting a spectral analysis of the wall-coherent self-similar u-structures extracted from low-Re_τ DNS simulations. $\Phi_{uu,y}$ is also observed to have a plateau at $A'_{1y} \approx 1.3$ (at $z_o^+ \approx 100$), a value which is consistent with that reported by Lee and Moser (2015). However, $A'_{1y} \neq A'_{1x}$, with both values changing as a function of z_o^+. This behaviour can be associated with the non-self-similar contributions in Φ_{uu} obscuring the pure self-similar characteristics, which have been successfully isolated in the present study in the form of $\Phi_{uu}^{ia,AE}$.

7.8 Concluding remarks

The present study proposes a methodology to extract the u-energy spectrum associated with the active and inactive motions (Townsend, 1961, 1976) coexisting at any z_o in the inertially-dominated region of a wall-bounded flow. The methodology is based on isolating the streamwise turbulent energy associated with the inactive motions from the total energy, based on their known characteristic of being larger than the coexisting active motions and coherent across a substantial wall-normal range (Townsend, 1961, 1976). This is tested using ZPG TBL datasets comprising two-point u-signals, synchronously acquired at z_o and a near-wall location (z_r), such that $z_r \ll z_o$. The velocity-velocity coupling, constructed by cross-correlating these u-signals, is fed into an SLSE-based procedure which linearly decomposes the full 2-D spectrum $\Phi_{uu}(z_o)$ into components representative of the active (Φ_{uu}^{a}) and inactive (Φ_{uu}^{ia}) motions at z_o.

Φ^a_{uu} is found to exhibit z_o-scaling across a decade of Re_τ, and is also consistent with the characteristics depicted by the Reynolds shear stress cospectra, thereby confirming the association of Φ^a_{uu} with the active motions. Analysis conducted across both spatially-(DNS) and temporally-resolved (experimental) datasets also confirms the validity of Taylor's hypothesis for the active motions. Further, decomposition of Φ_{uu} into Φ^a_{uu} and Φ^{ia}_{uu} brings out the self-similar characteristic of the two spectra, which is consistent with Townsend's hypothesis on both active and inactive motions essentially being associated with contributions from the attached eddies, but of different sizes.

While $\Phi^a_{uu}(z_o)$ is found to be associated predominantly with the self-similar attached eddies of height $\mathcal{H} \sim \mathcal{O}(z_o)$, $\Phi^{ia}_{uu}(z_o)$ is found to have contributions from both, the relatively tall self-similar attached eddies ($\mathcal{O}(z_o) \ll \mathcal{H} \lesssim \mathcal{O}(\delta)$) as well as the large δ-scaled eddies associated with the superstructures. The latter is confirmed by the reduced self-similar contributions to Φ^{ia}_{uu} with increasing z_o, due to the large attached eddies qualifying as active in accordance to the original concept given by Townsend (1961, 1976). The present study also segregates the inactive contributions from the attached eddies ($\Phi^{ia,AE}_{uu}$), from those coming from the δ-scaled superstructures ($\Phi^{ia,SS}_{uu}$), by utilizing the same SLSE-based methodology used earlier. The estimation of $\Phi^{ia,AE}_{uu}$ reveals the constant energy plateau, representative of k^{-1}-scaling, in the corresponding premultiplied streamwise and spanwise 1-D u-spectra. Both these spectra were found to plateau at $A_1 \approx 0.98$ (nominally), yielding the first empirical evidence to establish the consistency with A_1 obtained from the streamwise turbulence intensity profiles (Baars and Marusic, 2020b), as argued by Perry and Chong (1982) for the case of pure attached eddy contributions.

Acknowledgements

The authors wish to acknowledge the Australian Research Council for financial support and are thankful to the authors of Sillero et al. (2014) and Baidya et al. (2017) for making their respective data available. The authors also thank Dr. D. Chandran for assistance with the experiments, and Dr. W. J. Baars and Dr. A. Madhusudanan for helpful discussions related to SLSE. The authors are also grateful to the anonymous reviewers for their helpful comments which significantly improved the quality of the manuscript.

Appendix 1: SLSE methodology adopted for energy decomposition

Here, we demonstrate the methodology to estimate a component of the full u-energy spectrum at z_o, comprising contributions from specific coherent motions coexisting at z_o, via the spectral linear stochastic estimation (SLSE) approach. The procedure has been adopted from previous studies in the literature employing SLSE (Tinney et al., 2006; Baars et al., 2016a; Madhusudanan et al., 2019; Encinar and Jiménez, 2019), which may be referred to for further understanding on this topic. The SLSE considers a scale-specific unconditional input (at z_r) to give a scale-specific conditional output (at z_o) following:

$$\widetilde{u}^E(z_o;\lambda_x,\lambda_y) = H_L(z_o,z_r;\lambda_x,\lambda_y)\widetilde{u}(z_r;\lambda_x,\lambda_y), \tag{7.12}$$

where $\tilde{u}(z_r;\lambda_x,\lambda_y)$ is the 2-D Fourier transform of $u(z_r)$ in x and y. Here, the superscript E represents the estimated quantity and H_L represents the scale-specific linear transfer kernel. It should be noted that the SLSE approach enables accurate estimation of only those scales (at z_o) that are coherent across z_o and z_r. Equation (7.12) can be further used to estimate the 2-D energy spectrum, Φ^E_{uu} at z_o (Madhusudanan et al., 2019) following:

$$\Phi^E_{uu}(z_o;\lambda_x,\lambda_y) = \mid H_L(z_o,z_r;\lambda_x,\lambda_y) \mid^2 \Phi_{uu}(z_r;\lambda_x,\lambda_y). \tag{7.13}$$

To obtain u^E and Φ^E_{uu} at z_o, the transfer kernel H_L is required to be computed from an ensemble of data following:

$$H_L(z_o,z_r;\lambda_x,\lambda_y) = \frac{\langle \widetilde{u}(z_o;\lambda_x,\lambda_y)\widetilde{u}^*(z_r;\lambda_x,\lambda_y)\rangle}{\langle \widetilde{u}(z_r;\lambda_x,\lambda_y)\widetilde{u}^*(z_r;\lambda_x,\lambda_y)\rangle} = \mid H_L(z_o,z_r;\lambda_x,\lambda_y) \mid e^{i\psi(z_o,z_r;\lambda_x,\lambda_y)}, \tag{7.14}$$

with $\mid H_L \mid$ and ψ the scale-specific gain and phase respectively, and the asterisk ($*$), angle brackets ($\langle\rangle$) and vertical bars ($||$) denoting the complex conjugate, ensemble averaging and modulus, respectively. Considering z_r^+ as the reference wall-normal location used in the present study, $\mid H_L \mid$ from equation (7.14) can be simply expressed as a function of the two types of 2-D spectra computed from the multi-point datasets (refer §7.4) at various z_o^+ in the inertial region following:

$$\mid H_L(z_o^+,z_r^+;\lambda_x,\lambda_y) \mid = \frac{\Phi^{cross}_{uu}(z_o^+,z_r^+;\lambda_x,\lambda_y)}{\Phi_{uu}(z_r^+;\lambda_x,\lambda_y)}. \tag{7.15}$$

In the case of $z_r^+ \ll z_o^+$, $\Phi^E_{uu}(z_o;\lambda_x,\lambda_y)$ would be representative of the energy contributions

from all coexisting motions taller than z_o, which as per our discussion in §7.5 leads to $\Phi^E_{uu}(z_o;\lambda_x,\lambda_y)|_{z_r^+\approx 15} \rightarrow \Phi^{ia}_{uu}(z_o;\lambda_x,\lambda_y)$. A simplified expression for Φ^{ia}_{uu} can be deduced from (7.13) and (7.15) as follows:

$$\begin{aligned}\Phi^{ia}_{uu}(z_o^+;\lambda_x,\lambda_y) &= \mid H_L(z_o^+, z_r^+ \approx 15;\lambda_x,\lambda_y) \mid^2 \Phi_{uu}(z_r^+ \approx 15;\lambda_x,\lambda_y) \\ &= \frac{[\Phi^{cross}_{uu}(z_o^+, z_r^+ \approx 15;\lambda_x,\lambda_y)]^2}{\Phi_{uu}(z_r^+ \approx 15;\lambda_x,\lambda_y)}.\end{aligned} \tag{7.16}$$

Similarly, in case of $z_r^+ \gg z_o^+$, $\Phi^E_{uu}(z_o;\lambda_x,\lambda_y)$ would be representative of the energy contributions from all coexisting motions at z_o that are taller than z_r, which as per our discussion in §7.7.1 leads to $\Phi^E_{uu}(z_o;\lambda_x,\lambda_y)|_{z_r^+\approx 0.15Re_\tau} \rightarrow \Phi^{ia,SS}_{uu}(z_o;\lambda_x,\lambda_y)$, and can be estimated following:

$$\Phi^{ia,SS}_{uu}(z_o^+;\lambda_x,\lambda_y) = \frac{[\Phi^{cross}_{uu}(z_o^+, z_r^+ \approx 0.15Re_\tau;\lambda_x,\lambda_y)]^2}{\Phi_{uu}(z_r^+ \approx 0.15Re_\tau;\lambda_x,\lambda_y)}. \tag{7.17}$$

Availability of both the numerator and denominator in the above expressions (table 7.1) allows direct computation of Φ^{ia}_{uu} and $\Phi^{ia,SS}_{uu}$, without separately estimating $\mid H_L \mid^2$, for both the datasets. It should be noted here that Φ^{ia}_{uu} is computed in the frequency domain for the experimental dataset, with the conversion to λ_x obtained by invoking Taylor's hypothesis, using $U_c = U(z_o)$ (Baars et al., 2016a, 2017). $\Phi^{ia,SS}_{uu}$ is also computed in the similar manner, however with the conversion to λ_x achieved by using $U_c = U(z_r^+ \approx 0.15Re_\tau)$ (Baars and Marusic, 2020a,b).

As can be noted from (7.16), the essential information on energetic motions coherent across z_o and z_r is embedded in $\mid H_L \mid^2$ which is translated into Φ^{ia}_{uu} (or $\Phi^{ia,SS}_{uu}$) via scale-by-scale amplification/attenuation provided by $\Phi_{uu}(z_r^+)$. For example, figure 7.8(a) shows the $\mid H_L(z_o^+, z_r^+\approx 15) \mid^2$ computed from the DNS dataset at various z_o^+ listed in table 7.1, along with $\Phi_{uu}(z_r^+ \approx 15)$ for the same dataset. It is evident from the plot that $\mid H_L(z_o^+\approx 100, z_r^+\approx 15) \mid^2$ contours conform predominantly to the large scales of the spectrum, with the contours moving very gradually to even larger scales with increase in z_o^+. This explains the observation noted in §7.5 on Φ^{ia}_{uu} and Φ^{a}_{uu} respectively taking up the higher and lower end of the full spectrum, $\Phi_{uu}(z_o)$.

We also use this opportunity to test the efficacy of the SLSE-based methodology, used here to estimate energy contributions from the active motions. To this end, the same procedure as that outlined in (7.12) – (7.16), is implemented on the wall-parallel w-velocity fields also retrieved from the DNS dataset, at the same z_o^+ and z_r^+ as that selected for the u-velocity field (table 7.1). The w-velocity fields are used to compute the two types of 2-D spectra,

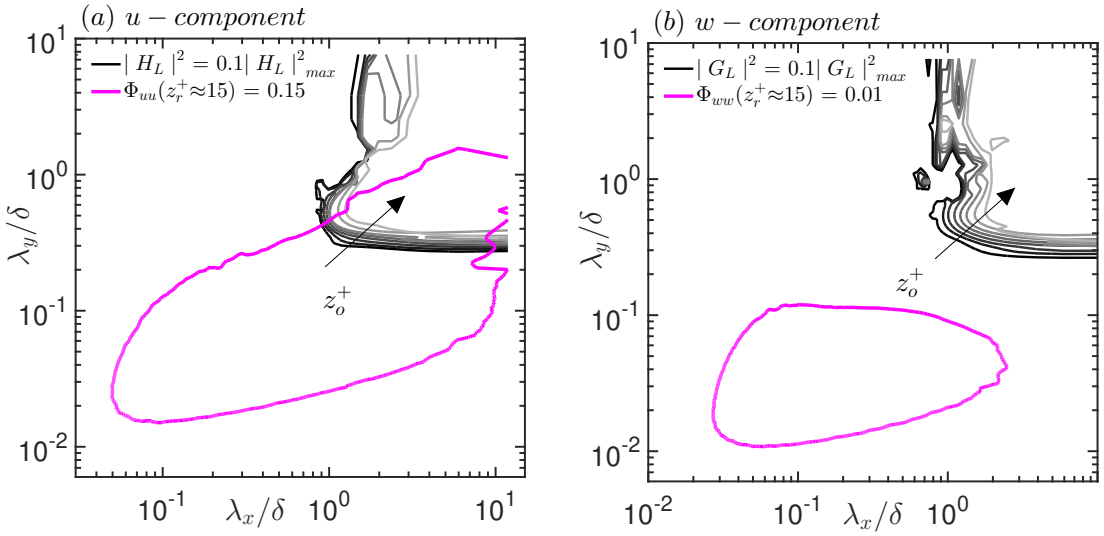

FIGURE 7.8: Contours for the linear transfer kernel (black), for $z_r^+ \approx 15$, and the near-wall 2-D spectra (magenta) for the (a) u- and (b) w-velocity component. Here, the transfer kernels are computed at various z_o^+ from the DNS dataset of Sillero et al. (2014), described in table 7.1. Dark to light shading indicates an increase in z_o^+ following $100 \lesssim z_o^+ \lesssim 0.15Re_\tau$. The contour levels for the transfer kernels, $|H_L|^2$ and $|G_L|^2$ correspond to approximately 10% of the maximum value recorded for the kernel at the respective z_o^+, while that for $\Phi_{ww}(z_r^+ \approx 15)$ has intentionally been kept very low to highlight no overlap with the associated transfer kernel, $|G_L|^2$.

computed previously for the u-component, at the same z_o^+ in the inertial region following:

$$\begin{aligned}\Phi_{ww}(z_o^+;\lambda_x,\lambda_y) &= |k_x^+ k_y^+ \phi_{ww}^+(z_o^+;\lambda_x,\lambda_y)| \text{ and} \\ \Phi_{ww}^{cross}(z_o^+, z_r^+{\approx}15;\lambda_x,\lambda_y) &= |k_x^+ k_y^+ \phi_{w_o w_r}^+(z_o^+, z_r^+ \approx 15;\lambda_x,\lambda_y)|,\end{aligned} \tag{7.18}$$

where (7.18) is analogous to (7.7) expressed for the u-component. Similarly, the inactive component Φ_{ww}^{ia} of the w-velocity field can be computed via an expression similar to (7.16) given previously for the u-component:

$$\begin{aligned}\Phi_{ww}^{ia}(z_o^+;\lambda_x,\lambda_y) &= |\,G_L(z_o^+, z_r^+ \approx 15;\lambda_x,\lambda_y)\,|^2 \Phi_{ww}(z_r^+ \approx 15;\lambda_x,\lambda_y), \text{ where} \\ |\,G_L(z_o^+, z_r^+ \approx 15;\lambda_x,\lambda_y)\,| &= \frac{\Phi_{ww}^{cross}(z_o^+, z_r^+{\approx}15;\lambda_x,\lambda_y)}{\Phi_{ww}(z_r^+ \approx 15;\lambda_x,\lambda_y)}.\end{aligned} \tag{7.19}$$

Accordingly, $\Phi_{ww}^{a}(z_o) = \Phi_{ww}(z_o) - \Phi_{ww}^{ia}(z_o)$. Given the fact that the w-component is predominantly associated with the active motions (Bradshaw, 1967; Morrison et al., 1992; Baidya et al., 2017), i.e. $\Phi_{ww}^{a}(z_o) \approx \Phi_{ww}(z_o)$, we would expect the SLSE procedure to reveal cumulative energy contributions from Φ_{ww}^{ia} to be negligible. This is possible if $|G_L|^2$ and $\Phi_{ww}(z_r^+ \approx 15)$ do not overlap at common scales (as per equation 7.19). Figure 7.8(b) shows $|G_L|^2$ contours computed for various z_o^+ from the DNS dataset alongside $\Phi_{ww}(z_r^+$

≈ 15), clearly suggesting an insignificant overlap between the two. Accordingly, $\Phi^{ia}_{ww}(z_o) \approx 0$ in the inertial region leading to $\Phi^{a}_{ww}(z_o) \approx \Phi_{ww}(z_o)$, which proves the effectiveness of the SLSE-based methodology in extracting the energy spectrum associated with the active motions.

Chapter 8

Active and inactive motions in wall turbulence

[Published paper V[1]]

8.1 Preface to the chapter

This chapter is published in the *Proceedings of 22nd Australasian Fluid Mechanics Conference*, titled "Active and inactive motions in wall turbulence" (Deshpande et al., 2020c). Here, the energy decomposition methodology proposed previously in chapter 7, to segregate contributions associated with the active and inactive components (Townsend, 1976), is implemented on the lateral velocity components extracted from previously published low-Re_τ DNS datasets (del Álamo et al., 2004; Sillero et al., 2014). Hence, chapters 7 and 8 cumulatively establish the validity of Townsend's (1961, 1976) hypothesis on the active and inactive motions by testing it on all three velocity components, paving the way towards attached eddy-based modelling of the inertial region of wall turbulence.

Readers should note that the §8.3, 8.4, 8.5 and figure 8.2 of this chapter are directly inspired from §7.3, 7.4, 7.5 and figure 7.2 of chapter 7, and essentially explain Townsend's hypothesis, wall-turbulence datasets and the energy decomposition methodology, respectively.

[1]Deshpande, R., Monty, J.P. & Marusic, I. (2020). Active and inactive motions in wall turbulence. In *Proceedings of 22nd Australasian Fluid Mechanics Conference, Brisbane, Australia*. DOI: https://doi.org/10.14264/ad70392

8.2 Abstract

Reynolds shear stress is the key momentum transport term in wall turbulence and as a consequence has been the focus of numerous theoretical modelling attempts in the past. Here, we investigate the seminal proposal by Townsend (1961, 1976) that wall-bounded flows are comprised of active and inactive motions; the active motions being those that are solely responsible for producing Reynolds shear stress and follow self-similarity when normalised with the wall-normal distance and friction velocity. This chapter builds on the recent work of Deshpande et al. (2021), where a methodology is proposed to segregate the active and inactive contributions to the total turbulent kinetic energy. The effectiveness of this methodology is demonstrated here by applying it to three published wall-turbulence datasets, spanning over a decade change in friction Reynolds number (Re_τ). Active contributions to the streamwise, spanwise and wall-normal turbulence intensities are estimated individually and found to exhibit self-similar characteristics consistent with Townsend's hypothesis. The Reynolds shear stress, estimated solely from the active contributions, is also found to closely match the one obtained conventionally from the dataset, providing direct empirical support for the concept of active and inactive motions.

8.3 Introduction

The logarithmic (log) region of a wall-bounded flow has long been the focus of research from the perspective of turbulence modelling. It derives its name from the logarithmic variation of the mean velocity (U) as a function of the distance from the wall, z, following:

$$U^+ = \frac{1}{\kappa}\log(z^+) + A. \tag{8.1}$$

Here, $U^+ = U/U_\tau$, where U_τ is the friction velocity, $z^+ = zU_\tau/\nu$, where ν is the kinematic viscosity, κ is the von Kármán constant, and A is a constant. While (8.1) has been derived from a number of previous approaches, starting from the mixing length theory of Prandtl (1925), the present manuscript focuses on the arguments proposed by Townsend (1961, 1976) in the context of the log-region, which he referred to as the 'equilibrium layer.' Townsend considered the local rates of energy production and dissipation to be in balance in this region, leading him to the same expression as that reached by Prandtl (1925):

$$-\overline{uw}^+ = l_m U_\tau \frac{dU^+}{dz^+}, \tag{8.2}$$

were, l_m is the mixing length. Throughout this chapter, we denote the velocity fluctuations along streamwise (x), spanwise (y) and wall-normal (z) directions by u, v and w, respectively. $\overline{uw}^+$, is the (kinematic) Reynolds shear stress. Equation (8.2) leads to the log-law (8.1) when $l_m = \kappa z$ and -$\overline{uw}^+ = 1$. Townsend (1961) interpreted this condition ($l_m \propto z$) in a physical sense in terms of an attached eddy: "*if the Reynolds stress at any point were caused mostly by contributions from eddies whose scales are comparable with distance of the point from the wall since they all extend to the wall and are, in a sense, attached to it.*"

The aforementioned arguments laid the foundation of Townsend's attached eddy hypothesis (Townsend, 1976), from which the attached eddy model (AEM) of wall turbulence (Perry and Chong, 1982; Marusic and Monty, 2019) has evolved over time. The term 'attached' used here refers to any flow structure whose geometric lengths scale with z, respectively. The AEM conceptually models the kinematics in the log-region of a canonical wall-bounded flow by a hierarchy of randomly distributed, geometrically self-similar attached eddies, with a population density inversely proportional to their height ($\mathcal{H}$). According to Townsend (Townsend, 1976), the heights of the attached eddies can vary in the range $\mathcal{O}(z_l) \lesssim \mathcal{H} \lesssim \mathcal{O}(\delta)$, with δ corresponding to the characteristic outer scale of the wall-bounded flow while z_l corresponding to the start of the log-region. In addition to complying with the log-law given in (8.1), the AEM also proposes the streamwise ($\overline{u^2}$) and spanwise ($\overline{v^2}$) turbulence intensities, resulting from the combined contributions from all attached eddies, to vary logarithmically with respect to the distance from the wall (z) in the log-region, while the variance of the wall-normal velocity ($\overline{w^2}$) remains constant. This can be expressed mathematically as:

$$\begin{aligned} \overline{u^2}^+ &= B_1 - A_1 \log\left(\frac{z}{\delta}\right), \\ \overline{v^2}^+ &= B_2 - A_2 \log\left(\frac{z}{\delta}\right), \\ \overline{w^2}^+ &= B_3, \quad \text{and} \quad \overline{uw}^+ = B_4, \end{aligned} \tag{8.3}$$

where A_{1-3} and B_{1-3} are constants. These expressions have received substantial support in the recent literature from experiments (Hultmark et al., 2012; Marusic et al., 2013; Baidya et al., 2014) as well as simulations (Jimenez and Hoyas, 2008; Lee and Moser, 2015; Orlandi et al., 2015).

Considering the differing trends amongst the Reynolds stresses in (8.3), where the variances of the wall-parallel velocity components vary with Re_τ at a fixed z^+, while $\overline{w^2}^+$ and $\overline{uw}^+$ do not, Townsend (1961) commented that: "*it is difficult to reconcile these observations*

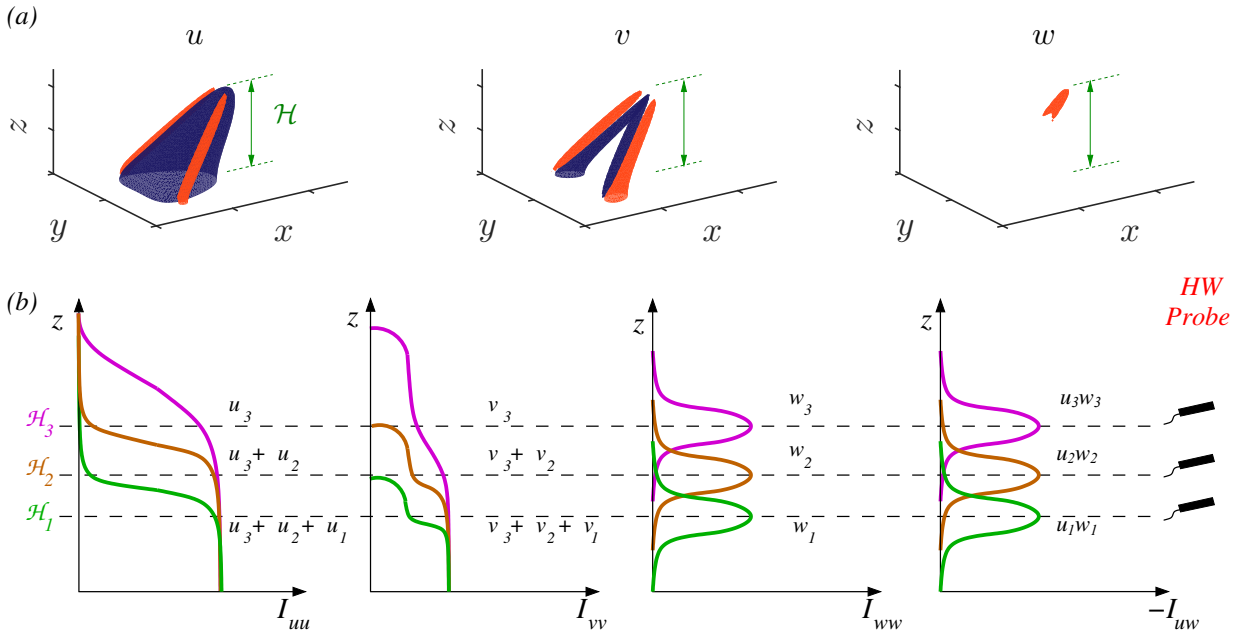

FIGURE 8.1: (a) Streamwise, spanwise and wall-normal velocity signatures from a typical attached eddy of height $\mathcal{H}$, where the blue and red regions denote the low- and high-momentum regions for the corresponding velocity fluctuations. (b) Townsend eddy intensity functions (I) for attached eddies of three different heights $\mathcal{H}_i$, with $\mathcal{H}_1 < \mathcal{H}_2 < \mathcal{H}_3$. Here, u_i, v_i and w_i denote the velocity signatures from the corresponding attached eddies which are sensed by the hotwire (HW) probe depending on its wall-normal position z, indicated by a dash line.

without supposing that the motion at any point consists of two components, an active component responsible for turbulent transfer and determined by the stress distribution and an inactive component which does not transfer momentum or interact with the universal component." He further added "*that the inactive motion is a meandering or swirling motion made up from attached eddies of large size which contribute to the Reynolds stress much further from the wall than the point of observation*". The present manuscript further elaborates on these interpretations by presenting a simple mathematical description, combined with appropriate empirical support, for the concept of active and inactive motions.

For this, we begin by considering the simplest attached eddy model for a wall-bounded flow (de Silva et al., 2018), comprising attached eddies as the only eddying motions. Figure 8.1(a) schematically depicts the signatures of all three velocity components from a simplified vortex structure, which is representative of an attached eddy of height $\mathcal{H}$. Given the inviscid nature of the model, slip is allowed at the wall (i.e. a finite u and v), while $w = 0$ due to the impermeability condition at the wall. This is ensured by using an image vortex about the plane of the wall. The final result is that the u- and v- signatures are present all the way from $\mathcal{H}$, down to the wall, while the w-signature remains spatially localized at $\mathcal{H}$.

It is this very nature of the velocity signatures which results in the 'active' and 'inactive' contributions from the individual attached eddies, as will be explained below.

To highlight the difference between the two contributions, figure 8.1(b) depicts the Townsend eddy intensity function, I_{ij} (where i, $j = u$, v or w), which represents the contribution of each eddy to the individual turbulence stresses as a function of z (Perry and Chong, 1982; Marusic and Monty, 2019). Here, I_{ij} is considered for the Reynolds stresses listed in (8.3), for eddies of three different heights ($\mathcal{H}_1$–$\mathcal{H}_3$), each symbolic of a hierarchy of attached eddies as per Townsend's hypothesis. The intensity functions associated with the normal stresses (I_{ii}) are representative of the corresponding velocity signatures depicted in figure 8.1(a). Using these functions, figure 8.1(b) depicts the cumulative contribution from the three different eddies to the Reynolds stresses measured by a hotwire probe. For the probe positioned at $z \sim \mathcal{H}_1$ for example, contributions to $\overline{u^2}(z)$ and $\overline{v^2}(z)$ would come from all three eddies, while the contributions to $\overline{w^2}(z)$ (and consequently to $\overline{uw}$) would be solely from the eddy of height $\mathcal{H}_1$. On increasing the probe wall-normal location to $z \sim \mathcal{H}_2$, contributions to the wall-parallel stresses now come from the tallest two eddies while those to $\overline{w^2}(z)$ and $\overline{uw}(z)$ would only be from the eddy of height $\mathcal{H}_2$, and so on. Correlating the observations from figure 8.1 with Townsend's definition, the active motions at any z would thus correspond solely due to the attached eddies of height, $\mathcal{H} \sim \mathcal{O}(z)$. On the other hand, the inactive motions at z are a consequence of comparatively taller and larger attached eddies of height $\mathcal{O}(z) \ll \mathcal{H} \lesssim \mathcal{O}(\delta)$. Such attached eddies add to $u(z)$ and $v(z)$ without making any substantial addition to $w(z)$ (and thus to $uw(z)$). Therefore, while only active motions contribute to the Reynolds shear stress and the wall-normal velocity variance at z, the wall-parallel velocity variances receive contributions from both active and inactive motions. As a consequence, the active motions are defined as the fraction of attached eddy contributions which exhibit scaling with z and U_τ (i.e. wall-scaling). The logarithmic decay of the wall-parallel velocity variances (equation 8.3), on the other hand, is a consequence of the comparatively large scale inactive motions with a population density inversely proportional to their size.

The aforementioned discussion motivates the decomposition of the attached eddy fields as per Panton (Panton, 2007):

$$\begin{aligned} u &= u_{\text{active}} + u_{\text{inactive}}, \\ v &= v_{\text{active}} + v_{\text{inactive}}, \\ w &= w_{\text{active}}. \end{aligned} \tag{8.4}$$

Given that the active and inactive velocity fields are uncorrelated (Townsend, 1961; Bradshaw, 1967), the Reynolds stresses in (8.3) can also be decomposed as:

$$\begin{aligned} \overline{u^2} &= \overline{u^2}_{\text{active}} + \overline{u^2}_{\text{inactive}}, \\ \overline{v^2} &= \overline{v^2}_{\text{active}} + \overline{v^2}_{\text{inactive}}, \\ \overline{w^2} &= \overline{w^2}_{\text{active}}, \\ \overline{uw} &= \overline{(u_{\text{active}})(w_{\text{active}})} = \overline{(u_{\text{active}})(w)}. \end{aligned} \tag{8.5}$$

This decomposition is based on neglecting the non-linear interactions (like modulation) across these motions known from previous studies (Morrison, 2007; Mathis et al., 2009; Marusic et al., 2010a; Chernyshenko et al., 2012; Wu et al., 2019). These interactions, however, do not show up in the second-order velocity statistics (i.e., the Reynolds stresses), which are of prime interest in the present work.

While (8.4) and (8.5) provide a mathematical description of the active and inactive contributions to the total energy, they have been defined considering a pure attached eddy field. A real wall-bounded flow, however, also comprises of other 'non-self-similar' contributions (Baars and Marusic, 2020a; Deshpande et al., 2020a; Yoon et al., 2020), which also need to be recognized and correctly accounted for while considering these decompositions. These include the small-scale energy contributions from the inertial sub-range (Perry et al., 1986; Saddoughi and Veeravalli, 1994), as well as those corresponding to the fine dissipative scales, which are small compared to the inertial motions in the log-region. Other contributions come from the δ-scaled superstructures or very-large-scale motions, which add to $\overline{u^2}$ and $\overline{v^2}$ (Baars and Marusic, 2020a; Deshpande et al., 2020a; Yoon et al., 2020) but not to $\overline{w^2}$, the latter being confirmed by the w-velocity energy spectra exhibiting wall-scaling (Bradshaw, 1967; Morrison et al., 1992; Katul and Vidakovic, 1996; Kunkel and Marusic, 2006; Baidya et al., 2017). These characteristics suggest the δ-scaled superstructure behaviour to be aligned with the inactive motions, meaning their contributions would end up in $\overline{u^2}_{\text{inactive}}$ and $\overline{v^2}_{\text{inactive}}$ (Deshpande et al., 2021) in the context of the decomposition given in (8.5).

Recently, Deshpande et al. (2021) proposed a methodology to segregate $\overline{u^2}_{\text{inactive}}$ and $\overline{u^2}_{\text{active}}$ in the logarithmic layer of a zero pressure gradient turbulent boundary layer (ZPG TBL). The present manuscript reviews their methodology, and demonstrates its applicability to decompose the inactive and active contributions for all three velocity components, and for canonical wall-bounded flows in general. The methodology utilizes the characteristic of the inactive motions, say at any z_o in the log-region, to be associated predominantly

with the large eddies in comparison to the motions 'active' at the same location, which means the coherence of the inactive motions extends across a significant wall-normal distance (Townsend, 1976; Baars and Marusic, 2020a). This is consistent with Townsend's ideas (Townsend, 1961, 1976), who described the inactive motions (at z_o) to be superimposing a low-frequency signature across the entire wall-normal range below z_o, including the near-wall region (Hwang, 2015) where we consider our reference location, z_r. The presence of their signatures across the large wall-normal range ($z_r \ll z_o$) provides an opportunity to isolate the inactive motions via a scale-specific cross-correlation of the velocity signals synchronously acquired at z_r and z_o, as demonstrated previously in Deshpande et al. (2019a) and Baars and Marusic (2020a). Once the inactive component is estimated ($\overline{v^2}_{\text{inactive}}$ or $\overline{u^2}_{\text{inactive}}$), it can be simply subtracted from the respective Reynolds stress at z_o ($\overline{v^2}$ or $\overline{u^2}$) to estimate the energy associated with the active motions at z_o (equation 8.5). In the case of the wall-normal component, however, $\overline{w^2}_{\text{inactive}} \approx 0$ as per our earlier discussion (Deshpande et al., 2021), and hence $\overline{w^2}$ should reflect the characteristic features expected of $\overline{w^2}_{\text{active}}$ (Bradshaw, 1967; Morrison et al., 1992; Katul and Vidakovic, 1996; Kunkel and Marusic, 2006; Baidya et al., 2017).

To demonstrate the efficacy of the decomposition methodology, several published wall-turbulence datasets with synchronized multi-point velocity signals measured across a large domain of spanwise (Δy) and wall-normal ($|z_r - z_o|$) offsets are considered. The data spans over a decade of Re_τ, with the velocity signals in each dataset considered across the log-region of the shear flow, making it possible to test the velocity spectra associated with the active motions for their expected wall-scaling. The methodology involves first computing the two-dimensional (2-D) energy spectrum from the available velocity components at z_o and z_r, thereby giving a map of the energetic motions of various spanwise ($\lambda_y = 2\pi/k_y$) and streamwise ($\lambda_x = 2\pi/k_x$) wavelengths coherent across z_r and z_o (Deshpande et al., 2020a). These two-point statistics, can be utilized in conjunction with a spectral linear stochastic estimation (SLSE) based procedure (Tinney et al., 2006; Baars et al., 2016a; Deshpande et al., 2021), to compute the fraction of the two-dimensional spectrum (at z_o) corresponding to the inactive motions at z_o.

8.4 Experimental and numerical data

Three published datasets ranging over a decade of Re_τ are analyzed in the present study. Two are low-Re_τ direct numerical simulation (DNS) datasets for the turbulent channel flow ($Re_\tau \approx 934$; del Álamo et al. (2004)) and the ZPG TBL ($Re_\tau \approx 2\,000$; Sillero et al. (2014)),

Flow	Channel		ZPG TBL		ZPG TBL	
$Re_\tau \approx$	934		2 000		15 000	
Dataset	del Álamo et al. (2004)		Sillero et al. (2014)		Deshpande et al. (2021)	
Symbol	$\mathcal{C}_1$		$\mathcal{B}_1$		$\mathcal{B}_2$	
Set-up	z_o^+	z_r^+	z_o^+	z_r^+	z_o^+	z_r^+
Φ_{ii}	**15**, $2.6\sqrt{Re_\tau} - 0.15Re_\tau$	$= z_o^+$	**15**, $2.6\sqrt{Re_\tau} - 0.15Re_\tau$	$= z_o^+$	**15**, $2.6\sqrt{Re_\tau} - 0.15Re_\tau$	$\approx z_o^+$
Φ_{ii}^{cross}	$2.6\sqrt{Re_\tau} - 0.15Re_\tau$	**15**	$2.6\sqrt{Re_\tau} - 0.15Re_\tau$	**15**	$2.6\sqrt{Re_\tau} - 0.15Re_\tau$	**15**

TABLE 8.1: Table summarizing the various published wall-turbulence datasets, with synchronized multi-point velocity signals across several z_r^+ and z_o^+, utilized to estimate two different types of two-dimensional spectra, Φ_{ii} and Φ_{ii}^{cross}. Terminology used in the table has been defined in the text, where i represents the velocity fluctuations u, v or w. Highlighted values (in bold) are used to indicate the reference location close to the wall, while $2.6\sqrt{Re_\tau}$ and $0.15Re_\tau$ are the lower and upper bounds of the log-region (Marusic et al., 2013). Normalization in viscous units is denoted by the superscript '+'.

while the third is a high Reynolds number ($Re_\tau \approx 15\ 000$) experimental dataset for the ZPG TBL (Deshpande et al., 2020a, 2021). Information associated with these datasets is briefly described below.

8.4.1 High-Re_τ experimental dataset

The experimental dataset ($\mathcal{B}_2$) was acquired in the High Reynolds Number Boundary Layer Wind Tunnel (HRNBLWT) at the University of Melbourne under nominally ZPG conditions and acceptable free-stream turbulence levels (Marusic et al., 2015) across its test section dimensions of $\simeq 1.89$ m $\times$ 0.92 m $\times$ 27 m. All the measurements associated with the present dataset were conducted at free-stream velocities of $U_\infty \approx 20$ ms^{-1} in the working section, at a streamwise location approximately 20 m from the beginning of the working section, resulting in a boundary layer at $Re_\tau \approx 15\ 000$. The experiments were conducted via a unique experimental set-up employing four single-wire hotwire probes, the positioning of which has been depicted schematically in figure 1 of Deshpande et al. (2020a) and Deshpande et al. (2021). The set-up consisted of all four probes positioned at the same streamwise location but at different spanwise positions, with the capability to vary the latter for two of the four probes. This facilitated synchronous measurement of the u-signals over a large domain of spanwise offsets (Δy), ranging between $0 \lesssim \Delta y \lesssim 2.7\delta$, where δ is the TBL thickness. During each experiment, the pair of spanwise-traversing probes were always positioned at the same wall-normal location z_o, while the pair of spanwise-fixed probes were maintained at a different wall-normal position, z_r. The synchronous u-signals acquired from such an arrangement is utilized to compute the two-point cross-correlation following:

$$R_{i_o i_r}(z_o, z_r; \Delta x, \Delta y) = \overline{i(z_o; x + \Delta x, y + \Delta y) i(z_r; x, y)}, \tag{8.6}$$

with the overbar denoting ensemble time average, and $i = u$ in case of the experimental dataset. $R_{i_o i_r}$ is converted from a function of time to that of Δx by using Taylor's hypothesis, which assumes flow structures coexisting at z_o to be moving along x at the mean flow velocity at z_o. Subsequently, the 2-D Fourier transform of $R_{i_o i_r}$ is computed to obtain the 2-D spectrum following:

$$\phi_{i_o i_r}(z_o, z_r; k_x, k_y) = \int \int_{-\infty}^{\infty} R_{i_o i_r}(z_o, z_r; \Delta x, \Delta y) e^{-j2\pi(k_x \Delta x + k_y \Delta y)} d(\Delta x) d(\Delta y), \tag{8.7}$$

where j is a unit imaginary number.

The present study focuses on two types of 2-D spectra, Φ_{ii} and Φ_{ii}^{cross}, which are defined following:

$$\begin{aligned} \Phi_{ii}(z_o^+;\lambda_x,\lambda_y) &= |k_x^+ k_y^+ \phi_{ii}^+(z_o^+;\lambda_x,\lambda_y)| \text{ and} \\ \Phi_{ii}^{cross}(z_o^+,z_r^+;\lambda_x,\lambda_y) &= |k_x^+ k_y^+ \phi_{i_o i_r}^+(z_o^+,z_r^+ \approx 15;\lambda_x,\lambda_y)|, \end{aligned} \tag{8.8}$$

where i corresponds to the velocity fluctuations in either of the three directions: u, v or w, while $(||)$ denotes the modulus operation. While Φ_{ii} consists of contributions from all coexisting eddies at z_o, Φ_{ii}^{cross} is representative of contributions from only those eddies that are coherent across z_o and z_r (Deshpande et al., 2020a). The two spectra are fed in to the SLSE methodology (Deshpande et al., 2021) to compute the subsets of Φ_{ii} comprising of the inactive and active contributions at z_o. In the case of dataset $\mathcal{B}_2$, the analysis is solely restricted to Φ_{uu} and Φ_{uu}^{cross}, with the details of their wall-normal locations listed in table 8.1. Interested readers may refer to Deshpande et al. (2020a) and Deshpande et al. (2021) for a comprehensive discussion and full details of the aforementioned measurements.

8.4.2 Low-Re_τ DNS datasets

Two low-Re_τ datasets from the ZPG TBL DNS of Sillero et al. (2014) and channel flow DNS of del Álamo et al. (2004) are also considered in the present study. Availability of all three velocity components from both these datasets allows computation of $\Phi_{ii}(z_o^+)$ and $\Phi_{ii}^{cross}(z_o^+,z_r^+)$ following (8.6) – (8.8) for $i = u$, v and w, at z_o^+ and z_r^+ consistent with the experimental dataset (table 8.1). Thirteen DNS time blocks of each of these datasets are selected for achieving a reasonable convergence of these statistics. Hence, in the present study, while the characteristics of the u-motions are tested across a decade of Re_τ, the analysis of the v- and w-motions is limited only to the low Re_τ regime.

8.5 Methodology to decompose inactive and active contributions to the total energy

As discussed previously in the introduction, the inactive motions at z_o predominantly conform to the large motions that are spatially coherent over a significant wall-normal distance. Deshpande et al. (2021) used this as the basis to decompose $\Phi_{ii}(z_o)$. They performed a scale-specific linear decomposition of $\Phi_{ii}(z_o)$, into its inactive and residual

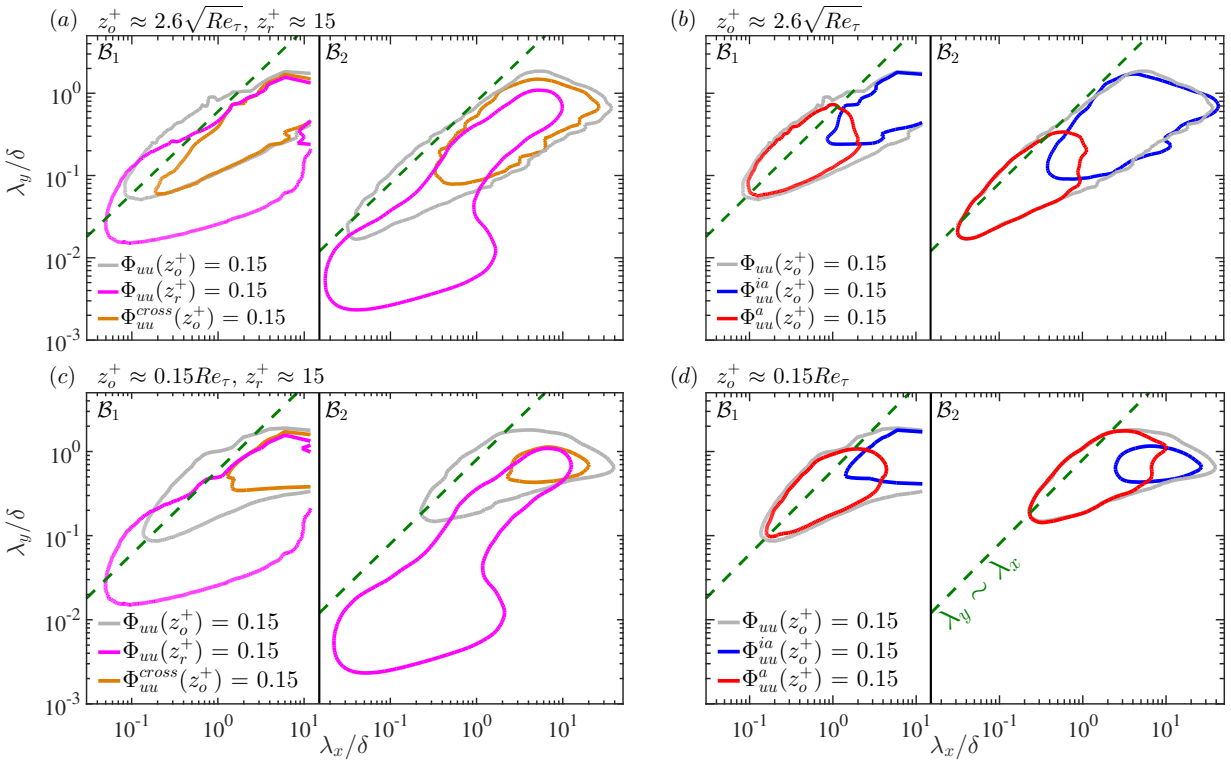

FIGURE 8.2: (a,c) Constant energy contours for $\Phi_{uu}(z_o^+)$, $\Phi_{uu}^{cross}(z_o^+,\ z_r^+ \approx 15)$ and $\Phi_{uu}(z_r^+ \approx 15)$ at energy level of 0.15 plotted for (a) $z_o^+ \approx 2.6\sqrt{Re_\tau}$ and (c) $z_o^+ \approx 0.15Re_\tau$. (b,d) Constant energy contours for $\Phi_{uu}^{ia}(z_o^+)$ and $\Phi_{uu}^{a}(z_o^+)$, computed via (8.9) and (8.10), plotted at the same energy level and z_o^+ as in (a,c), respectively. In (a-d), contours on the left and right side correspond to those computed from datasets $\mathcal{B}_1$ and $\mathcal{B}_2$, respectively. Dashed green lines represent the linear relationship, $\lambda_y \sim \lambda_x$. The figure has been adapted from Deshpande et al. (2021).

component, by making use of the scale-by-scale coupling that exists between the velocity signals measured simultaneously at the two locations, $z_r^+ \approx 15$ and z_o^+ (in the log-region), such that $z_r^+ \ll z_o^+$. The scale-by-scale coupling is represented here in the form of Φ_{ii}^{cross}, which is considered at various z_o^+ for both the DNS as well as experimental datasets (table 8.1).

To give a qualitative indication of how Φ_{ii}^{cross} differs from Φ_{ii}, figures 8.2(a,c) show Φ_{uu}^{cross} and Φ_{uu} contours from the two ZPG TBL datasets at z_o^+ across the log-region as an example. It is evident that the former represents the large energetic motions associated with the inactive motions at z_o^+. Φ_{ii}^{cross} also comprises energy signatures from the very large-scale superstructures (scaling with δ), which are known to span across the entire log-region and extend all the way down to the wall (Baars and Marusic, 2020a; Deshpande et al., 2020a; Yoon et al., 2020). These observations motivate the use of Φ_{ii}^{cross} in conjunction with the SLSE (Tinney et al., 2006; Baars et al., 2016a; Deshpande et al., 2021), to compute the linear stochastic estimate of the energy contributions (Φ_{ii}^{ia}) from the motions inactive

at z_o following:

$$\Phi_{ii}^{ia}(z_o^+;\lambda_x,\lambda_y) = \frac{\left[\Phi_{ii}^{cross}(z_o^+, z_r^+ \approx 15;\lambda_x,\lambda_y)\right]^2}{\Phi_{ii}(z_r^+ \approx 15;\lambda_x,\lambda_y)}, \tag{8.9}$$

whereby $\Phi_{ii}^{ia}(z_o^+)$ is essentially a normalized version of $\Phi_{ii}^{cross}(z_o^+, z_r^+ \approx 15)$, with the scale-by-scale normalization done by $\Phi_{ii}(z_r^+ \approx 15)$. Readers interested to see the step-by-step procedure to arrive at the expression in (8.9) may refer to appendix 1 of Deshpande et al. (2021). It is important to note here that the calculations in (8.9), in case of the experimental dataset, are conducted in the frequency domain, and are later converted to λ_x by invoking Taylor's hypothesis, using the mean streamwise velocity at z_o as the convection velocity (Baars et al., 2016a; Deshpande et al., 2021). In accordance to the linear superposition assumption in (8.5), subtracting Φ_{ii}^{ia} from Φ leaves a residual:

$$\Phi_{ii}^{a}(z_o^+;\lambda_x,\lambda_y) = \Phi_{ii}(z_o^+;\lambda_x,\lambda_y) - \Phi_{ii}^{ia}(z_o^+;\lambda_x,\lambda_y). \tag{8.10}$$

This is because for $i = u$, as an example, Φ_{uu}, Φ_{uu}^{a} and Φ_{uu}^{ia} are representative of $\overline{u^2}^+$, $\overline{u^2}^+_{\text{active}}$ and $\overline{u^2}^+_{\text{inactive}}$, respectively. If the flow comprised of only inactive and active inertial motions, Φ_{ii}^{ia} and Φ_{ii}^{a} would respectively be the inactive and active component. We, however, refer to Φ_{ii}^{a} as the residual spectrum, since it also consists of small energy contributions from the inertial sub-range as well as fine dissipative scales, apart from the more energetic active motions.

Figures 8.2(b,d) plots the constant energy contours for the two sub-components $\Phi_{uu}^{ia}(z_o^+)$ and $\Phi_{uu}^{a}(z_o^+)$, for the two ZPG TBL datasets at z_o^+ across the log-region as an example. These subsets have been estimated using (8.9) and (8.10), using the corresponding spectra shown in figures 8.2(a,c), respectively. While Φ_{uu}^{a} takes up the small-scale end of the spectrum, Φ_{uu}^{ia} is restricted to the large-scale portion of Φ. Figure 8.2 also shows the line $\lambda_y \sim \lambda_x$, which is indicative of geometric self-similarity. For the wall-normal location at the lower end (figure 8.2(b)) of the log-region, both $\Phi_{uu}^{a}(z_o^+)$ and $\Phi_{uu}^{ia}(z_o^+)$ nominally follow the $\lambda_y \sim \lambda_x$ line, while this is obscured for Φ_{uu}, in the intermediate and large-scale range (Deshpande et al., 2020a). The conformance of Φ_{uu}^{ia} and Φ_{uu}^{a} contours to the linear relationship is consistent with the hypothesis of Townsend (1961, 1976), who proposed both the inactive and active motions to be related to the self-similar attached eddy contributions. The two motions, however, correspond to different hierarchies of the attached eddies: while the active motions at z_o^+ are associated with the attached eddies of height, $\mathcal{H} \sim \mathcal{O}(z_o)$, the inactive motions conform to larger eddies of height $\mathcal{O}(z_o) \ll \mathcal{H} \lesssim \mathcal{O}(\delta)$. This explains why the contribution from the inactive motions to Φ_{uu}^{ia} reduces with increase in z_o^+ (figures 8.2(b,d)). In contrast, a substantial scale range is observed in the case of the Φ_{ii}^{a} contours

irrespective of the increase in z_o^+, with the contours displaced to comparitively larger scales, which is indicative of its z_o-scaling. With the procedure to estimate Φ_{ii}^a and Φ_{ii}^{ia} now defined, next the spectra contours are tested for δ- and z_o-scaling to investigate the extent to which the respective contours relate with the characteristics of the inactive and active motions. Due to the limited availability of space here, the present analysis has been limited to active motions only. Interested readers are referred to Deshpande et al. (2021) for a thorough analysis on both the inactive and active contributions.

8.6 Active motions

Figure 8.3 shows the constant energy contours of Φ_{ii}^a (for $i = u$, v or w), estimated for the three datasets at z_o^+ across the log-region. The contours are plotted as a function of wavelengths scaled with δ (figures 8.3(d-f)) as well as z_o (figures 8.3(a-c)). Given the exclusive association of the w-velocity component with the active motions (Bradshaw, 1967; Morrison et al., 1992; Baidya et al., 2017; Deshpande et al., 2021), i.e $\Phi_{ww} \approx \Phi_{ww}^a$, here we have directly considered the energy contours of Φ_{ww} for comparison. The residual component of each velocity spectrum can be noted to obey reasonable wall-scaling, which is evident from the overlapping Φ_{ii}^a contours plotted with the wavelengths scaled with z_o. On the other hand, no overlap can be noted in case of the wavelengths normalized by δ. The fact that the Φ_{ii}^a contours follow wall-scaling, reaffirms the efficacy of the present methodology to segregate the inactive and active contributions from the total energy, for all three velocity components in a wall-bounded flow. Further, the good agreement between Φ_{uu}^a (figure 8.3(a)) estimated from both the DNS and experimental datasets suggests the local mean streamwise velocity to be a reasonable choice for the convection velocity for the active motions.

The residual component of the 2-D spectra also conveys important information related to the geometric characteristics of the active motions, which may prove useful for future conceptual modelling efforts. Φ_{ii}^a contours, corresponding to all the velocity components, align along the linear relationship ($\lambda_y \sim \lambda_x$) which is indicative of geometric self-similarity. It suggests that the active motions can be conceptually modelled using Townsend's self-similar attached eddies. The results in figure 8.3 indicate that such an attached eddy should have its dominant streamwise/spanwise aspect ratios following $\lambda_x/\lambda_y \approx 3$ (for u), $\lambda_x/\lambda_y \approx 1.4$ (for w) and $\lambda_x/\lambda_y \approx 1$ (for v). Amongst these ratios, interestingly, the aspect ratio corresponding to the u-contributions closely relates with the self-similar wall-coherent vortex clusters ($\lambda_x \sim$ 2-3 λ_y) analyzed previously by del Álamo et al. (2006) and

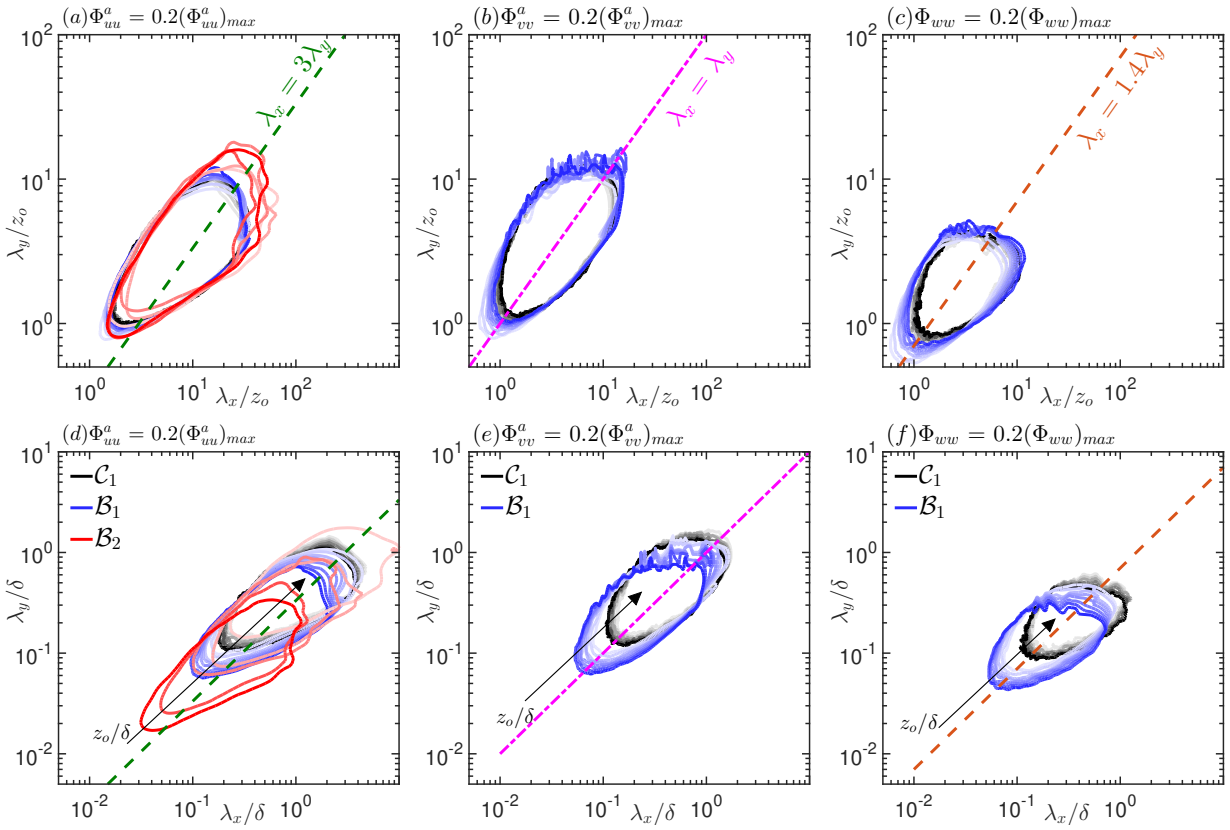

FIGURE 8.3: Constant energy contours for (a,d) $\Phi^a_{uu}(z_o^+)$, (b,e) $\Phi^a_{vv}(z_o^+)$ and (c,f) $\Phi_{ww}(z_o^+)$ ($\approx \Phi^a_{ww}(z_o^+)$) plotted for various z_o^+ as a function of wavelengths scaled with (a-c) z_o and (d-f) δ. Contours in black, blue and red correspond to $\Phi^a_{ii}(z_o^+)$ estimated for datasets $\mathcal{C}_1$, $\mathcal{B}_1$ and $\mathcal{B}_2$, respectively. Dark to light shading indicate an increase in z_o^+ following $2.6\sqrt{Re_\tau} \leq z_o^+ \leq 0.15Re_\tau$, for Re_τ corresponding to the respective datasets. Dashed green, magenta and brown lines represent the linear relationships empirically noted for Φ^a_{uu}, Φ^a_{vv} and Φ_{ww}, respectively.

Hwang (2015). This close agreement suggests the decomposition of Φ_{ii} into the two sub-components Φ^{ia}_{ii} and Φ^a_{ii}, comprising significant self-similar attached eddy contributions, and relating well to the two-component attached eddy structure hypothesized by Hwang (2015).

8.6.1 Reynolds shear stress co-spectra

Townsend (1961, 1976) defined the active motions to be the sole Reynolds shear stress carrying motions at any z_o, with the coexisting inactive motions contributing negligibly to the shear stress at z_o. This means that the Reynolds shear stress co-spectra, which is defined as:

$$\Phi_{uw}(z_o^+;\lambda_x,\lambda_y) \quad = \quad \Re[k_x^+ k_y^+ \phi^+_{uw}(z_o^+;\lambda_x,\lambda_y)], \tag{8.11}$$

should also exhibit wall-scaling (Bradshaw, 1967; Morrison et al., 1992; Baidya et al., 2017), analogous to Φ_{ww} shown in figure 8.3. Here, $\Re$ refers to the real value of the complex-valued spectrum Φ_{uw}, which is estimated via cross-correlating the instantaneous velocity fluctuations, $u(z_o^+)$ and $w(z_o^+)$. While the former comprises of both the active (u_{active}) and inactive ($u_{inactive}$) contributions, it is u_{active} which contributes predominantly to Φ_{uw} as per Townsend's hypothesis (Townsend, 1961, 1976). We test this here for the low-Re_τ DNS data by separately estimating Φ^a_{uw}, defined as:

$$\Phi^a_{uw}(z_o^+;\lambda_x,\lambda_y) \;=\; \mathrm{Re}[k_x^+ k_y^+ \phi^+_{u_{active}w}(z_o^+;\lambda_x,\lambda_y)], \tag{8.12}$$

wherein Φ^a_{uw} is estimated by cross-correlating the active component of the instantaneous streamwise velocity, $u_{active}(z_o^+)$ and $w(z_o^+)$. To estimate the active and inactive contributions to the instantaneous flow field $u(z_o^+)$, we use the same SLSE methodology employed previously for segregating the two contributions to the energy spectrum. As per the SLSE methodology (Baars et al., 2016a; Deshpande et al., 2021):

$$\widetilde{u}_{inactive}(z_o^+;\lambda_x,\lambda_y) = H_L(z_o^+, z_r^+{\approx}15;\lambda_x,\lambda_y)\widetilde{u}(z_r^+{\approx}15;\lambda_x,\lambda_y), \tag{8.13}$$

where $\widetilde{u}(z_r^+ \approx 15;\, \lambda_x,\, \lambda_y)$ is the 2-D Fourier transform of the instantaneous wall-parallel flow field, $u(z_r^+ \approx 15)$ in x and y. Here, H_L represents the scale-specific linear transfer kernel, and is estimated from an ensemble of data following:

$$H_L(z_o^+, z_r^+{\approx}15;\lambda_x,\lambda_y) = \frac{\langle \widetilde{u}(z_o^+;\lambda_x,\lambda_y)\widetilde{u}^*(z_r^+{\approx}15;\lambda_x,\lambda_y)\rangle}{\langle \widetilde{u}(z_r^+{\approx}15;\lambda_x,\lambda_y)\widetilde{u}^*(z_r^+{\approx}15;\lambda_x,\lambda_y)\rangle}, \tag{8.14}$$

where the asterisk ($*$) and angle brackets ($\langle\rangle$) denote the complex conjugate and ensemble averaging, respectively (Deshpande et al., 2021). $u_{inactive}(z_o^+)$, which can be retrieved on inverse Fourier transforming $\widetilde{u}_{inactive}(z_o^+)$, is then used to obtain $u_{active}(z_o^+)$ following the linear decomposition of $u(z_o^+)$ given in (8.3).

Figure 8.4 compares Φ_{uw} and Φ^a_{uw} estimated for the two DNS datasets $\mathcal{B}_1$ (figure 8.4(b)) and $\mathcal{C}_1$ (figure 8.4(a)) at z_o^+ across the log-region. It can be observed that both Φ_{uw} and Φ^a_{uw} exhibit reasonable wall-scaling, with $\Phi_{uw} \approx \Phi^a_{uw}$ in the small and intermediate-scale range. The good overlap of contours in figure 8.4 is a testament to Townsend's hypothesis on the active motions being solely responsible for producing the Reynolds shear stress. There is, however, some disagreement between Φ_{uw} and Φ^a_{uw} at large scales, where Φ_{uw} contours can be seen deviating away from the z_o-scaling. This may be owing to the influence of the large δ-scaled motions via non-linear interactions with the active motions (Morrison, 2007;

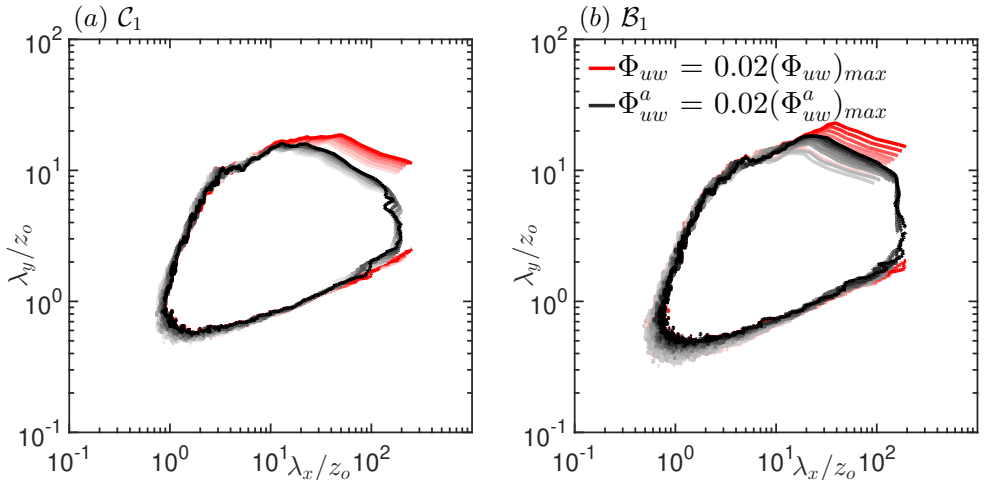

FIGURE 8.4: Constant energy contours for $\Phi_{uw}(z_o^+)$ (in red) and $\Phi^a_{uw}(z_o^+)$ (in black) computed for datasets (a) $\mathcal{C}_1$ and (b) $\mathcal{B}_1$ and plotted for various z_o^+ as a function of wavelengths scaled with z_o. Dark to light shading indicates an increase in z_o^+ following $2.6\sqrt{Re_\tau} \leq z_o^+ \leq 0.15Re_\tau$, for Re_τ corresponding to the respective datasets.

Mathis et al., 2009), and is currently under investigation by the authors.

8.7 Conclusions

This chapter presents arguments in support of Townsend's hypothesis (Townsend, 1961, 1976) on the statistical nature of the Reynolds stress carrying motions in wall-bounded turbulent flows. As per Townsend, the wall-bounded flow at any point comprises of two components – (i) active motions, which are responsible for transferring the momentum, and (ii) inactive motions, with both conforming to Townsend's self-similar attached eddies. Empirical support is provided to these arguments via implementation of an SLSE-based energy decomposition methodology on previously published wall-turbulence datasets. The procedure first isolates the turbulent kinetic energy associated with the inactive motions, by exploiting their known characteristic of being comparatively larger than the coexisting active motions (Townsend, 1961, 1976). Energy associated with the active motions (Φ^a_{ii}, where $i = u$, v or w) is then estimated by subtracting this 'inactive' energy from the total energy.

The SLSE methodology is demonstrated to be effective for all three velocity components in a wall-bounded turbulent flow by testing the scaling characteristics of the active motions. Φ^a_{ii} contours are noted to obey wall-scaling across a large Re_τ range. The good overlap between the estimates from both the experimental and DNS datasets also establishes Taylor's hypothesis to be a reasonable assumption for the active motions. Further,

the decomposition of Φ_{ii} into Φ_{ii}^{a} and Φ_{ii}^{ia} reveals the geometric self-similarity of the inactive and active motions, suggesting they can be conceptually modelled using the attached eddy model framework (Perry and Chong, 1982; Marusic and Monty, 2019). The ability to decompose the active and inactive contributions also permits computation of Φ_{uw}^{a}, which considers the cross-correlation exclusively between u_{active} and w. Φ_{uw}^{a} contours are found to agree well with the Φ_{uw} contours, thus endorsing Townsend's hypothesis on the active motions as the sole Reynolds shear stress carrying motions in wall-bounded flows. In the present work, support towards the validity of Townsend's hypothesis, for the lateral velocity components, has only been possible via low-Re_{τ} datasets. This motivates undertaking of multi-component multi-point high Reynolds number experiments in the future to firmly establish the validity of this hypothesis for all three velocity components.

8.8 Acknowledgements

The authors wish to acknowledge the Australian Research Council for financial support and are thankful to the authors of del Álamo et al. (2004) and Sillero et al. (2014) for making their respective data available. The authors also thank Drs Dileep Chandran, Woutijn Baars, Charitha de Silva and Anagha Madhusudanan for their valued support at various stages of this work.

Chapter 9

A scheme to correct the influence of calibration misalignment for cross-wire probes in turbulent shear flows

[Published paper VI[1]]

9.1 Preface to the chapter

This chapter is an article published in the *Experiments in Fluids* journal, titled "A scheme to correct the influence of calibration misalignment for cross-wire probes in turbulent shear flows" (Deshpande et al., 2020d). The study proposes a scheme to correct the erroneous statistics processed from a misaligned 2-D calibration of an X-wire probe by using synthetic experiments on a published DNS dataset. This, consequently, establishes an experimental procedure to accurately estimate the lateral velocity statistics using an X-wire probe, which are known to be highly sensitive to any inaccuracies in the calibration procedure (Jørgensen, 1996; Baidya et al., 2019b). It would facilitate the multi-component multi-point measurements in the high-Re_τ TBL, to be conducted in the near future, to firmly

[1]Deshpande, R., Monty, J.P. & Marusic, I. (2020). A scheme to correct the influence of calibration misalignment for cross-wire probes in turbulent shear flows. *Experiments in Fluids* 61(85). DOI: https://doi.org/10.1007/s00348-020-2918-8

establish the validity of Townsend's hypothesis (discussed in chapters 7 and 8) for the lateral velocity components.

9.2 Abstract

Velocity fluctuations, measured via multi-wire probes, are very sensitive to misalignment between the calibration coordinate system and that of the wind tunnel. The present study proposes a scheme to correct the erroneous velocity fluctuations processed from a misaligned calibration while investigating a wall-bounded turbulent shear flow. The scheme is based on the premise that the viscous-scaled spectral energy distribution in the small-scales is invariant with Reynolds number and solely depends on the viscous scaled spatial resolution of the sensor. Energy spectra processed from the misaligned calibration, in this small-scale range, are compared with the 'expected' spectra obtained via synthetic experiments on a direct numerical simulation (DNS) data set. The erroneous lateral velocity spectra is found to be either relatively amplified or attenuated, by almost the same factor, at all wall-normal distances across the shear flow. A unique *gain*, defined to be the correction ratio, is thus obtained by forcing the erroneous spectra onto the reference spectra in this scale range. This ratio is further used to rectify the time series of the lateral velocity fluctuations, acquired across the shear flow, via Fourier analysis. The scheme is shown to be effective for experiments conducted across a decade of Reynolds number and using probes of varying spatial resolution.

9.3 Introduction

Development of a variety of multi-wire probes over the last three decades has allowed for a deeper investigation into the high Reynolds number dynamics of wall-bounded turbulence (Wallace and Vukoslavčević, 2010). Multi-wire probes are highly complex instruments, however, and are prone to error from a range of sources. For example, errors due to the inadequate spatial resolution of these probes, owing to the size of their measuring volumes, have been recognized and investigated previously (Strohl and Comte-Bellot, 1973; Browne et al., 1988; Suzuki and Kasagi, 1992; Burattini, 2008). Availability of direct numerical simulation (DNS) flow fields has allowed researchers (Burattini et al., 2007; Philip et al., 2013; Baidya et al., 2019c; Zimmerman et al., 2017) to perform synthetic experiments and explain these spatially attenuated statistics, in turn inspiring the development of miniature probes

(Baidya et al., 2012; Zimmerman et al., 2017). Apart from the issue of spatial resolution, uncertainties in the probe calibration procedure also bring in additional errors and these have been investigated to a limited extent in the literature (Yavuzkurt, 1984; Jørgensen, 1996). Given the uniqueness of each hotwire sensor in terms of its response (voltage) to the surrounding flow (velocity), calibration of each sensor is critical to determine its velocity-voltage mapping. For a multi-wire probe, the calibration is typically carried out by placing the probe in front of an articulating jet with the capability of varying the flow speed and the incident flow angle. This practise is hence referred as a two-dimensional (2-D) calibration and provides a map between the three velocity components and the corresponding voltages from each sensor.

Jørgensen (1996) found that the lateral velocity fluctuations are more sensitive to the uncertainties in the 2-D calibration than the streamwise velocity fluctuations. Recently, Baidya et al. (2019b) have utilized channel DNS flow fields to investigate the sensitivity of the turbulent stresses to various uncertainties in the calibration procedure for a cross-wire probe (henceforth referred as an X-probe). One of the uncertainties investigated was the misalignment of a 2-D calibration. A 2-D calibration is said to be misaligned when the coordinate system of the jet does not align with the coordinate system of the wind-tunnel. Figure 9.1 explains this for the case of a uv X-probe with x, y and z denoting the streamwise, spanwise and wall-normal directions respectively, with u, v and w denoting the velocities corresponding to these directions (this convention is followed throughout the manuscript). For the probe shown in figure 9.1, angles ϕ' and ψ' denote the misalignment in the sensor plane and out of the sensor plane, respectively (figure 9.1). Baidya et al. (2019b), through synthetic experiment, showed that all the turbulence stresses are adversely affected by the misalignment, especially the Reynolds shear stress ($\overline{uw}$). Further, they proposed that the angular misalignment for 2-D calibration can be accounted for by rotating the jet reference plane to match a reference 'zero-angle' calibration performed in the wind tunnel, an idea also implemented by Zimmerman et al. (2017). However, this practise of accounting for the misalignment was found to be effective for angular offsets only within ϕ',$\psi' \approx \pm$ 0.5°, which is the accuracy level obtained when the jet calibrator is aligned using typical reference devices (eg. laser sheets; refer § 9.4.1.3).

The problem becomes serious when there are no references available to aid the alignment procedure. Such a situation may be encountered when the probes are not calibrated *in situ*, i.e. they need to be unmounted from the tunnel traverse to be calibrated at a different location. *In situ* calibration of a multi-wire probe, which is to be used for measurement in an internal flow geometry (eg. channel, pipe flow), is also challenging given that the

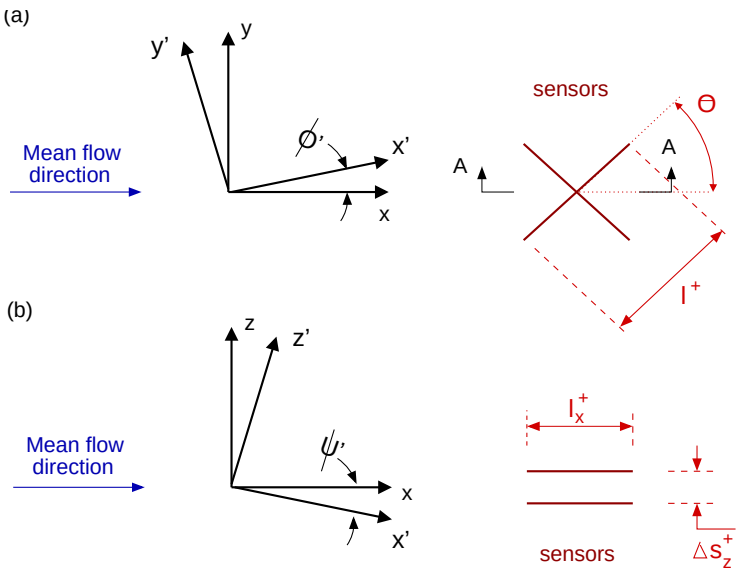

FIGURE 9.1: A schematic representation of the misalignment between the wind-tunnel coordinate system (x-y-z) and the coordinate system for the 2-D jet calibrator (x'-y'-z') for an X-probe oriented to measure the u and v velocities. Sensors are represented by solid lines in red. The angles (a) ϕ' and (b) ψ' correspond to the in-plane and out-of-plane misalignment with reference to the sensor plane (which is x-y for the uv X-probe), respectively. Also highlighted is the sensor length (l^+), spacing between the two sensors (Δs^+) and angle (θ) made by each sensor with x, with subscripts denoting the direction in which they are measured.

jet calibrator cannot be taken inside the working section due to physical constraints (in a majority of cases). The angular offset (ϕ',ψ'), which signifies the degree of misalignment in the 2-D calibration, can be greater than 2° degrees (shown later) in such cases and hence cannot be accounted for by using the methodology implemented by Baidya et al. (2019b), which is applicable only for very small offsets where a linear response of the sensor (with flow angle) may be assumed. In the present study, we encountered a similar scenario while attempting to conduct velocity profile measurements using an X-probe in a channel flow facility (refer 9.4.1.1). Here, we attempt to highlight the effect of such a calibration misalignment on the velocity statistics and spectra, followed by proposal of a scheme to correct the erroneous velocity fluctuations using synthetic experiments as a reference. Throughout this article, capitalization and over-bars indicate time-averaged quantities, while superscript '+' denotes normalization by viscous units (eg., $U^+ = U/U_\tau$ and $z^+ = zU_\tau/\nu$, where U_τ and ν correspond to the mean friction velocity and kinematic viscosity, respectively).

Probe	Ref.	Re_τ	Probe type	Flow type	h or δ (in m)	ν/U_τ (in μm)	θ (in deg)	l_x^+, l_y^+ or l_z^+	Δs_y^+ or Δs_z^+	l/d	Symbol	Misaligned 2-D Cal only
Auspex A55P51	$AX1$	1 000	uv,uw	Channel	0.05	50	45	14	10	200	▲	✓
Auspex A55P61	$AX2$	1 000	uv,uw	Channel	0.05	50	45	7	10	200	▼	✓
Custom	CX	1 000	uv,uw	Channel	0.05	50	45	7	4	200	♦	✓
		10 000	uv,uw	ZPG TBL	0.32	32	45	12	7	200	●	

TABLE 9.1: A summary of the various physical experiments conducted. Terminology has been described in § 9.4.1.2. Synthetic experiments were conducted corresponding to the viscous-scaled measuring volume (a function of l^+ and Δs^+) for each case mentioned. Statistics from these synthetic experiments are plotted with the same symbol and a lighter color shade as for the corresponding physical experiments. A checkmark (✓) in the last column refers to experimental cases where all available 2-D calibrations were misaligned, i.e. no 'accurate' 2-D calibration could be conducted.

9.4 Experimental set-up

Physical experiments have been performed in the channel and boundary layer flow to demonstrate the effect of 2-D calibration misalignment on the velocity statistics. Table 9.1 gives details of these experiments and the various X-probes used. Synthetic experiments, corresponding to these X-probes, are also performed on DNS flow fields of a turbulent channel flow (del Álamo et al., 2004) and are used as a basis to correct the erroneous statistics.

9.4.1 Physical experiments

9.4.1.1 Flow facilities

Physical experiments were conducted in the channel flow facility and the high Reynolds number boundary layer wind tunnel (HRNBLWT) housed in the University of Melbourne. Each of these is a blow-down type non-recirculating wind tunnel with the inlet flow tripped via sandpaper strips to ensure a fully turbulent flow at the X-probe measuring station. During zero pressure gradient turbulent boundary layer (ZPG TBL) measurements, the free-stream speed of the tunnel was maintained at 15 ms^{-1} and the probe was located at 13 m from the start of the working section, giving a friction Reynolds number, Re_τ ($= U_\tau\delta/\nu$) $\approx$ 10 000 for the measurement. Both U_τ and δ (boundary layer thickness) were obtained by fitting the mean velocity profile to the composite velocity formulation given by Chauhan et al. (2009). More details regarding HRNBLWT may be found in Baars et al. (2016b).

The channel flow experiments were performed in the same facility used by Monty et al. (2007) and Monty et al. (2009). The aspect ratio of the channel cross section is 11.7:1 which is sufficient to ensure minimal sidewall influence and the measurement station was located at nearly $410h$ from the beginning of the working section, with h being the channel half-height. The channel centreline speed was maintained at 6.5 ms^{-1} approximately to achieve an Re_τ ($= U_\tau h/\nu$) $\approx$ 1 000, where U_τ is estimated by recording the pressure gradient across the channel working section.

During velocity profile measurements in each facility, the X-probe was traversed across the turbulent shear flow beginning from the position closest to the wall, which was estimated by using a traversable microscope. From thereon, the probe was traversed to logarithmically spaced locations by a linear rail mechanism governed by a *Renishaw* linear encoder with

a resolution of 0.5 μm, approximately. Such a resolution allows estimation of z^+ within error margin of $O(10^{-2})$ which, as will be seen ahead, is important for the effectiveness of the correction scheme proposed in this study.

9.4.1.2 Hotwire sensor and anemometry details

The X-probes listed in table 9.1 differ in terms of their viscous-scaled measuring volumes. Here, l_i^+ refers to the length of the sensing element while Δs_i^+ refers to the spacing between the two sensors with subscript i specifying the direction in which it is measured, which depends on type of the probe (uv or uw) . For example, for a uv X-probe (figure 9.1), the measuring volume is given by $l_x^+ \times l_y^+ \times \Delta s_z^+$. θ refers to the angle made by both the sensing elements with the free-stream (x) direction and d refers to the diameter of the sensor. Accordingly, the included angle of the X-probe is two times θ, which is 90° for all X-probes used in the present study. Since here we are solely dealing with canonical wall-bounded turbulence, an included angle of 90° is deemed sufficient (Tagawa et al., 1992) to avoid errors due to rectification (Tutu and Chevray, 1975). This angle should however be greater than 90° for measurements in high turbulence intensity fields such as rough wall flows (Perry et al., 1987) and flows with adverse pressure gradients (APG; Marusic and Perry (1995)) in order to avoid the scenario where the erroneous statistics due to rectification are misrepresented as a calibration error, which is being investigated in this study.

Probes $AX1$ and $AX2$ are standard probes purchased from Auspex Corporation, whereas the CX probe is manufactured in-house (Baidya et al., 2012) with the aim of minimizing the measuring volume and the associated errors due to spatial resolution. During measurement, the probes were connected to a Dantec 55H25 X-probe holder and operated by an in-house Melbourne University Constant Temperature Anemometer (MUCTA) at an overheat ratio of 1.8. Negligible thermal cross-talk was noted between the two hotwire sensors when exposed to the velocity range of interest. A high overheat ratio allowed us to set a system frequency response corresponding to $t^+ < 1.5$ which is sufficient to capture the highest frequency information in a wall-bounded turbulent flow (Hutchins et al., 2009). The hotwire signals were sampled at an interval of $\Delta t^+ \leq 0.6$ for a minimum duration of $15000\delta/U_\infty$ seconds, where U_∞ is the mean centreline or free-stream velocity.

9.4.1.3 Probe calibration and data processing technique

The 2-D calibration of the X-probes was performed with an articulating compressed-air driven jet facility. During calibration, the X-probe was positioned such that the two sensors were in the central 'irrotational' portion of the flow exiting the jet nozzle. The jet was rotated through a series of angles: -30° $< \beta <$ 30° in the sensor plane of the probe, which is sufficient for calibrating an X-probe (Baidya, 2016). Angular encoders positioned along both the rotation axes provided accurate measurement of the change in jet angle relative to an initially declared reference location of $\beta = 0°$. This sweep of the jet angles is repeated for multiple jet velocities (U_{jet}) to record the corresponding voltages from wire 1 and wire 2 (E_1 and E_2) and obtain a one-to-one mapping between the voltage-velocity pairs following: $E_1 = a(U_{jet},\beta)$ and $E_2 = b(U_{jet},\beta)$. Figure 9.2(a) shows the voltage pairs acquired during a typical 2-D calibration, as an example. Next, the voltages are fitted to smooth functions of jet velocities and angles determined based on the effective angle method (EAM;Bradshaw (2013)), giving $E_1 = f_1(U_{jet},\beta)$ and $E_2 = f_2(U_{jet},\beta)$. These functions are then solved for a linearly distributed set of U_{jet} and β to get a voltage map as shown in figure 9.2(b). The fitted functions are finally inverted to generate calibration surfaces of the form: $u = f(E_1,E_2)$ and v (or w) $= g(E_1,E_2)$. It is worth mentioning that although the look-up table technique (LUT; Willmarth and Bogar (1977)) has been found to be more reliable than EAM (Burattini and Antonia, 2005), the latter was preferred in the present study. This is because most LUT schemes do not use theoretical equations but rather rely on a one-to-one voltage pair to velocity relationship obtained from the calibration. Since the measured velocity fluctuations are directly influenced by the gradient of the LUT scheme (Morrill-Winter et al., 2015; Baidya, 2016), a fit selected without a theoretical basis has a potential to introduce uncertainties. Since the present study is focused on identifying, as well as correcting, the errors due to calibration misalignment, the intention was to avoid introduction of any further (intractable) errors into the data reduction procedure, and thus EAM was chosen over LUT.

Apart from the 2-D calibration, another calibration (henceforth referred as 1-D calibration) is performed by traversing the X-probe to the free-stream (or centreline in case of the channel) and recording voltages corresponding to various known free-stream (or centreline) speeds. This calibration is similar to the conventional calibration for a single-wire hotwire sensor (Talluru et al., 2014) and is the reference 'zero-angle' calibration used by Baidya et al. (2019b) to check for misalignment between the tunnel and the jet calibrator coordinate system. For an accurately aligned jet calibrator, the voltage pairs corresponding to $\beta = 0°$ (from the 2-D calibration) should align with the voltage pairs recorded during 1-D

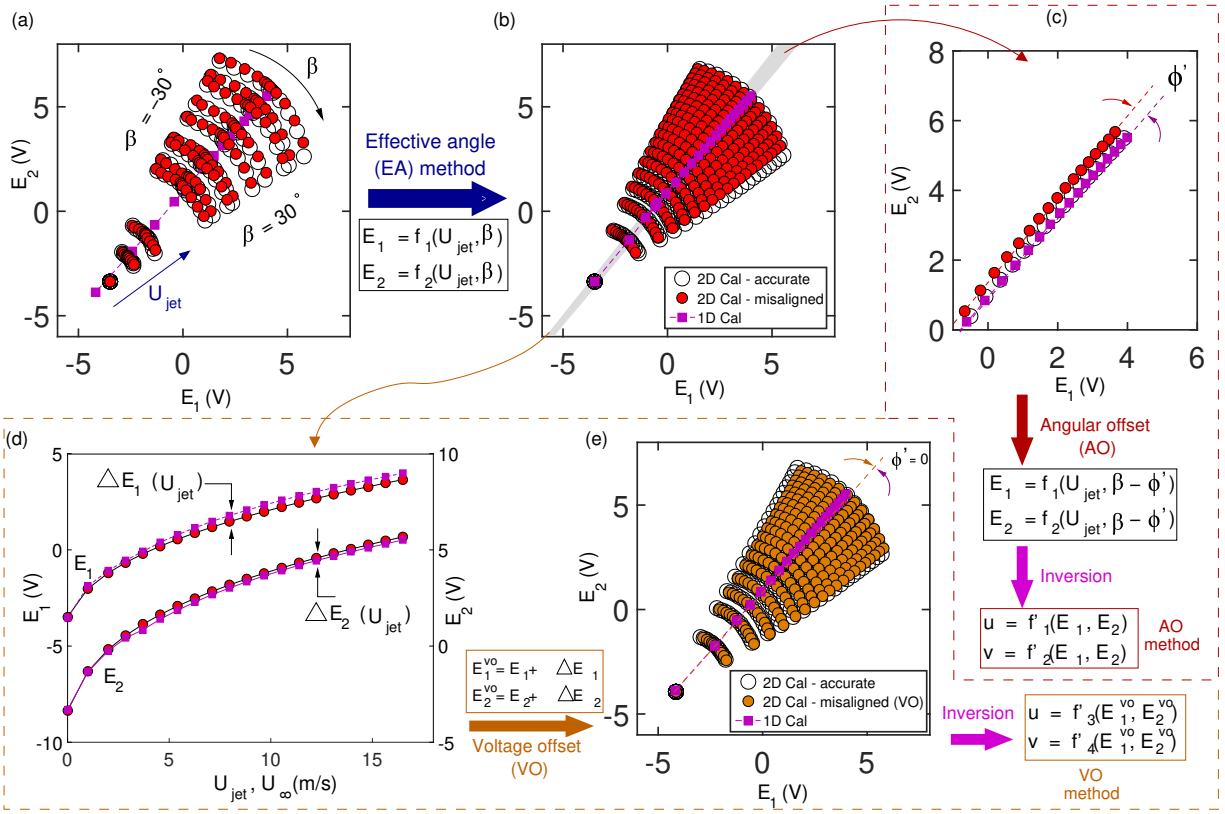

FIGURE 9.2: Procedure to account for misalignment while processing 2-D calibration of a *uv*-CX probe, explained by using an 'accurate' 2-D calibration as a reference: (a) Voltage pairs obtained by varying the U_{jet} and β for an *accurate* and misaligned 2-D calibration along with the voltages obtained from the 1-D calibration in *HRNBLWT* just before the measurement. (b) Voltages in (a) interpolated onto a linearly distributed set of U_{jet} and β based on effective angle method. (c) Comparison of 2-D calibration voltage pairs corresponding to $\beta = 0°$ (highlighted by gray background in (b)) with 1-D calibration to obtain the angular offset ϕ'. (d) The same voltage pairs as in (c), but compared individually for the two sensors to obtain the voltage offset $\Delta E_1(U_{jet})$ and $\Delta E_2(U_{jet})$. (e) Comparison between voltage pairs from the *accurate* and the misaligned calibration, with the latter shifted after application of the voltage offset estimated in (d).

calibration, meaning that the jet flow direction (at $\beta = 0°$) is parallel to the streamwise direction x. Apart from this, the 1-D calibration is also used to take into account the drift of the hotwire sensors over time, with the calibration conducted both before (pre 1-D) and after (post 1-D) the velocity profile measurement. In addition to this, the X-probe was also periodically traversed to the free-stream during the measurement to acquire one additional voltage-velocity relationship, following a practise known as 'free-stream' checks proposed by Talluru et al. (2014). These checks, combined with the pre and post 1-D calibrations, are used to obtain an updated 1-D calibration (via interpolation) for each wall-normal location of the profile. In the case of an X-probe, however, the u and v (or w) information is retrieved from the 2-D calibration surfaces, $f(E_1,E_2)$ and $g(E_1,E_2)$, respectively. We utilize the interpolated 1-D calibrations as references to subsequently generate new 2-D

calibration surfaces for each wall-normal location to account for the sensor drift. This procedure is discussed in detail in the appendix A (§ 9.10).

In the case of measurements in $HRNBLWT$, the jet calibrator could be set-up inside the test section. This allowed for an accurate alignment of the jet coordinate system with the tunnel coordinate system through the use of laser sheets. This involved creating laser sheet planes parallel and perpendicular to the tunnel side walls which were used as references for the alignment procedure, ensuring ϕ',$\psi' \approx 0°$ (figure 9.1). This position of the jet was set as the reference position ($\beta = 0°$) for the jet encoders. Hence, an '*accurate*' 2-D calibration (i.e. one without any misalignment) of the X-probe could be achieved during the boundary layer measurement. Another calibration was carried out for the same X-probe, immediately after the *accurate* 2-D calibration, where the jet was intentionally aligned via visual inspection only (i.e. without using the laser sheets), resulting in ϕ',$\psi' \neq 0°$ (refer § 9.5).

During channel flow measurements, given the limited cross-section of the working section ($1{,}170 \times 100\ mm^2$), the jet facility was positioned on the top outer surface of this section. The X-probe was hence traversed outside of this section, using the linear rail mechanism, for conducting the 2-D calibration. However, unlike the case of $HRNBLWT$, there were no reliable reference planes at the channel top for accurately aligning the jet using laser sheets. Irrespectively, due to physical restrictions, it was not possible to set-up a laser arrangement on the channel top surface. Hence, the alignment of the jet was always carried out through visual inspection, a method which is prone to misalignment (ϕ',$\psi' \neq 0°$). Accordingly, as marked in table 9.1, all the 2-D calibrations in the case of the channel flow measurements were misaligned. This was confirmed on comparing these calibrations with the reference 1-D calibration as discussed previously. The 2-D calibration in $HRNBLWT$, where the jet was aligned via visual inspection only, was conducted to mimic the situation experienced during channel measurements.

9.4.2 Synthetic experiments

Here, since the focus is on canonical wall-bounded flows, synthetic probe experiments were conducted on published DNS fields of a turbulent channel flow at $Re_\tau = 934$ (del Álamo et al., 2004). It is to be noted that the Re_τ for this dataset is very close to the physical experiments in the channel flow facility. Researchers interested in implementing the correction scheme for measurements in other flow configurations, for example APG TBL flow, would have to select a corresponding APG TBL DNS dataset. The synthetic experiments

are based on the argument that the spatial attenuation corresponding to sensor measuring volume scales with viscous units (i.e. independent of Re_τ). The resolution of the original DNS data set in the streamwise-spanwise ($\Delta x^+ \times \Delta y^+$) plane is 7.6×3.8, better than any of the physical experiments in the channel (table 9.1). In the present study, we compare the spatially filtered statistics from the synthetic experiments with those from physical experiments and the differences between the two are assigned to calibration misalignment. To this end, spatially filtered velocity fields are computed for each X-probe measuring volume and probe type mentioned in table 9.1, from which the statistics and spectra are obtained at the same wall-normal locations as the corresponding physical experiment (limited up to $z^+ \leq 934$). All the statistics and spectra presented here are averaged over 15 similarly spatially filtered DNS flow fields to obtain a reasonable convergence. Interested readers may refer to Philip et al. (2013) or Baidya et al. (2019c) for more details on the methodology adopted for these synthetic experiments. It is important to note here that these synthetic experiments imitate the approach through which instantaneous velocity is obtained from the X-probe sensor in a physical experiment, i.e. by computation of the effective velocities over the sensor length. It is thus different from a simple box filtering approach across the measuring volume which is done while emulating PIV datasets (Lee et al., 2016).

With the focus being on wall-bounded flows in the present study, we primarily utilize the viscous-scaled premultiplied energy spectra obtained from the synthetic experiments to correct our experimental observations. A database (appendix D) of this spectra, obtained for varying X-probe geometric parameters: l^+, Δs^+ and θ, has been compiled and provided for convenience of the researchers who are interested in utilizing the correction scheme being proposed later in §9.6.2. In case of measurements in other flow configurations, however, researchers interested in implementing this correction scheme would have to choose a relevant DNS dataset and utilize the scaling behavior relevant to the flow. For example, Burattini et al. (2007) in their study of an isotropic flow, used the Batchelor scaling argument to correct their X-probe measurements using an isotropic flow DNS.

9.5 2-D calibration misalignment

In this section, we discuss possible ways to identify and account for calibration misalignment before generating the calibration surfaces for processing the velocity time series. For this, we consider the two 2-D calibrations - *accurate* and misaligned (refer § 9.4.1.3), conducted for a *uv-CX* probe before the high Re_τ measurement in $HRNBLWT$ (table 9.1). Both these calibrations are used to process this boundary layer data set and compute the

velocity statistics and spectra, allowing us to observe the effect of misalignment on these statistics.

9.5.1 2-D calibration misalignment: identification and subsequent processing

Figure 9.2 gives a flowchart-type description of identifying a misaligned calibration followed by two possible ways of accounting for it while processing. We begin by considering the mean voltages in figure 9.2(b) associated with the accurate and misaligned 2-D calibration, along with the pre 1-D calibration interpolated over the same range of U_{jet}. The difference between the misaligned and the *accurate* 2-D calibration is apparent. It can be noted that a similar voltage pair is recorded at the lowest U_{jet} ($U_{jet} \approx 0$) during both the 2-D calibrations and they differ only for higher U_{jet}, suggesting that the mismatch is an artifact of misalignment and not sensor drift. The angular offset for the misaligned calibration, which is representative of the in-plane misalignment angle (ϕ'), is estimated to be $+2.5°$ approximately by following the procedure outlined by Baidya et al. (2019b) (§9.3; figure 9.2(c)) and can be accounted for in the calibration map as shown in the flowchart. Here, ϕ' is positive for counter-clockwise orientation and negative for clockwise orientation. This method, however, doesn't account for the out-of-plane misalignment angle (ψ') since its effect does not show up as an angular offset, as seen for ϕ', in an X-probe calibration. The 'angular-offset' map is then inverted to obtain the calibration surfaces f_1' and f_2' for u and v, respectively. This method is henceforth referred as the angular offset (AO) method.

Given that the estimated ϕ' lies beyond the scope of correction of the AO method (Baidya et al., 2019b), we propose another method to account for misalignment wherein ϕ',ψ' are forced to $0°$ by offsetting the calibration voltages instead of the jet angles. We do this by forcing the 2-D calibration voltage pairs recorded for $\beta = 0°$ at various U_{jet} (henceforth referred as β_o points), to be equivalent to those recorded during the 1-D calibration (figure 9.2(d)). Based on the comparison, unique voltage offsets $\Delta E_1(U_{jet})$ and $\Delta E_2(U_{jet})$ are estimated for both the sensors which are applied across the entire calibration map for the corresponding U_{jet}. Figure 9.2(e) shows the resulting 'voltage-offset' 2-D calibration which gives another pair of calibration surfaces for u (f_3') and v (f_4') on inversion. It can be noted that the 'voltage-offset' calibration map, in general, is still different compared to the *accurate* 2-D calibration map shown in the background. This is because of the estimated voltage offsets being a function of U_{jet} only, effectively assuming that the hotwire sensor responds linearly to the change in flow angle. This assumption, however, is incorrect

given the known fact about the non-linear response of the sensor to flow angles (Hinze, 1975; Bradshaw, 2013) the consequences of which will be discussed ahead. This method of accounting for misalignment is henceforth referred as voltage offset (VO) method. We shall compare the performance of the two methods in the forthcoming discussion.

9.5.2 2-D calibration misalignment: effect on velocity statistics and spectra

We now process the high-Re_τ boundary layer dataset using the two different sets of calibration surfaces obtained from the misaligned 2-D calibration (i.e. AO and VO), in addition to using the calibration surfaces obtained from the *accurate* 2-D calibration. The statistics obtained on processing via the *accurate* 2-D calibration compare well with results of Baidya et al. (2012) (not shown here) at a similar Re_τ and are being used simply as a reference to bring out the effect of a misaligned 2-D calibration. Comparing and contrasting the statistics obtained from the AO method with those from the VO method in figure 9.3, the latter performs better than the former by at least yielding reasonably accurate streamwise statistics. Poor performance by the AO method was expected since $|\phi'| > 0.5°$ (Baidya et al., 2019b), and hence only the VO method of processing the misaligned calibration is considered henceforth. In figure 3, the terminology 'viscous-scaled streamwise turbulence intensity' refers to the variance of the streamwise velocity fluctuation normalized by the square of the friction velocity (i.e. $\overline{u^2}^+ = \overline{u^2}/U_\tau^2$). Readers should note that a similar terminology has been used to refer to the normalized variance of all the velocity components throughout this manuscript.

The fact that $\overline{v^2}^+$ estimated from the VO method deviates from the reference values may be attributed to the application of a voltage offset ($\Delta E_1(U_{jet})$, $\Delta E_2(U_{jet})$) independent of β, incorrectly assuming a linear response of the hotwire sensor to flow angles. To further investigate this, we compare the viscous-scaled premultiplied 1-D streamwise energy spectra of both the streamwise ($k_x^+\phi_{uu}^+$) as well as spanwise ($k_x^+\phi_{vv}^+$) velocity components at $z^+ = 100$ in figure 9.4. Although $k_x^+\phi_{uu}^+$ processed via misaligned calibration compares well with the reference spectra, $k_x^+\phi_{vv}^+$ from the misaligned calibration seems to be attenuated across the entire range of scales (λ_x^+). However, the shape/form of the erroneous spectra is similar to that of the reference spectra and a similar observation is noted at all z^+. Here, $\lambda_x = 2\pi/k_x$ where k_x is the streamwise wavenumber and is obtained from the temporal frequency by invoking the Taylor's hypothesis which assumes the convection velocity (U_c) for all scales to be equal to $U(z^+)$. Since $\overline{v^2}^+(z^+) = \int_0^\infty k_x^+\phi_{vv}^+(\lambda_x^+; z^+)\, d(\ln \lambda_x^+)$, the comparison between

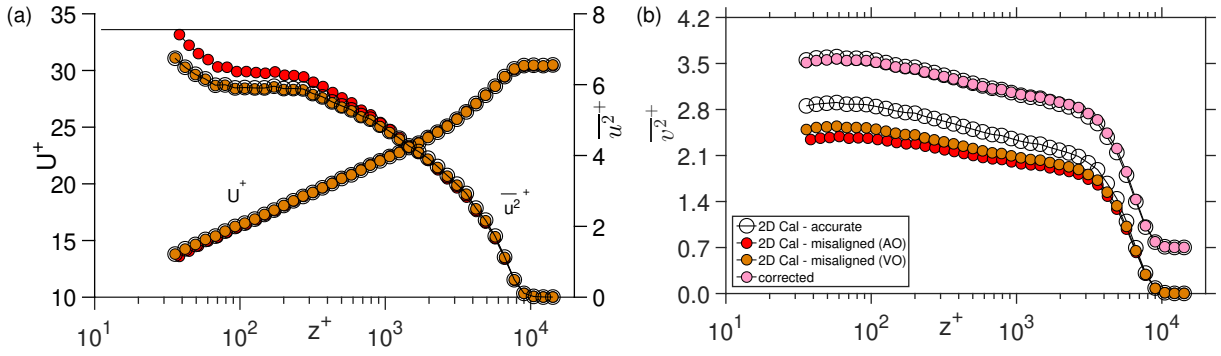

FIGURE 9.3: Viscous-scaled profiles of (a) mean streamwise velocity and streamwise turbulence intensity and (b) spanwise turbulence intensity obtained on processing the high-Re_τ boundary layer data set using the *accurate* and misaligned 2-D calibrations. In case of the misaligned calibration, data processing is carried out using both *AO* and *VO* methods. In (b), the corrected turbulence intensity is plotted with a vertical shift and compared with $\overline{v^2}^+$ obtained from the *accurate* 2-D calibration.

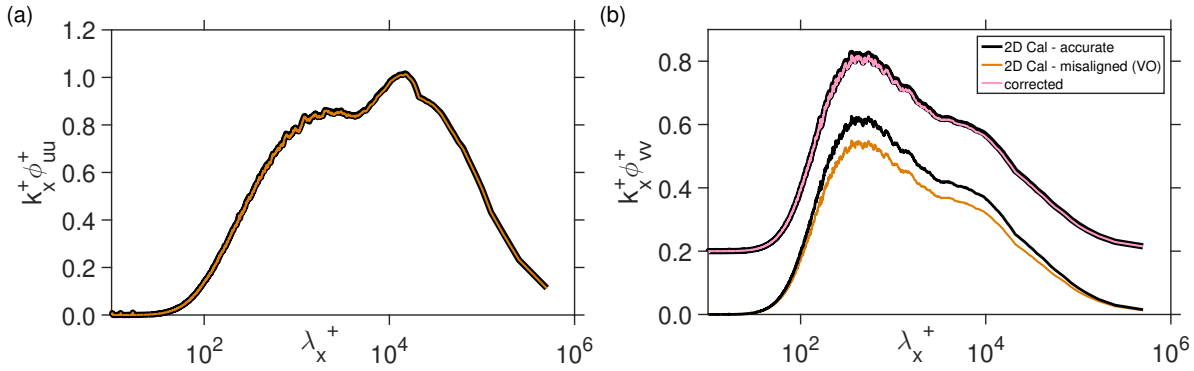

FIGURE 9.4: Viscous-scaled 1-D premultiplied streamwise energy spectra of the (a) streamwise and (b) spanwise velocity obtained on processing the high-Re_τ boundary layer data set using the *accurate* and misaligned 2-D calibrations. In case of the misaligned calibration, data processing is carried out using the *VO* method only. In (b), the corrected spectra of the spanwise velocity is plotted with a vertical shift and compared with spectra obtained from the *accurate* 2-D calibration.

the spectra can explain why the $\overline{v^2}^+$ profile from the misaligned calibration appears to be an attenuated version of the reference profile (figure 9.3(b)). Based on this observation, we hypothesize that a misaligned calibration, when processed via the *VO* method, yields lateral velocity variance which is an amplified/attenuated version of the accurate one. The method, however, estimates the relative energy distribution across the entire range of scales in the flow reasonably accurately. The nature of deviation, i.e. amplification or attenuation, is dependent on the voltage offset ($\Delta E_1(U_{jet})$ and $\Delta E_2(U_{jet})$) applicable for the respective case, as is shown ahead.

The aforementioned hypothesis can be confirmed by systematically varying ϕ' (figure 9.2) and investigating its effect on the processed statistics, $\overline{u^2}^+$ and $\overline{v^2}^+$. The availability of the

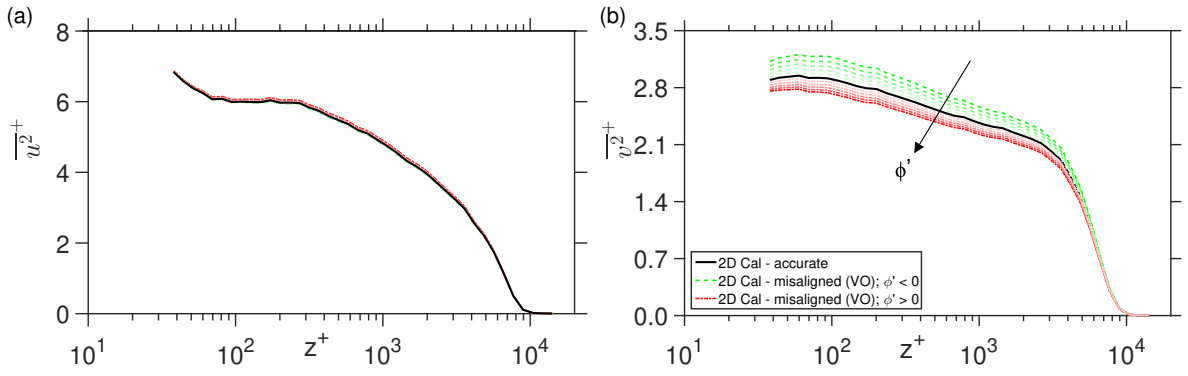

FIGURE 9.5: Viscous-scaled profiles of (a) streamwise and (b) spanwise turbulence intensity obtained on processing the high Re_τ boundary layer data set using 2-D calibrations with known misalignments in the range -5° $< \phi' <$ 5°. Dashed green lines represent $\phi' <$ 0, while dot-dashed red represent $\phi' > 0$ with the shading intensity increasing with the degree of misalignment for both cases. Note that all calibrations are processed via the VO method only.

functions $E_1 = f_1(U_{jet},\beta)$ and $E_2 = f_2(U_{jet},\beta)$, obtained via the EAM (refer §9.4.1.3) for the 'accurate' 2-D calibration, facilitates such an investigation wherein known misalignments, atleast in the sensor plane, can be introduced artificially during the data reduction process. To this end, the functions are used to generate new 2-D calibration maps such that ϕ' systematically varies between -5° $\leq \phi' \leq$ 5°. These maps are then 'voltage-offset' by following the same procedure as outlined in figure 9.2 and then used to process the high-Re_τ boundary layer dataset. Figures 9.5(a) and (b) respectively show the $\overline{u^2}^+$ and $\overline{v^2}^+$ processed from these calibration maps with known angular misalignments. Consistent with what was observed in figure 9.3, $\overline{u^2}^+$ is estimated reasonably accurately via the VO method for the ϕ' range considered. While, $\overline{v^2}^+$ appears to be: (i) amplified when $\phi' <$ 0 and (ii) attenuated when $\phi' > 0$, as compared to $\overline{v^2}^+$ estimated via the 'accurate' 2-D calibration ($\phi' = 0°$). Not surprisingly, the degree of attenuation/amplification increases with increase in the severity of misalignment (i.e. $|\phi'|$). With the hypothesis confirmed, we now utilize this property to propose a scheme to correct the erroneous spanwise spectra in figure 9.4(b) by estimation of a correction ratio which can be used as a *gain* to amplify the spectra.

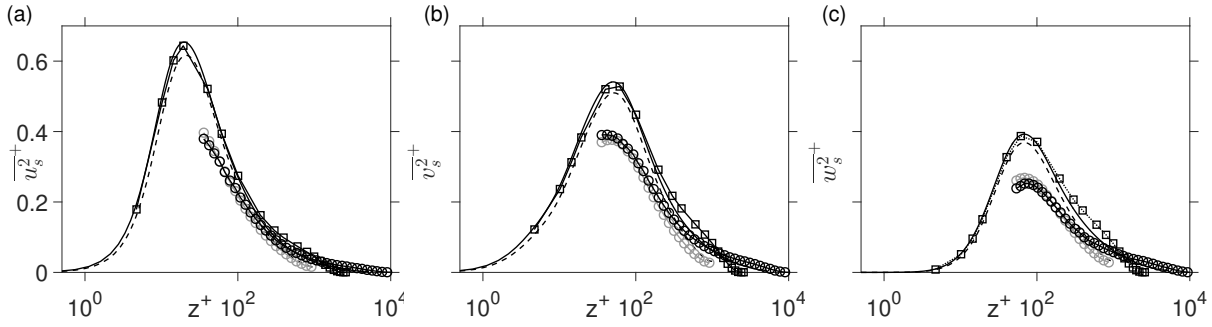

FIGURE 9.6: Viscous-scaled turbulence intensity profiles of the (a) streamwise, (b) spanwise and (c) wall-normal velocity decomposed into small-scale component based on a cut-off wavelength of $\lambda_x^+ \approx 210$ for various data sets: lines (- -) and (-) represent channel DNS data at $Re_\tau = 1\,000$ and 5 200 respectively (Lee and Moser, 2015). (□) represents ZPG TBL DNS data at $Re_\tau \approx 2\,000$ (Sillero et al., 2013). (◯) in dark shading represent ZPG TBL data from present physical experiments at $Re_\tau \approx 10\,000$ processed via *accurate* 2-D calibration, while those in light shading represent statistics from the corresponding synthetic experiments.

9.6 Correction scheme

9.6.1 Re_τ-invariance of the turbulent kinetic energy in the small scales

The correction scheme is based on the premise that the viscous-scaled small-scale turbulence energy is invariant with Re_τ and solely depends on the viscous-scaled spatial resolution of the sensor measuring the velocity fluctuations. Hutchins et al. (2009) have demonstrated this previously for $\overline{u^2}^+$, while Baidya et al. (2012) and Baidya (2016) have demonstrated the same for $\overline{v^2}^+$ and $\overline{w^2}^+$. Here, we analyze various turbulence datasets, with Re_τ spanning $O(10^3)$ – $O(10^4)$, to establish a spectral cut-off (λ_x^+) for which the premise would be true for all three velocity components. Further on, we highlight how the data processed from misaligned 2-D calibrations is inconsistent with the premise.

Datasets considered are the channel DNS at $Re_\tau \approx 1\,000$ and 5 200 (Lee and Moser, 2015), ZPG TBL DNS at $Re_\tau \approx 2\,000$ (Sillero et al., 2013) and the present experimental dataset for the ZPG TBL at $Re_\tau \approx 10\,000$ (table 9.1) processed using an *accurate* 2-D calibration. Also considered are the statistics from the synthetic experiment, with X-probe volume corresponding to the high-Re_τ experimental dataset, to take into account the attenuated small-scale energy due to the spatial resolution issue. It was found, based on careful observation, that energy contained in the scales smaller than $\lambda_x^+ \approx 210$ is consistent with the premise. To prove this, figure 9.6 showcases the turbulence stress profiles from the

aforementioned datasets, decomposed into small-scale ($\overline{u^2_{i,S}}^+$) components considering $\lambda_x^+ \approx 210$ as the cut-off. Here, since $\overline{u_i^2}^+(z^+) = \int_0^\infty k_x^+\phi_{ii}^+(\lambda_x^+; z^+)\, d(\ln \lambda_x^+)$, hence $\overline{u^2_{i,S}}^+(z^+) = \int_0^{210} k_x^+\phi_{ii}^+(\lambda_x^+; z^+)\, d(\ln \lambda_x^+)$ for $i = u$, v or w. The cut-off considered here is much smaller than that considered in the literature (Hutchins et al., 2009; Baidya et al., 2012) due to the minimum Re_τ amongst selected data sets being as low as 934. The good comparison amongst various datasets, with comparable spatial resolutions, gives a convincing evidence supporting the premise. Also, the small scale energy component for a boundary layer (external) flow matches well with that for channel (internal) flow (Monty et al., 2009), making the premise valid for all canonical wall-bounded flows. It should however be noted that the overlap between $\overline{u^2_{i,S}}^+$ from the physical and synthetic experiments is best closest to the wall and the two profiles deviate gradually as we go away from the wall ($z^+ > 300$). This has also been noted by Hutchins et al. (2009) and Lee et al. (2016) for high Re_τ experimental datasets, at $z/\delta > 0.5$, and is likely an artifact of the decreasing small-scale energy content in the outer region of the flow.

With $\lambda_x^+ \approx 210$ established as a reasonable spectral cut-off, one should ideally see an overlap of $k_x^+\phi_{ii}^+(\lambda_x^+; z^+)$ at various Re_τ at least for $\lambda_x^+ < 210$, where $i = u$, v or w. Ganapathisubramani (2018) has previously demonstrated this to be true for the experimentally acquired $k_x^+\phi_{uu}^+$. With the intention to establish the basis for the correction scheme, we consider $k_x^+\phi_{ii}^+$ at $z^+ \approx 100$ (figure 9.7) from datasets at $Re_\tau \approx 1\,000$ and 10 000 processed using the misaligned 2-D calibration for CX probe. Also plotted is the premultiplied spectra obtained from the corresponding synthetic experiments, which form a part of the database being shared for convenience of interested users. As expected from figure 9.4(a), the experimentally obtained premultiplied spectra of u ($(k_x^+\phi_{uu}^+)_{Exp}$) matches reasonably well with its counterpart from the synthetic experiment ($(k_x^+\phi_{uu}^+)_{sDNS}$) for $\lambda_x^+ < 210$. On the other hand, $(k_x^+\phi_{vv}^+)_{Exp}$ and $((k_x^+\phi_{ww}^+)_{Exp})$ appear to be either amplified or attenuated compared to their counterparts from the synthetic experiments in the same scale range. Drawing inspiration from our earlier discussions based on figure 9.4(b), the mismatch we observe in figures 9.7(b,c) is also considered to be an artifact of using a misaligned calibration. Based on the aforementioned premise, we propose a methodology to force a collapse of $((k_x^+\phi_{vv}^+)_{Exp})$ and $((k_x^+\phi_{ww}^+)_{Exp})$ onto the corresponding $((k_x^+\phi_{vv}^+)_{sDNS})$ and $((k_x^+\phi_{ww}^+)_{sDNS})$ for $\lambda_x^+ < 210$, by computing a correction ratio.

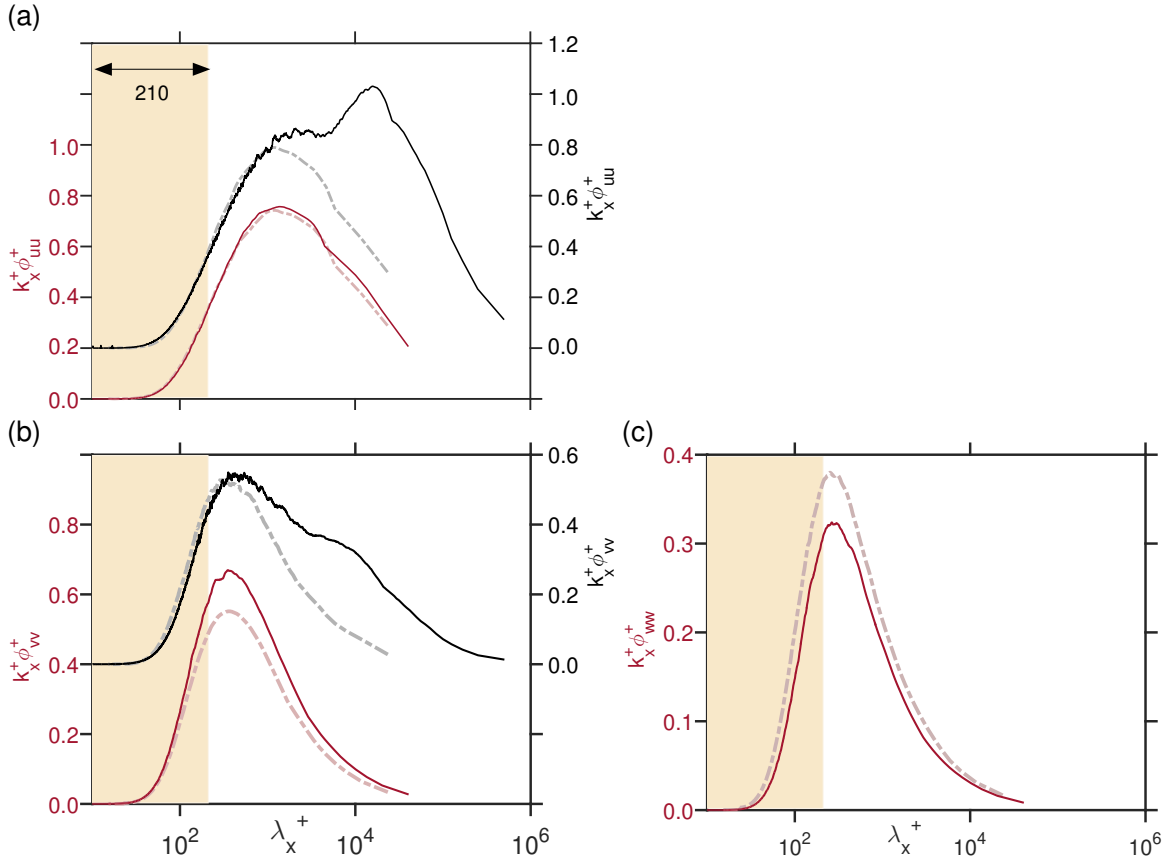

FIGURE 9.7: Viscous-scaled premultiplied energy spectra of the (a) streamwise, (b) spanwise and (c) wall-normal velocity components at $z^+ \approx 100$ for $Re_\tau \approx 10\,000$ ZPG TBL data set (heavy black) and $Re_\tau \approx 1\,000$ channel data set (dark red) acquired using CX probe (table 9.1) and processed using a misaligned 2-D calibration. Dot-dashed lines in light shading represent data from the synthetic experiments corresponding to the probe volume in the physical experiments. The yellow background highlights the wavelength range $0 < \lambda_x^+ < 210$.

9.6.2 Defining the correction scheme

We propose to compute a ratio (r) for every z^+ as follows:

$$r(z^+) = \overline{\left(\frac{(k_x^+ \phi_{ii}^+(\lambda_x^+; z^+))_{sDNS}}{(k_x^+ \phi_{ii}^+(\lambda_x^+; z^+))_{Exp}} \right)} \tag{9.1}$$

for $i = v$ or w and $190 < \lambda_x^+ < 210$, with the overbar indicating averaging over this range. The ratio r is computed individually at each z^+ up to $z^+ = 934$, which is limited by the DNS dataset. We consider the mean value, $r^c = \overline{r(z^+)}$ for $0 < z^+ < 300$ as the unique correction ratio for the entire velocity profile. Figure 9.8 depicts the percentage deviation of $r(z^+)$ from r^c, across all wall-normal spacings, for all the velocity profile measurements

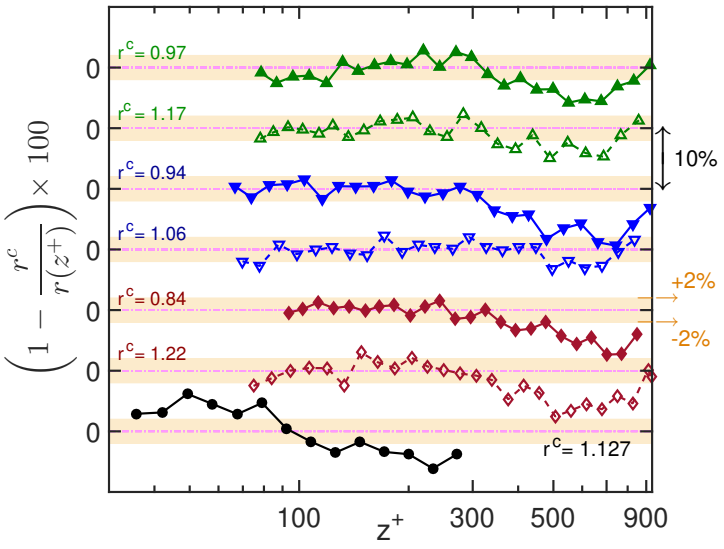

FIGURE 9.8: Percent deviation of r from the correction ratio r^c across the measurement locations (z^+), computed for the physical experiments with a misaligned calibration. Symbols represent physical experiments with various X-probes as mentioned in table 9.1, with (–) and (- -) line types representing a uv and uw X-probe, respectively. For the case of high-Re_τ experimental data (◯), deviations only up to $z^+ \approx 300$ have been shown. Zero labels corresponding to each profile are vertically offset by 10% from one another and the light yellow background highlights deviation in the range ±2% for each profile.

listed in table 9.1. r^c appears to be a reasonably good representative value since r doesn't vary significantly with z^+, at least for low-Re_τ channel measurements.

Next, the correction ratio r^c is used as a *gain* to amplify or attenuate the premultiplied 1-D spectra as follows: $(k_x^+\phi_{ii}^+)^c_{Exp} = r^c(k_x^+\phi_{ii}^+)_{Exp}$ for $i = v$ or w, where $(k_x^+\phi_{ii}^+)^c_{Exp}$ is the corrected spectra. Figure 9.9 shows the corrected version of the premultiplied 1-D spectra shown in figure 9.7. It can be observed that although r^c was estimated purely based on the spectra in the range $190 < \lambda_i^+ < 210$, the corrected spectra shows a reasonable overlap with the corresponding $(k_x^+\phi_{ii}^+)_{sDNS}$ in the entire small-scale range, $\lambda_x^+ < 210$, and for both the low (channel) and high-Re_τ (boundary layer) cases. This is observed for the spectra at all z^+. It suggests that a unique correction ratio (r^c) for the entire velocity profile performs reasonably well. The comparison between $(k_x^+\phi_{ii}^+)^c_{Exp}$ from the channel flow experiment with the corresponding $(k_x^+\phi_{ii}^+)_{sDNS}$ is especially interesting due to the Re_τ for the two cases being similar. After correction, the spectra seem to match reasonably well for the entire range of scales, λ_x^+.

It is to be noted that for estimating r^c, $z^+ \approx 300$ was considered as an upper bound because of a gradual deviation of $r(z^+)$ from r^c for $z^+ > 300$, seen consistently for all cases, especially for the high Re_τ measurements. It should be noted that a mismatch was

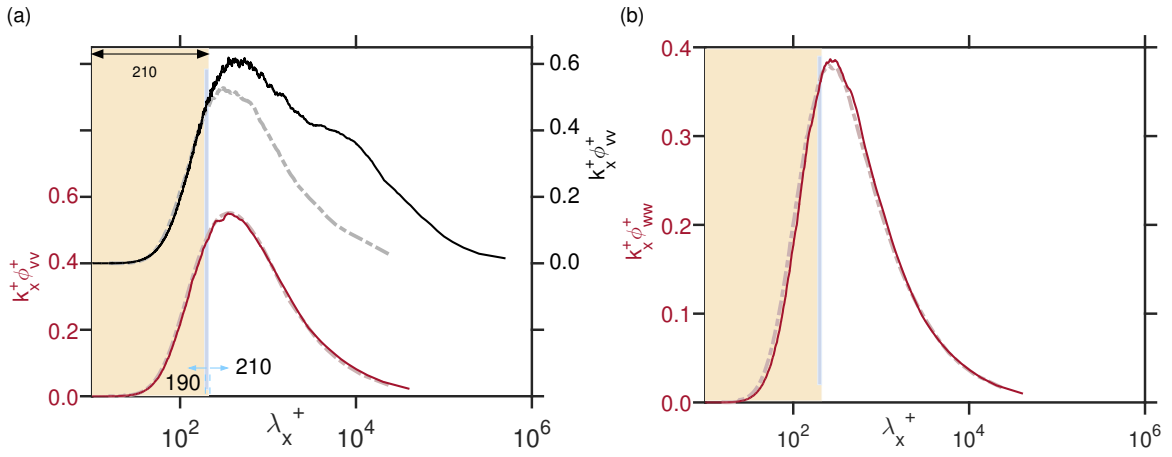

FIGURE 9.9: Corrected viscous-scaled premultiplied energy spectra of the (a) spanwise and (b) wall-normal velocity components at $z^+ \approx 100$ for $Re_\tau \approx 10\,000$ ZPG TBL data set (heavy black) and $Re_\tau \approx 1\,000$ channel data set (dark red) acquired using CX probe (table 9.1) and processed using a misaligned 2-D calibration. Dot-dashed lines in light shading represent spectra from the synthetic experiments corresponding to the probe volume in the physical experiments. The yellow and blue backgrounds highlight the wavelength range $0 < \lambda_x^+ < 210$ and $190 < \lambda_x^+ < 210$, respectively.

observed between the $\overline{u_{i,S}^2}^+$ profiles (figures 9.6(b),(c)), in the similar wall-normal range, likely due to the decreasing small-scale energy content in the outer region of the flow. Further, in equation 9.1, only a subset of the small-scale range $\lambda_i^+ < \lambda_x^+ < 210$, with $\lambda_i^+ = 190$ instead of 0, has been considered for the purpose of computing the ratio, $r(z^+)$. This is because the magnitude of $k_x^+\phi_{ii}^+$ ($i = v$ or w) for the smallest scales drops significantly with increase in z^+ (Baidya et al., 2012, 2017). In addition, inaccuracies due to experimental uncertainty or noise also influence the spectra in the smallest scales, thereby leading to non-physical values of the ratio $r(z^+)$. A sensitivity analysis was carried out (not shown here) to quantify the effect of varying λ_i^+ on the value of $r(z^+)$. It was found that the ratio changes within $\pm 2\%$ for $130 < \lambda_i^+ < 190$. For $\lambda_i^+ < 130$, the change is significant.

With the correction scheme established, we shift our focus to correcting the time series of the lateral velocity fluctuations by using r^c. Essentially, the corrected time series can be obtained by simply performing an inverse Fourier transform on the corrected energy spectra, $(k_x^+\phi_{ii}^+)_{Exp}^c$ for $i = v$ or w. The complete methodology to obtain the corrected v (or w) time series has been presented in appendix B, with equation 9.3 giving the final result. In the next section, we compare the uncorrected and corrected statistics, computed from the respective velocity time series, for all the measurements shown in table 9.1.

9.7 Comparing uncorrected and corrected statistics

Figure 9.10 depicts the uncorrected and corrected statistics from the channel flow measurements using various X-probes. Also plotted in parallel are the statistics from the corresponding synthetic experiments as well as from the well-resolved (unfiltered) fields of the channel DNS data set. It should be noted that only those statistics which are associated with the lateral velocity fluctuations ($\overline{v^2}^+$, $\overline{w^2}^+$ and $\overline{uw}^+$) required a correction since $\overline{u^2}^+$ is estimated reasonably accurately after implementation of the VO method (refer 9.5.2). It is evident that the uncorrected statistics (figure 9.10; left column), which differ from the synthetic experiment estimates by up to 10%, compare reasonably well after correction (figure 9.10; right column) for all X-probes. On correction, the statistics differ by at the most 4% for $-\overline{uw}^+$, and upto 2% for the normal stresses, which is within acceptable experimental uncertainty (Baidya et al., 2019b). Here, the percentage difference has been calculated at $z/h \approx 0.1$ ($z^+ \sim 100$) for the $AX1$ X-probe following:

$$\text{Percent error} = \left|\frac{(\overline{u_i u_i}^+)_{Exp} - (\overline{u_i u_i}^+)_{sDNS}}{(\overline{u_i u_i}^+)_{sDNS}}\right| \times 100, \tag{9.2}$$

where i is used to denote velocity fluctuations along x, y or z.

The correction technique is also applied to the high-Re_τ measurements in the boundary layer and its effectiveness is shown in figure 9.3(b) and 9.4(b) plotted earlier. $\overline{v^2}^+(z^+)$ and $(k_x^+\phi_{vv}^+)(\lambda_x^+, z^+ \approx 100)$, processed using misaligned 2-D calibration, is corrected and compared with the statistics processed using the *accurate* 2-D calibration. A reasonably good match is observed on comparison, reinforcing the effectiveness of the correction technique across a decade of Re_τ variation. It would also be worthwhile to comment on the second part of the premise, forming the basis for the correction scheme, which argues that the viscous-scaled energy in the small-scales is a function of the X-probe spatial resolution. It is for this reason that filtered DNS estimates corresponding to each X-probe measuring volume (table 9.1) need to be considered for successful implementation of the scheme. Interested readers may refer to appendix C where the velocity statistics from (i) the corrected experimental time series and (ii) the synthetic experiment have been shown to be following consistent trends for varying spatial resolution of the X-probes, reaffirming the effectiveness of the scheme.

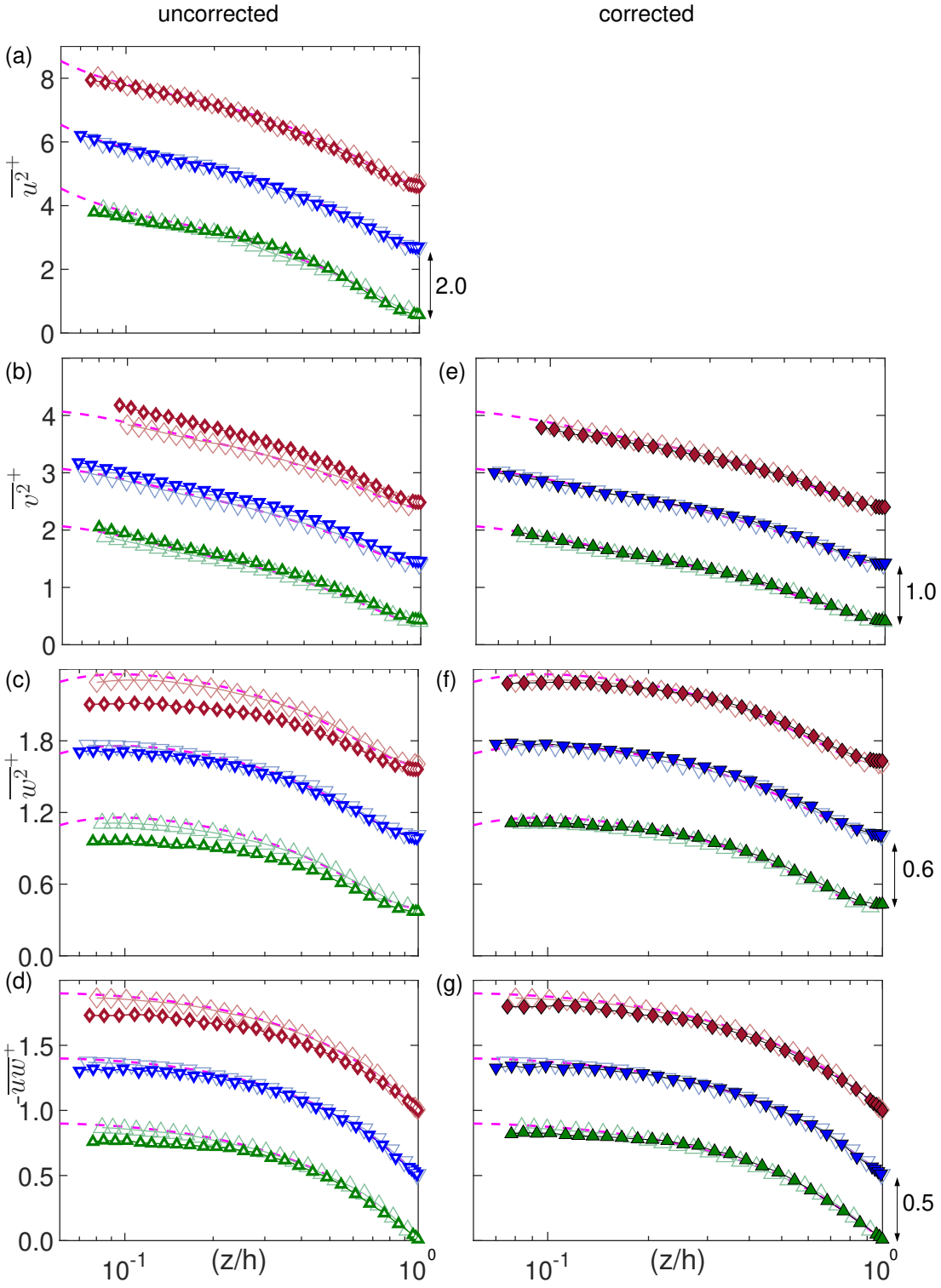

FIGURE 9.10: The uncorrected (dark, partially-filled) and corrected (dark, fully-filled) (a) streamwise, (b,e) spanwise, (c,f) wall-normal and (d,g) Reynolds shear stresses for the $Re_\tau \approx 1\,000$ channel flow experiments. The uncorrected statistics are plotted in (a-d), while the corrected ones are plotted in (e-g). Symbols represent experiments with various X-probes as mentioned in table 9.1. Empty symbols in light shading represent statistics from the corresponding synthetic experiments. (- -) represents the unfiltered statistics from the channel DNS at $Re_\tau = 934$. Note the vertical shift in profiles.

9.8 Summary of the steps for implementing the correction scheme

With the correction scheme established, here we summarize the steps to be followed while implementing the scheme for any turbulent shear flow measurement, in general. References are provided, wherever required, to the relevant section in the manuscript where the specific procedure has been discussed in detail.

1. Choose an appropriate X-probe configuration for the flow being investigated (§9.4.1.2).
2. After the measurements are conducted, check the 2-D calibration for misalignment by comparing the voltage pairs corresponding to the β_o points with the 1-D calibration (figure 9.2d).
3. If an angular offset is observed on comparison, implement the VO method to obtain the 'voltage-offset' calibration map (§9.5.1).
4. Process the data by using the new calibration map. It is this dataset which will be corrected with the help of a DNS database as a reference, based on a scaling behavior characteristic of the flow.
5. Select the appropriate DNS dataset (§9.4.2) for the flow being measured and obtain the filtered estimates corresponding to the X-probe volume.
6. Choose the relevant scaling, depending on the flow type, for comparing the experimental and filtered DNS results (§9.4.2).
7. Check if the u-statistics obtained from the measurements overlap with the filtered DNS estimates in the relevant scale range (§9.5.2).
8. To correct the v/w statistics, use equation 9.1 and the associated methodology given in §9.6.2 to determine the unique correction ratio (r^c) for the measurements.
9. On determination of r^c, correct the entire time series of v/w by following the methodology given in appendix B. Recompute the statistics from the corrected time series and compare with the filtered DNS to verify the correction.

9.9 Summary and conclusions

The present study experimentally investigated the effect of misalignment between the calibration and tunnel coordinate system for an X-probe calibration. The emphasis was on scenarios where the calibration is severely misaligned ($|\phi'| > 2°$) due to the absence of reference planes required to accurately orient the calibration jet with the probe. Since

the previously used methodology of offsetting the calibration jet angles by ϕ' (Baidya et al., 2019b; Zimmerman et al., 2017) fails to provide acceptable velocity statistics, a new methodology based on offsetting the calibration voltages was implemented to account for the misalignment. It was found that the streamwise velocity statistics processed from such a calibration agreed reasonably well with the reference statistics from the *accurate* (well-aligned) calibration. Normal stresses of the lateral velocity components, however, appeared to be either amplified or attenuated relative to the reference profiles. Analysis of the corresponding energy spectra revealed that the energy is amplified/attenuated across the entire range of scales by a *gain*. Subsequently, it was hypothesized that a misaligned calibration does not influence the relative energy distribution in the energy spectra but simply magnifies/dampens it by a factor. A separate analysis (appendix A), conducted with a calibration map obtained from a *drifted* X-probe sensor, confirmed that these observations were not an artifact of the drift in the sensor voltages with time.

The consistent nature of deviation of the erroneous statistics, from the reference statistics, inspired the proposal of a correction scheme to rectify such errors arising in any other canonical wall-bounded flow experiment. The scheme is based on the premise that the viscous-scaled small-scale contributions to the turbulence stresses is invariant with Re_τ and solely dependent on the viscous-scaled spatial resolution of the probe. The spectral energy distribution obtained from the misaligned calibration is compared against the expected spectral energy distribution in the small-scale range, obtained via synthetic experiments on well-resolved DNS fields. Any differences, on comparison, were assumed to be due to calibration misalignment. Subsequently, a forced overlap of the erroneous and expected spectra was carried out in the small-scale range at each wall normal location of the velocity profile (up to $z^+ = 934$). It yielded the ratio r which varied insignificantly in the inner-region, $z^+ < 300$. The mean, $r^c = \overline{r(z^+)}$ in this range was hence considered to be a good representative value as a unique correction ratio for the entire velocity profile. r^c was hence used to rectify the time series of the lateral velocity fluctuations, acquired across the shear flow, via Fourier analysis. Velocity statistics obtained from the corrected time series agree reasonably well with the reference statistics, for experiments conducted across a decade of Re_τ and using X-probes of varying spatial resolution. The effectiveness of the correction scheme also gives credence to the hypothesis proposed on the effect of a misaligned calibration on the processed velocity statistics, via the VO method. For the convenience of researchers interested in using this correction scheme, a database (appendix D) of the premultiplied energy spectra, obtained via synthetic experiments on the channel flow for various X-probe measuring volumes, has been made openly accessible on the group website.

Acknowledgement

The authors would like to thank Dr. Rio Baidya for helpful discussions and sharing his code for the synthetic experiments on the DNS data set. They also thank the authors of del Álamo et al. (2004) for making their DNS data available. Financial support of this research from the Australian Research Council is gratefully acknowledged.

9.10 Appendix A: accounting for the drift in hotwire voltage

It is a very well known fact that hotwire sensors drift owing to various reasons (Talluru et al., 2014) and this phenomena can lead to erroneous velocity statistics unless accounted for. In this regard, we have implemented the practice of doing periodical 'free-stream' checks (Talluru et al., 2014) for the X-probe to obtain an updated 1-D calibration curve (for both sensors) at each wall-normal location of the profile (refer 9.4.1.3). These 1-D calibration curves are used as references to generate unique u and v (or w) calibration surfaces at corresponding z^+. To this end, we process the 2-D calibrations via the voltage offset (VO) method demonstrated previously (§ 9.5.1) and show that the sensor drift is implicitly accounted on using this method. Through this, we intend to strengthen our argument that the attenuated lateral velocity statistics (shown in figures 9.3(b) and 9.4(b)), obtained on processing the data via the misaligned calibration, are an artifact of the misalignment and not the hotwire sensor drift.

To demonstrate this, an additional *drifted* 2-D calibration, apart from the 'accurate' and misaligned 2-D calibrations, was performed on the same uv-CX probe used in the $Re_\tau \approx 10\,000$ experiments in the ZPG TBL (table 9.1). It was performed approximately 12 hours after the end of measurement to ensure that the sensor drifts sufficiently. During this calibration, the jet coordinate system was aligned with the measurement coordinate system in the same manner as done for the *accurate* 2-D calibration, to rule out any misalignment. Figure 9.11(a) shows the raw voltage pairs acquired during the *accurate* and the *drifted* 2-D calibration on the uv X-probe. Also plotted are the mean voltages acquired during the 1-D calibration done immediately before the measurements. Similar to figure 9.2(b), figure 9.11(b) shows the raw calibration voltages fitted to smooth functions of jet velocity and angles based on the EAM and solved for a linearly distributed set of U_{jet} and β for a meaningful comparison. The difference between the $drifted$ and the *accurate*

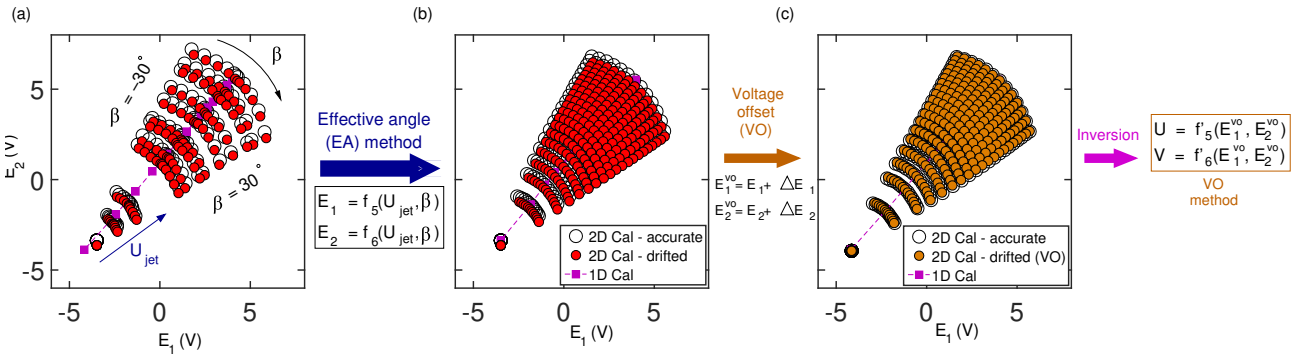

FIGURE 9.11: Procedure to account for drift while processing 2-D calibration of an X-probe, explained by using an *accurate* 2-D calibration as a reference: (a) Voltage pairs obtained by varying the U_{jet} and β for an *accurate* and *drifted* 2-D calibration along with voltages obtained from the 1-D calibration in $HRNBLWT$ just before the measurement. (b) Voltages in (a) interpolated onto a linearly distributed set of U_{jet} and β based on EAM. (c) Comparison between voltage pairs from the *accurate* and $drifted$ calibration, with the latter shifted after application of the voltage offset estimated by following the procedure shown in figure 9.2(d).

2-D calibration is pretty clear. The voltage drift is apparent from the difference between the voltage pairs from the two calibrations at $U_{jet} \approx 0$. It is different from the case of a misaligned 2-D calibration (figure 9.2(b)), where a difference was noted only for voltages acquired at $U_{jet} > 0$.

Following the VO method, the voltages corresponding to β_o for the $drifted$ 2-D calibration are forced to be equivalent to the 1-D calibration voltages, through which a set of unique voltage offsets ($\Delta E_1(U_{jet})$, $\Delta E_2(U_{jet})$) is estimated for both the sensors. This offset is applied across the entire calibration map, resulting in a 'voltage offset' 2-D calibration map shown in figure 9.11(c). On performing the voltage shift, the difference between the *accurate* and $drifted$ 2-D calibration appears to be negligible, suggesting that the effect of drift has been accounted by processing through the VO method. To confirm this, we process the boundary layer dataset acquired with the same probe via the two calibration surfaces. A good agreement is observed between the mean statistics (figure 9.12) processed via the two calibrations.

9.11 Appendix B: methodology to correct the time series of v or w

Let us consider the time series of the uncorrected lateral velocity fluctuations as $Q(p)$, where Q represents v or w and $p = 1, 2 \ldots N$ represents the discrete samples of the

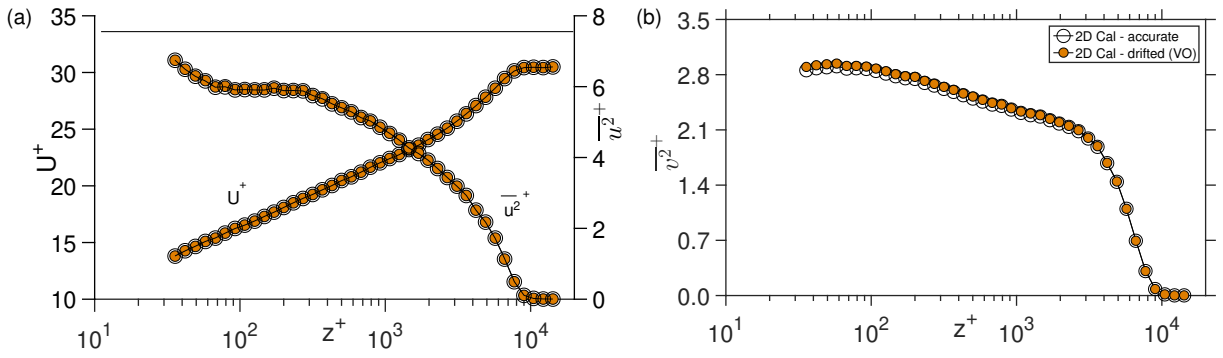

FIGURE 9.12: Viscous-scaled profiles of (a) mean streamwise velocity and streamwise turbulence intensity and (b) spanwise turbulence intensity obtained on processing the high-Re_τ boundary layer data set using the *accurate* and *drifted* 2-D calibrations. Data processing, in case of the *drifted* calibration, is carried out using the VO method.

fluctuations with N equaling the total number of samples (sampling frequency times the total time period of acquisition). Similarly, let the corrected time series be denoted as $Q^c(m)$. If $\widetilde{Q}(n)$ and $\widetilde{Q}^c(n)$ denote the complex Fourier coefficients obtained on computing the Fourier transform ($\mathcal{F}$) of $Q(p)$ and $Q^c(p)$ respectively, then $\widetilde{Q^c}(n) = \sqrt{r^c}\widetilde{Q}(n)$ according to the correction scheme proposed in § 9.6.2, with n being the mode number. Here, $\sqrt{r^c}$ being real-valued will only influence the magnitude of the Fourier coefficient. The time series of the corrected velocity fluctuations can thus be found by simply computing the inverse discrete Fourier transform for $\widetilde{Q^c}(n)$:

$$\begin{aligned} Q^c(p) &= \mathcal{F}^{-1}[\widetilde{Q^c}(n)] = \frac{1}{N}\sum_{n=0}^{N-1}\widetilde{Q}^c(n)exp(\frac{i2\pi pn}{N}), or \\ Q^c(p) &= \frac{1}{N}\sum_{n=0}^{N-1}\sqrt{r^c}\widetilde{Q}_n exp(\frac{i2\pi pn}{N}) \end{aligned} \tag{9.3}$$

9.12 Appendix C: investigating the effect of X-probe spatial resolution

The three types of X-probes chosen to conduct experiments in the channel flow have systematically varying l^+ and Δs^+ (refer table 9.1). Here, we compare the trends observed in the corrected experimental dataset, due to variation of these parameters, with those from the corresponding synthetic experiments. For brevity, we restrict ourselves solely to studying these for the uw X-probe.

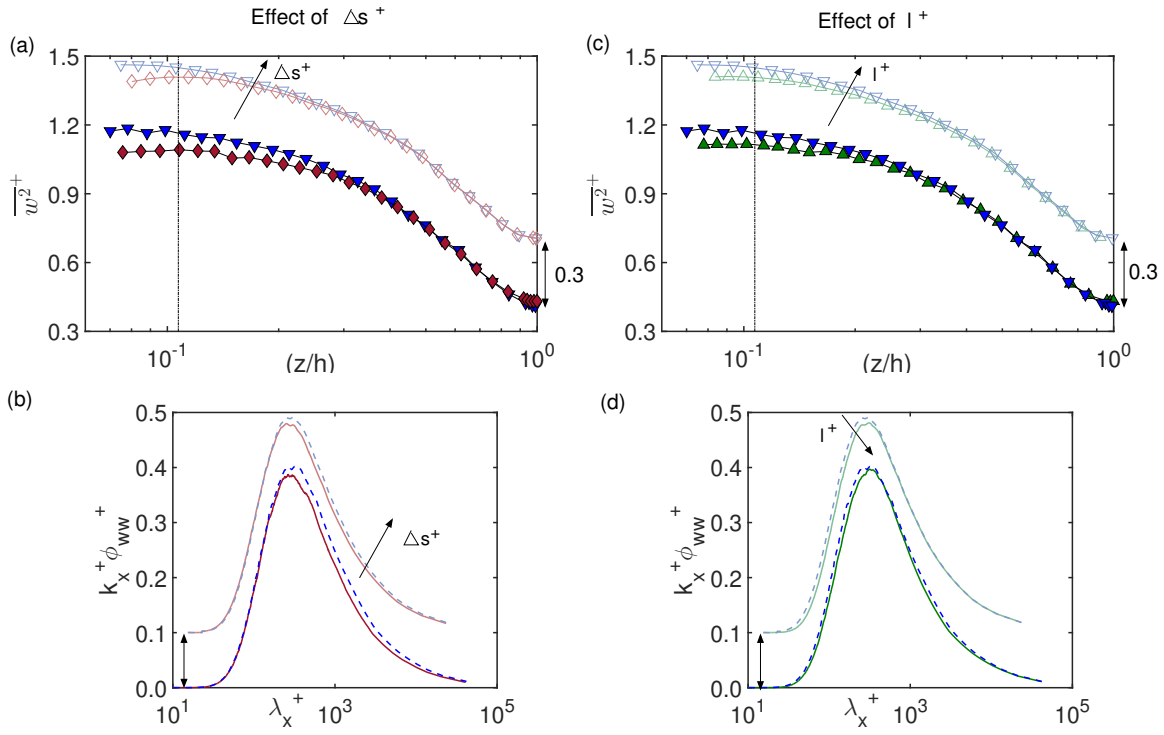

FIGURE 9.13: (a,c) Corrected viscous-scaled wall-normal turbulence intensity profiles and (b,d) premultiplied energy spectra of the wall-normal velocity at $z^+ \approx 100$ (marked by black line in a,c) obtained from various X-probes for a channel flow. These profiles are selectively plotted in a way to demonstrate the effect of varying Δs^+ (a,b) and l^+ (c,d). Colour coding corresponding to the X-probes is given in table 9.1. Dark and light shading represents data from the $Re_\tau \approx 1\,000$ channel flow experiments and the corresponding synthetic experiments, respectively. Note the vertical shift in profiles for the synthetic experiments.

Figure 9.13 shows the corrected $\overline{w^2}^+$ and $k_x^+\phi_{ww}^+$ at $z^+ \approx 100$ from the three different uw X-probes. The Δs^+ and l^+ trends observed in the $\overline{w^2}^+$ profiles from the corrected experimental data are consistent with those from the synthetic experiments. It is interesting to see the qualitative agreement between the pair of spectra, from the two sources, in figures 9.13(b,d). For the large scales ($\lambda_x^+ > 300$), the difference in the energy distribution for varying Δs^+ is very similar in both the datasets. Similarly, for the case of varying l^+, the spectra from the corrected experimental dataset nearly overlap in the large-scale range as seen for the synthetic experiment dataset. The consistency of the corrected dataset with the synthetic experiments demonstrates the effectiveness of the correction scheme, which is facilitated by the availability of DNS flow fields to simulate the 'expected' spectra in the small-scale range.

9.13 Appendix D: database of energy spectra obtained from synthetic experiments

A database of the viscous-scaled premultiplied energy spectra, obtained via synthetic experiments for varying measuring volumes of the X-probes, can be accessed at http://fluids.eng.unimelb.edu.au/. The users can follow the steps summarized in §9.8 to correct their X-probe dataset for canonical wall-bounded flows in case of calibration misalignments.

Chapter 10

Conclusions

10.1 Summary and conclusions

The thesis presents a new and unique set of multi-point measurements in a zero-pressure gradient (ZPG) turbulent boundary layer (TBL) to facilitate examination of the three-dimensional (3-D) structure of the energetic motions which predominate in its inertial region. The uniqueness of these measurements lies in the way this multi-point dataset was acquired and subsequently analyzed, which involved u-velocity fluctuations synchronously measured over a wide range of spanwise ($0 \lesssim \Delta y \lesssim 2.5\delta$) and wall-normal ($100 \lesssim \Delta z^+ \lesssim 0.15Re_\tau$) offsets, and subsequently used to reconstruct the 3-D statistical picture of the inertial region of a high-Re_τ ($\approx$ 15 000) TBL. These measurements were complemented by the publicly available low-Re_τ ($\approx$ 2 000) ZPG TBL DNS dataset of Sillero et al. (2014), which cumulatively facilitated the investigation of the characteristics of the energetic motions over a decade of Re_τ. Preceding chapters (4-9) include detailed discussions on the conclusions from each sub-study conducted as part of this thesis. This chapter is used to reiterate these key findings in the context of the original aims of this thesis, in a consolidated manner. The aims of this thesis reproduced from chapter 1 are as follows:

Aim 1: Test the notion of geometric self-similarity, along both the streamwise and spanwise directions, for energetic wall-coherent motions of u coexisting in the log-region.

Aim 2: Investigate the spanwise geometry and organization of wall-coherent u-motions in the log-region.

Aim 3: Estimate the streamwise inclination angle of the large wall-coherent motions of u, by physically isolating them from the influence of the relatively smaller motions coexisting in the log-region.

Aim 4: Develop a methodology to segregate the energy contributions associated with the active and inactive components (Townsend, 1976) of all three velocity components in wall-bounded turbulent flows.

Aim 5: Develop an experimental procedure to accurately estimate the velocity statistics processed from an X-wire probe, and validate them via synthetic experiments conducted on a DNS dataset which take into account the spatial resolution of the probe.

In a broader sense, *Aims 1 – 3* facilitate the attached eddy-based modelling of the wall-coherent structures, which in the case of a high-Re_τ TBL, are responsible for the high skin-friction experienced at the wall (Deck et al., 2014; de Giovanetti et al., 2016; Abbassi et al., 2017). While, *Aims 4* and *5* are directed towards providing empirical support to Townsend's hypothesis on the two-component (active and inactive) structure of the inertial region of a canonical wall-bounded flow (Townsend, 1961, 1976), with both the active and inactive motions essentially conforming to Townsend's attached eddies.

10.1.1 Attached eddy modelling of the wall-coherent motions

The notion of whether the wall-coherent motions can be modelled based on Townsend's attached eddy hypothesis is tested in chapter 4. For this, the 2-D u-cross-spectrum ($\Phi_{uu}^{cross}(z_o)$), representing the energy distribution across a range of wall-coherent eddies coexisting at z_o, is investigated across the entire log-region. The energetic scales contributing to Φ_{uu}^{cross} are observed to follow a $\lambda_y/z_o \sim \lambda_x/z_o$ power law, giving strong evidence of geometric self-similarity ingrained in the wall-coherent subset of the TBL. This is further substantiated by Φ_{uu}^{cross} closely resembling the qualitative 2-D spectrum obtained from an attached eddy-based model (Φ_{uu}^{AEH}), in terms of scale-specific energy distribution as well as obeyance of the self-similar scaling laws. It is shown, however, that the wall-coherent

motions also comprise of large δ-scaled eddies (also known as superstructures), apart from the range of scales exhibiting self-similarity, which also need to be taken into account while modelling the flow.

Chapter 5 discusses the spanwise organization of the wall-coherent u-motions in the log-region of the ZPG TBL. It is found that the wall-coherent motions with spanwise width up to 0.35δ, conform to the geometrically self-similar motions associated with Townsend's attached eddies. This spanwise width is also equivalent to that noted for the large δ-scaled motions (or superstructures) in the literature (Dennis and Nickels, 2011; Gao et al., 2011). These findings, thus, have direct ramifications towards attached-eddy based modelling of the wall-coherent portion of the high-Re_τ ZPG TBL flow. The superstructures are also found to be organized in a spanwise periodic manner in a statistical sense, an observation which can facilitate active flow-control strategies aimed towards manipulating these highly energized motions to achieve drag reduction.

Chapter 6 discusses the analysis used to reveal the streamwise inclination of large wall-coherent structures in the log-region of the TBL. This estimation comes after isolating the large motions from the remaining (smaller) assemblage of eddies by considering the synchronous u-velocity signals over a large spanwise offset – a methodology which was shown to be effective for various TBL datasets across $Re_\tau \sim \mathcal{O}(10^3)$ – $\mathcal{O}(10^6)$. The inclination angle is found to be nominally 45°, which closely resembles the inclination of individual hairpin-type structures noted previously via flow visualization and DNS studies at low Re_τ, suggesting large-scale wall-coherent motions to be of similar type. Although this empirical result is limited to the large motions, theoretical arguments discussed in chapter 6 suggest the same inclination angle to exist for the relatively smaller wall-coherent motions. These findings hence, provide a data-driven choice for the eddy inclination angle when simulating the wall-coherent motions via the attached eddy-based simulations.

In its present state, the attached eddy model of the TBL (Marusic, 2001; Baidya et al., 2014; Woodcock and Marusic, 2015; Marusic and Monty, 2019; Eich et al., 2020; Chandran et al., 2020) considers a packet of Λ-eddies (shown in figures 2.11 and 4.3) as the statistically representative coherent structure for the wall-bounded flow. In this packet, an individual Λ-eddy represents the hairpin vortex type structure, deemed to be the dominant feature of any wall-bounded turbulent flow (Moin and Kim, 1985; Adrian et al., 2000; Wu and Moin, 2009), and is oriented at an angle relative to the streamwise direction owing to the mean shear. The findings from chapters 4 – 6 discussed above can cumulatively facilitate data-driven choices for the size and orientation of the representative structures in the attached eddy model.

10.1.2 Attached eddy modelling of the inertial region

Chapters 7 and 8 together present arguments in support of Townsend's hypothesis on the statistical nature of the Reynolds stress carrying motions in canonical wall-bounded turbulent flows. As per Townsend (1961, 1976), the wall-bounded flow at any point in the inertial region comprises of two components – (i) active motions, which are responsible for transferring the momentum, and (ii) inactive motions, with both motions conforming to Townsend's self-similar attached eddies. In chapter 7, a methodology is proposed to decompose the inertial region of canonical wall-bounded turbulence into the two-components. This is made possible via the velocity-velocity coupling (Φ_{ii}^{cross}, with $i = u$, v or w) reconstructed in chapter 4, which is used as an input for a spectral linear stochastic estimation (SLSE) based procedure that linearly decomposes the total energy at z_o (represented by the full 2-D spectrum, $\Phi_{ii}(z_o)$) into the two corresponding components. The methodology is tested on the u-velocity component in chapter 7, and on the lateral velocity components in chapter 8.

The decomposition of Φ_{ii} into Φ_{ii}^{a} (active) and Φ_{ii}^{ia} (inactive) reveals the geometric self-similarity of the inactive and active motions, suggesting they can be conceptually modelled using the attached eddy model framework. Furthermore, Φ_{ii}^{a} contours are noted to obey wall-scaling across a large Re_τ range, and are consistent with the characteristics depicted by Φ_{uw}, thereby confirming the association of Φ_{ii}^{a} with the active motions. The ability to decompose the instantaneous active and inactive contributions also permits computation of Φ_{uw}^{a}, which considers the cross-correlation exclusively between u_{active} and w. Φ_{uw}^{a} contours are found to agree well with the Φ_{uw} contours, thus endorsing Townsend's hypothesis on the active motions as the sole Reynolds shear stress carrying motions in wall-bounded flows.

While $\Phi_{ii}^{a}(z_o)$ is found to be associated predominantly with the self-similar attached eddies of height $\mathcal{H} \sim \mathcal{O}(z_o)$, $\Phi_{uu}^{ia}(z_o)$ is found to have contributions from both, the relatively tall self-similar attached eddies ($\mathcal{O}(z_o) \ll \mathcal{H} \lesssim \mathcal{O}(\delta)$) as well as the large δ-scaled eddies associated with superstructures. The latter is confirmed by the reduced self-similar contributions to Φ_{uu}^{ia} with increasing z_o, due to the large attached eddies qualifying as active in accordance to the original concept given by Townsend (1961, 1976). The present study also segregates the inactive contributions from the attached eddies ($\Phi_{uu}^{ia,AE}$), from those coming from the δ-scaled superstructures ($\Phi_{uu}^{ia,SS}$), by utilizing the same SLSE-based methodology used for the first decomposition. The estimation of $\Phi_{uu}^{ia,AE}$ reveals the constant energy plateau, representative of k^{-1}-scaling, in the corresponding premultiplied streamwise and

spanwise 1-D u-spectra. Both these spectra were found to plateau at $A_1 \approx 0.98$ (nominally), yielding the first empirical evidence to establish the consistency with A_1 obtained from the streamwise turbulence intensity profiles (Baars and Marusic, 2020b), as argued by Perry and Chong (1982) for the case of pure attached eddy contributions.

In the present work, support towards the validity of Townsend's hypothesis, for the lateral velocity components, has only been possible via low-Re_τ datasets. This motivates the undertaking of multi-component multi-point high Reynolds number experiments in future, to firmly establish the validity of this hypothesis for all three velocity components. One way of conducting these measurements is by replacing the single wires with miniature X-probes (figure 3.8) in the same experimental setup (figure 3.2), such that the velocity-velocity coupling can be constructed for one of the lateral velocity components (at a time), in addition to that for the streamwise velocity component. The former, however, are known to be very sensitive to any inaccuracy in the probe calibration procedure (Baidya et al., 2019b), for example the misalignment between the calibration coordinate system and that of the TBL in the wind tunnel. As a first step towards accurately conducting the multi-point measurements using X-probes, chapter 9 proposes a scheme to correct the erroneous velocity fluctuations processed from a misaligned 2-D calibration of an X-probe. The scheme is demonstrated to be effective for experiments conducted across a decade of Re_τ and for probes of varying spatial resolution, and may come in handy to improve the estimation of the lateral velocity fluctuations in future measurements.

10.2 Possible directions for future work

The observations noted in this thesis encourage future course of work in the following directions:

(i) **Multi-component multi-point measurements at high-Re_τ:** As discussed in the previous section, Townsend's hypothesis on the active and inactive motions has been tested for the v- and w-velocity components extracted from low-Re_τ datasets only. The methodology can be firmly established by testing it on a high-Re_τ dataset, which can be acquired via repeating the same experimental methodology using X-probes. 2-D spectra (Φ_{ii}) computed from this high-Re_τ dataset, for all three velocity components, can also be compared

with that estimated from the recently published extended attached eddy model of Chandran et al. (2020).

(*ii*) **Attached eddy-based framework to facilitate active flow control:** Chapters 4 and 5 in the present thesis report observations in strong support of the attached eddy-based modelling of the energetic wall-coherent u-motions. In chapter 4, the attached eddy model was used to replicate only the ensemble-averaged statistics, such as the 2-D spectra, for comparison with the same estimated from the experiments. It would also be interesting to compare the instantaneous flow statistics, generated from a semi-empirical attached eddy model based on the findings of chapters 4 – 6, with those measured in a real ZPG TBL. Development of such a capability can also be extremely useful to optimize the active flow control schemes, as described ahead.

The wall-coherent motions coexisting in the log-region are responsible for the high skin-friction drag experienced at the wall in a high Re_τ TBL. Recent studies (Abbassi et al., 2017) have demonstrated the capability to manipulate these energetic motions via active flow control schemes, employing multiple jets aligned along the spanwise direction to inject momentum into the TBL. At present, the control scheme is designed based on only the information of the streamwise and spanwise extent of the incoming coherent motions, estimated at a relatively upstream location, to decide the jet parameters for momentum injection at a downstream location. The present work reveals the geometric self-similarity of the wall-coherent motions in all three directions, encouraging implementation of an attached-eddy inspired control scheme to optimize the injection parameters. Such a scheme would consider the 3-D extent of the approaching coherent motions detected upstream, to decide the number of activated jets along the span (based on the spanwise width of the approaching structure) and the momentum flux from each activated jet (based on the height of the approaching structure) to manipulate the energetic motions efficiently.

(*ii*) **Multi-point measurements in non-canonical TBL:** Turbulent boundary layers, in majority of the cases observed in nature, are in a non-canonical state. This occurs due to the influence of either a hydraulically rough wall, pressure gradients or thermal stratification, each of which may exist independently or coexist at the same time. It would be interesting to conduct multi-point measurements, similar to those reported in this thesis, in such non-canonical flows to investigate how the 3-D characteristics of the coherent motions are influenced by these additional disturbances. Investigations in a 'fully-rough' turbulent boundary layer, in particular, seem very promising given the validity of Townsend's hypothesis over a wide range of Re_τ as noted recently by Squire et al. (2016).

Bibliography

M. R. Abbassi, W. J. Baars, N. Hutchins, and I. Marusic. Skin-friction drag reduction in a high-Reynolds-number turbulent boundary layer via real-time control of large-scale structures. *International Journal of Heat and Fluid Flow*, 67:30–41, 2017.

R. J. Adrian. Conditional eddies in isotropic turbulence. *The Physics of Fluids*, 22(11): 2065–2070, 1979.

R. J. Adrian. Hairpin vortex organization in wall turbulence. *Physics of Fluids*, 19(4): 041301, 2007.

R. J. Adrian, P. Moin, and R. D. Moser. Stochastic estimation of conditional eddies in turbulent channel flow. In *Proc. of the Summer Program 1987, Center for Turbulence Research*, pages 7–19. Stanford University, CTR-S87, 1987.

R. J. Adrian, C. D. Meinhart, and C. D. Tomkins. Vortex organization in the outer region of the turbulent boundary layer. *Journal of Fluid Mechanics*, 422:1–54, 2000.

L. Agostini and M. Leschziner. Spectral analysis of near-wall turbulence in channel flow at $Re_\tau = 4200$ with emphasis on the attached-eddy hypothesis. *Physical Review Fluids*, 2(1):014603, 2017.

A. E. Alving, A. J. Smits, and J. H. Watmuff. Turbulent boundary layer relaxation from convex curvature. *Journal of Fluid Mechanics*, 211:529–556, 1990.

W. J. Baars and I. Marusic. Data-driven decomposition of the streamwise turbulence kinetic energy in boundary layers. Part 1. Energy spectra. *Journal of Fluid Mechanics*, 882:A25, 2020a.

W. J. Baars and I. Marusic. Data-driven decomposition of the streamwise turbulence kinetic energy in boundary layers. Part 2. Integrated energy and A_1. *Journal of Fluid Mechanics*, 882:A26, 2020b.

W. J. Baars, N. Hutchins, and I. Marusic. Spectral stochastic estimation of high-Reynolds-number wall-bounded turbulence for a refined inner-outer interaction model. *Physical Review Fluids*, 1(5):054406, 2016a.

W. J. Baars, D. T. Squire, K. M. Talluru, M. R. Abbassi, N. Hutchins, and I. Marusic. Wall-drag measurements of smooth-and rough-wall turbulent boundary layers using a floating element. *Experiments in Fluids*, 57(90):1–16, 2016b.

W. J. Baars, N. Hutchins, and I. Marusic. Self-similarity of wall-attached turbulence in boundary layers. *Journal of Fluid Mechanics*, 823:R2, 2017.

R. Baidya. *Multi-component velocity measurements in turbulent boundary layers*. PhD thesis, University of Melbourne, Department of Mechanical and Manufacturing Engineering, 2016.

R. Baidya, J. Philip, N. Hutchins, J. P. Monty, and I. Marusic. Measurements of streamwise and spanwise fluctuating velocity components in a high Reynolds number turbulent boundary layer. *in Proceedings of 18th Australasian Fluid Mechanics Conference*, 2012.

R. Baidya, J. Philip, J. P. Monty, N. Hutchins, and I. Marusic. Comparisons of turbulence stresses from experiments against the attached eddy hypothesis in boundary layers. In *Proceedings of 19th Australasan Fluid Mechanics Conference*, 2014.

R. Baidya, J. Philip, N. Hutchins, J. P. Monty, and I. Marusic. Distance-from-the-wall scaling of turbulent motions in wall-bounded flows. *Physics of Fluids*, 29(2):020712, 2017.

R. Baidya, W. J. Baars, S. Zimmerman, M. Samie, R. J. Hearst, E. Dogan, L. Mascotelli, X. Zheng, G. Bellani, A. Talamelli, B. Ganapathisubramani, N. Hutchins, I. Marusic, J. Klewicki, and J. Monty. Simultaneous skin friction and velocity measurements in high Reynolds number pipe and boundary layer flows. *Journal of Fluid Mechanics*, 871: 377–400, 2019a.

R. Baidya, J. Philip, N. Hutchins, J. P. Monty, and I. Marusic. Sensitivity of turbulent stresses in boundary layers to cross-wire probe uncertainties in the geometry and calibration procedure. *Measurement Science and Technology*, 30(8):085301, 2019b.

R. Baidya, J. Philip, N. Hutchins, J. P. Monty, and I. Marusic. Spatial averaging effects on the streamwise and wall-normal velocity measurements in a wall-bounded turbulence using a cross-wire probe. *Measurement Science and Technology*, 30(8):085303, 2019c.

S. C. C. Bailey, M. Hultmark, A. J. Smits, and M. P. Schultz. Azimuthal structure of turbulence in high Reynolds number pipe flow. *Journal of Fluid Mechanics*, 615:121–138, 2008.

B. J. Balakumar and R. J. Adrian. Large-and very-large-scale motions in channel and boundary-layer flows. *Philosophical Transactions of the Royal Society A: Mathematical, Physical and Engineering Sciences*, 365(1852):665–681, 2007.

J. R. Baltzer, R. J. Adrian, and X. Wu. Structural organization of large and very large scales in turbulent pipe flow simulation. *Journal of Fluid Mechanics*, 720:236–279, 2013.

J. S. Bendat and A. G. Piersol. *Random Data Analysis and Measurement Procedures*. John Wiley & Sons, 1986.

P. Bradshaw. 'Inactive' motion and pressure fluctuations in turbulent boundary layers. *Journal of Fluid Mechanics*, 30(2):241–258, 1967.

P. Bradshaw. *An introduction to turbulence and its measurement: thermodynamics and fluid mechanics series*. Elsevier, 2013.

G. L. Brown and A. Roshko. On density effects and large structure in turbulent mixing layers. *Journal of Fluid Mechanics*, 64(4):775–816, 1974.

G. L. Brown and A. S. W. Thomas. Large structure in a turbulent boundary layer. *The Physics of fluids*, 20(10):S243–S252, 1977.

L. W. B. Browne, R. A. Antonia, and D. A. Shah. Selection of wires and wire spacing for x-wires. *Experiments in fluids*, 6(4):286–288, 1988.

H. H. Bruun. *Hot-wire anemometry: principles and signal analysis*. IOP Publishing, 1996.

P. Burattini. The effect of the x-wire probe resolution in measurements of isotropic turbulence. *Measurement Science and Technology*, 19(11):115405, 2008.

P. Burattini and R. A. Antonia. The effect of different x-wire calibration schemes on some turbulence statistics. *Experiments in Fluids*, 38(1):80–89, 2005.

P. Burattini, M. Kinet, D. Carati, and B. Knaepen. Corrections for underresolved scalar measurements in turbulent flows using a dns database. *Experiments in Fluids*, 43(1): 31–37, 2007.

M. A. Carper and F. Porte-Agel. The role of coherent structures in subfilter-scale dissipation of turbulence measured in the atmospheric surface layer. *Journal of Turbulence*, 5: 32, 2004.

D. Chandran. *Characteristics of energetic motions in turbulent boundary layers.* PhD thesis, University of Melbourne, Department of Mechanical Engineering, 2019.

D. Chandran, R. Baidya, J. P. Monty, and I. Marusic. Measurement of two-dimensional energy spectra in a turbulent boundary layer. In *Proceedings of 20th Australasan Fluid Mechanics Conference*, 2016.

D. Chandran, R. Baidya, J. P. Monty, and I. Marusic. Two-dimensional energy spectra in high-Reynolds-number turbulent boundary layers. *Journal of Fluid Mechanics*, 826:R1, 2017.

D. Chandran, J. P. Monty, and I. Marusic. Spectral-scaling-based extension to the attached eddy model of wall turbulence. *Physical Review Fluids*, 5(10):104606, 2020.

K. A. Chauhan, P. A. Monkewitz, and H. M. Nagib. Criteria for assessing experiments in zero pressure gradient boundary layers. *Fluid Dynamics Research*, 41(2):021404, 2009.

S. I. Chernyshenko, I. Marusic, and R. Mathis. Quasi-steady description of modulation effects in wall turbulence. arXiv:1203.3714 [physics.flu-dyn], 2012.

C. C. Chin, N. Hutchins, A. S. H. Ooi, and I. Marusic. Use of direct numerical simulation (DNS) data to investigate spatial resolution issues in measurements of wall-bounded turbulence. *Measurement Science and Technology*, 20(11):115401, 2009.

D. Chung, I. Marusic, J. P. Monty, M. Vallikivi, and A. J. Smits. On the universality of inertial energy in the log layer of turbulent boundary layer and pipe flows. *Experiments in Fluids*, 56(7):141, 2015.

D. Coles. The turbulent boundary layer in a compressible fluid. *Technical Report R-403-PR*, 1962.

P. A. Davidson and P. Å. Krogstad. A simple model for the streamwise fluctuations in the log-law region of a boundary layer. *Physics of Fluids*, 21(5):055105, 2009.

P. A. Davidson, T. B. Nickels, and P.-Å. Krogstad. The logarithmic structure function law in wall-layer turbulence. *Journal of Fluid Mechanics*, 550:51–60, 2006.

M. de Giovanetti, Y. Hwang, and H. Choi. Skin-friction generation by attached eddies in turbulent channel flow. *Journal of Fluid Mechanics*, 808:511–538, 2016.

C. de Silva, K. Kevin, R. Baidya, N. Hutchins, and I. Marusic. Large coherence of spanwise velocity in turbulent boundary layers. *Journal of Fluid Mechanics*, 847:161–185, 2018.

C. de Silva, D. Chandran, R. Baidya, N. Hutchins, and I. Marusic. Periodicity of large-scale coherence in turbulent boundary layers. *International Journal of Heat and Fluid Flow*, 83:108575, 2020.

C. M. de Silva, D. T. Squire, N. Hutchins, and I. Marusic. Towards capturing large scale coherent structures in boundary layers using particle image velocimetry. In *Proceedings of the 7th Australian Conference on Laser Diagnostics in Fluid Mechanics and Combustion, Melbourne, Australia*, 2015.

C. M. de Silva, J. D. Woodcock, N. Hutchins, and I. Marusic. Influence of spatial exclusion on the statistical behavior of attached eddies. *Physical Review Fluids*, 1(2):022401, 2016.

R. B. Dean. Reynolds number dependence of skin friction and other bulk flow variables in two-dimensional rectangular duct flow. *Journal of Fluids Engineering*, 100(2):215–223, 1978.

S. Deck, N. Renard, R. Laraufie, and P. Weiss. Large-scale contribution to mean wall shear stress in high-Reynolds-number flat-plate boundary layers up to $Re_\theta = 13650$. *Journal of Fluid Mechanics*, 743:202–248, 2014.

J. C. del Álamo and J. Jiménez. Estimation of turbulent convection velocities and corrections to Taylor's approximation. *Journal of Fluid Mechanics*, 640:5–26, 2009.

J. C. del Álamo, J. Jiménez, P. Zandonade, and R. D. Moser. Scaling of the energy spectra of turbulent channels. *Journal of Fluid Mechanics*, 500:135–144, 2004.

J. C. del Álamo, J. Jiménez, P. Zandonade, and R. D. Moser. Self-similar vortex clusters in the turbulent logarithmic region. *Journal of Fluid Mechanics*, 561:329–358, 2006.

D. J. C. Dennis and T. B. Nickels. On the limitations of taylor's hypothesis in constructing long structures in a turbulent boundary layer. *Journal of Fluid Mechanics*, 614:197–206, 2008.

D. J. C. Dennis and T. B. Nickels. Experimental measurement of large-scale three-dimensional structures in a turbulent boundary layer. Part 2. Long structures. *Journal of Fluid Mechanics*, 673:218–244, 2011.

R. Deshpande, J. P. Monty, and I. Marusic. Streamwise inclination angle of large wall-attached structures in turbulent boundary layers. *Journal of Fluid Mechanics*, 877:R4, 2019a.

R. Deshpande, J. P. Monty, and I. Marusic. Correcting hotwire misalignment errors for wall-bounded turbulence measurements. In *Proceedings of the International Symposium on Turbulence & Shear Flow Phenomena (TSFP-11), Southampton, United Kingdom*, 2019b.

R. Deshpande, D. Chandran, J. P. Monty, and I. Marusic. Two-dimensional cross-spectrum of the streamwise velocity in turbulent boundary layers. *Journal of Fluid Mechanics*, 890:R2, 2020a.

R. Deshpande, J. P. Monty, and I. Marusic. Large-scale spanwise periodicity in a canonical turbulent boundary layer. In *Proceedings of 22nd Australasian Fluid Mechanics Conference, Brisbane, Australia*, 2020b.

R. Deshpande, J. P. Monty, and I. Marusic. Active and inactive motions in wall turbulence. In *Proceedings of 22nd Australasian Fluid Mechanics Conference, Brisbane, Australia*, 2020c.

R. Deshpande, J. P. Monty, and I. Marusic. A scheme to correct the influence of calibration misalignment for cross-wire probes in turbulent shear flows. *Experiments in Fluids*, 61 (3):1–17, 2020d.

R. Deshpande, J. P. Monty, and I. Marusic. Active and inactive components of the streamwise velocity in wall-bounded turbulence. *Journal of Fluid Mechanics*, 914:A5, 2021.

F. Eich, C. M. de Silva, I. Marusic, and C. J. Kähler. Towards an improved spatial representation of a boundary layer from the attached eddy model. *Physical Review Fluids*, 5(3):034601, 2020.

M. P. Encinar and J. Jiménez. Logarithmic-layer turbulence: A view from the wall. *Physical Review Fluids*, 4(11):114603, 2019.

M. P. Encinar, A. Vela-Martín, A. García-Gutiérrez, and J. Jiménez. A second-order consistent, low-storage method for time-resolved channel flow simulations. arXiv:1808.06461, 2018.

P. Fife, T. Wei, J. Klewicki, and P. McMurtry. Stress gradient balance layers and scale hierarchies in wall-bounded turbulent flows. *Journal of Fluid Mechanics*, 532:165–189, 2005.

B. Ganapathisubramani. Law of the wall for small-scale streamwise turbulence intensity in high-Reynolds-number turbulent boundary layers. *Physical Review Fluids*, 3(10):104607, 2018.

B. Ganapathisubramani, E. Longmire, and I. Marusic. Characteristics of vortex packets in turbulent boundary layers. *Journal of Fluid Mechanics*, 478:35–46, 2003.

B. Ganapathisubramani, N. Hutchins, W. Hambleton, E. K. Longmire, and I. Marusic. Investigation of large-scale coherence in a turbulent boundary layer using two-point correlations. *Journal of Fluid Mechanics*, 524:57–80, 2005.

B. Ganapathisubramani, N. Hutchins, J. P. Monty, D. Chung, and I. Marusic. Amplitude and frequency modulation in wall turbulence. *Journal of Fluid Mechanics*, 712(61): 064602–17, 2012.

Q. Gao, C. Ortiz-Duenas, and E. K. Longmire. Analysis of vortex populations in turbulent wall-bounded flows. *Journal of Fluid Mechanics*, 678:87–123, 2011.

H. L. Grant. The large eddies of turbulent motion. *Journal of Fluid Mechanics*, 4(2): 149–190, 1958.

Y. G. Guezennec. Stochastic estimation of coherent structures in turbulent boundary layers. *Physics of Fluids A: Fluid Dynamics*, 1(6):1054–1060, 1989.

J. M. Hamilton, J. Kim, and F. Waleffe. Regeneration mechanisms of near-wall turbulence structures. *Journal of Fluid Mechanics*, 287(1):317–348, 1995.

M. R. Head and P. Bandyopadhyay. New aspects of turbulent boundary-layer structure. *Journal of Fluid Mechanics*, 107:297–338, 1981.

M. Heisel, C. M. de Silva, N. Hutchins, I. Marusic, and M. Guala. On the mixing length eddies and logarithmic mean velocity profile in wall turbulence. *Journal of Fluid Mechanics*, 887, 2020.

S. Herpin, M. Stanislas, J. M. Foucaut, and S. Coudert. Influence of the Reynolds number on the vortical structures in the logarithmic region of turbulent boundary layers. *Journal of Fluid Mechanics*, 716:5, 2013.

J. O. Hinze. *Turbulence*, volume 218. McGraw-Hill New York, 1975.

U. Högström, J. C. R. Hunt, and A.-S. Smedman. Theory and measurements for turbulence spectra and variances in the atmospheric neutral surface layer. *Boundary-Layer Meteorology*, 103(1):101–124, 2002.

M. Hultmark, M. Vallikivi, S. C. C. Bailey, and A. J. Smits. Turbulent pipe flow at extreme Reynolds numbers. *Physical Review Letters*, 108(9):094501, 2012.

J. C. R. Hunt and P. Carlotti. Statistical Structure at the Wall of the High Reynolds Number Turbulent Boundary Layer. *Flow, Turbulence and Combustion*, 66(4):453–475, 2001.

J. C. R. Hunt and J. F. Morrison. Eddy structure in turbulent boundary layers. *European Journal of Mechanics-B/Fluids*, 19(5):673–694, 2000.

N. Hutchins and I. Marusic. Evidence of very long meandering features in the logarithmic region of turbulent boundary layers. *Journal of Fluid Mechanics*, 579:1–28, 2007.

N. Hutchins, T. B. Nickels, I. Marusic, and M. S. Chong. Hot-wire spatial resolution issues in wall-bounded turbulence. *Journal of Fluid Mechanics*, 635:103–136, 2009.

N. Hutchins, J. P. Monty, B. Ganapathisubramani, H. C. Ng, and I. Marusic. Three-dimensional conditional structure of a high-reynolds-number turbulent boundary layer. *Journal of Fluid Mechanics*, 673:255–285, 2011.

N. Hutchins, K. Chauhan, I. Marusic, J. Monty, and J. Klewicki. Towards reconciling the large-scale structure of turbulent boundary layers in the atmosphere and laboratory. *Boundary-layer meteorology*, 145(2):273–306, 2012.

J. Hwang and H. J. Sung. Wall-attached structures of velocity fluctuations in a turbulent boundary layer. *Journal of Fluid Mechanics*, 856:958–983, 2018.

J. Hwang, J. H. Lee, and H. J. Sung. Statistical behaviour of self-similar structures in canonical wall turbulence. *Journal of Fluid Mechanics*, 905:A6, 2020.

Y. Hwang. Statistical structure of self-sustaining attached eddies in turbulent channel flow. *Journal of Fluid Mechanics*, 767:254–289, 2015.

Y. Hwang and C. Cossu. Self-sustained process at large scales in turbulent channel flow. *Physical review letters*, 105(4):044505, 2010.

Y. Hwang and C. Cossu. Self-sustained processes in the logarithmic layer of turbulent channel flows. *Physics of Fluids*, 23(6):061702, 2011.

J. Jeong, F. Hussain, W. Schoppa, and J. Kim. Coherent structures near the wall in a turbulent channel flow. *Journal of Fluid Mechanics*, 332(185-214):188, 1997.

J. Jiménez. Cascades in wall-bounded turbulence. *Annual Review of Fluid Mechanics*, 44: 27–45, 2012.

J. Jiménez. Coherent structures in wall-bounded turbulence. *Journal of Fluid Mechanics*, 842, 2018.

J. Jimenez and S. Hoyas. Turbulent fluctuations above the buffer layer of wall-bounded flows. *Journal of Fluid Mechanics*, 611:215–236, 2008.

J. Jiménez and A. Pinelli. The autonomous cycle of near-wall turbulence. *Journal of Fluid Mechanics*, 389:335–359, 1999.

M. B. Jones, I. Marusic, and A. E. Perry. Evolution and structure of sink-flow turbulent boundary layers. *Journal of Fluid Mechanics*, 428:1–27, 2001.

F. E. Jørgensen. The computer-controlled constant-temperature anemometer. aspects of set-up, probe calibration, data acquisition and data conversion. *Measurement Science and Technology*, 7(10):1378, 1996.

G. Katul and C.-R. Chu. A theoretical and experimental investigation of energy-containing scales in the dynamic sublayer of boundary-layer flows. *Boundary-Layer Meteorology*, 86 (2):279–312, 1998.

G. Katul and B. Vidakovic. The partitioning of attached and detached eddy motion in the atmospheric surface layer using Lorentz wavelet filtering. *Boundary-Layer Meteorology*, 77(2):153–172, 1996.

G. G. Katul, A. Porporato, and V. Nikora. Existence of k^{-1} power-law scaling in the equilibrium regions of wall-bounded turbulence explained by Heisenberg's eddy viscosity. *Physical Review E*, 86(6):066311, 2012.

K. C. Kim and R. J. Adrian. Very large-scale motion in the outer layer. *Physics of Fluids*, 11(2):417–422, 1999.

L. V. King. On the convection of heat from small cylinders in a stream of fluid: Determination of the convection constants of small platinum wires with applications to hot-wire anemometry. *Phil. Trans. R. Soc. Lond. A*, 214(509-522):373–432, 1914.

J. Klewicki, P. Fife, and T. Wei. On the logarithmic mean profile. *Journal of Fluid Mechanics*, 638:73–93, 2009.

J. C. Klewicki. Reynolds number dependence, scaling, and dynamics of turbulent boundary layers. *Journal of Fluids Engineering*, 132(9), 2010.

S. J. Kline, W. C. Reynolds, F. Schraub, and P. Runstadler. The structure of turbulent boundary layers. *Journal of Fluid Mechanics*, 30(4):741–773, 1967.

A. N. Kolmogorov. The local structure of turbulence in incompressible viscous fluid for very large Reynolds numbers. In *Dokl. Akad. Nauk SSSR*, volume 30, pages 299–303, 1941.

V. Kulandaivelu. *Evolution of zero pressure gradient turbulent boundary layers from different initial conditions*. PhD thesis, University of Melbourne, Department of Mechanical Engineering, 2012.

G. J. Kunkel and I. Marusic. Study of the near-wall-turbulent region of the high-Reynolds-number boundary layer using an atmospheric flow. *Journal of Fluid Mechanics*, 548: 375–402, 2006.

J. Lee, J. H. Lee, J. Choi, and H. J. Sung. Spatial organization of large-and very-large-scale motions in a turbulent channel flow. *Journal of Fluid Mechanics*, 749:818–840, 2014.

J. H. Lee and H. J. Sung. Very-large-scale motions in a turbulent boundary layer. *Journal of Fluid Mechanics*, 673:80–120, 2011.

J. H. Lee, J. P. Monty, and N. Hutchins. Validating under-resolved turbulence intensities for piv experiments in canonical wall-bounded turbulence. *Experiments in Fluids*, 57(8): 129, 2016.

M. Lee and R. D. Moser. Direct numerical simulation of turbulent channel flow up to $Re_\tau \approx 5200$. *Journal of Fluid Mechanics*, 774:395–415, 2015.

M. Lee and R. D. Moser. Spectral analysis of the budget equation in turbulent channel flows at high Reynolds number. *Journal of Fluid Mechanics*, 860:886–938, 2019.

P. M. Ligrani and P. Bradshaw. Spatial resolution and measurement of turbulence in the viscous sublayer using subminiature hot-wire probes. *Experiments in Fluids*, 5(6): 407–417, 1987.

C. Liu and D. F. Gayme. An input–output based analysis of convective velocity in turbulent channels. *Journal of Fluid Mechanics*, 888, 2020.

A. Lozano-Durán, O. Flores, and J. Jiménez. The three-dimensional structure of momentum transfer in turbulent channels. *Journal of Fluid Mechanics*, 694:100–130, 2012.

A. Madhusudanan, S. J. Illingworth, and I. Marusic. Coherent large-scale structures from the linearized Navier–Stokes equations. *Journal of Fluid Mechanics*, 873:89–109, 2019.

I. Marusic. On the role of large-scale structures in wall turbulence. *Physics of Fluids*, 13 (3):735–743, 2001.

I. Marusic and R. J. Adrian. The eddies and scales of wall turbulence. In *Ten chapters in turbulence*, pages 176–220. Cambridge University Press, 2010.

I. Marusic and W. D. C. Heuer. Reynolds number invariance of the structure inclination angle in wall turbulence. *Physical review letters*, 99(11):114504, 2007.

I. Marusic and J. P. Monty. Attached eddy model of wall turbulence. *Annual Review of Fluid Mechanics*, 51:49–74, 2019.

I. Marusic and A. E. Perry. A wall-wake model for the turbulence structure of boundary layers. Part 2. Further experimental support. *Journal of Fluid Mechanics*, 298:389–407, 1995.

I. Marusic, G. J. Kunkel, and F. Porte-Agel. Experimental study of wall boundary conditions for large-eddy simulation. *Journal of Fluid Mechanics*, 446:309–320, 2001.

I. Marusic, R. Mathis, and N. Hutchins. Predictive model for wall-bounded turbulent flow. *Science*, 329(5988):193–196, 2010a.

I. Marusic, R. Mathis, and N. Hutchins. High Reynolds number effects in wall turbulence. *International Journal of Heat and Fluid Flow*, 31(3):418 – 428, 2010b.

I. Marusic, B. J. McKeon, P. A. Monkewitz, H. M. Nagib, A. J. Smits, and K. R. Sreenivasan. Wall-bounded turbulent flows at high Reynolds numbers: recent advances and key issues. *Physics of Fluids*, 22(6):065103, 2010c.

I. Marusic, J. P. Monty, M. Hultmark, and A. J. Smits. On the logarithmic region in wall turbulence. *Journal of Fluid Mechanics*, 716:R3, 2013.

I. Marusic, K. A. Chauhan, V. Kulandaivelu, and N. Hutchins. Evolution of zero-pressure-gradient boundary layers from different tripping conditions. *Journal of Fluid Mechanics*, 783:379–411, 2015.

R. Mathis, N. Hutchins, and I. Marusic. Large-scale amplitude modulation of the small-scale structures in turbulent boundary layers. *Journal of Fluid Mechanics*, 628:311–337, 2009.

R. Mathis, I. Marusic, S. I. Chernyshenko, and N. Hutchins. Estimating wall-shear-stress fluctuations given an outer region input. *Journal of Fluid Mechanics*, 715:163, 2013.

B. J. McKeon and J. F. Morrison. Asymptotic scaling in turbulent pipe flow. *Philosophical Transactions of the Royal Society A: Mathematical, Physical and Engineering Sciences*, 365(1852):771–787, 2007.

C. D. Meinhart and R. J. Adrian. On the existence of uniform momentum zones in a turbulent boundary layer. *Physics of Fluids*, 7(4):694–696, 1995.

C. B. Millikan. A critical discussion of turbulent flow in channels and circular tubes. In *Proc. 5th Int. Congress on Applied Mechanics (Cambridge, MA, 1938)*, pages 386–392. Wiley, 1939.

P. Moin and J. Kim. The structure of the vorticity field in turbulent channel flow. Part 1. Analysis of instantaneous fields and statistical correlations. *Journal of Fluid Mechanics*, 155:441–464, 1985.

J. P. Monty. *Developments in smooth wall turbulent duct flows*. PhD thesis, University of Melbourne, Department of Mechanical and Manufacturing Engineering, 2005.

J. P. Monty and M. S. Chong. Turbulent channel flow: comparison of streamwise velocity data from experiments and direct numerical simulation. *Journal of Fluid Mechanics*, 633:461–474, 2009.

J. P. Monty, J. A. Stewart, R. C. Williams, and M. S. Chong. Large-scale features in turbulent pipe and channel flows. *Journal of Fluid Mechanics*, 589:147–156, 2007.

J. P. Monty, N. Hutchins, H. C. H. Ng, I. Marusic, and M. S. Chong. A comparison of turbulent pipe, channel and boundary layer flows. *Journal of Fluid Mechanics*, 632: 431–442, 2009.

C. Morrill-Winter, J. Klewicki, R. Baidya, and I. Marusic. Temporally optimized spanwise vorticity sensor measurements in turbulent boundary layers. *Experiments in Fluids*, 56 (12):216, 2015.

J. F. Morrison. The interaction between inner and outer regions of turbulent wall-bounded flow. *Philosophical Transactions of the Royal Society A: Mathematical, Physical and Engineering Sciences*, 365(1852):683–698, 2007.

J. F. Morrison, C. S. Subramanian, and P. Bradshaw. Bursts and the law of the wall in turbulent boundary layers. *Journal of Fluid Mechanics*, 241:75–108, 1992.

W. R. B. Morrison and R. E. Kronauer. Structural similarity for fully developed turbulence in smooth tubes. *Journal of Fluid Mechanics*, 39(1):117–141, 1969.

A. M. Naguib, C. E. Wark, and O. Juckenhöfel. Stochastic estimation and flow sources associated with surface pressure events in a turbulent boundary layer. *Physics of Fluids*, 13(9):2611–2626, 2001.

H. C. H. Ng. *Experiments in smooth wall turbulent channel and pipe flows.* PhD thesis, University of Melbourne, Department of Mechanical and Manufacturing Engineering, 2011.

T. B. Nickels, I. Marusic, S. Hafez, and M. S. Chong. Evidence of the k_1^{-1} Law in a High-Reynolds-Number Turbulent Boundary Layer. *Physical Review Letters*, 95(7):074501, 2005.

T. B. Nickels, I. Marusic, S. Hafez, N. Hutchins, and M. S. Chong. Some predictions of the attached eddy model for a high Reynolds number boundary layer. *Philosophical Transactions of the Royal Society A: Mathematical, Physical and Engineering Sciences*, 365(1852):807–822, 2007.

V. Nikora. Origin of the "- 1" spectral law in wall-bounded turbulence. *Physical Review Letters*, 83(4):734, 1999.

M. Oberlack. A unified approach for symmetries in plane parallel turbulent shear flows. *Journal of Fluid Mechanics*, 427:299, 2001.

G. R. Offen and S. J. Kline. A proposed model of the bursting process in turbulent boundary layers. *Journal of Fluid Mechanics*, 70(2):209–228, 1975.

P. Orlandi, M. Bernardini, and S. Pirozzoli. Poiseuille and Couette flows in the transitional and fully turbulent regime. *Journal of Fluid Mechanics*, 770:424–441, 2015.

R. L. Panton. Overview of the self-sustaining mechanisms of wall turbulence. *Progress in Aerospace Sciences*, 37(4):341–383, 2001.

R. L. Panton. Composite asymptotic expansions and scaling wall turbulence. *Philosophical Transactions of the Royal Society A: Mathematical, Physical and Engineering Sciences*, 365(1852):733–754, 2007.

A. Perry and M. Chong. On the mechanism of wall turbulence. *Journal of Fluid Mechanics*, 119:173–217, 1982.

A. E. Perry. *Hot-wire anemometry.* Oxford Science Publication, 1982.

A. E. Perry and C. J. Abell. Asymptotic similarity of turbulence structures in smooth-and rough-walled pipes. *Journal of Fluid Mechanics*, 79(4):785–799, 1977.

A. E. Perry and I. Marusic. A wall-wake model for the turbulence structure of boundary layers. Part 1. Extension of the attached eddy hypothesis. *Journal of Fluid Mechanics*, 298:361–388, 1995.

A. E. Perry, T. T. Lim, and E. W. Teh. A visual study of turbulent spots. *J. Fluid Mech*, 104:387–405, 1981.

A. E. Perry, S. Henbest, and M. S. Chong. A theoretical and experimental study of wall turbulence. *Journal of Fluid Mechanics*, 165:163–199, 1986.

A. E. Perry, K. L. Lim, and S. M. Henbest. An experimental study of the turbulence structure in smooth-and rough-wall boundary layers. *Journal of Fluid Mechanics*, 177: 437–466, 1987.

A. E. Perry, A. K. M. Uddin, and I. Marusic. An experimental and computational study on the orientation of attached eddies in turbulent boundary layers. In *Proceedings of the 11th Australasian Fluid Mechanics Conference, Hobart, Australia*, 1992.

J. Philip, R. Baidya, N. Hutchins, J. P. Monty, and I. Marusic. Spatial averaging of streamwise and spanwise velocity measurements in wall-bounded turbulence using v- and ×-probes. *Measurement Science and Technology*, 24(11):115302, 2013.

U. Piomelli and E. Balaras. Wall-layer models for large-eddy simulations. *Annual review of fluid mechanics*, 34(1):349–374, 2002.

U. Piomelli, J. Ferziger, P. Moin, and J. Kim. New approximate boundary conditions for large eddy simulations of wall-bounded flows. *Physics of Fluids A: Fluid Dynamics*, 1 (6):1061–1068, 1989.

S. Pirozzoli and M. Bernardini. Probing high-Reynolds-number effects in numerical boundary layers. *Physics of Fluids*, 25(2):021704, 2013.

L. Prandtl. Über flussigkeitsbewegung bei sehr kleiner reibung. *Verhandl. III, Internat. Math.-Kong., Heidelberg, Teubner, Leipzig, 1904*, pages 484–491, 1904.

L. Prandtl. Bericht über untersuchungen zur ausgebildeten turbulenz. *ZAMM*, 5(2):136–139, 1925.

S. K. Robinson. Coherent motions in the turbulent boundary layer. *Annual Review of Fluid Mechanics*, 23(1):601–639, 1991.

B. J. Rosenberg, M. Hultmark, M. Vallikivi, S. C. C. Bailey, and A. J. Smits. Turbulence spectra in smooth-and rough-wall pipe flow at extreme Reynolds numbers. *Journal of Fluid Mechanics*, 731:46, 2013.

S. G. Saddoughi and S. V. Veeravalli. Local isotropy in turbulent boundary layers at high Reynolds number. *Journal of Fluid Mechanics*, 268:333–372, 1994.

M. Samie, I. Marusic, N. Hutchins, M. K. Fu, Y. Fan, M. Hultmark, and A. J. Smits. Fully resolved measurements of turbulent boundary layer flows up to $Re_\tau = 20\,000$. *Journal of Fluid Mechanics*, 851:391–415, 2018.

J. A. Sillero, J. Jiménez, and R. D. Moser. One-point statistics for turbulent wall-bounded flows at Reynolds numbers up to $\delta^+ \approx 2000$. *Physics of Fluids*, 25(10):105102, 2013.

J. A. Sillero, J. Jiménez, and R. D. Moser. Two-point statistics for turbulent boundary layers and channels at Reynolds numbers up to $\delta^+ \approx 2000$. *Physics of Fluids*, 26(10): 105109, 2014.

A. J. Smits and I. Marusic. Wall-bounded turbulence. *Phys. Today*, 66(9):25–30, 2013.

A. J. Smits, B. J. McKeon, and I. Marusic. High–Reynolds number wall turbulence. *Annual Review of Fluid Mechanics*, 43, 2011.

D. T. Squire, C. Morrill-Winter, N. Hutchins, M. P. Schultz, J. C. Klewicki, and I. Marusic. Comparison of turbulent boundary layers over smooth and rough surfaces up to high reynolds numbers. *Journal of Fluid Mechanics*, 795:210, 2016.

A. Strohl and G. Comte-Bellot. Aerodynamic effects due to configuration of x-wire anemometers. *Journal of Applied Mechanics*, 40(3):661–667, 1973.

Y. Suzuki and N. Kasagi. Evaluation of hot-wire measurements in wall shear turbulence using a direct numerical simulation database. *Experimental thermal and fluid science*, 5 (1):69–77, 1992.

M. Tagawa, T. Tsuji, and Y. Nagano. Evaluation of x-probe response to wire separation for wall turbulence measurements. *Experiments in Fluids*, 12(6):413–421, 1992.

K. M. Talluru, V. Kulandaivelu, N. Hutchins, and I. Marusic. A calibration technique to correct sensor drift issues in hot-wire anemometry. *Measurement Science and Technology*, 25(10):105304, 2014.

G. I. Taylor. The spectrum of turbulence. *Proceedings of the Royal Society of London. Series A-Mathematical and Physical Sciences*, 164(919):476–490, 1938.

H. Tennekes and J. L. Lumley. *A First Course in Turbulence*. MIT Press, 1972.

T. Theodorsen. Mechanisms of turbulence. In *Proceedings of the 2nd Midwestern Conference on Fluid Mechanics, 1952*, 1952.

C. Tinney, F. Coiffet, J. Delville, A. M. Hall, P. Jordan, and M. N. Glauser. On spectral linear stochastic estimation. *Experiments in Fluids*, 41(5):763–775, 2006.

C. D. Tomkins and R. J. Adrian. Spanwise structure and scale growth in turbulent boundary layers. *Journal of Fluid Mechanics*, 490:37–74, 2003.

C. D. Tomkins and R. J. Adrian. Energetic spanwise modes in the logarithmic layer of a turbulent boundary layer. *Journal of Fluid Mechanics*, 545:141–162, 2005.

A. A. Townsend. Equilibrium layers and wall turbulence. *Journal of Fluid Mechanics*, 11 (1):97–120, 1961.

A. A. Townsend. *The structure of turbulent shear flow*. Cambridge University Press, 2nd edn. Cambridge University Press edition, 1976.

C. Tropea and A. L. Yarin. *Springer handbook of experimental fluid mechanics*, volume 1. Springer Science & Business Media, 2007.

N. K. Tutu and R. Chevray. Cross-wire anemometry in high intensity turbulence. *Journal of Fluid Mechanics*, 71(4):785–800, 1975.

A. K. M. Uddin. *The structure of a turbulent boundary layer*. PhD thesis, University of Melbourne, Department of Mechanical and Manufacturing Engineering, 1994.

M. Van Dyke. *An album of fluid motion*. Parabolic Press Stanford, 1982.

T. von Kármán. Mechanische ahnlichkeit und turbulenz. *Math.-Phys. Klasse*, 1930.

J. M. Wallace and P. V. Vukoslavčević. Measurement of the velocity gradient tensor in turbulent flows. *Annual Review of Fluid Mechanics*, 42:157–181, 2010.

W. W. Willmarth and T. J. Bogar. Survey and new measurements of turbulent structure near the wall. *The Physics of Fluids*, 20(10):S9–S21, 1977.

J. D. Woodcock and I. Marusic. The statistical behaviour of attached eddies. *Physics of Fluids*, 27(1):015104, 2015.

S. Wu, K. Christensen, and P. C. Modelling smooth- and transitionally rough-wall turbulent channel flow by leveraging inner–outer interactions and principal component analysis. *Journal of Fluid Mechanics*, 863:407–453, 2019.

X. Wu and P. Moin. Direct numerical simulation of turbulence in a nominally zero-pressure-gradient flat-plate boundary layer. *Journal of Fluid Mechanics*, 630:5–41, 2009.

X. Wu, J. R. Baltzer, and R. J. Adrian. Direct numerical simulation of a 30R long turbulent pipe flow at R$\hat{}$+ = 685: large-and very large-scale motions. *Journal of Fluid Mechanics*, 698:235–281, 2012.

S. Yavuzkurt. A guide to uncertainty analysis of hot-wire data. *ASME, Transactions, Journal of Fluids Engineering*, 106(2):181–186, 1984.

M. Yoon, J. Hwang, J. Yang, and H. J. Sung. Wall-attached structures of streamwise velocity fluctuations in an adverse-pressure-gradient turbulent boundary layer. *Journal of Fluid Mechanics*, 885:A12, 2020.

M. V. Zagarola and A. J. Smits. Mean-flow scaling of turbulent pipe flow. *Journal of Fluid Mechanics*, 373:33–79, 1998.

J. Zhou, R. J. Adrian, S. Balachandar, and T. M. Kendall. Mechanisms for generating coherent packets of hairpin vortices in channel flow. *Journal of Fluid Mechanics*, 387: 353–396, 1999.

S. Zimmerman, C. Morrill-Winter, and J. Klewicki. Design and implementation of a hot-wire probe for simultaneous velocity and vorticity vector measurements in boundary layers. *Experiments in Fluids*, 58(10):148, 2017.